Coarse–Grained Models for the Kinetics of Polymeric Systems

Vergröberte Modelle zur Beschreibung
der Kinetik von Polymersystemen

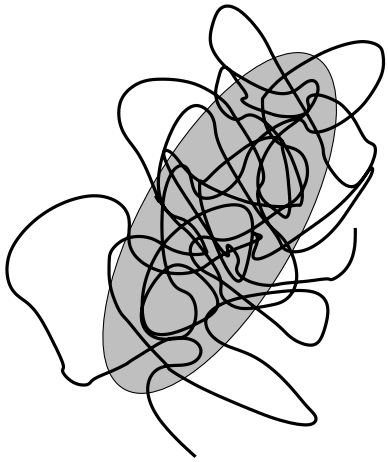

Dissertation
zur Erlangung des akademischen Grades
des Doktors der Naturwissenschaften (Dr. rer. nat.)
an der Universität Konstanz
Fachbereich Physik

vorgelegt von

Frank Eurich

Tag der mündlichen Prüfung: 18. Juli 2002
Referent: Prof. Dr. Philipp Maaß
Referent: Prof. Dr. Peter Nielaba

Bibliografische Information Der Deutschen Bibliothek

Die Deutsche Bibliothek verzeichnet diese Publikation in der Deutschen Nationalbibliografie; detaillierte bibliografische Daten sind im Internet über <http://dnb.ddb.de> abrufbar.

Es wird ausschließlich chlorfrei gebleichtes
Papier (TCF) nach DIN-ISO 9706 verwendet.
Printed in Germany.

dissertation.de - Verlag im Internet GmbH
Pestalozzistraße 9
10 625 Berlin

URL: http://www.dissertation.de

Zusammenfassung

Diese Arbeit befasst sich mit der Beschreibung des kinetischen Verhaltens von Polymersystemen auf halbmakroskopischen Zeit– und Längenskalen. Grundlage der Beschreibung sind hierbei aus mikroskopischen Konzepten abgeleitete, vergröberte Modelle. Ein besonderes Augenmerk liegt auf der Entmischungskinetik von binären Polymermischungen in eingeschränkten Geometrien. Dabei werden sowohl homogene, als auch heterogene Substrate untersucht. Letztere sind von besonderem technologischen Interesse, da man mit ihrer Hilfe versucht, gezielt Polymerstrukturen im μm und sub–μm Bereich herzustellen. Solche Strukturen könnten zum Beispiel dazu dienen, mikroelektronische Schaltkreise aus organischen Halbleitern aufzubauen. Verwendung finden könnten sie weiterhin als polymere Masken in der Lithographie bei der Herstellung von Prozessoren oder als Materialien mit besonderen optischen Eigenschaften. Eine bereits realisierte Anwendung ist eine verbesserte Antireflexbeschichtung.

Die Diffusion von langkettigen Polymeren wird dadurch verlangsamt, dass in einem dichten System die Kettenmoleküle Verschlaufungen bilden. Die charakteristische Zeitskala, auf der sich diese Verschlaufungen auflösen, skaliert mit der dritten Potenz der Kettenlänge. Daher kann das Langzeitverhalten von Polymersystemen kaum in Simulationen von Modellen erreicht werden, welche die Kettenstruktur der Moleküle berücksichtigen. Wir verwenden daher eine gröbere Beschreibung der Systeme.

Zunächst betrachten wir Systeme im Rahmen der zeitabhängigen Ginzburg–Landau Theorie. Für den Fall einer binären Mischung entspricht diesem Zugang die Beschreibung des Systems durch die Cahn–Hilliard Gleichung, welche eine nichtlineare, partielle Differentialgleichung für das Ordnungsparameterfeld darstellt. Der Ordnungsparameter ist in diesem Fall die Differenz der entsprechenden Konzentrationen beider Komponenten. Das Kurzzeitverhalten des Systems kann im Rahmen der Theorie durch eine Stabilitätsanalyse beschrieben werden, die bezüglich des Anfangszustandes des linearisierten Problems durchgeführt wird. Aus dieser Analyse leiten wir ein Kriterium für die Unterdrückung von oberflächeninduzierten spinodalen Wellen in dünnen Filmen ab.

In einer früheren Stabilitätsanalyse der Cahn–Hilliard Gleichung [Fis98b] wird das Auftreten von neuen charakteristischen Längen– und Zeitskalen bei Entmischungsprozessen in eingeschränkten Geometrien vorhergesagt. In sehr dünnen Filmen kann dabei die spinodale Entmischung unterdrückt werden. Um diese Vorhersagen zu testen, wird die Cahn–Hilliard Gleichung in zwei Dimensionen numerisch gelöst. Dass das entsprechende Liniensystem der Gleichung "steif" ist, führt zu einer Beschränkung der möglichen Zeitschritte bei der Anwendung von expliziten Verfahren zur numerischen Integration der Gleichung in der Zeit. Durch die Anwendung eines impliziten Verfahrens können diese Beschränkungen umgangen und die gesamte Kinetik des System von den Anfängen der Phasenseparation bis hin zum Gleichgewicht

verfolgt werden. Dies ist besonders für den uns interessierenden Fall einer binären Mischung zwischen zwei Wänden wichtig. Zum einen wächst die charakteristische Zeitskala bei der Entmischung mit einer Verringerung der Filmdicke an, zum anderen findet zu späten Zeiten ein extrem langsamer, quasi–eindimensionaler Periodenverdopplungsprozess statt. Die Vorhersagen der Stabilitätsanalyse werden durch die numerischen Studien bestätigt. Eine Übertragung des Verfahrens auf dreidimensionale Systeme ist allerdings aufgrund der momentan verfügbaren Computerkapazitäten nicht praktikabel.

Eine realistischere Beschreibung der Systeme geben Modelle, in denen ein Polymer als ein weiches Teilchen mit inneren Freiheitsgraden beschrieben wird. Eine Möglichkeit, Polymersysteme auf diese Weise zu beschreiben, wurde von Murat und Kremer vorgeschlagen [Mur98]. Im Prinzip werden bei dieser Art von Modell die möglichen Zustände einer Polymerkette durch einen oder mehrere Parameter charakterisiert, zum Beispiel durch die Eigenwerte des Trägheitstensors. Alle Polymere mit der gleichen Charakteristik, d.h. den gleichen Parametern, werden als äquivalente weiche Teilchen betrachtet. Die Kette selbst wird durch eine mittlere Monomerdichte bei einer gegebenen Charakteristik beschrieben. Für ein System aus solchen weichen Teilchen wird das Funktional der Freien Energie in einen intramolekularen und einen intermolekularen Anteil separiert. Bei diesem Ansatz wird der intramolekulare Anteil durch die Wahrscheinlichkeit für das Auftreten bestimmter Teilchenformen festgelegt, der intermolekulare Anteil durch das Überlappintegral der Monomerdichten. Da Polymere oft durch vergröberte Kettenmodelle beschrieben werden, bei denen mehrere Monomere auf ein effektives Kettenglied abgebildet werden, kann man diese Art der Beschreibung als einen zweiten Vergröberungsschritt auffassen. Die Kinetik des Systems weicher Teilchen wird durch einen Monte Carlo Algorithmus definiert.

Als zu Grunde liegendes Kettenmodel für die Beschreibung von Polymeren durch weiche Teilchen wählen wir die Gauß'sche Kette. Für diese werden in einer detaillierten Studie die für den Aufbau der Modelle notwendigen Eingangsgrößen bestimmt. Dies sind zum einen die Wahrscheinlichkeitsverteilungen für das Auftreten einer bestimmten Form, zum anderen die entsprechenden bedingten Monomerdichten für eine gegebene Form. Es zeigt sich, dass durch geeignete Skalen– und Separationsansätze die Komplexität dieser Funktionen deutlich reduziert werden kann. Inwieweit diese Ansätze eine Näherung darstellen, wird ausführlich diskutiert. Schließlich werden geschlossene Ausdrücke für die Eingangsgrößen angegeben, die bei ihrer Implementierung das Modell weicher Teilchen sehr effizient machen. Die Simulationen des Systems weicher Teilchen werden für das Ellipsoid–Modell durchgeführt.

In der Arbeit von Murat und Kremer stellte das Bead–Spring Modell das zu Grunde liegende Kettenmodell dar [Mur98]. Ein wesentlicher Aspekt dieser Arbeit ist die Anbindung des Modells weicher Teilchen an Kettenmodelle. Es wurde gezeigt, dass ein entsprechendes dichtes System weicher Teilchen wesentliche Eigenschaften von Polymersystemen aufweist. Das korrekte Skalenverhalten des Gyrationsradius in dichten Systemen konnte allerdings nur durch die Einführung eines von der Kettenlänge abhängigen Wechselwirkungsparameters erreicht werden. Dieser wurde durch Anpassung der Teilchengröße an Ergebnisse von Simulationen des Bead–Spring Modells bestimmt.

Die Wahl der Gauß'schen Kette hat den Vorteil, dass das Model unter Berücksichtigung eines Selbstwechselwirkungsterms die wesentlichen Skalenrelationen der Polymerphysik in natürlicher Weise, d.h. ohne die Anpassung eines Wechselwirkungsparameters, erfüllt. Insbeson-

dere sind auch keine Simulationen von Kettensystemen für eine vollständige Definition des Modells erforderlich. Das Skalenverhalten des Gyrationsradius wird in Abhängigkeit von der Kettenlänge und der Teilchendichte richtig wiedergegeben, allerdings mit Florys Resultat für den Exponenten ν. Das Modell ist nicht nur effizient, so dass das Langzeitverhalten der Phasenseparation in dreidimensionalen Systemen beschrieben werden kann, sondern weist auch viele charakteristische Eigenschaften von Polymersystemen auf, so zum Beispiel die Existenz eines Korrelationslochs, sowie Umorientierungen und Deformationen der Ellipsoide an Phasengrenzflächen.

Schließlich werden Polymersysteme in eingeschränkten Geometrien im Rahmen dieses Ellipsoid–Modells beschrieben. Die Ergebnisse für eine binäre Mischung zwischen zwei homogenen und neutralen Wänden bestätigt qualitativ die Vorhersagen der Cahn–Hilliard Theorie, nämlich ein Wachstum der lateralen Entmischunglänge und der entsprechenden Zeiten mit abnehmender Filmdicke. Eine Unterdrückung der spinodalen Entmischung wie von der Cahn–Hilliard Theorie vorhergesagt wird allerdings aufgrund der in diesem System vorhandenen thermischen Fluktuationen nicht gefunden.

Zur Untersuchung der Entmischungskinetik auf heterogenen Substraten wird der Fall betrachtet, dass eine der beiden Wände mit einem periodischen Streifenmuster strukturiert ist. Verschiedene Bereiche des Substrats bevorzugen unterschiedliche Komponenten. Wir finden hierbei zwei unterschiedliche Gleichgewichtsstrukturen. Entweder wird das Substratmuster vollständig auf die Domänenstruktur übertragen, oder das von der Oberfläche induzierte Muster dringt nur ein Stück weit in den Film ein. Der Übergang zwischen den beiden Strukturen findet bei einem bestimmten Verhältnis von Periodizität und Filmdicke statt, was durch eine Betrachtung der Grenzflächenenergien erklärt werden kann.

Betrachtet man den Verlauf des Entmischungsprozesses, so werden die unterschiedlichen Gleichgewichtsstrukturen auf verschiedene Art und Weise angenommen. Für den Fall, dass die Oberflächenstruktur vollständig abgebildet wird, ist die Ausbildung einer musterinduzierten spinodalen Welle – in Analogie zur oberflächeninduzierten spinodalen Welle – der zu Grunde liegende Prozess. Die periodische Ordnung des Domänenmusters friert ein, sobald die gegenüberliegende Oberfläche erreicht ist. Ist die Eindringtiefe der Struktur dagegen endlich, so findet zusätzlich eine laterale Vergröberung der Domänenstruktur statt. Für den Fall, dass die Periodizität des Musters kleiner ist als die charakteristische Entmischungslänge des "ungestörten" Systems, wird der Einfluß des Substratmusters auf die Domänenstruktur reduziert, da dem System durch die Oberfläche energetisch ungünstige Strukturen mit zu vielen Grenzflächen aufgeprägt werden.

Contents

List of Figures

List of Tables

Notation

Throughout this work we denote spatial indices by lowercase Greek letters and particle indices by lowercase Latin letters. Indices referring to a grid are also denoted by lowercase Latin letters. Quantities referring to components of a mixture or copolymer are marked by respective uppercase Latin indices A, B, C or X.

If the components are not explicitely denoted by respective indices, matrices are usually denoted by calligraphic letters and vectors are typed in bold. If a vector symbol is not typed bold, then usually the norm of the respective vector is meant.

The coordinates in the laboratory system are denoted by $\mathbf{y} \equiv (y_1, y_2, y_3) \equiv (x, y, z)$, the coordinates in the principal axis system of a chain or an ellipsoid by $\mathbf{x} \equiv (x_1, x_2, x_3)$.

Averages of a quantity Q are denoted either by $\langle Q \rangle$ or by $\bar{Q}$.

List of Abbreviations

AFM	atomic force microscopy
BDF	backward differentiation formulae
CDS	cell dynamical system
CHE	Cahn–Hilliard equation
CPU	central processing unit
DSCFT	dynamic self–consistent–field theory
EPD	external potential dynamics
GEM	Gaussian ellipsoid model
MCS	Monte Carlo step
ODT	octadecylthiol
OM	optical microscopy
PB	polybutadiene
PEP	poly(ethylene–propylene)
PMMA	polymethylmethacrylate
PS	polystyrene
PVP	polyvinylpyridine
RIS	rotational isomeric state
SAM	self assembled monolayer
SCFT	self–consistent–field theory
SDW	surface directed spinodal wave
TOF–ERD	time–of–flight elastic–recoil–detection
TOF–FRES	time–of–flight forward–recoil–spectrometry

List of Symbols

$\langle A \rangle$	average asphericity
A, B	first and second component of a mixture or block copolymer
$A_n, B_n, A_{n,r}, B_{n,r}$	Fourier coefficients
$B_2(T)$	second virial coefficient
$C_R(t), C_O(t)$	autocorrelation functions of shape and orientation
D	diffusion constant
$D(\phi)$	order parameter distribution
E_1	typical energy of a covalent bond
E_2	typical contact energy between two monomers
F	free energy, free energy functional
$F_b[\phi], F_s[\phi]$	bulk and surface part of the free energy functional
$F_{\text{inter}}, F_{\text{intra}}, F_{\text{wall}}$	intermolecular, intramolecular, and wall interaction part of the free energy functional
$G(\mathbf{y}, t)$	correlation function of the order parameter
$G_{\parallel}(\mathbf{y}_{\parallel}, z, t)$	lateral correlation function
$G_0(\mathbf{y}, \mathbf{y}')$	pair correlation function
$G_{\text{cm}}(r)$	correlation function of centers of mass
$H(.)$	step function
$I(\mathbf{k}, t)$	intermediate scattering function
$I_{\parallel}(\mathbf{k}_{\parallel}, z, t)$	lateral intermediate scattering function
$K(\rho)$	characteristic function of $P_R(R_G^2)$
$K_n(.)$	modified Bessel function of n'th order
L	system size
$L_{\parallel}$	periodicity of substrate pattern
L_{crit}	critical thickness for SDW formation
L_p	contour length of a polymer chain
L_t	contour length of the primitive path of the tube
L_D	average domain size
M, M_A, M_B	number of polymers or ellipsoids
$N+1$	number of beads of a Gaussian polymer chain
N_A, N_B	number of beads of components A and B
N_A, N_B	number of beads of a block
N_e	entanglement length
N_p+1	number of monomers in a polymer
$P(.)$	probability distribution of a quantity
$P(.\,,.)$	joint probability distribution
$P(.\,;.)$	conditional probability distribution
$\tilde{P}(.)$	scaling function for a probability distribution
Q_A, Q_B	partition function of a single chain of type A or B
$\mathbf{R}$	end–to–end vector of a polymer chain
$\mathcal{R}$	rotation matrix
$R(t)$	inverse of $k_n(t)$

$R_0(t)$	first zero of $g(r,t)$
$R_{0,\|\|}(t)$	first zero of $G_{\|\|}(\mathbf{y}_{\|\|},0,t)$
R_e	root mean square end–to–end distance
R_G	radius of gyration
$\bar{R}_G$	average radius of gyration
ΔR_G^2	random change of R_G^2
R_A, R_B	radius of gyration of a block
$R_\alpha \equiv \sqrt{S_\alpha}$	extension of ellipsoid with respect to principal axis
$R_{G\|\|}, R_{G\perp}$	lateral and perpendicular radius of gyration with respect to a wall
$S(\mathbf{q})$	structure function
$S_{\alpha\beta},\ \mathbf{S} \equiv S_\alpha$	radius of gyration tensor and its eigenvalues
ΔS_α	random change of S_α
$T,\ T_c$	temperature, critical temperature
$U(\mathbf{u})$	effective bond potential of a Gaussian chain
$V,\ \partial V$	volume, surface
$V_w(z)$	wall potential
W_A, W_B	auxiliary fields in self–consistent field theory
$W_A(\rho_A), W_B(\rho_B)$	quantities needed in the calculation of $P_{AB}(\mathbf{r}_{AB}, R_A^2, R_B^2)$
Z	partition sum
$a(T),\ b$	parameters in Ginzburg–Landau free energy density
b	root mean square bond length of a Gaussian chain
c	monomer concentration in a polymeric system
c_cm	concentration of centers of mass
$c_\star$	crossover monomer concentration from the dilute to the semi–dilute regime
d_t	tube diameter
f	free energy, free energy density
$f(u)$	scaling function
$f_b,\ f_s$	bulk and surface free energy density
$f(\{\mathbf{y}_i\}),\ f_G(\{\mathbf{y}_i\})$	partition function of a single polymer, a Gaussian coil
f_A, f_B	fraction of chains of one component
$\mathbf{f}_i$	force on bead i
g	number of beads in a blob
g	parameter in f_s describing modification of interactions
g_s	scaled surface parameter
$g(r,t)$	circular averaged correlation function $G(\mathbf{y},t)$
h	parameter in f_s describing external surface field
h_l	scaled surface parameter in linearized CHE
$\mathbf{j}(\mathbf{y},t)$	interdiffusive current
k_c	critical wave vector
$k_n(t)$	nth moment of $I(k,t)$
k_n	discrete wave vectors
$k_{1,\|\|}(t)$	film averaged first moment of $I_{\|\|}(k_{\|\|},z,t)$
k_B	Boltzmann constant, $k_B = 1,380662 \cdot 10^{-23}$ J/K
l	Kuhn's segment length

$\tilde{l}$	persistence length
l_w	wall interaction range
m	mass of a bead
$p(\mathbf{u})$	bond probability distribution for Gaussian chains
p_{if}	transition probability
$\mathbf{r}$	center of mass
$\Delta\mathbf{r}$	random displacement of the center of mass
$\mathbf{r}_{AB}$	vector between the centers of mass of two blocks
s	distance between two monomers along the contour of a polymer
s	contour parameter of a polymer coil
t	time
Δt	time discretization length
u	scaling variable
$\mathbf{u}_i$	bond vector between two beads i and $i-1$
$\mathbf{v}_i$	bond vector between two monomers i and $i-1$
v_0	excluded volume of one monomer or bead
$v_{\text{eff}}(r)$	effective potential between monomers
w_A, w_B	external field in the saddle–point approximation of the SCFT
$\Delta x, \Delta y$	spatial discretization lengths
$\mathbf{y}_i$	position of the i'th bead of a polymer coil
z	lattice coordination number
$\mathbf{z}_i$	position of the i'th monomer of a polymer
$\Gamma(.)$	gamma function
Γ_b	bulk kinetic coefficient
Γ_s	kinetic coefficient at the surface
Γ_{sl}	scaled kinetic coefficient Γ_s in linearized CHE
Θ	temperature, defined by $B_2(\Theta) = 0$
Θ	inertia moment
Φ	polymer concentration
$\Phi_\star$	crossover polymer concentration from dilute to semi–dilute regime
Φ_A, Φ_B	auxiliary fields in self–consistent field theory
α	ratio of Δx and Δy
$\gamma_{\alpha\beta}$	correlation coefficients
δ	Dirac's δ–function or Kronecker's δ
$\delta,\ \delta_w$	AB–interaction, wall–interaction mismatch parameter
$\epsilon \equiv \hat{\epsilon}/k_BT$	interaction between two monomers
$\hat{\epsilon}_w$	interaction between wall and monomer
$\epsilon_\star$	crossover interaction from Gauss to Flory type behavior
ζ	friction coefficient
η	viscosity
$\eta(\mathbf{y}, t)$	noise field
θ	contact angle
θ_{ij}	angle between two bond vectors i and j
λ_m	bulk demixing length
$\mu(\mathbf{y}, t)$	chemical potential

ν	scaling exponent
ξ, ξ_b	bulk correlation length
$\xi_\times$	crossover length from mean field type to Ising type behavior
ξ_m	blob size, screening length in semi–dilute solution
$\varrho(\mathbf{y};\mathbf{X})$	conditional monomer density
$\varrho'(\mathbf{y})$	total monomer density
$\varrho'_i(\mathbf{y})$	actual monomer density of particle i in a laboratory fixed coordinate system
$\hat{\varrho}(\mathbf{u};\mathbf{X})$	test function for scaling of the monomer density
$\tilde{\varrho}(\mathbf{u})$	effective scaling function of the monomer density
$\bar{\varrho}(\mathbf{x})$	average monomer density
$\rho(\mathbf{k})$	Fourier transform of $\varrho'(\mathbf{y})$
$\rho_\parallel(\mathbf{k}_\parallel, z)$	lateral Fourier transform of $\varrho'(\mathbf{y})$
σ_b, σ_s	measure for the interfacial tension in the bulk and at the surface
σ_{sl}	scaled σ_s in linearized CHE
σ_{XY}	surface tension of XY–interface
τ	characteristic time scale of the CHE
τ_1	Rouse time
τ_d	disentanglement time
τ_e	entanglement time
τ_0	elementary Monte Carlo time
τ_S, τ_O	characteristic times for shape and orientation changes in the GEM
$\phi(\mathbf{y}, t)$	order parameter field of a binary mixture
$\bar{\phi}$	average order parameter value
$\delta\phi(\mathbf{y}, t)$	perturbation of the order parameter field
$\phi_p(z,t),\ \phi_{\mathrm{hom}}(\mathbf{y}_\parallel, z, t)$	particular and homogeneous solution of linearized CHE
ϕ_c	critical value of the order parameter
ϕ_1, ϕ_2	order parameter at coexistence
$\phi_{\mathrm{s}1}, \phi_{\mathrm{s}2}$	order parameter at the spinodal
ϕ_A, ϕ_B	monomer concentrations of components
$\tilde{\phi}_A, \tilde{\phi}_B$	microscopic monomer density of components
χ	Flory–Huggins parameter
$\omega_b(k)$	bulk dispersion relation

1 Introduction

Materials based on polymers exhibit a vast variety of different properties. These range from simple rubber that can be found on every desk, to DNA in which the genetic information of all creatures is encoded. Due to this fact, it is clear that the physics of polymers is a broad research field, which, despite fifty or sixty years of intensive studies and many important progresses, entails many problems that up to now are only poorly understood or have not been investigated in detail. The large variety of the properties of polymer materials is a chance for material scientists to tailor substances with certain desired properties. An optimization of such properties requires an understanding of the physical processes involved.

In this work we will focus on the modeling of homopolymer melts and polymer blends from a phenomenological point of view, but we will keep a link to microscopic models. With the help of these coarse–grained models we will describe demixing processes of polymer blends in slab geometry with patterned substrates. These processes are of importance in experiments that try to translate a substrate pattern into a polymer pattern [Böl98, Kar98, Roc99, Fuk00]. Such polymer patterns might, for example, be used to fabricate microelectronic circuits consisting of organic semiconductors or polymer resists for lithographic semiconductor processing.

In the following sections we shortly present the necessary background in polymer physics and phase separation processes. Thereafter we show some experimental results that, apart from other aspects, motivated this work. Finally we address the issue of practical problems in the theoretical and computational description of such systems.

1.1 Polymer Systems

Polymers are molecules, which consist of many monomer units that are chemically linked together to form a chain. The most simple polymers are *homopolymers* $(-A-)_{N_A}$, where one chemical monomer unit A is repeated $N_A \gg 1$ times. Polymers, that are build of different monomers, are called *copolymers*. The different monomers can have an arbitrary order along the chain. For example, DNA consists of four types of monomers and their order along the chain encodes the genetic information. A polymer, that consists only of two homopolymers $(-A-)_{N_A}$ and $(-B-)_{N_B}$ linked together at one end of each other, is called a diblock copolymer $(-A-)_{N_A}(-B-)_{N_B}$. Triblock copolymers are build of three homopolymer blocks and so on. At this point we only note, that polymers may not only differ in chemical composition, but also in topology. There are ring polymers, where the two chain ends are bound together, star polymers, where the ends of some polymer chains are attached to one point, polymer combs, brushes and whole polymer networks, where many polymers are cross linked randomly, the most prominent example of which is rubber. However, these more complicated topologies will

not be considered in this work.

Homopolymers exhibit a variety of macroscopic states. Perhaps the most simple is a dilute solution of homopolymers in a solvent, i.e. the distances between the polymers in solution are so large, that they do not interact with each other. This state can be considered as an ideal "gas" state. On increasing the concentration, there will be a certain monomer concentration $c_\star$, where the interaction between the polymers becomes important, but the volume fraction of the polymers is still much less than the volume fraction of the solvent. Those solutions are called semi–dilute. The solution is called concentrated, when the volume fractions of both polymer and solvent are comparable. Concentrated solutions or pure polymer substances can exist in crystalline, glassy, high elastic or viscoelastic states. While the crystalline state is in some – but not all – properties similar to the crystalline state of low–molecular–weight substances, the glassy, high elastic, and viscoelastic phase states correspond to the "liquid" state of simple fluids. At low temperatures many polymer liquids have such a high viscosity, that their flow is invisible during reasonable observation times. They form a glass and many plastics are actually glassy polymers. Above the glass transition temperature the mobility of individual links increases strongly. If the relative motion of whole chains is constricted due to chemical cross–links or remaining glassy regions that form effective cross–links, the polymer is in a state characterized by a high elasticity. Otherwise, if the relative motion of the macromolecules is possible, either because there are no chemical cross–links or because the temperature is so high that no glassy domains exist, the polymer begins to flow on large time scales, but retains elastic behavior on short time scales. This is the *viscoelastic state*, also called a *polymer melt*.

Despite the obvious complexity of such molecules, let alone the complexity of systems composed of such molecules, there has been great success in describing the various states of polymers theoretically by adequate models. The reason for this is, that it is possible to identify two essential "large" parameters for such models. The first is the chain length L_p. The second one is the ratio between the energies of covalent bonds $E_1 \approx 5$ eV between neighboring monomers and the contact energies between non–neighboring monomers or monomers and solvent molecules $E_2 \approx 0.1$ eV. Since $E_1/k_BT \gg 1$ at room temperature and $E_1/E_2 \gg 1$, neither thermal fluctuations nor direct interactions at contact can break a covalent bond. Therefore the monomers are fixed along the chain and the chain length L_p is constant. All interactions, that are not associated with covalent bonds are called volume interactions.

The following parts of this section summarize important results of the theory of polymer physics. The reader, who is interested in more details, is referred to refs. [Gen79, Doi88, Gro94]. In a first step we present the results for ideal chains. Then we turn to volume interactions and show, that single chains are not ideal. We then discuss, why polymers in dense systems behave like ideal chains. We conclude this section with a short summary of the dynamic behavior of polymer chains in dense systems.

1.1.1 Ideal Chains

We consider a polymer consisting of N_p+1 identical monomers at positions $\mathbf{z}_k$, where $k = 0, \ldots, N_p$. All models of ideal chains have in common that volume interactions are neglected, but they usually differ in the probability distribution of the bond vectors $\mathbf{v}_k \equiv \mathbf{z}_k - \mathbf{z}_{k-1}$, with $k = 1, \ldots, N_p$. This probability distribution depends essentially on effective bond potentials between the monomers, that can be derived by quantum mechanical calculations, and the

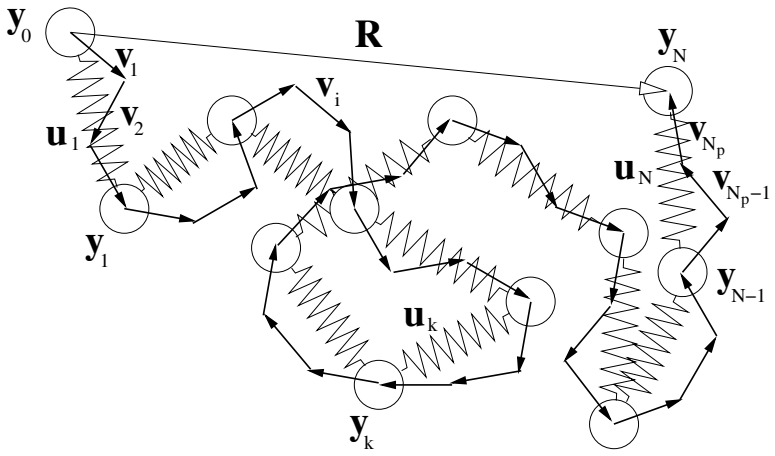

Figure 1.1: The figure illustrates the mapping of a polymer to a Gaussian chain. The polymer is described by N_p bond vectors $\mathbf{v}_i$ and the end–to–end vector $\mathbf{R}$. The Gaussian chain is represented by $N+1$ beads at positions $\mathbf{y}_k$ that are connected by thermal springs along the vectors $\mathbf{u}_k$.

temperature.

In random walk theory it can be shown, that under quite general conditions correlations along the chain decay exponentially [Gro94]. The orientational correlation function $\langle \mathbf{v}_i \cdot \mathbf{v}_j \rangle$ is given essentially by the average cosine of the angle θ_{ij} between the two links i and j and depends for a homopolymer only on the distance s between the two links along the chain. If the length of the bond vectors is (almost) constant, which is a very good approximation, then the orientation correlation function reads

$$\langle \mathbf{v}_i \cdot \mathbf{v}_j \rangle \simeq v^2 \langle \cos \theta_{ij}(s) \rangle = v^2 \exp\left(-s \Big/ \tilde{l}\right) . \tag{1.1}$$

This equation defines the so called *persistence length* $\tilde{l}$. It is a measure of the maximum length over which a polymer remains straight.

A quantity characterizing the size of a polymer coil is the root mean square end–to–end distance $R_\mathrm{e} \equiv \sqrt{\langle R^2 \rangle}$, where the end–to–end vector of a polymer chain is given by

$$\mathbf{R} = \sum_{k=1}^{N_p} \mathbf{v}_k \, . \tag{1.2}$$

By using eq. (1.1) one finds $\langle R^2 \rangle \sim (L_p/\tilde{l})\tilde{l}^2 \sim L_p \, \tilde{l} = N_p v \, \tilde{l}$ for $N_p \gg 1$, where L_p is the contour length of the polymer chain. Thus for ideal chains $R_\mathrm{e} \sim \sqrt{N_p}$ holds. Because the persistent length $\tilde{l}$ can not be determined experimentally, usually *Kuhn's segment length* l defined by

$$\langle R^2 \rangle = L_p \, l \, , \tag{1.3}$$

is used to characterize the flexibility of macromolecules and the decay of correlations. The Kuhn length l is of the same order of magnitude as the persistence length $\tilde{l}$. A general approach to determine $\langle R^2 \rangle$ approximately in terms of microscopic model parameters and thus Kuhn's length l is the *rotational isomeric state theory* (RIS) [Flo74].

Because the correlations between the bonds decay exponentially and the second moment $\langle v^2 \rangle$ exists, it follows from the central limit theorem of probability theory, that if $L_p \gg l$ the probability distribution of the end–to–end vector is Gaussian

$$P_{N_p}(\mathbf{R}) = \left(\frac{3}{2\pi \langle R^2 \rangle} \right)^{3/2} \exp\left(-\frac{3R^2}{2\langle R^2 \rangle} \right) . \tag{1.4}$$

The second moment $\langle R^2 \rangle$ is given by eq. (1.3), therefore l is the only microscopic parameter, that enters this distribution. The same argument, that applies to the distribution of the end–to–end vector, applies to all vectors between two points $\mathbf{z}_i$ and $\mathbf{z}_j$ along the chain, as long as their distance s along the chain is large in comparison to $\tilde{l}$. If we are only interested in the large scale properties of polymers, it is therefore always possible to do a coarse–graining on the scale of l, i.e. to describe an ideal polymer chain consisting of N_p monomers by $N < N_p$ beads at positions $\mathbf{y}_k$ with an equal distance $s \gg l$ along the chain. This kind of coarse–graining is illustrated in fig. 1.1. The beads are connected by bonds $\mathbf{u}_k = \mathbf{y}_k - \mathbf{y}_{k-1}$, that satisfy a Gaussian distribution

$$p(\mathbf{u}) = \left(\frac{3}{2\pi b^2} \right)^{3/2} \exp\left(-\frac{3u^2}{2b^2} \right) . \tag{1.5}$$

We denoted the root mean square bond length $\sqrt{\langle u^2 \rangle}$ between beads in the chain by b. This model is called the *standard Gaussian model of the polymer chain* and we emphasize, that all large scale properties of all ideal chain models can be described in terms of this model. The beads can be interpreted to represent a certain part of the macromolecule, while the bonds $\mathbf{u}$ provide effective connections between the beads. Given the number of beads N, the effective bond length b for a special chain model can be determined by the condition

$$\langle R^2 \rangle = N b^2 = L_p \, l \, , \tag{1.6}$$

cf. eq. (1.3). In order to have an "optimal" description of a polymer in terms of a Gaussian chain, N has to be maximal, while not violating the condition $s \gg l$. For example it would be possible to set the effective bond length equal to Kuhn's segment length, i.e. $b = l$. Therefore one would have to determine either l (numerically or by RIS theory) or give a more direct criterium, at which distance s the distribution function of vectors $\mathbf{z}_i - \mathbf{z}_j$ is Gaussian.

The distribution function of a Gaussian chain with N beads is given by

$$f_G(\{\mathbf{y}_i\}) = \left(\frac{3}{2\pi b^2} \right)^{3N/2} \exp\left(-\frac{3}{2b^2} \sum_{i=1}^{N} (\mathbf{y}_i - \mathbf{y}_{i-1})^2 \right) , \tag{1.7}$$

because its bonds are uncorrelated. Introducing the potential

$$U(\mathbf{u}) = k_B T \frac{3}{2b^2} u^2 \, , \tag{1.8}$$

we find, that eq. (1.7) can be interpreted as the equilibrium Boltzmann distribution of ideal particles interconnected by thermic springs. It is convenient to rewrite the distribution function by taking the continuum limit. Parameterizing the coil with the variable s, with $(0 \leq s \leq 1)$,

substituting $\mathbf{y}_{i+1} - \mathbf{y}_i$ by $\partial y/\partial s$ and replacing the sum by an integral, we can rewrite eq. (1.7) by the *Wiener measure*

$$f_G[\mathbf{y}(s)] \propto \exp\left(-\frac{3}{2\langle R^2\rangle}\int_0^1 ds\,\left(\frac{\partial y}{\partial s}\right)^2\right)\,. \tag{1.9}$$

Finally, we note that another important quantity characterizing the overall size of a polymer coil is given by the radius of gyration

$$R_G^2 = \frac{1}{N+1}\sum_{k=0}^{N}(\mathbf{y}_k - \mathbf{r})^2\,, \tag{1.10}$$

defined by the average squared distances of the beads from the center of mass

$$\mathbf{r} = \frac{1}{N+1}\sum_{i=0}^{N}\mathbf{y}_i\,. \tag{1.11}$$

For large $N \gg 1$ the average radius of gyration is for Gaussian chains given by

$$\langle R_G^2\rangle \sim \frac{1}{6}\langle R^2\rangle = \frac{1}{6}N\,b^2\,. \tag{1.12}$$

1.1.2 Excluded Volume Effects

While ideal chains are a good starting point for the understanding of polymer physics, they neglect the interactions between the monomers, that do not arise from the chemical bonds, but the "contacts" of non–neighboring monomers. These *volume interactions* involve strong short range repulsions of the monomers and long range attractions. Excluded volume effects are typically of universal nature and therefore independent on the specific chain structure. Thus it is possible to choose a mathematically convenient model for their description. The standard Gaussian model is often used, where spherically symmetric beads are connected by links with Gaussian correlations and interact via an effective potential $v_{\text{eff}}(r)$ that might for example be of the Lennard–Jones type. If one neglects the attractive part of the interaction, which is possible at high temperatures, then the short range repulsion of $v_{\text{eff}}(r)$ might have the form of a δ–function. In this effective potential interactions with a solvent may be incorporated, too. The simplest realization to study excluded volume effects experimentally is the case of a dilute polymer solution.

Macroscopically the volume interactions are described by the thermodynamic characteristics of a system of disconnected beads. The partition function (of a single chain) splits into two parts, one accounting for volume interactions, the other for the effective Gaussian bonds

$$f(\{\mathbf{y}_i\}) = \exp\left(-\beta\sum_{i\neq j} v_{\text{eff}}\big(\,|\mathbf{y}_i - \mathbf{y}_j|\,\big)\right)\,f_G(\{\mathbf{y}_i\})\,, \tag{1.13}$$

with $f_G(\{\mathbf{y}_i\})$ given by eq. (1.7). As long as the monomer concentration in the system remains moderate, the volume interactions are reduced to relative rare link collisions and can be described by a virial expansion. The second virial coefficient is given by

$$B_2(T) = \frac{1}{2}\int d^3r \left[1 - \exp\left(-\beta v_{\text{eff}}(r)\right)\right] . \tag{1.14}$$

By splitting $v_{\text{eff}}(r)$ into an attractive and a repulsive part [Doi88], we find that for high enough temperatures

$$B_2(T) = v_0 \frac{T-\Theta}{T} , \tag{1.15}$$

where v_0 is the excluded volume of one particle (bead) and Θ a certain temperature, where the second virial coefficient vanishes. For flexible chains v_0 is essentially determined by the effective link length $v_0 \sim b^3$. It can be shown, that in a dilute polymer system binary collisions are dominant, i.e. they occur N times more frequently, than triple collisions. Therefore triple (and higher) collisions do not affect the conformation of the chain and in the special case $B_2(T) \approx 0$ (or $T \approx \Theta$) volume interactions can be neglected and the chains are ideal. For $B_2(T) > 0$ the chains swell and conversely shrink in case $B_2(T) < 0$. Thus the Θ–temperature separates two regimes of good and bad solvent. The properties of a polymer coil in a good solvent are universal, in the sense, that they only depend on the contour length L_p, Kuhn's segment length l and the second virial coefficient B_2. More precisely, they depend on the dimensionless parameter B_2/b^3. In a poor solvent (but not too far from the Θ–temperature) the coil properties remain mostly universal, but the third virial coefficient becomes important also. In the following we will no longer consider poor solvents and attractive forces, but restrict ourselves to the case of *athermal chains*, i.e. consider only repulsive interactions. For our purposes this is not a major restriction.

The most striking effect of excluded volume is that the typical size of a polymer chain scales no longer with $\sqrt{N}$, but with a higher power

$$\langle R^2 \rangle \sim N^{2\nu} . \tag{1.16}$$

While the exact value of ν is unknown, renormalization group calculations and Monte Carlo simulations yield $\nu \approx 0.588$ in $d = 3$ dimensions. However, there is a simple argument by Flory, that gives an excellent estimate of ν. According to this argument, two effects have to balance each other: The excluded volume tends to swell the coil, while the elastic forces shrink it. The elastic part of the free energy is of entropic nature and given by $F_{el}(R) = -k_B T \ln P_N(R) \sim k_B T\, 3R^2/2Nb^2$, cf. eqs. (1.4, 1.6). Neglecting prefactors and estimating the energy of the excluded volume by $U_V(R) \sim k_B T\, v_0 \bar{c}^2 R^3$, where $\bar{c} \sim N/R^3$ is the average bead concentration within the area of the polymer, the free energy is given by

$$F(R) = k_B T \left(\frac{3R^2}{2Nb^2} + v_0 \frac{N^2}{R^3} \right) . \tag{1.17}$$

Minimizing eq. (1.17) with respect to R yields $R_e \sim N^{3/5}$. However, this kind of calculation benefits from the cancellation of two errors: First, in the ansatz for the excluded volume energy all correlations between the particles are neglected, therefore the interaction energy is strongly overestimated. Secondly, the elastic energy is also overestimated, because it is a function of $R^2/\langle R^2 \rangle$, rather than of R^2/Nb^2. Further on, there are quantities that are simply inconsistent with this simple theory, for example the end–to–end distance probability distribution of a polymer with excluded volume effects. Because a single polymer coil is a very loose and strongly fluctuating system, it is not surprising, that this kind of mean–field argument provides not in all aspects a good description.

1.1.3 Dense Systems of Polymer Chains

Until now we shortly summarized the properties of single polymer chains or dilute polymer systems. Now we regard the opposite case, a concentrated polymer solution or polymer melt. Again we want to estimate the size of a polymer chain by a mean–field argument. Therefore we consider one single chain C_s in a dense system surrounded by other chains. As argued in the previous section, the interaction of the chain C_s with its own monomer density field will lead to a swelling of the chain. On the other hand in a dense polymer system the fluctuations of the total monomer concentrations are very weak. Therefore the monomer density of all other chains is reduced in the region of C_s and thus leads to a compression of the coil. Therefore both, the expansion forces due to self–interaction of C_s and the compression forces due to the interactions with surrounding polymers, balance each other and the chain remains ideal [Gen79]. This kind of *self–consistent–field* argument is valid, because in this case fluctuations are negligible and therefore mean–field theory applies.

From a more microscopic point of view the ideal behavior of chains in a melt means that the exclude volume effect between the beads of C_s is screened. To understand this we first consider the more general situation of arbitrary monomer concentration c. Starting from the dilute limit the chains will begin to overlap at $c_\star \sim N/R_e^3 \sim N^{1-3\nu}$. In the semi–dilute region ($c > c_\star$) the system consists of an interpenetrating network of chains that has some average mesh size ξ_m. For ξ_m the following two statements are certainly correct: First, for $c > c_\star$ the mesh size depends only on the monomer concentration c but not on the chain length N. Secondly, at the crossover concentration the mesh size is of the order of $\xi_m \sim R_e \sim N^\nu$. Therefore we have $\xi_m \sim bN^\nu (c/c_\star)^{\nu/(1-3\nu)}$ in the semi–dilute region.

The polymers are virtually undisturbed on scales smaller than ξ_m. Such an undisturbed part of a chain is called a *blob* and the number of beads of a blob g is given by $\xi_m = bg^\nu$. From this definition and the scaling relation above it follows that $g \sim c\xi_m^3$. Therefore the semi–dilute solution is essentially a closely packed – dense – system of blobs. If now we consider the polymer as a chain of N/g blobs, i.e. we look at the polymer on a scale much larger than ξ_m, the polymer will show ideal behavior. The volume interactions are screened on the length scale ξ_m, fluctuations on larger scales are suppressed. The average end–to–end distance can be estimated by $R_e^2 \sim \xi_m^2 N/g$ and finally yields

$$R_e^2(c) \sim Nb^2 c^{-1/4} \qquad c_\star \ll c\,. \tag{1.18}$$

Of course the notion of blobs becomes meaningless as soon as the mesh size becomes comparable to the link size $\xi_m \sim b$. In this case the volume interactions are totally screened, fluctuations suppressed and a mean field description correct. Thus a second crossover concentration exists, that can be estimated from the breakdown of mean field theory and amounts to $c_{\star\star} \sim v_0/b^6$.

1.1.4 Dynamics of Polymer Chains

So far we have considered only time independent properties of polymer coils. Now we take a short look at the characteristic properties of the dynamics of those macromolecules. We restrict the discussion to polymer melts, where hydrodynamic interactions are screened.

The simplest and most common model concerning polymer dynamics is the *Rouse model*. In the framework of this model one considers an ideal Gaussian chain, neglecting all topological

constraints and hydrodynamic interactions. The equation of motion for the beads of a Gaussian chain on a time–scale much larger than typical atomistic relaxation times is then given by a *Langevin* equation

$$m\frac{d^2\mathbf{y}_i}{dt^2} = \mathbf{f}_i^{(\mathrm{ch})} + \mathbf{f}_i^{(\mathrm{fr})} + \mathbf{f}_i^{(\mathrm{st})} \,. \tag{1.19}$$

The terms in this equation have the following meaning: The chain force is given by the respective terms of the potential U in eq. (1.8)

$$\mathbf{f}_i^{(\mathrm{ch})} = k_B T \,\frac{3}{b^2}(\mathbf{y}_{i+1} - 2\,\mathbf{y}_i + \mathbf{y}_{i-1}) \,. \tag{1.20}$$

The friction due to the solvent and other beads is assumed to be proportional to the bead velocity

$$\mathbf{f}_i^{(\mathrm{fr})} = -\zeta\frac{d\mathbf{y}_i}{dt} \,, \tag{1.21}$$

where we defined the friction coefficient ζ. The stochastic force $\mathbf{f}^{(\mathrm{st})}$ accounts for thermal excitations of the beads or the solvent. Its average is zero, otherwise the force would lead to a drift. The probability distribution of $\mathbf{f}^{(\mathrm{st})}$ is assumed to be Gaussian and delta–correlated with respect to time, spatial components and different beads, thus

$$\left\langle \mathbf{f}_i^{(\mathrm{st})} \right\rangle = 0 \quad \text{and} \quad \left\langle \mathbf{f}_i^{(\mathrm{st})}(t)\mathbf{f}_j^{(\mathrm{st})}(t') \right\rangle = 2\,\zeta\delta_{ij}\delta_{\alpha\beta}\delta(t-t') \,. \tag{1.22}$$

This kind of stochastic force is consistent with the *fluctuation–dissipation* theorem. As the friction acting on the beads is much stronger than the inertia forces, the term $\propto d^2\mathbf{y}/dt^2$ is neglected. Therefore the set of differential equations to be solved is

$$\zeta\frac{d\mathbf{y}_i}{dt} = k_B T \,\frac{3}{b^2}(\mathbf{y}_{i+1} - 2\,\mathbf{y}_i + \mathbf{y}_{i-1}) + \mathbf{f}_i^{(\mathrm{st})} \,, \tag{1.23}$$

with obvious modifications at the chain ends for $i = 0$ and $i = N$. This linear set of equations can be cast into a diffusion type equation in the continuum limit and solved by Fourier techniques, i.e. an expansion of the solution into *Rouse modes*. The solution yields a characteristic set of relaxation times [Gro94]

$$\tau_1 = \frac{N^2 b^2 \zeta}{3\,\pi^2 k_B T} \,, \qquad \tau_p = \tau_1/p^2 \,, \qquad p = 1, 2, \ldots, N \,, \tag{1.24}$$

where τ_1 is the largest relaxation time and grows quadratically with N. The mean square displacement of the beads is proportional to the square root of time for times $t \ll \tau_1$,

$$\left\langle [\mathbf{y}_i(t) - \mathbf{y}_i(0)]^2 \right\rangle \simeq \left(\frac{12\,k_B T\, b^2}{\pi\,\zeta}\, t \right)^{1/2} \tag{1.25}$$

For times $t \gg \tau_1$ the behavior is governed by the diffusion of the center of mass $\mathbf{r}$. The mean square displacement of $\mathbf{r}$ is for all times t given by

$$\left\langle [\mathbf{r}(t) - \mathbf{r}(0)]^2 \right\rangle = 6\, D\, t\,, \quad \text{with} \quad D = \frac{k_B T}{\zeta N}\,. \tag{1.26}$$

This is a normal diffusion process with a diffusion constant $D \propto N^{-1}$. Although the Rouse model is very simple and is not valid for the description of the real dynamics of polymers in solution, the short time behavior of polymer chains in dense systems, can be analyzed in terms of the Rouse model.

A major shortcoming of the Rouse model concerning the dynamics in a polymer melt is the neglect of topological constraints, that arise from the interactions between the chains and restrict the motion of the beads. Contacts between two polymers that hinder their motion significantly, are called *entanglements*, but most contacts are non–entangled. These entanglements lead to the formation of an effective *tube* around the contour of the macromolecule, with a tube diameter d_t that significantly exceeds the size of a monomer. Defining the average number of links between two entanglements by the phenomenological parameter N_e, the tube diameter is determined by $d_t \sim \sqrt{N_e} b$. The contour of the axis of the tube is called its *primitive path*. As the tube follows the contour of the polymer but only on a coarser scale d_t, the primitive path is coiled in a Gaussian state, too. The contour length L_t of the primitive path is given by $L_t \sim N\, d_t / N_e \sim N\, b / \sqrt{N_e}$.

In the *reptation* model one considers a polymer motion, that resembles a diffusive creep along the tube. The friction ζ_t for such a motion is N times larger than the friction acting on a single bead $\zeta_t \sim N\zeta$. According to the *Nernst–Einstein relation* the diffusion coefficient is given by $D_t = k_B T / \zeta_t$. Therefore we can estimate the time τ_d needed for a polymer to leave the original tube to which it was confined at $t = 0$ by

$$\tau_d \sim \frac{L_t^2}{D_t} \sim \frac{\zeta b^2 N^3}{k_B T N_e}\,. \tag{1.27}$$

This time τ_d is called *disentanglement* time or *disengagement* time, because on larger time scales entanglements do no longer restrict the dynamic behavior. The self–diffusion coefficient for the reptation model is given by $D_{\text{self}} \sim R_e^2 / \tau_d \sim k_b T N_e / N^2 \zeta$ yielding a stronger N–dependence as in the Rouse model. Thus due to entanglement effects the diffusion of long polymers is slowed down dramatically.

There is a discrepancy between the prediction of the reptation model and experimental data concerning the N–dependence of τ_d. While the reptation model predicts $\tau_d \sim N^3$, experiments yield $\tau_d \sim N^{3.4}$. This discrepancy might be due to the fact, that in experiments a broad crossover regime is observed that should on practically unobservable times finally yield $\tau_d \sim N^3$. Newer analytical results including reptation and contour length fluctuations of the tube show, that such a crossover actually can occur in the reptation model, too [Min98].

The overall behavior of the mean square displacement of a bead, as a function of time is depicted in fig. 1.2. For very short times the motion of the monomers is not restricted by the entanglements. Therefore the Rouse model applies. From the mean square displacement according to the Rouse model eq. (1.26), and the tube diameter $d_t \sim \sqrt{N_e} b$, it is possible to estimate the entanglement time $\tau_e \sim d_t^4 \zeta / k_B T b^2$. This is the first time when entanglements begin to restrict the dynamics. Afterwards the polymer relaxes by one dimensional Rouse dynamics along the tube, until the time exceeds τ_1. In this time regime a result analogous to eq. (1.25) in one dimension holds for the mean square displacements along the contour,

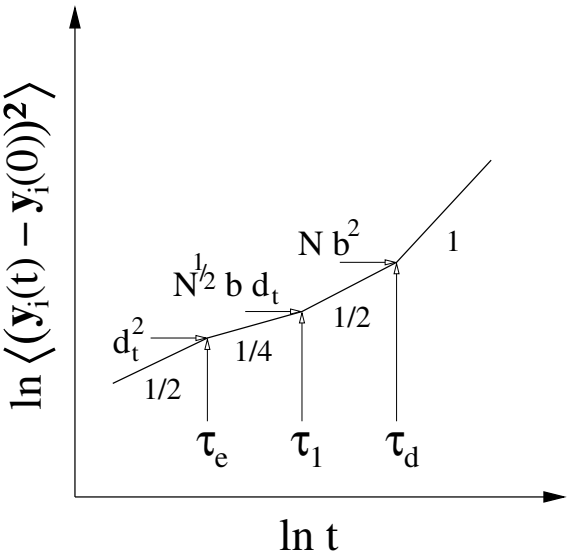

Figure 1.2: Schematic behavior of the mean square displacement as a function of time in a polymer melt, after [Doi88]. Three characteristic times, the entanglement time τ_e, the Rouse time τ_1 and the disentanglement time τ_d are marked in, as well as the respective mean square displacements. The numbers state the slope of $\langle(\mathbf{y}(t) - \mathbf{y}(0))^2\rangle$ in double logarithmic representation, corresponding to a power law.

$\langle(s_i(t) - s_i(0))^2\rangle \sim t^{1/2}$. Because the tube itself forms a Gaussian coil on a scale large compared to d_t, it follows that $\langle(\mathbf{y}_i(t) - \mathbf{y}_i(0))^2\rangle \sim d_t\langle|s_i(t) - s_i(0)|\rangle \sim d_t\, t^{1/4}$. Thereafter the behavior is governed by the creeping diffusion along the tube. Finally, on time–scales larger than the disentanglement time τ_d the entanglements restrict no longer the diffusion. Throughout the rest of this work we are only interested in processes, that occur on times $t \gg \tau_d$.

1.2 Phase Separation

Considering a simple system of two components A and B there are two macroscopic states in which the system can be found, a homogeneous – mixed – state and an inhomogeneous – demixed – state. The phase diagram describes which state is found with respect to external macroscopic variables. The line separating the two states in the phase diagram is called *binodal* or coexistence curve. Parts of the phase diagram, in which the system is thermodynamically unstable, are subdivided by the *spinodal* line, see fig. 1.3 for a schematic illustration.

1.2.1 Flory–Huggins Theory

A simple description of the phase separation of binary polymer blends in terms of a lattice model was given by Flory and Huggins, see e.g. [Bin94]. This model covers many essential aspects and is often used as a reference, therefore we describe it briefly.

In this model all lattice sides are occupied either by an A–monomer or a B–monomer, cf. fig. 1.4. Only nearest neighbor monomers interact. The interaction energies are given by

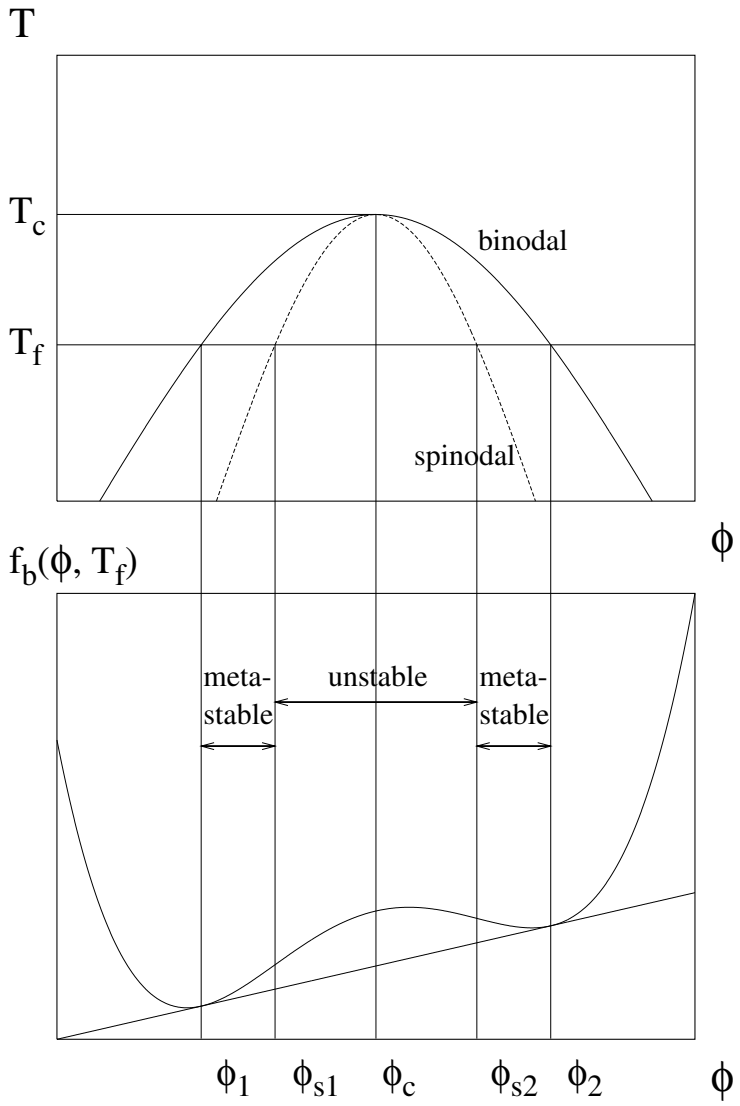

Figure 1.3: Phase diagram and free energy of a binary mixture.

$\hat{\epsilon}_{AA}, \hat{\epsilon}_{BB}$ and $\hat{\epsilon}_{AB}$ according to the kind of neighbors. The connectivity of the chains leads to a restriction with respect to the possibilities of depositing monomers on the lattice and thus to a modification of the entropy of the system with respect to simple "atomic" mixtures. This kind of model leads to the following mean field expression for the free energy of the system

$$\frac{f_{\mathrm{FH}}}{k_B T} = \frac{\phi_A}{N_A} \ln \phi_A + \frac{\phi_B}{N_B} \ln \phi_B + \chi \, \phi_A \phi_B \, . \tag{1.28}$$

Here $\phi_A = M_A N_A/(M_A N_A + M_B N_B)$ and $\phi_B = M_B N_B/(M_A N_A + M_B N_B)$ denote the monomer concentration of the respective components. The number of A and B polymers is denoted by M_A and M_B, the respective chain lengths are given by N_A and N_B. The mixture is incompressible ($\phi_A + \phi_B = 1$). The first two parts of expression (1.28) denote the entropy of mixing. For large chain lengths $N_A, N_B \gg 1$ this entropy is small, therefore binary blends of long polymer chains demix easily. The last term in eq. (1.28) accounts for the energy due to the interaction

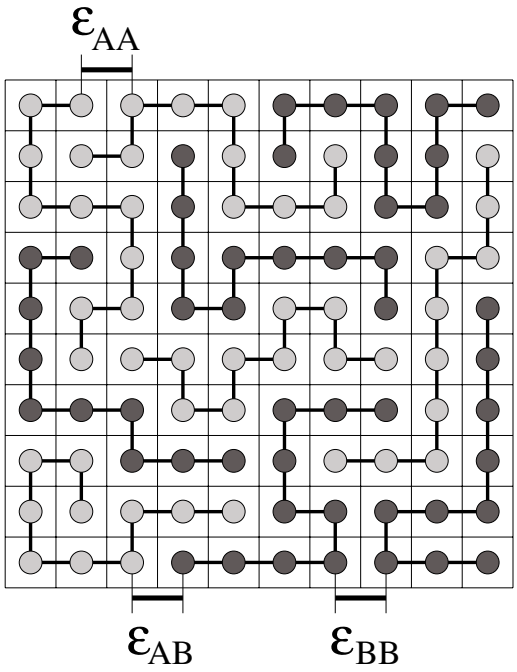

Figure 1.4: Illustration of the lattice polymer model used in Flory–Huggins theory.

of the different components. The dimensionless *Flory–Huggins parameter* is

$$\chi(T) = \frac{z}{k_B T}\left(\hat{\epsilon}_{AB} - \frac{\hat{\epsilon}_{AA} + \hat{\epsilon}_{BB}}{2}\right), \tag{1.29}$$

where z denotes the coordination number of the lattice. This is the original form of χ for the lattice model, but more generally χ can be treated as a phenomenological parameter. Experiments yield typically

$$\chi(T) = C_1 + \frac{C_2}{T}, \tag{1.30}$$

and values in the range $10^{-4} < \chi < 10^{-1}$. In the following we restrict our discussion to the case $N_A = N_B = N+1$ and $N \gg 1$, such that $N+1 \simeq N$.

The binodal can be calculated from eq. (1.28) by *Maxwells construction* leading to the following implicit equation

$$N\chi(T)\,\phi = 2\,\mathrm{arctanh}(\phi) \tag{1.31}$$

where for convenience we introduced the *order parameter* $\phi = \phi_A - \phi_B$. This equation has one single solution corresponding to a stable minimum in the case $\chi(T) < \chi_c = 2/N$ at the critical concentration $\phi_c = 0$. Otherwise ($\chi > \chi_c$) three solutions exist, where the solution $\phi = 0$ yields a maximum, the other two solutions ϕ_1, ϕ_2 have to be determined numerically and yield stable minima. The stable solutions determine the binodal in dependence on χ or T. The system decomposes into two homogeneous parts with concentrations ϕ_1 and ϕ_2. The size of the two phases is given by the *lever rule*. The coexistence curve depends only on the

parameter $N\chi(T)$ as can be seen directly from eq. (1.31). Particularly, the *critical temperature* T_c corresponding to $\chi(T_c) \equiv \chi_c = 2/N$ is proportional to the chain length, $T_c \sim N$. The spinodal can be determined explicitely by the condition $\partial^2 f_{\mathrm{FH}}(\phi)/\partial\phi^2 = 0$ yielding

$$\frac{\chi_{\mathrm{sp}}}{\chi_c} = \frac{1}{1-\phi^2} \quad \text{or} \quad \frac{T_{\mathrm{sp}}}{T_c} = 1 - \phi^2 \,, \tag{1.32}$$

where in the last step we used $\chi(T) \propto 1/T$ as in eq. (1.29).

An alternative and generic form of a free energy is given by the Landau expression

$$\frac{f_{\mathrm{GL}}(\phi)}{k_B T} = -\frac{1}{2} a(T)\, \phi^2 + \frac{1}{4} b\, \phi^4 \,. \tag{1.33}$$

It is possible to identify $a(T)$ and b in terms of χ and N, in regions of the phase diagram not too far away from the critical point. Expanding eq. (1.28) to fourth order in ϕ yields

$$a(T) = \frac{1}{2}\left[\chi(T) - \chi_c\right] \,, \qquad b = \frac{1}{3N} \,. \tag{1.34}$$

1.2.2 Ginzburg–Landau Theory

In the previous section we described equilibrium properties of a binary polymer blend. However, when we think about a demixing process, where the system starts from a homogeneous phase and separates into two phases, inhomogeneous states will occur. Therefore the order parameter ϕ will be a local quantity $\phi(\mathbf{y})$, where $\phi(\mathbf{y})$ denotes a concentration averaged over a small part of space. It is possible to define a constrained partition sum $Z[\phi(\mathbf{y})]$ where all microscopic states consistent with the order parameter field $\phi(\mathbf{y})$ are integrated out. From this definition a functional of the free energy $F[\phi(\mathbf{y})] = -k_B T \ln Z[\phi(\mathbf{y})]$ can in principle be derived. Since a direct calculation of $F[\phi(\mathbf{y})]$ is not possible, phenomenological expressions are used, as for example,

$$\frac{F_{\mathrm{GL}}[\phi(\mathbf{y})]}{k_B T} = \int_V d^d y \, \left[f_b(\phi) + \frac{1}{2}\sigma_b \left(\nabla\phi\right)^2 \right] \,. \tag{1.35}$$

The squared gradient term accounts for contributions of interfacial tension to the free energy, provided that the spatial variations of ϕ are small. For the bulk free energy density $f_b(\phi)$ one can, under the assumption of local equilibrium, use the Landau expression (1.33), but now with a spatial varying order parameter.

This kind of description is very general and valid for a much broader class of materials. The chain length N entering via the effective parameters $a(T)$ and b, eq. (1.34), is the only parameter specific for polymers. Therefore one cannot expect, that the results can yield more than a qualitative description of polymer systems. To improve this kind of description the Flory–Huggins expression (1.28) is used for the bulk free energy. Further on, a dependence of the prefactor of the squared gradient term σ_B on the actual density ϕ is taken into account, in such a way that in the limit of long wavelengths and weak fluctuations $\delta\phi$ the inverse structure

function $S(\mathbf{q})^{-1}$, as known from the random phase approximation, is recovered [Bin94]. The result is known as Flory–Huggins–de Gennes free energy functional

$$\frac{F_{\mathrm{FHG}}[\phi_A(\mathbf{y}),\phi_B(\mathbf{y})]}{k_BT} = \int d^dy \left[\frac{\phi_A}{N_A}\ln\phi_A + \frac{\phi_B}{N_B}\ln\phi_B + \chi\,\phi_A\phi_B + \frac{l^2}{36\,\phi_A\phi_B}\left(\nabla\phi_A\right)^2\right] . \quad (1.36)$$

It is convention to write $F_{\mathrm{FHG}}[\phi_A,\phi_B]$ as a functional of ϕ_A and ϕ_B instead of the order parameter $\phi=\phi_A-\phi_B$. However, both concentrations are related by the *incompressibility condition* $\phi_A(\mathbf{y})+\phi_B(\mathbf{y})=1$ that is valid also locally. As the chain connectivity does not enter this description, it is valid for length scales larger than $\bar{R}_G$.

1.2.3 Self–Consistent–Field Theory

The *self–consistent–field theory* is an alternative approach for the description of inhomogeneous polymer mixtures, that can account better for some specific properties of polymer systems, see ref. [Sch98] for a review. Consider an incompressible polymer mixture of components $X\in\{A,B\}$ with $N_A=N_B=N+1$. The microscopic monomer density of a component X in terms of chain configurations $\{\mathbf{y}_{i_X}(s)\}$ is given by

$$\tilde{\phi}_X(\mathbf{y}) = \frac{(N+1)}{c}\sum_{i_X=1}^{M_X}\int_0^1 ds\,\delta\left[\mathbf{y}-\mathbf{y}_{i_X}(s)\right] , \quad (1.37)$$

where $c=M(N+1)/V$ is the average total monomer density and $M=M_A+M_B$. Because a polymer melt is a dense system, it is justified to describe the single chain configurations in terms of Gaussian chains. The respective statistical weight is given by the Wiener measure (1.9). Describing the excess interaction between unlike components A and B by a Flory–Huggins parameter χ, the partition function is then given by the functional integral

$$Z \propto \frac{1}{M_A!M_B!}\int\left(\prod_{X=A,B}\prod_{i_X=1}^{M_X}\mathcal{D}[\mathbf{y}_{i_X}]f_{G,X}[\mathbf{y}_{i_X}]\right)\exp\left[-c\int d^3y\,\chi\tilde{\phi}_A\tilde{\phi}_B\right]\delta[\tilde{\phi}_A+\tilde{\phi}_B-1] , \quad (1.38)$$

where $\int\mathcal{D}[\mathbf{y}]$ denotes the integration over all possible configurations. The δ–function accounts for the incompressibility condition $\tilde{\phi}_A+\tilde{\phi}_B=1$ that has to be fulfilled in a small volume at every position $\mathbf{y}$. As the partition function (1.38) is not analytically integrable, a description in terms of a field theory is convenient. By a *Hubbard–Stratonovich transformation* [Cha95] the many polymer problem is recast in terms of a single polymer in external fields. The partition sum Z is written as an appropriate functional integral over auxiliary fields Φ_X and W_X. Inserting the Fourier integral representation of functional integrals

$$\int\prod_{X=A,B}\mathcal{D}W_X\mathcal{D}\Phi_X\,\exp\left[c\int d^3\mathbf{y}\,W_X(\Phi_X-\tilde{\phi}_X)\right] = \int\prod_{X=A,B}\mathcal{D}\Phi_X\,\delta(\Phi_X-\tilde{\phi}_X) = 1 \quad (1.39)$$

in eq. (1.38) permits the replacement of the operators $\hat{\phi}_X$ by the fields Φ_X and leads to a more tractable form of the partition function [Hon81, Mat94]

$$Z \propto \int \left(\prod_{X=A,B} \mathcal{D}W_X \mathcal{D}\Phi_X \right) \delta[\Phi_A + \Phi_B - 1] \, \exp\left(-\beta F[W_A, W_B, \Phi_A, \Phi_B]\right) . \tag{1.40}$$

The inverse temperature is $\beta \equiv 1/k_B T$ and the canonical free energy is given by

$$\frac{F[W_X, \Phi_X]}{k_B T} = -M_A \ln \frac{Q_A}{M_A} - M_B \ln \frac{Q_B}{M_B} - \frac{M}{V} \int d^3\mathbf{y} \left[W_A \Phi_A + W_B \Phi_B - \chi N \, \Phi_A \Phi_B \right] . \tag{1.41}$$

This expression depends on the single chain partition function Q_X in an external field W_X

$$Q_X = \int \mathcal{D}[\mathbf{y}_X] f_{G,X}[\mathbf{y}_X] \exp\left(- \int ds \, W_X[\mathbf{y}(s)] \right) . \tag{1.42}$$

The calculation of Q_X can be reduced to the solution of a diffusion equation with an external field [Rei01].

The equilibrium solution can be calculated approximately by a saddle–point approximation. Denoting the values of the fields at the saddle–point by lower case letters ϕ_X and w_X respectively, the following set of equations has to be solved self–consistently

$$\left. \frac{\delta F}{\delta W_X} \right|_{w_X} = 0 : \qquad \phi_X = -\frac{c_X V}{Q_X} \frac{\partial Q_X}{\partial w_X} = \langle \tilde{\phi}_X \rangle \tag{1.43}$$

$$\left. \frac{\delta F}{\delta \Phi_A} \right|_{\phi_A} - \left. \frac{\delta F}{\delta \Phi_B} \right|_{\phi_B} = 0 : \qquad w_A - w_B = \chi N \left(\phi_B - \phi_A \right) \tag{1.44}$$

$$\text{incompressibility} \; : \qquad \phi_A + \phi_B = 1 \, , \tag{1.45}$$

where the average monomer density $c_X = N_X M_X / (N+1) M$ of one component X is introduced. The average densities in equilibrium $\langle \tilde{\phi}_X \rangle$ equal the thermal average monomer densities ϕ_X of a single chain of component X in an external field w_X expressing the mean–field character of the approximation.

The Flory–Huggins theory can be recovered easily from the self–consistent–field theory, by replacing all spatially varying functions in eq. (1.41) by their average. This leads – except for irrelevant additive constants – directly to the form for the free energy f_{FH} given in eq. (1.28).

A better treatment than the saddle–point approximation can be achieved, by regarding the fields W_X as a small perturbation and as slowly varying functions. This leads to a Gaussian approximation of the partition sum Z in eq. (1.40) and an expression for the free energy in terms of the single chain scattering function $S_X(\mathbf{q})$. In the *weak segregation limit* ($\mathbf{q} \to 0$) the Flory–Huggins–de Gennes free energy functional (1.36) can be derived.

1.3 Demixing Processes

The process of demixing occurs, when the system is brought from the homogeneous to the inhomogeneous state by varying some external parameter, for example the temperature T. Concerning the demixing process one usually distinguishes between *nucleation* and *spinodal decomposition* [Lag92]. The latter occurs, when the system is quenched rapidly into a part of the phase diagram, where it is thermodynamically unstable, see fig. 1.3. Otherwise the system

is metastable and can reach the new preferential state only through a thermally activated process.

However, the concept of the spinodal results from mean–field theory. Due to thermal fluctuations there is in reality no sharp transition between nucleation and spinodal decomposition. From this point of view the spinodal can be considered as the line, where the nucleation barrier vanishes. We will restrict ourselves to spinodal decomposition in the following and briefly review its description in the framework of *time dependent Ginzburg–Landau theory*.

1.3.1 Spinodal Decomposition in Bulk Systems

Because the concentration of the components is a conserved quantity, the description of spinodal decomposition is based on the continuity equation for the order parameter $\phi = \phi_A - \phi_B$

$$\frac{\partial}{\partial t}\phi(\mathbf{y},t) + \nabla \cdot \mathbf{j}(\mathbf{y},t) = 0\,. \tag{1.46}$$

It is assumed, that the interdiffusive current $\mathbf{j}(\mathbf{y},t)$ is driven by the gradient of a chemical potential for exchange of A and B particles. In the simplest case the mobility Γ_b is assumed to be a constant kinetic coefficient

$$\mathbf{j}(\mathbf{y},t) = -\Gamma_b \nabla \mu(\mathbf{y},t)\,. \tag{1.47}$$

The chemical potential is given by the functional derivative of the free energy

$$\mu(\mathbf{y},t) = \frac{\delta F[\phi]}{\delta \phi}\,. \tag{1.48}$$

Inserting the Ginzburg–Landau functional F_{GL} (1.35) in eqs. (1.46–1.48) yields the *Cahn–Hilliard equation* (CHE) [Bra94]

$$\frac{\partial}{\partial t}\phi(\mathbf{y},t) = \Gamma_b \Delta \left[-\sigma_b \Delta \phi(\mathbf{y},t) + \frac{\partial}{\partial \phi} f_b(\phi) \right]\,. \tag{1.49}$$

The initial condition for the order parameter field $\phi(\mathbf{y},t)$ is usually given by small uncorrelated random fluctuations added to the average order parameter value $\bar{\phi}$.

For short times, eq. (1.49) may be linearized with respect to $\delta\phi(\mathbf{y},t) = \phi(\mathbf{y},t) - \bar{\phi}$ [Bin91b]. In this case the solution is given in terms of Fourier modes

$$\delta\hat{\phi}(\mathbf{k},t) \equiv \int d^3y\, e^{i\mathbf{k}\cdot\mathbf{y}} \delta\phi(\mathbf{y},t) = \delta\hat{\phi}(\mathbf{k},0)\exp[\omega_b(k)t]\,, \tag{1.50}$$

with the dispersion relation

$$\omega_b(k) = -\Gamma_b k^2 \left(\sigma_b k^2 + \left.\frac{\partial^2 f_b(\phi)}{\partial \phi}\right|_{\bar{\phi}} \right)\,. \tag{1.51}$$

The intermediate scattering function reads

$$I(k,t) \equiv \left\langle |\delta\hat{\phi}(\mathbf{k},t)|^2 \right\rangle = I(k,0)\exp\left[2\,\omega_b(k)t\right]\,. \tag{1.52}$$

Equation (1.51) predicts a critical wave vector

$$k_c^2 = -\frac{1}{\sigma_b} \left. \frac{\partial^2 f_b(\phi)}{\partial \phi^2} \right|_{\bar{\phi}} . \tag{1.53}$$

Short wavelength fluctuations with $k > k_c$ decay exponentially ($\omega_b(k) < 0$), while modes with $k < k_c$ grow ($\omega_b(k) > 0$). The maximum growth rate is given by $\omega_b(k_m)$, where the characteristic inverse length scale is the *bulk demixing length* $k_m = k_c/\sqrt{2}$. Shortly summarized, in the early stages of spinodal decomposition concentration fluctuations on a length scale of the bulk demixing length $\lambda_m = 2\pi/k_m$ grow rapidly and form a domain pattern. This stage ends, when the order parameter reaches values comparable to its equilibrium value within the domains and therefore the non–linear terms become important.

The late stage behavior is dominated by domain coarsening, as the systems reduces energetically unfavorable interfaces. In this time regime the average domain size L_D grows according to the *Lifshitz–Slyozov law* [Bra94]

$$L_D \sim t^{1/3} . \tag{1.54}$$

The Cahn–Hilliard equation, eq. (1.49), gives a good qualitative description of spinodal decomposition. However, several aspects are not described, for example thermal fluctuations and hydrodynamic flows.

Thermal fluctuations may be included in this description by adding a noise term $\eta(\mathbf{y}, t)$ on the right hand side of eq. (1.49), yielding the Cahn–Hilliard–Cook equation [Bin91b]. The noise is related to the kinetic coefficient Γ_b by a *fluctuation–dissipation* theorem

$$\langle \eta(\mathbf{y}) \rangle = 0 \quad \text{and} \quad \langle \eta(\mathbf{y}, t) \eta(\mathbf{y}', t') \rangle = 2\, k_B T\, \Gamma_b\, \Delta\delta(\mathbf{y} - \mathbf{y}')\delta(t - t') . \tag{1.55}$$

Thermal fluctuations are only important for short times, where they lead to a shift of k_m to smaller values [Bin91b]. The late stage behavior is dominated by systematic forces, especially the Lifshitz–Slyozov growth is not affected by noise terms of the form (1.55).

To describe advective processes due to hydrodynamic flows, a coupling of the gradient of the order parameter to the velocity has to be taken into account [Bra94]. The velocity field itself is described by the *Navier–Stokes* equation. This leads to a description in terms of two coupled partial differential equations. A scaling analysis yields, that after the Lifshitz–Slyozov diffusive domain growth another time regime exists, where viscous hydrodynamic flows drive coarsening. These flows become important, as soon as the domain size becomes comparable to $L_D \sim (\Gamma_b \eta)^{1/2}$, where η denotes the viscosity. In this regime the domains grow according to $L_D \sim t$ [Bra94].

For polymeric systems, there are some modifications of the concept presented above, that should be taken into account. Thus, instead of the generic Ginzburg–Landau functional the Flory–Huggins–de Gennes functional that is more specific for polymer systems should be used in eq. (1.48). Further on, the kinetic coefficient depends on the concentration

$$\Gamma_b = D_{\text{self}} N\, \phi_A(\mathbf{y}, t) \phi_B(\mathbf{y}, t) , \tag{1.56}$$

where D_{self} is the self diffusion coefficient of a polymer [Gen80]. The main modifications with respect to the results of the Cahn–Hilliard theory are on one hand a change of the k–dependence of the dispersion relation $\omega_b(k) \propto D_{\text{self}} N k^4 b^2 [2 - (k^2 b^2)/(9\chi)]$ for short times. On the other hand, if reptation is the underlying polymer dynamics, an additional coarsening regime $L_D \sim t^{1/5}$ for domain sizes $L_D \ll R_G$ occurs, preceeding the Lifshitz–Slyozov growth [Gen80].

1.3.2 Demixing Processes in Confined Geometries

In the case, where the system is confined by hard walls, for example by substrates, the interaction of the particle with the walls and the general modification of the neighborhood of a particle near the wall lead to a change of the free energy. If the wall–particle interaction is short ranged, the functional of the free energy may be decomposed into a bulk and a surface term

$$F[\phi] = F_b[\phi] + F_s[\phi] \,. \tag{1.57}$$

The form of $F_b[\phi]$ has been discussed already in sec. 1.2.2. Here, we will consider the Ginzburg–Landau expression, i.e. $F_b[\phi] = F_{\mathrm{GL}}[\phi]$ and $F_{\mathrm{GL}}[\phi]$ as given in eq. (1.35). The surface part is

$$F_s[\phi] = \int_{\partial V} d^{d-1}y \, \left[f_s(\phi) + \frac{1}{2}\sigma_s (\nabla_{\|}\phi)^2 \right] \,, \tag{1.58}$$

where $\nabla_{\|} = \nabla - \mathbf{n}(\mathbf{n}\cdot\nabla)$ and $\mathbf{n}$ denotes a unit vector normal to the surface ∂V pointing in outward direction. A phenomenological expression for the surface free energy density is given in terms of an expansion with respect to the order parameter

$$f_s(\phi) = -h\,\phi + \frac{1}{2} g\,\phi^2 \,. \tag{1.59}$$

The linear term describes the preference of the wall for one of the components A or B and has a major influence on the wetting behavior of the system [Bin83]. The quadratic term accounts for an increase of the disorder near the wall due to missing interactions and a possible modification of the interactions between the particles near the wall. In the case $g < 0$ the surface favors ordering and a surface phase transition occurs, even before the bulk system orders. The parameters h and g can be spatially varying functions to account for inhomogeneous substrates.

To describe phase separation processes in the presence of a confining wall, the kinetic equation, for example the Cahn–Hilliard equation (1.49), has to be supplemented by appropriate boundary conditions. Because this equation is of fourth order in the spatial derivatives, two boundary conditions are needed at each point of the surface. Assuming impermeable walls, the first boundary condition describes that the normal component of the interdiffusive current $\mathbf{j}$ must vanish at the boundary. Using eq. (1.47) for $\mathbf{j}$ yields

$$\mathbf{n}\cdot\nabla \left[-\sigma_b \phi + \frac{\partial f_b}{\partial \phi} \right]_{\partial V} = 0 \,. \tag{1.60}$$

The second boundary condition follows from the assumption, that the order parameter at the surface is driven by the variation of the total free energy $(\delta F[\phi]/\delta\phi)_{\partial V}$, cf. eq. (1.57), yielding

$$\left.\frac{\partial \phi}{\partial t}\right|_{\partial V} = -\Gamma_s \left[\sigma_b (\mathbf{n}\cdot\nabla)\phi - \sigma_s \Delta_{\|}\phi + \frac{\partial f_s}{\partial \phi} \right]_{\partial V} \,, \tag{1.61}$$

where Γ_s is a new kinetic coefficient at the surface. This equation is similar to the kinetic equation for a phase separating system with a non–conserved order parameter. This is reasonable, since the order parameter, averaged over the surface solely, is a non–conserved quantity.

Alternatively, one may obtain similar boundary conditions by taking the continuum limit of simple lattice models within a direct mean–field approximation [Bin91a] or by applying density functional theory [Fis98a].

It is straightforward to show that, with the kinetics specified by eqs. (1.49, 1.60, 1.61), $F[\phi]$ is a monotonously decreasing function of time as long as $\mathbf{j}(\mathbf{y}, t)$ is different from zero and that $F[\phi]$ does not change in time if and only if $\mu(\mathbf{y}, t)$ is a constant. Moreover, the existence of a solution for the boundary value problem eqs. (1.49, 1.60, 1.61) could be proven, thus the problem is well–posed [Rac01].

The boundaries can have a strong influence on the demixing processes. A surface field, for instance, preferentially attracting one component induces demixing waves normal to the surface, so called "surface directed spinodal waves" (SDW). These waves have been studied numerically in terms of a "cell dynamical system" (CDS), see [Pur97] for a review. While the setup of the CDS is guided by Cahn–Hilliard theory, it should be viewed as a further phenomenological description of phase separation processes in its own rather, than it provides a real solution of the CHE [Oon87].[1] The essential result of these studies is that the growth of the SDW in the late time regime again obeys the Lifshitz–Slyozov law in the case of rather weak surface fields and strong noise. Without noise (and in the case of strong surface fields) a wetting layer forms near the surface that grows very slowly.

For short times, a stability analysis of the linearized Cahn–Hilliard equation, supplemented by boundary conditions slightly different from those presented above, shows that the penetration of the surface effects is determined by bulk properties only and not by surface parameters. Especially the wavelength of the SDW is approximately given by the bulk demixing length λ_m [Fri95]. It is worth noting that even in the homogeneous phase a surface field has a pronounced influence on the concentration field and leads to an enhancement of one component at the surface. Considering a quench from high temperatures into the one phase region a diffusive saturation of the order parameter value at the surface is found even in the case of long ranged surface potentials [Fri99].

If the surface favors neither of the two components, other interesting effects can occur. An analysis of the linearized CHE with linearized boundary conditions eqs. (1.60, 1.61) yields that near the surface the lateral demixing length can be altered due to the modified interaction between the components near the wall and may not be equal to the bulk demixing length λ_m [Fis97a]. Moreover, in thin films the lateral demixing length diverges and the corresponding characteristic times grow with decreasing L_z. Ultimately, if the film thickness becomes smaller than some critical value $L_z < L_c$, the instability vanishes and spinodal decomposition may be suppressed [Fis98b].

1.4 Experiments with Polymer Blends

Demixing processes of polymer blends in confined geometries have been studied extensively. The major advantage of these systems from an experimental point of view is that the corresponding time and length scales of structure formation are large as compared to simple liquids, giving easy experimental access to the phenomena.

[1] The reason for the application of the CDS to phase separation were technical difficulties in solving the CHE numerically, cf. sec. 2.2.

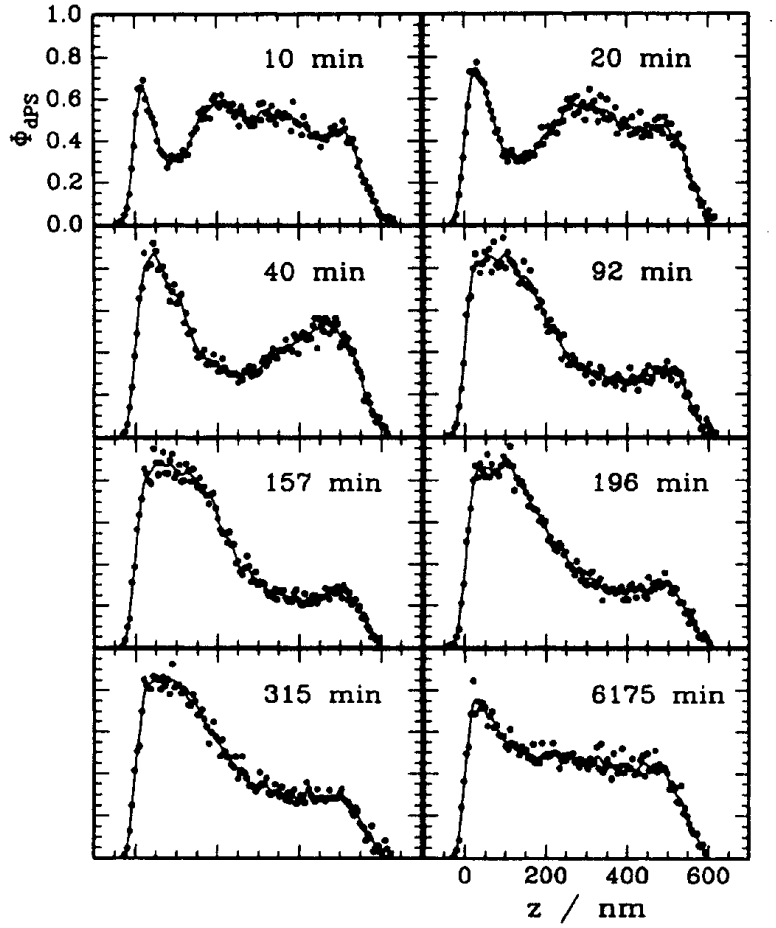

Figure 1.5: Volume fraction of dPS ϕ_{dPS} as a function of depth z normal to the film surface, after various annealing times t. The vacuum surface is at $z = 0$ nm, the silicon wafer with a native oxide layer at $z = 550$ nm. The lines are cubic splines to guide the eye, after [Bru92].

The perhaps most pronounced effect of demixing near an interface is the formation of a *surface directed spinodal decomposition wave* (SDW). Such a wave forms, if one component, e.g. A, of the mixture is preferentially attracted by the surface. This leads to an enrichment of A near the surface and, for conservation reasons, to a depletion zone in a second layer. Thus concentration gradients are build up in normal direction to the surface and are amplified by the bulk instability, leading to further, damped oscillations of the concentration profile.

As an example, we show experimental results of Bruder and Brenn [Bru92]. They studied thin films of a binary polymer blend consisting of deuterated polystyrene (dPS) and poly(styrene–co–4–bromostyrene) ($\mathrm{PBr}_x\mathrm{S}$) on a silicon substrate, with a native oxide layer. The critical Flory–Huggins parameter and the critical composition for this system are $\chi_c = 1.69 \times 10^{-3}$ and $\phi_{\mathrm{dPS},c} = 0.52$ and both species have similar degrees of polymerization. The films were prepared by *spin coating*, i.e. a drop of both components in toluene solution with a composition of $\bar{\phi}_{\mathrm{dPS}} = 0.50$ was spread by rapid rotation of the substrate, leading to homogeneous films of 550 nm thickness. Afterwards the films were heated under vacuum conditions

to 180 ° C. At this temperature the compositions of the coexisting phases are $\phi_{\mathrm{dPS},1} = 0.15$ and $\phi_{\mathrm{dPS},2} = 0.87$, and the Flory–Huggins parameter is $\chi = 2.12 \times 10^{-3}$. After annealing the films for various times, they were rapidly quenched to ambient temperature and the laterally averaged concentration profiles were measured by *time–of–flight elastic–recoil–detection* (TOF–ERD) [Kra95]. Note that the structure of the films is stable at ambient temperature on experimental relevant time scales.

Their results, concentration profiles of $\phi_{\mathrm{dPS}}(z)$ at various annealing times, are shown in fig. 1.5. The vacuum surface is at $z = 0$ nm, the silicium substrate at $z = 550$ nm. For $t = 0$ (not show), the concentration profile is flat, $\phi_{\mathrm{dPS}}(z) = \bar{\phi}_{dPS}$. At early times ($t = 10$ min) a SDW emerges at the vacuum surface and propagates into the film. The silicon substrate is neutral with respect to both components, because no SDW is visible on the side of the substrate. At later times $t > 40$ min, the concentrations at coexistence $\phi_{\mathrm{dPS},1}, \phi_{\mathrm{dPS},2}$ are almost reached near the silicon and the vacuum surface respectively, separated by an interface parallel to the substrate. Additional light microscopy observations show that at this time lateral structures, i.e. droplets of regions rich in dPS begin to form near the silicon surface. This droplet pattern coarsens by interdiffusion. In the final stages $t > 315$ min the droplets have reached a size comparable to the film thickness. The interface parallel to the substrate begins to resolve and at very late times the lateral coarsening of the droplets is effectively a two dimensional process.

This experiment exemplifies that the kinetics of demixing in confined geometries yield rich phenomena and that one has to care about the whole three dimensional structure of the system to interpret the experimental results properly. Therefore different measurements are needed for a full characterization of the sample.

Similar experiments were made by Krausch et al. [Kra93] investigating the dependence of the SDW on the film thickness. They considered films of a nearly symmetrical mixture of poly(ethylene–propylene) PEP and deuterized poly(ethylene–propylene) dPEP on a pure silicon surface. While the vacuum surface prefers dPEP, the silicon surface attracts preferably PEP, leading to an antisymmetric situation. After annealing the films at $T = 321$ ° K for 5.5 h, the resulting composition profiles were examined using *nuclear reaction analysis* (NRA) and *time–of–flight forward–recoil–spectrometry* (TOF–FRES) [Kra95]. The results are shown in fig. 1.6 for various film thicknesses L_z. The authors found constructive interference, cf. fig. 1.6b, and destructive interference, cf. fig. 1.6d, of the two SDWs emerging from each surface. For very thin films $L_z \approx \lambda_b$ rather a weak segregation than a formation of a SDW is found, i.e. the SDW is suppressed in thin films, see fig. 1.6e.

Effects of a confinement on the lateral domain growth were studied by Sung et al. with optical microscopy (OM) [Sun96]. They examined binary blends of deuterated polystyrene (dPS) and polybutadiene (PB) with a near critical composition $\phi_{\mathrm{dPS},c} = 0.7$ on a pure Si substrate in films of thicknesses $L_z = 200$ μm, 100 nm, and 20 nm. The films are thin enough such that no SDWs could occur and the lateral pattern could be studied without superposition by them. While their focus was on the crossover from three dimensional to two dimensional lateral domain coarsening in the hydrodynamic regime, their data show also that the characteristic domain sizes at short times ($t \approx 100$ min) grow with decreasing film thickness. If the film thickness is about 10% of the bulk demixing length λ_m, the lateral demixing length amounts to about 25 times λ_m.

A question of high technological importance is, whether the structure of the domain pattern can be controlled by the properties of the substrate. This would be an essential step towards

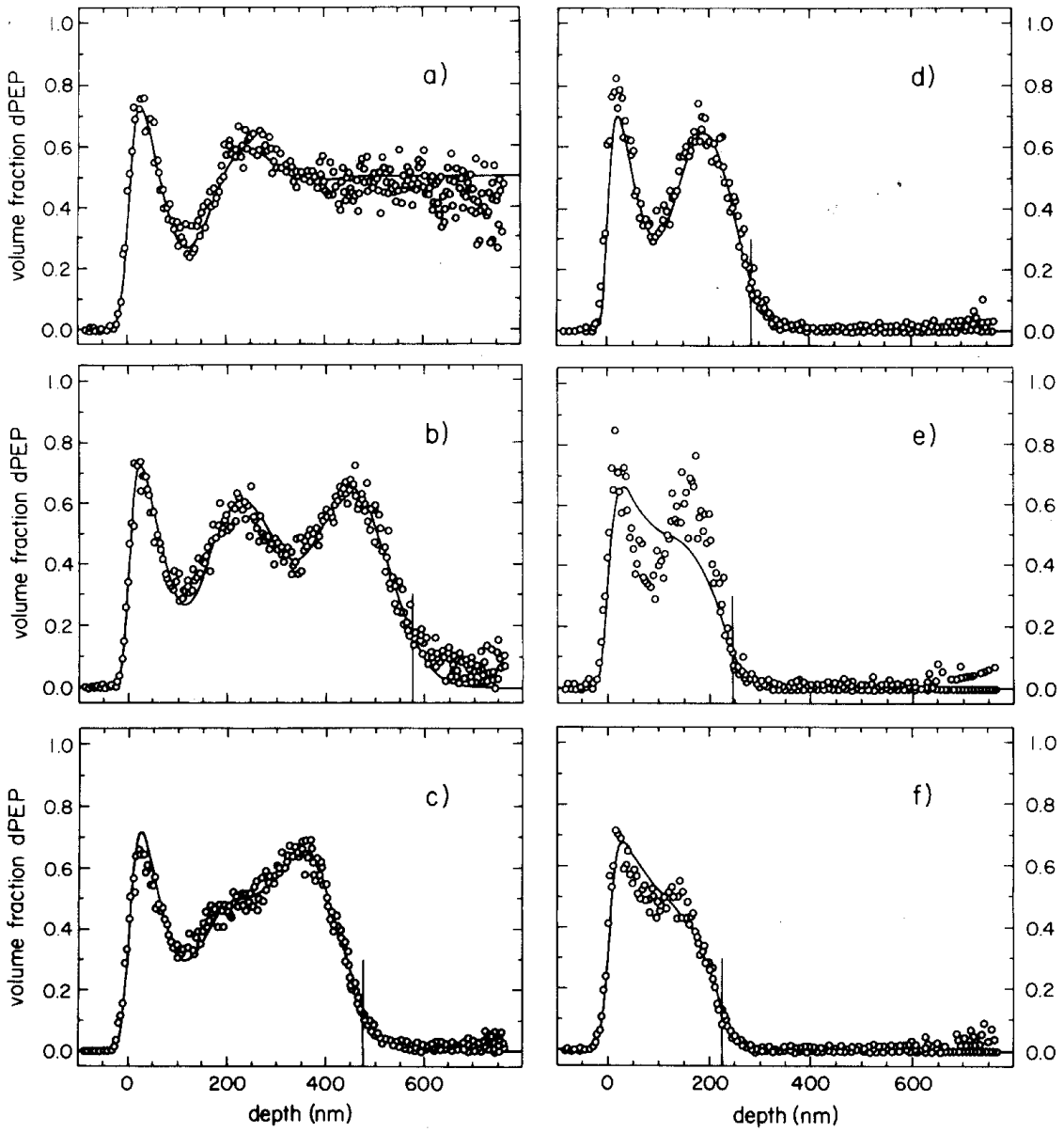

Figure 1.6: Volume fraction of dPEP ϕ_{dPEP} as a function of depth z for different film thicknesses L_z, as determined by NRA. The locations of the Si substrates are indicated by vertical lines, a) $L_z > 1000$ nm, b) $L_z = 574$ nm, c) $L_z = 474$ nm, d) $L_z = 282$ nm, and e) $L_z = 220$ nm. The lines are fit functions consisting of a superposition of shifted cosini multiplied by a Gaussian, after [Kra93].

an easy fabrication of optical devices, microelectronic circuits, e.g. transistors, consisting of polymeric semiconductors, or other small scale organic structures.

That a transference of a substrate pattern onto the decomposition pattern of a binary polymer blend is indeed possible, was shown by Böltau et al. [Böl98]. They considered a symmetric mixture of PS and polyvinylpyridine (PVP) on a gold substrate, partly covered by a self assembled monolayer (SAM) of octadecylthiol (ODT). While PVP is preferentially attracted by

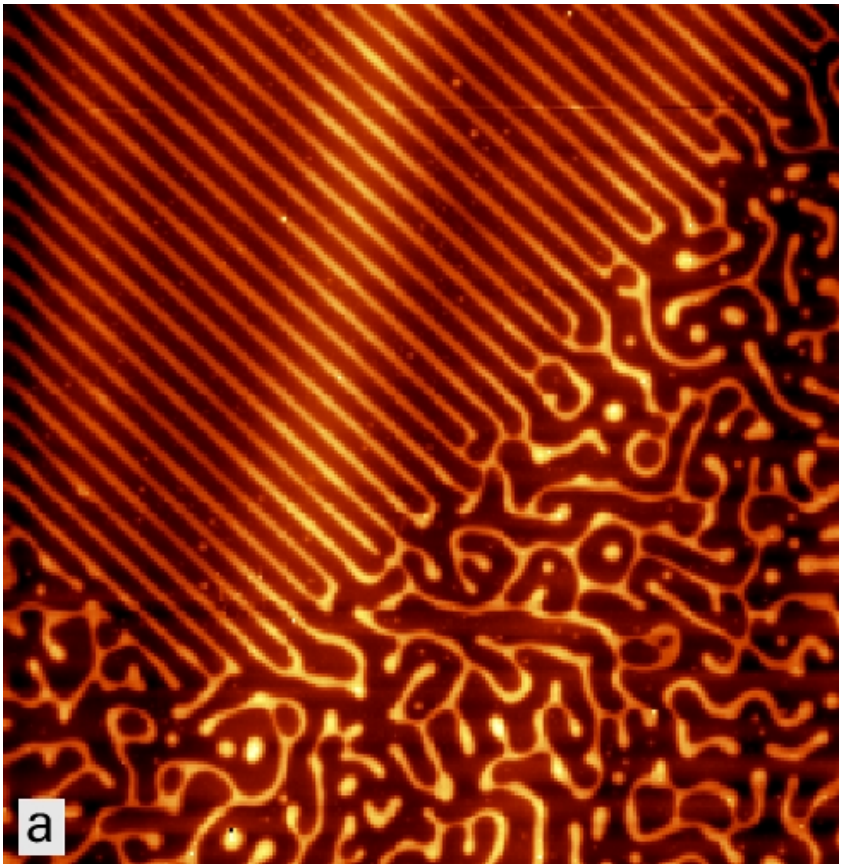

Figure 1.7: Atomic force microscopy (AFM) image of a PS/PVP blend on a Au/SAM surface with an area of 80×80 μm^2. Light regions correspond to PVP–rich domains, while dark regions to PS–rich domains accordingly. In the region of the structured substrate the domain pattern adopts to the surface, while on the pure SAM surface an irregular domain pattern is found. The picture is taken from [Wal00].

the gold substrate, the SAM prefers neither of both components, leading to a lateral demixing pattern. Using the microcontact printing technique, they structured the substrate with a stripped pattern and considered the demixing process on such a substrate during spin coating. As it is shown in fig. 1.7, the polar gold surface attracts PVP and leads to a surplus of PS on the SAM in the structured region. Thus the pattern of the substrate is successfully transferred onto the domain pattern. On the pure SAM layer, however, an irregural lateral domain pattern is observed. The obviously non–equilibrium structure is stable, because the mixture solidifies after the spincoating process, i.e. after evaporation of the solvent. They could achieve a clear transference of the pattern only after carefully tuning several experimental parameters, especially the film thickness and the periodicity of the substrate.

Experiments of Karim et al. [Kar98] showed similar results. They found that the relative polymer volume fractions and the relative areas of the surface pattern seem to be the primary parameters controlling the reproduction of the surface pattern by the domains.

While the structure of the surface pattern in previous experiments was on the scale of a few micrometer, newer experiments reduced this length scale to the nanometer regime. Exam-

ining a symmetric binary mixture of PS and polymethylmethacrylate (PMMA) on a stripped Au/SiO substrate with a periodicity of 60 nm, Rockford et al. found that the surface is on large scales (μm) virtually neutral with respect to both components [Roc99]. The blend ignores the nanoscopic patterning to which the domain structure cannot adhere and experiences effectively a homogeneous surface field. However, on removing the large scale domains by selective solvents, a nanoscopic domain pattern structure near the substrate is found. Therefore locally the structure of the substrate is found in the pattern of the blend. In the same work the authors also showed, that with the help of nanoscopically patterned substrates microphase separation of block copolymers can be controlled. In this case the pattern periodicity has to be commensurate with the block copolymer periodicity in the bulk, i.e. of order R_G.

As a last example for the rich phenomena occurring in these systems, we present results of Fukunaga et al., who considered an AC–mixture consisting of PS and poly(tert–butyl methacrylate) (PtBMA) on an ABC–block copolymer brush of poly(styrene–block–2–vinylpyridine–block–tert–butyl methacrylate) [Fuk00]. As the B component (vinylpyridine–block) is attracted by the SiO substrate the brush forms on microphase separation effectively a checkerboard like surface pattern with a typical size of $L_{\|}$ =80 nm. The brush and the resulting lateral domains were characterized by height sensitive atomic force measurements (AFM). Phase separation of a L_z =20 nm thick film of PS/PtBMA on this brush yields, upon annealing, stable lateral structures with sizes comparable to the characteristic length scale of the brush. To explain this result, the authors considered the surfaces energies involved and found a maximal film height of $L_z \approx L_{\|}/4$ for stability of the small lateral structures. The hypotheses was tested by experiments with homopolymer films on the same substrate yielding qualitative agreement with their considerations.

To conclude this section, phase separation processes of polymer blends in confined geometries lead to a variety of interesting domain morphologies with a high potential for technological applications. The length scales of the demixing pattern and the film thickness thereby can become comparable to the radius of gyration, typically a few 10 nm. However, experimental characterization of the whole three dimensional pattern, especially a time resolved measurement is sumptuous. Therefore simulations and theoretical treatment are needed to give a deeper insight in the complex processes involved.

1.5 Theoretical Approaches

While the slow kinetics of demixing processes in polymer systems is an advantage for the experimentalist because he can examine the dynamics in real time on the time scale of seconds, minutes or days, it poses a major problem for a theoretical or computational description. The typical atomistic vibrational times in these systems are of order 10^{-13} s, thus there is a time scale gap of at least 13 orders of magnitude between an elementary process and the observed kinetics. Therefore a direct simulation of demixing processes on a molecular scale is not possible. Further on it would not necessarily make much sense to do such a simulation in first place, because it would be difficult to identify the generic behavior of different kinds of polymers in an overwhelming amount of data specific for one kind of polymer. Coarse–grained polymer models are used instead, where some monomers are described by one bead, in principle similar to the procedure described in sections 1.1.1 and 1.1.2 but, of course, much more sophisticated,

starting from atomistic polymer models and not ideal chains. An extensive review of this kind of coarse–graining is given in ref. [Bas00a]. The perhaps most common types of such models are the *bead–spring* model [Kre95] that is typically used in *molecular dynamic* simulations of polymer systems, and the *bond–fluctuation* model [Pau95], a lattice model used in *Monte Carlo* simulations.

While it is possible to study phase separation phenomena in the framework of such coarse–grained models [Bin95b], the method is limited to rather short chain lengths, small systems and early time regimes. The main reason for these limitations is the fact, that real chains form entanglements in dense systems slowing down diffusive processes on a length scale $\gtrsim R_e$ by the disentanglement time $\tau_d \sim N^3$, cf. eq. (1.27). The overall computational effort at fixed polymer number M for simulating such a process is therefore of order $\mathcal{O}(N^4)$. In fact, the crossover from Rouse to reptation dynamics has been studied in simulations only recently [Kre00]. On the other hand, as discussed in sec. 1.1.4, the kinetic behavior of polymer melts on time scales $t \gg \tau_d$ is simple diffusive. For this reason it is possible to neglect the entanglement effects on large time scales and absorb them in a rescaling of the time, where τ_d now sets the time–unit.

One possibility to deal with this problem is to employ macroscopic continuum models, for example the time dependent Ginzburg–Landau theory discussed in sec. 1.3. An improved way to build in polymer specific properties in this kind of treatment has been recently developed in terms of a *dynamic self–consistent–field theory* (DSCFT) [Rei01]. Starting from the continuity equation (1.46), this theory also assumes a linear relation between the current and the gradient of the chemical potential

$$\mathbf{j}(\mathbf{y},t) = \int d^3y'\, \Gamma_b(\mathbf{y},\mathbf{y}')\, \nabla\mu(\mathbf{y}',t)\,, \tag{1.62}$$

but now allows for a varying kinetic coefficient $\Gamma_b(\mathbf{y},\mathbf{y}')$ describing the connection between the force acting on the monomers by $\nabla\mu(\mathbf{y}',t)$ at position $\mathbf{y}'$ and the resulting current at position $\mathbf{y}$. Considering the Rouse model as the underlying polymer kinetics, the kinetic coefficient may be approximated by

$$\Gamma_b(\mathbf{y},\mathbf{y}') \approx D_{\text{self}} N \bar{\phi}_A \bar{\phi}_B\, G_0(\mathbf{y},\mathbf{y}')\,, \tag{1.63}$$

where $G_0(\mathbf{y},\mathbf{y}')$ denotes the pair correlation function. Inserting eq. (1.62) into the continuity equation (1.46) yields after Fourier transformation the kinetic equation

$$\frac{\partial}{\partial t}\hat{\phi}_A(\mathbf{k},t) = -\hat{\Gamma}_b(\mathbf{k}) k^2 \hat{\mu}(\mathbf{k},t) + \hat{\eta}(\mathbf{q},t)\,. \tag{1.64}$$

The relation between ϕ_A and ϕ_B is given by the incompressibility condition eq. (1.45). Then the free energy functional needed for the calculation of the chemical potential, eq. (1.48), is taken from the saddle–point approximation of the self–consistent–field theory, see sec. 1.2.3, yielding [Rei01]

$$\frac{\mu(\mathbf{y})}{k_B T} = \chi\big(\phi_B(\mathbf{y}) - \phi_A(\mathbf{y})\big) - \frac{1}{N}\big(w_A[\phi_A(\mathbf{y})] - w_B[\phi_B(\mathbf{y})]\big) \tag{1.65}$$

The fields $w_X[\phi_X(\mathbf{y})]$ are determined uniquely in terms of the concentrations $\phi_X(\mathbf{y})$ by eq. (1.43). By solving the corresponding set of equations for this description, Reister et al. studied the

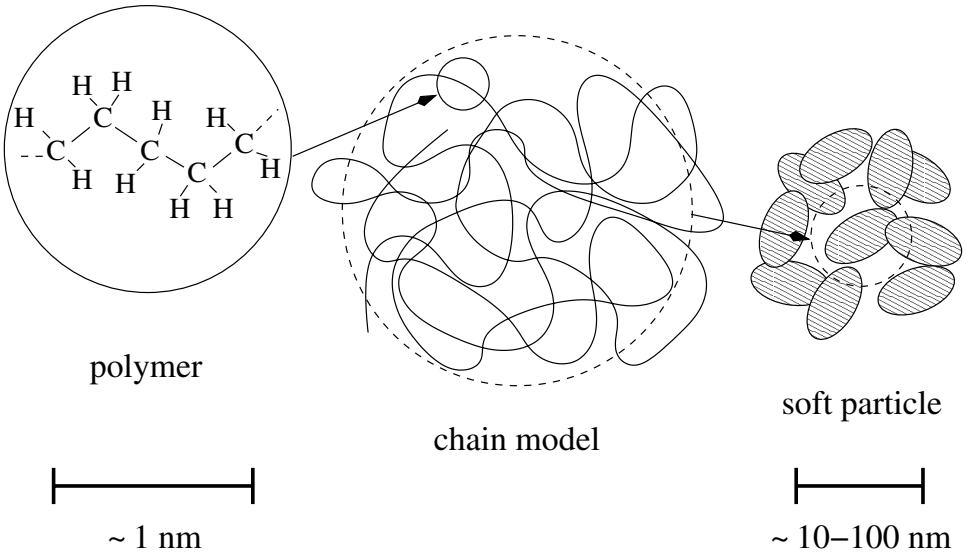

Figure 1.8: Hierarchy of coarse–graining from atomistic/microscopic to semi–microscopic and further to semi–macroscopic. The molecular realistic polymer models are in a first step mapped onto coarse–grained chain models and afterwards onto one soft particle.

early time kinetics of spinodal decomposition of a binary polymer blend and found quantitative agreement with Monte Carlo simulations of the bond fluctuation model [Rei01]. However, the involved calculations are numerically expensive, therefore it is hard to reach the late time coarsening regime. The numerical performance can be improved by deriving kinetic equations for the external fields of the SCFT leading to an *external potential dynamics* (EPD), which is about an order of magnitude faster that DSCFT.

An alternative approach in treating the problem of dense polymer systems is to do an additional second coarse–graining step, cf. fig. 1.8. In this step one chain molecule consisting of $N+1$ connected beads is mapped onto one particle. Because such a chain is a very dilute object, the corresponding particles should be in some sense very soft.

One possibility to do such a coarse–graining is, to derive a concentration dependent effective pair potential acting between the centers of mass of the polymers [Lou00]. This can be done, by obtaining the concentration dependent pair correlation function between the centers of mass $G_{\mathrm{cm}}(r)$ from Monte Carlo simulations of self avoiding chains in dilute and semi–dilute solution. Using the Ornstein–Zernike relation in combination with the hypernetted chain closure relation, a unique effective pair potential $v_{\mathrm{eff}}(r)$, capable of reproducing $G_{\mathrm{cm}}(r)$, can be obtained. The resulting effective potential is spherical symmetric, bell shaped, and has an extension of about $\bar{R}_G$ and a finite value at $r = 0$ for all N. While this approach is practicable in dilute and semi–dilute systems, i.e. for the description of solutions of polymer–colloid mixtures, in dense systems multi particle interactions are important, which are only partly included by introducing $v_{\mathrm{eff}}(r)$. Therefore this approach seems to be less suited for binary polymer blends.

An other possibility was given by Murat and Kremer, who proposed to map a chain molecule directly onto one soft ellipsoid by determining the average monomer density of the chain for a given ellipsoidal shape [Mur98]. The properties of the ellipsoid are determined fully in terms of the underlying chain model. The thermodynamics for an ensemble of ellipsoids then is

supplied by an ansatz for the free energy functional in terms of the monomer densities and the probabilities of the shapes of the ellipsoids. In their ansatz, however, an interaction parameter has to be adjusted to the results of simulations of chain molecule ensembles to obtain the right scaling $\bar{R}_G \sim \sqrt{N}$ in dense systems. The kinetic properties of the model are defined by a discrete time Monte Carlo algorithm, see chapter 3 for a detailed description of this model. With this approach many important features of dense polymer systems, e.g. the *correlation hole* occurring in a polymer melt or the scaling of the phase diagram of a polymer blend with N, could be described. Moreover, the late stage coarsening regime of spinodal decomposition in a large bulk system was approached. Therefore this model seems to be a promising starting point for the description of demixing processes of polymer blends in confined geometries.

1.6 Goals of this Work

In this work we aim at a qualitative description of generic processes occurring in the slow kinetics of demixing polymer blends in confined geometries. We focus especially on the investigation of the interplay between the different occurring length scales, i.e. the demixing length, the film thickness and the characteristic length scales of patterned substrates. A major point hereby is to set up an efficient model that on one hand does not suffer from the problems of explicit chain models, resulting from entanglement effects, and on the other hand can resolve the structure of the systems on the scale $\bar{R}_G$.

In a first step we will consider the description of such systems in the framework of Cahn–Hilliard theory. From a physical point of view we confirm the predictions of the short time stability analysis by Fischer et al. [Fis98b], regarding the growth of the lateral demixing length in thin films, by a numerical solution of the CHE with appropriate boundary conditions. As the numerical treatment of the Cahn–Hilliard equation poses difficulties due to numerical instabilities of the corresponding linesystem, an implicit scheme has been applied to the problem, allowing for a description of the whole kinetics from the earliest stages of phase separation until equilibrium is reached [Ken01]. A limitation is that the application of this scheme is at the moment practicable in two dimensions only. Moreover, this kind of description is not very specific for polymers.

In a second step we will therefore turn to a description of polymer systems in terms of a soft particle model. Building on ideas by Murat and Kremer [Mur98] we develop soft particle models for polymer chains on the basis of the Gaussian chain. This in turn will lead us to study the geometrical properties of Gaussian chains in detail, and thus to determine the properties of the soft particles for a given shape. In the rest of this work we will focus on the Gaussian ellipsoid model (GEM) and present results for bulk and slab systems. It is shown that in the GEM an adjustment of the interaction parameter is no longer necessary to obtain the right scaling relations between $\bar{R}_G, N$ and the monomer concentration c, however with the Flory exponent $\nu = 3/5$ instead of $\nu \approx 0.588$. Therefore it is possible to establish this model without simulations of chain molecule systems. Further on, we show that the model exhibits many properties characteristic for polymer systems, and it is very efficient so that the long time regime in demixing processes can be reached [Eur01].

Finally, we will extend the GEM to slab geometry. We study orientation and deformation of the ellipsoids near the walls and find agreement with previous results of chain simulations.

In the case of binary mixtures between two homogeneous and neutral walls we find again an increased lateral demixing length in thin films. If one of the two surfaces is patterned, the case corresponding to demixing experiments on prestructured substrates, we can give a simple criterium for the stability of a structured domain pattern. The kinetic pathways leading to the different equilibrium structures are examined and characterized [Eur02].

2 Cahn–Hilliard Theory

The Cahn–Hilliard equation (CHE) discussed in sec. 1.3 provides a good phenomenological description of phase separation processes both, in bulk systems and in confined systems. In this chapter we will focus on two aspects in the framework of the Cahn–Hilliard theory:

First, we present an analytical solution of the linearized CHE for the short–time regime in slab geometry, in the case when a surface directed spinodal decomposition wave (SDW) occurs. The result is given in terms of a Fourier series expansion with respect to the spatial coordinates. Especially, we derive a condition for the suppression of a SDW in thin films. While such a suppression for film thicknesses $\lesssim \lambda_m$ seems to be plausible in the light of the results derived in ref. [Fri95], a rigorous explanation has not been given so far.

Secondly, we solve the CHE (1.49) with periodic boundary conditions, as well as boundary conditions (1.60, 1.61) numerically by an implicit method. Thus we circumvent strong restrictions with respect to the time steps arising for explicit methods. In order to demonstrate the applicability of the procedure, we show that the new numerical scheme enables us to explore the whole dynamics of phase separation from the earliest stages up to the times, when stable equilibrium configurations form. Moreover, we use the procedure to confirm earlier analytical results for the short time regime in slab geometry and extend the studies to later times.

2.1 Linearized Problem

Let us assume, that a binary mixture of average composition $\bar{\phi}$ is brought instantaneously from an almost homogeneous state $\phi(\mathbf{y}, t=0) = \bar{\phi} + \eta(\mathbf{y})$ into the spinodal region. Here $\eta(\mathbf{y})$ denotes some small fluctuations around the homogeneous state. For short times it is possible to do a stability analysis of the kinetic system defined by eqs. (1.49, 1.60, 1.61) and to linearize the problem with respect to the initial state. This yields for the fluctuations $\delta\phi(\mathbf{y}, t) = \phi(\mathbf{y}, t) - \bar{\phi}$

$$\left[\partial_t + \Gamma_b \Delta \left(\sigma_b \Delta - f_b''(\bar{\phi})\right)\right] \delta\phi(\mathbf{y}, t) = 0 \tag{2.1a}$$

$$(\mathbf{n} \cdot \nabla) \left[\sigma_b \Delta - f_b''(\bar{\phi})\right]_{\partial V} \delta\phi(\mathbf{y}, t) = 0 \tag{2.1b}$$

$$\left[\Gamma_s^{-1} \partial_t + \sigma_b (\mathbf{n} \cdot \nabla) - \sigma_s \Delta_{\parallel} + f_s''(\bar{\phi})\right]_{\partial V} \delta\phi(\mathbf{y}, t) = -f_s'(\bar{\phi}), \tag{2.1c}$$

with the notation $f_s' = \partial_\phi f_s$, $f_s'' = \partial_\phi^2 f_s$ and so on. The characteristic length scale of the process is given by the correlation length $\xi_b = \sqrt{\sigma_b / f_b''(\phi_1)}$ and its time scale by $\tau = \xi_b^2 / \Gamma_b f_b''(\phi_1)$, where

ϕ_1 is the order parameter value at coexistence, see fig. 1.3. With the replacements

$$\begin{aligned} t_l &= t/\tau & \mathbf{y}_l &= \mathbf{y}/\xi_b \\ g_b &= f_b''(\bar{\phi})/f_b''(\phi_1) & g_s &= f_s''(\bar{\phi})/f_b''(\phi_1)\,\xi_b \\ h_l &= -f_s'(\bar{\phi})/f_b''(\phi_1)\,\xi_b & \sigma_{sl} &= \sigma_s/f_s''(\phi_1)\,\xi_b^3 \\ \Gamma_{sl} &= \Gamma_s\,\xi_b^3/\Gamma_b & \phi_l &= \delta\phi \end{aligned}$$

the linearized problem eqs. (2.1a–2.1c) can be rewritten in a scaled form

$$[\partial_{t_l} + \Delta\,(\Delta - g_b)]\,\phi_l(\mathbf{y}_l, t_l) = 0 \tag{2.2a}$$

$$(\mathbf{n}\cdot\nabla)\,[\Delta - g_b]_{\partial V}\,\phi_l(\mathbf{y}_l, t_l) = 0 \tag{2.2b}$$

$$\left[\Gamma_{sl}^{-1}\partial_{t_l} + (\mathbf{n}\cdot\nabla) - \sigma_{sl}\Delta_{\|} + g_s\right]_{\partial V}\phi_l(\mathbf{y}_l, t_l) = h_l\,. \tag{2.2c}$$

Here the operators ∇ and Δ are acting on $\mathbf{y}_l$. For convenience we will suppress the index l in t_l and $\mathbf{y}_l$ in the following and write again t and $\mathbf{y}$. Now we consider a slab of thickness L with homogeneous, planar walls. In contrast to a bulk system, there is no translational invariance perpendicular to the wall, but only in parallel direction. Introducing the lateral Fourier transform $\hat{\phi}_l(\mathbf{k}_{\|}, z, t)$ and denoting the perpendicular direction by z, yields

$$[\partial_t + (\partial_z^2 - k_{\|}^2)(\partial_z^2 - k_{\|}^2 - g_b)]\;\hat{\phi}_l(\mathbf{k}_{\|}, z, t) = 0 \tag{2.3a}$$

$$\partial_z[\partial_z^2 - k_{\|}^2 - g_b]_{z=0}\;\hat{\phi}_l(\mathbf{k}_{\|}, z, t) = 0 \tag{2.3b}$$

$$[\Gamma_{s0}^{-1}\partial_t - \partial_z + \sigma_{sl}k_{\|}^2 + g_{s0}]_{z=0}\;\hat{\phi}_l(\mathbf{k}_{\|}, z, t) = h_0\,\delta_{\mathbf{k}_{\|},0} \tag{2.3c}$$

$$\partial_z[\partial_z^2 - k_{\|}^2 - g_b]_{z=L}\;\hat{\phi}_l(\mathbf{k}_{\|}, z, t) = 0 \tag{2.3d}$$

$$[\Gamma_{sL}^{-1}\partial_t + \partial_z + \sigma_{sl}k_{\|}^2 + g_{sL}]_{z=L}\;\hat{\phi}_l(\mathbf{k}_{\|}, z, t) = h_L\,\delta_{\mathbf{k}_{\|},0}\,. \tag{2.3e}$$

Since both boundaries may be different, we denoted the (scaled) surface parameters by h_0, g_{s0} and Γ_{s0} for $z = 0$, and h_L, g_{sL} and Γ_{sL} for $z = L$. Equations (2.3a–2.3e) constitute an inhomogeneous boundary value problem. The solution is given by a superposition of the solution of the homogeneous system $\hat{\phi}_{\mathrm{hom}}$ and a particular solution ϕ_p of the inhomogeneous system

$$\hat{\phi}_l(\mathbf{k}_{\|}, z, t) = \hat{\phi}_{\mathrm{hom}}(\mathbf{k}_{\|}, z, t) + \phi_p(z, t)\,. \tag{2.4}$$

Since the inhomogeneity does not depend on $\mathbf{k}_{\|}$ in this case, neither does ϕ_p. The homogeneous problem has already been solved in ref. [Fis97b]. Here we will present an analysis for the particular solution ϕ_p. The corresponding solution for a semi–infinite system has been given by Frisch et al. in terms of a Laplace transform [Fri95].

2.1.1 Particular Solution for the Linearized Problem

In this section we treat the inhomogeneous linear problem eqs. (2.3a–2.3e). With the help of a Fourier series expansion the problem can be transformed into a coupled system of ordinary differential equations for the Fourier coefficients. For the relevant case $\Gamma_{sl} \to \infty$ and $g_s = 0$,

where Γ_{sl} and g_s denote the respective parameters at both boundaries, an exact solution is given.

We consider the following problem for the particular solution ϕ_p:

$$[\partial_t + \partial_z^4 - g_b\,\partial_z^2]\;\phi_p(z,t) \;=\; 0 \tag{2.5a}$$
$$[\partial_z^3 - g_b\,\partial_z]_{z=0}\;\phi_p(z,t) \;=\; 0 \tag{2.5b}$$
$$[\Gamma_{s0}^{-1}\partial_t - \partial_z + g_{s0}]_{z=0}\;\phi_p(z,t) \;=\; h_0 \tag{2.5c}$$
$$[\partial_z^3 - g_b\,\partial_z]_{z=L}\;\phi_p(z,t) \;=\; 0 \tag{2.5d}$$
$$[\Gamma_{sL}^{-1}\partial_t + \partial_z + g_{sL}]_{z=L}\;\phi_p(z,t) \;=\; h_l\,. \tag{2.5e}$$

As initial condition we choose $\phi_p(z,0) = 0$. By using the method of series expansion [Str95], each spatial derivative $\partial_z^r\phi_p(z,t)$ of order r is expanded into a Fourier series

$$\partial_z^r\phi_p(z,t) = \sum_{n=1}^{\infty} A_{n,r}(t)\sin(k_n z) + \frac{1}{2}B_{0,r}(t) + \sum_{n=1}^{\infty} B_{n,r}(t)\cos(k_n z)\,, \tag{2.6}$$

where $k_n = n\pi/L$. The time dependent Fourier coefficients are given by

$$A_{n,r}(t) \;=\; \frac{2}{L}\int_0^L dz\;\sin(k_n z)\,\partial_z^r\phi_p(z,t) \tag{2.7a}$$
$$B_{n,r}(t) \;=\; \frac{2}{L}\int_0^L dz\;\cos(k_n z)\,\partial_z^r\phi_p(z,t)\,. \tag{2.7b}$$

Integrating eqs. (2.7a, 2.7b) by parts, the $A_{n,r}$ and $B_{n,r}$ for $r > 0$ can be expressed in terms of $A_{n,0}$ and $B_{n,0}$. Introducing the shorthand notation $A_n \equiv A_{n,0}$ and $B_n \equiv B_{n,0}$ and denoting the partial derivatives $\partial_z^r\phi_p(z,t)$ at a fixed position z_0 by $\phi_p^{(r)}(z_0,t)$, we find

$$A_{n,2}(t) = -\frac{2}{L}k_n\left[(-1)^n\,\phi_p(L,t) - \phi_p(0,t)\right] - k_n^2 A_n(t) \tag{2.9}$$
$$B_{n,2}(t) = \frac{2}{L}\left[(-1)^n\,\phi_p^{(1)}(L,t) - \phi_p^{(1)}(0,t)\right] - k_n^2 B_n(t) \tag{2.10}$$
$$\begin{aligned} A_{n,4}(t) = -\frac{2}{L}k_n\Big\{&\left[(-1)^n\,\phi_p^{(2)}(L,t) - \phi_p^{(2)}(0,t)\right] \\ &- k_n^2\left[(-1)^n\,\phi_p(L,t) - \phi_p(0,t)\right]\Big\} + k_n^4 A_n(t) \end{aligned} \tag{2.11}$$
$$\begin{aligned} B_{n,4}(t) = \frac{2}{L}\Big\{&\left[(-1)^n\,\phi_p^{(3)}(L,t) - \phi_p^{(3)}(0,t)\right] \\ &- k_n^2\left[(-1)^n\,\phi_p^{(1)}(L,t) - \phi_p^{(1)}(0,t)\right]\Big\} + k_n^4 B_n(t)\,. \end{aligned} \tag{2.12}$$

Note that to obtain a relation between the coefficients, partial differentiation is not possible for convergence reasons [Str95]. Combining eqs. (2.9–2.12) with the linear partial differential

equation (2.5a) and using both impermeability conditions (2.5b, 2.5d) yields

$$\begin{aligned}\partial_t A_n(t) + \omega_n A_n(t) = \frac{2}{L} k_n \Big\{ &\left[(-1)^n \, \phi_p^{(2)}(L,t) - \phi_p^{(2)}(0,t)\right] \\ &- \left(k_n^2 + g_b\right) \left[(-1)^n \, \phi_p(L,t) - \phi_p(0,t)\right] \Big\}\end{aligned} \tag{2.13}$$

$$\partial_t B_n(t) + \omega_n B_n(t) = \frac{2}{L} k_n^2 \left[(-1)^n \, \phi_p^{(1)}(L,t) - \phi_p^{(1)}(0,t)\right] \tag{2.14}$$

where we defined

$$\omega_n \equiv k_n^4 + g_b k_n^2 \, . \tag{2.15}$$

The righthand sides of eqs. (2.13, 2.14) are given in terms of the values of the order parameter or its derivatives at the boundaries. Using boundary conditions eqs. (2.5c, 2.5e), the derivatives of first order $\phi_p^{(1)}(0,t)$ and $\phi_p^{(1)}(L,t)$ can be expressed in terms of $\phi_p(0,t)$ and $\phi_p(L,t)$ (and their time derivatives). The boundary values $\phi_p(0,t)$, $\phi_p(L,t)$ and $\phi_p^{(2)}(0,t)$, $\phi_p^{(2)}(L,t)$ depend solely on the coefficients $B_n(t)$. Combining the boundary conditions eqs. (2.5c, 2.5e) with eq. (2.14) and using expression (2.6) for the boundary values, yields a set of coupled ordinary differential equations for the coefficients $B_n(t)$,

$$\begin{aligned}\partial_t \, B_n(t) + \omega_n \, B_n(t) = \frac{2}{L} k_n^2 \Bigg\{ &\left[h_0 + (-1)^n h_L\right] - \sum_{m=1}^{\infty} \partial_t \, B_m(t) \left[(-1)^{m+n} \Gamma_{sL}^{-1} + \Gamma_{s0}^{-1}\right] + \\ &+ B_m(t) \left[(-1)^{m+n} g_{sL} + g_{s0}\right] \Bigg\} \, .\end{aligned} \tag{2.16}$$

The analogous result for the A_n reads

$$\partial_t A_n(t) + \omega_n A_n(t) = \frac{2}{L} k_n \sum_{m=1}^{\infty} \left[(-1)^{m+n} - 1\right] \left[\frac{1}{k_m^2} \partial_t \, B_m(t) - k_n^2 B_m(t)\right] \, . \tag{2.17}$$

If the solution for the $B_n(t)$ is known, then the inhomogeneity in eq. (2.17) is determined and the A_n can be calculated by standard methods.

2.1.2 The Case $\Gamma_{sl} \to \infty$ and $g_s = 0$

The conditions $\Gamma_{sl} \to \infty$ and $g_s = 0$ correspond to $\Gamma_s \to \infty$ and $g = 0$, using expression (1.59) for $f_s(\phi)$. From the physical point of view, the case of quasi–static boundary conditions $\Gamma_s \to \infty$ and $g = 0$ (special transition) is a rather generic one, because typically the relaxation of the order parameter near the surface is fast as compared to the bulk, and effects due to surface fields will dominate those of cut–off (or modified) interactions. That the role of Γ_{sl} and g_s is not very important in this analysis, can also be seen from the fact, that both terms are coupled with the order parameter values at the surface that are small for short times. Note, however, that a contribution of g enters the scaled surface field, $h_l = (h - g\bar{\phi})/f_b''(\phi_1)\,\xi_b$.

In the case $\Gamma_{sl} \to \infty$ and $g_s = 0$ at both boundaries ($\Gamma_{sL}, \Gamma_{s0} \to \infty$ and $g_{sL} = g_{s0} = 0$) the system of equations (2.16) decouples, and yields a set of ordinary differential equations for all $B_n(t)$,

$$\partial_t B_n(t) + \omega_n B_n(t) = \frac{2}{L} k_n^2 \left[h_0 + (-1)^n h_L\right] . \tag{2.18}$$

The solutions are

$$B_n(t) = \frac{H_n}{\omega_n}\left(1 - e^{-\omega_n t}\right) \text{, with} \quad H_n = \frac{2}{L} k_n^2 \left[h_0 + (-1)^n h_L\right] . \tag{2.19}$$

Inserting eq. (2.19) in the righthand side of eq. (2.17), and solving this equation for the A_n gives

$$A_n(t) = \frac{2}{L} k_n \sum_{m=1}^{\infty} \left[(-1)^{m+n} - 1\right] \frac{H_m}{\omega_n - \omega_m} \left[e^{-\omega_m t} \left(\frac{\omega_m + k_n^2 k_m^2}{\omega_m k_m^2} \right) - \right.$$
$$\left. - \frac{k_n^2(\omega_n - \omega_m)}{\omega_m \omega_n} - e^{-\omega_n t} \left(\frac{\omega_n + k_n^2 k_m^2}{\omega_n k_m^2} \right) \right] . \tag{2.20}$$

We note that the given solution is pointwise convergent in the open interval $(0, l)$ [Str95]. It is possible with the help of eqs. (2.19, 2.20) to do a perturbation calculation in the case of very large Γ_{sl} and small g_s. However, the analysis leads to clumsy results that will be not regarded further.

To determine, which length scales are dominant as a function of time, we calculate the maximum of the coefficients $B_n(t)$ as a function of k_n. Taking the continuum limit with respect to n for large L, the calculation is straightforward and yields for small times t

$$k_n^{(\max)}(t) \simeq \sqrt{\sqrt{2/t} - g_b} \,, \tag{2.21}$$

where $k_n^{(\max)}(t)$ denotes the wavenumber where $B_n(t)$ is maximal. For short times we have $k_n^{(\max)}(t) \sim t^{-1/4}$, while for large times (with respect to linear theory) we find $k_n^{(\max)}(t) \sim \sqrt{-g_b} = k_c$. Therefore the characteristic surface directed spinodal demixing length is of the order of the bulk demixing length. The preceeding power law growth corresponds to the earliest transport stages, where a small amplitude SDW develops that is strongly damped in the z–direction. As soon as the wavelength becomes comparable to λ_m, the SDW is amplified by the bulk instability and propagates into the bulk.

Another interesting question is, if a suppression of surface directed spinodal decomposition in thin films can be found, as it is observed experimentally. For such a suppression all modes must decay with time, thus from eqs. (2.19, 2.20) we have the condition $\omega_n > 0$ for all $n \geq 1$. The most restrictive condition is found for $n = 1$, yielding a critical film thickness

$$L_{\text{crit}} = \pi/\sqrt{-g_b} = \pi/k_c. \tag{2.22}$$

Therefore surface directed spinodal decomposition is suppressed as soon as the film thickness is smaller than a critical length being comparable to the bulk demixing length. This result is independent of the surface fields.

Numerical solutions of the nonlinear CHE for a one dimensional slab agree with the analytic results presented here. Of course, the linear theory can not describe the nonlinear problem quantitatively for order parameter values being comparable to the equilibrium values ϕ_1, ϕ_2 that occur at large times. These times, when non–linear effects become important, are strongly dependent on surface properties, because the amplitudes of the Fourier modes depend on the surface parameters, cf. eq. (2.19).

2.2 Numerical Solution

In what follows we study the CHE in two dimensions (x and y) numerically. We first consider a bulk system with periodic boundary conditions in both directions and afterwards a system with slab geometry, i.e. periodic boundaries in x–direction and impermeable boundary conditions, eqs. (1.60, 1.61), in y–direction.

For a full definition of the nonlinear CHE (1.49) we have to specify the bulk free energy density $f_b(\phi)$ and the surface free energy density $f_s(\phi)$. We choose the Landau expression (1.33) for $f_b(\phi)$ and expression (1.59) for $f_s(\phi)$. In the following, we set both $\Gamma_b \equiv 1$ and $\sigma_b \equiv 1$ without loss of generality. Moreover, we always consider a fifty–fifty composition, i.e. $\bar{\phi} = 0$. To prepare the initial homogeneous state, we assign uniformly distributed random numbers in the interval $[-\epsilon_0, +\epsilon_0]$ to each lattice site with $\epsilon_0 = 0.01$. To account for the final state in the spinodal region, the parameters a and b specifying f_b have to be positive.

With our choices, the CHE in two dimension reads

$$\frac{\partial}{\partial t}\phi(x,y,t) = \left(\frac{\partial^2}{\partial x^2} + \frac{\partial^2}{\partial y^2}\right)\mu(x,y,t) \tag{2.23a}$$

$$\mu(x,y,t) = -\left(\frac{\partial^2}{\partial x^2} + \frac{\partial^2}{\partial y^2}\right)\phi(x,y,t) + f_b'\big(\phi(x,y,t)\big)\,, \tag{2.23b}$$

with

$$f_b\big(\phi\big) = -\frac{a}{2}\phi^2 + \frac{b}{4}\phi^4\,. \tag{2.24}$$

The system sizes are defined by $x \in [0, L_x]$ and $y \in [0, L_y]$. For bulk systems periodic boundary conditions are used in both directions. In slab geometry the systems are periodic with respect to x–direction. The impermeability condition (1.60) yields

$$\frac{\partial \mu}{\partial y}(x,0,t) = \frac{\partial \mu}{\partial y}(x,L_y,t) = 0\,, \tag{2.25}$$

and the relaxation boundary condition (1.61) reads

$$\frac{\partial}{\partial t}\phi(x,0,t) = -\Gamma_s\left[-\frac{\partial \phi}{\partial y}(x,0,t) - \sigma_s\frac{\partial^2}{\partial x^2}\phi(x,0,t) + f_s'\big(\phi(x,0,t)\big)\right] \tag{2.26a}$$

$$\frac{\partial}{\partial t}\phi(x,L_y,t) = -\Gamma_s\left[\frac{\partial \phi}{\partial y}(x,L_y,t) - \sigma_s\frac{\partial^2}{\partial x^2}\phi(x,L_y,t) + f_s'\big(\phi(x,L_y,t)\big)\right]\,, \tag{2.26b}$$

with

$$f_s\big(\phi\big) = -h\phi + \frac{g}{2}\phi^2\,. \tag{2.27}$$

We also consider the boundary conditions eqs. (2.26a,b) in the static limit $\Gamma_s \to \infty$,

$$\frac{\partial \phi}{\partial y}(x,0,t) = -\sigma_s\frac{\partial^2}{\partial x^2}\phi(x,0,t) + f_s'\big(\phi(x,0,t)\big) \tag{2.28a}$$

$$\frac{\partial \phi}{\partial y}(x,L_y,t) = \sigma_s\frac{\partial^2}{\partial x^2}\phi(x,L_y,t) - f_s'\big(\phi(x,L_y,t)\big)\,. \tag{2.28b}$$

The problems are then solved numerically by the method of lines, leading to a coupled set of ordinary differential equations in time. The corresponding discrete line systems are derived in appendix A.

The numerical solution of the Cahn–Hilliard equation is complicated by the fact that the corresponding line system is stiff. Physically speaking, *stiffness* occurs, if there are two or more very different length scales in the system [Pre95]. In the present case there is the interfacial thickness, given by the bulk correlation length ξ_b and the domain size of the system. The minimal domain size is the bulk demixing length $\lambda_m = 4\pi\xi_b$, for $\bar{\phi} = 0$. A linear stability analysis of the discretized line system in the bulk case yields that apart from the natural instability of the continuous CHE an additional numerical instability may occur for too large time steps Δt, depending on the choice of the time stepping method [Sap96, Ken01]. In the case of an explicit time integrator, a hard restriction with respect to the time–interval arises [Ken01],

$$\Delta t \leq \frac{\Delta x^4}{8(1+\alpha^2)^2 + 2a(1+\alpha^2)\Delta x^2} = \mathcal{O}(\Delta x^4)\,, \tag{2.29}$$

where the spatial grid constants are denoted by $\Delta x, \Delta y$ and $\alpha \equiv \Delta x/\Delta y$. However, for good implicit methods $\Delta t = \mathcal{O}(1)$. Thus it is essential to choose the right implicit time integrator to avoid stability problems. Note that with implicit methods in every time step a coupled system of nonlinear equations has to be solved. Using Newton solvers, this leads to an increased requirement on computer memory due to inversion of big matrices.

We solved the numerical problem by choosing the *backward differentiation formulae* (BDF) as time integrator, see [Stu96] for definition. This method avoids stability problems due to stiffness of the line system. The NAG–routine D02NDF supplies a professional implementation of the BDF with an additional variable time–stepping method. The option "structural" was used, to exploit the sparsity structure of the *Jacobian*. The set of nonlinear equations in each time step were solved by Newton's method, using standard routines from the NAG–library.

2.2.1 Bulk Solutions in Two Dimensions

To demonstrate the usefulness of the new numerical treatment, we first consider spinodal decomposition in a bulk system. The parameters defining the free energy f_b after the quench at $t = 0$ are given by $a(T) = 1$ and $b = 1$.

Figure 2.1 shows snapshots of the emerging domain patterns for various times after the quench when starting from a given initial configuration. The system size is $L_x \times L_y = 128 \times 128$ and discretization lengths being equal to the bulk correlation length are used, i.e. $\Delta x = \Delta y = 1$ in our units. The pictures show bicontinuous domain morphologies typical for a symmetric overall composition. The colour coding is chosen such that the equilibrium value of the A–rich phase corresponding to $\phi_2 = +1$ appears red, while the equilibrium value of the B–rich phase corresponding to $\phi_1 = -1$ appears blue, cf. fig. 1.3. The interfacial regions, where the order parameter varies between -1 and $+1$, appear green.

The first picture at $t = 56.23$ corresponds to the situation at the end of the linear time regime, cf. fig. 2.4, when the order parameter within the domains starts to reach values comparable to the equilibrium values. The typical domain size at this point is given by the wavelength λ_m, see sec. 1.3.1. At early times $t \lesssim 5$, the values of the order parameter are very small, and corresponding plots of the order parameter field are uniformly green. After passing the linear

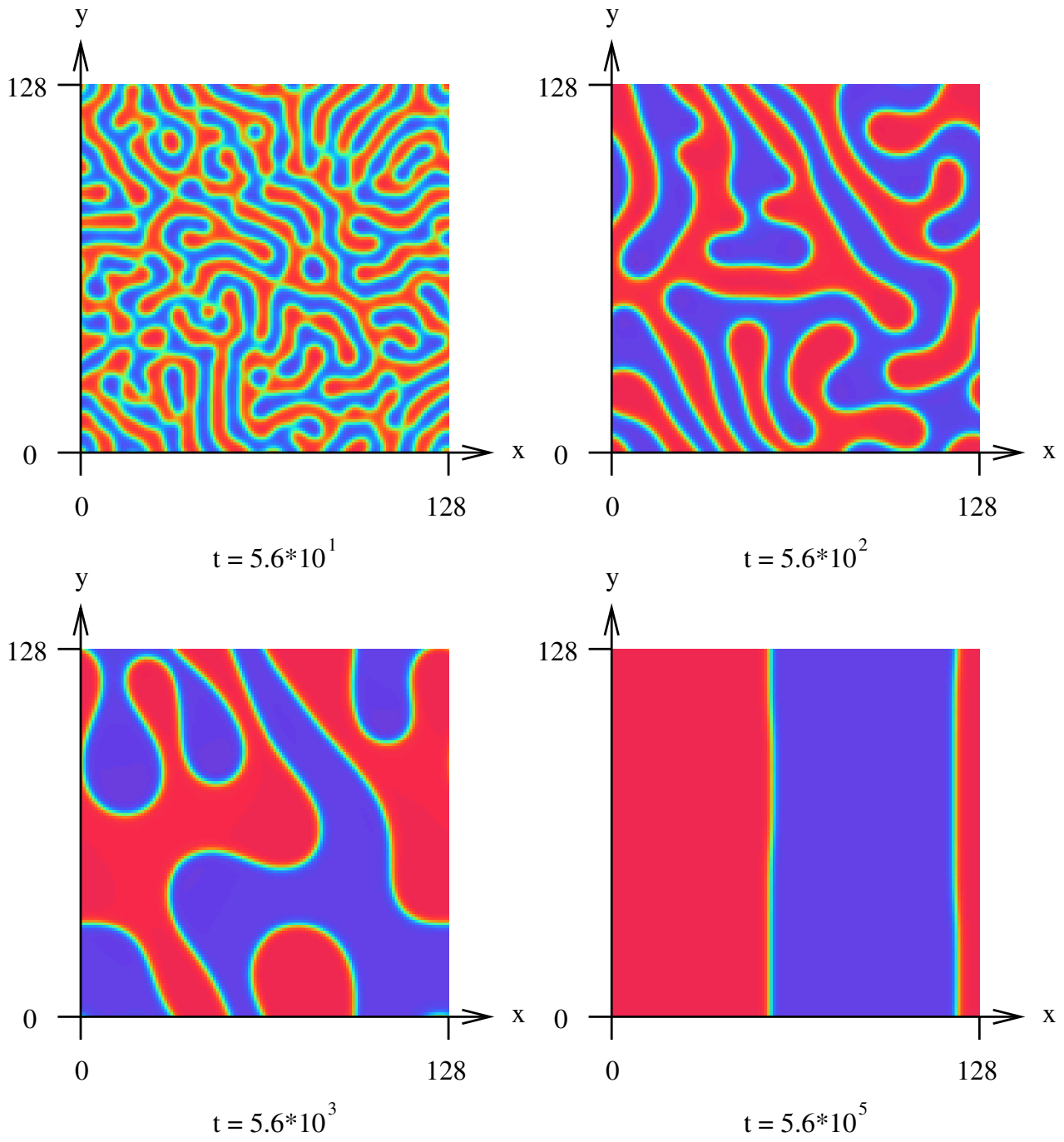

Figure 2.1: Snapshots of domain patterns in a bulk–system for various times after the quench.

time regime, for times $t = 562.3, 5623$ in fig. 2.1, the domains grow in size and the overall pattern coarsens. Finally, at $t = 562341$ the system reaches thermal equilibrium: Both phases are separated by two straight interfacial regions such that the total interface length has become minimal.

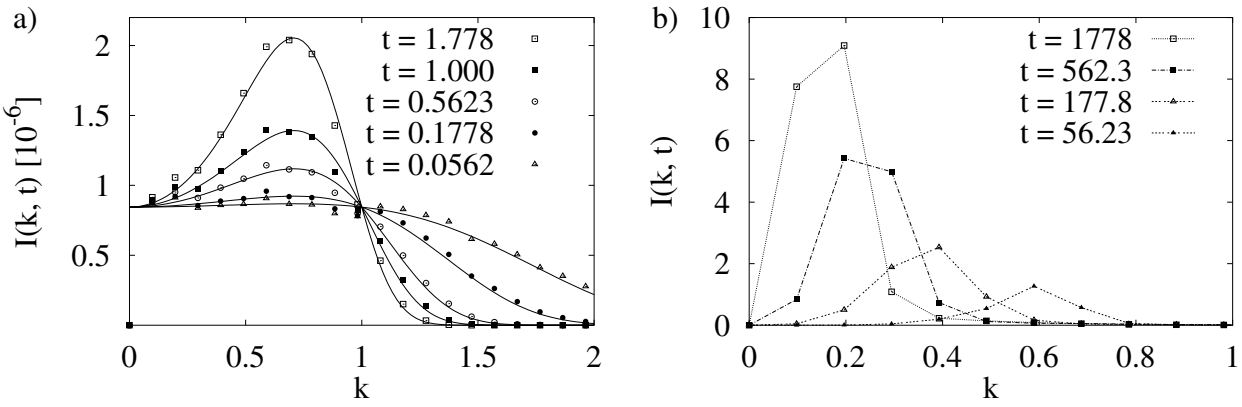

Figure 2.2: Circular averaged structure function $I(k,t)$ as a function of k for various fixed times, (a) in the early stages and (b) in the late stages of the demixing process. The data points are results from the numerical treatment. The lines in (a) correspond to the predictions of the linear theory, the lines in (b) are drawn as guides to the eye.

For a quantitative analysis, we consider the correlation function

$$G(\mathbf{y},t) = \langle \phi(\mathbf{y}+\mathbf{y}',t)\,\phi(\mathbf{y}',t)\rangle - \bar{\phi}^2\,, \tag{2.30}$$

where $\mathbf{y} = (x,y)$, and $\langle \ldots \rangle$ denotes an average over $\mathbf{y}'$ and many initial configurations. Due to the statistical translational and rotational invariance $G(\mathbf{y},t)$ depends on $r = |\mathbf{y}|$ only. It is therefore convenient to introduce the circular averaged correlation function $g(r,t) = (2\pi)^{-1}\int_0^{2\pi} d\varphi\, G(r\cos\varphi, r\sin\varphi, t)$. The Fourier transform of $G(\mathbf{y},t)$ gives the intermediate scattering function $(2\pi)^{-2}\int d^2x\, G(\mathbf{y},t)\exp(i\,\mathbf{k}\cdot\mathbf{y})$, which after circular averaging becomes

$$I(k,t) = \frac{1}{2\pi}\int_0^\infty dr\, r\, g(r,t)\, J_0(kr)\,, \tag{2.31}$$

where $k = |\mathbf{k}|$, and $J_0(kr)$ is the Bessel–function of zeroth order. In the discrete representation it is convenient for practical purposes first to calculate $\hat{\phi}(\mathbf{k},t) = \sum_{\mathbf{y}} \phi(\mathbf{y},t)\exp(i\,\mathbf{k}\cdot\mathbf{y})$, where the sum runs over all lattice points, by the Fast Fourier Transform technique. Then $I(k,t)$ reads

$$I(k,t) = \sum_{\mathbf{k}}{}' \left\langle \left|\hat{\phi}(\mathbf{k},t)\right|^2 \right\rangle \Bigg/ \sum_{\mathbf{k}}{}' 1\,, \tag{2.32}$$

where the dashed sum $\sum_{\mathbf{k}}{}'$ runs over all points in the first Brillouin zone satisfying the condition $k - \Delta k/2 < |\mathbf{k}| < k + \Delta k/2$. We define the nth moments of $I(k,t)$ as

$$k_n(t) = \int_0^\infty dk\, k^n I(k,t) \Bigg/ \int_0^\infty dk\, I(k,t)\ . \tag{2.33}$$

If $I(k,t)$ is peaked at some finite value of k, the inverse first moment $R(t) \equiv 2\pi/k_1(t)$ is a measure of the characteristic domain size L_D, while the square root of the second moment is a

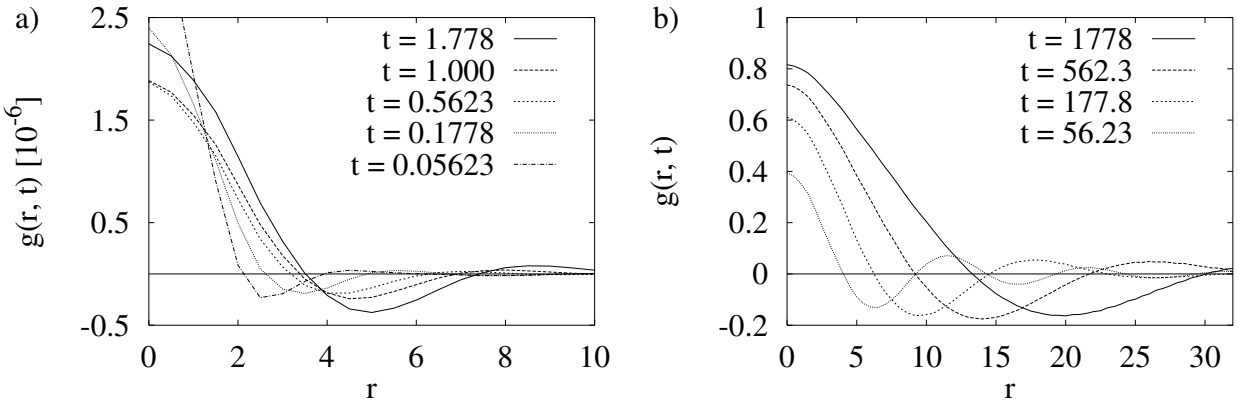

Figure 2.3: Circular averaged correlation function $g(r,t)$ as a function of r in (a) the early stages and (b) the late stages of the demixing process for the same fixed times chosen as in fig. 2.2.

measure of the width of the mode spectrum. Alternatively one may identify the characteristic domain size by the first zero $R_0(t)$ of $g(r,t)$ as a function of r.

In order to determine $g(r,t)$ and $I(k,t)$, the Cahn–Hilliard equation is solved numerically for a system of size $L_x \times L_y = 64 \times 64$ with $\Delta x = \Delta y = 0.5$. On a standard personal computer (Pentium 200), we succeeded to perform simulation runs up to $t = 10^6$ in a reasonable computation time for 20 different initial configurations that are sufficient to obtain good statistics. We note in passing that with our numerical method the CPU time depends only on the system size and not on the number of lattice points in the discretization.

Figure 2.2a shows $I(k,t)$ for the early stages of the spinodal decomposition process (data points) in comparison with the prediction of the linear theory eq. (1.52) (lines). For our initial conditions the amplitude is given by $I(k,0) = \epsilon_0^2/3(2\pi)^2$. The overall agreement between theory and numerics is very good. One can see that $I(k,t)$ starts to become peaked around $k = k_m$ after some time $t \approx 1$ and then the peak amplitude grows very rapidly by a factor of about 10^6 up to a time $t \approx 50$ (see fig. 2.2b), while the peak position k_m remains constant. At later times (fig. 2.2b) the peak of the structure function shifts to smaller values of k, as the domain pattern coarsens. The corresponding correlations functions $g(r,t)$ for early and late times are shown in figs. 2.3a,b. The shift of the peak position in $I(k,t)$ towards smaller k values at late times is reflected in the shift of the zeros of $g(r,t)$ towards larger r values.

Figure 2.4a shows the first and second moment $k_1(t)$ and $k_2(t)$ of $I(k,t)$ as a function of time in a double–logarithmic plot. We can distinguish between three different dynamical time regimes: For $t \lesssim t_1 \approx 1$ the first moment $k_1(t)$ decreases as $k_1(t) \propto t^{-1/4}$. This regime corresponds to the onset–regime observed in the linear theory for surface directed decomposition, see sec. 2.1.2. We note that due to the finite discretization lengths $\Delta x = \Delta y$ the spectrum has an upper cutoff at $k_{\max} = \pi/\Delta x$, which requires $k_1(t)$ to be smaller than $\pi/(2\Delta x)$. The power law thus must cease to be valid for very short times, which is also clear from the fact that $I(k,t)$ and hence $k_1(t)$ must be analytic at $t = 0$. After the onset–regime, $k_1(t)$ stays approximately constant for $t_1 \lesssim t \lesssim t_2 \simeq 50$, before finally decreasing with the Lifshitz–Slyozov law as $k_1(t) \propto t^{-1/3}$ for $t_2 \lesssim t$. Finally, when the characteristic domain size $R(t) = 2\pi/k_1(t)$ becomes

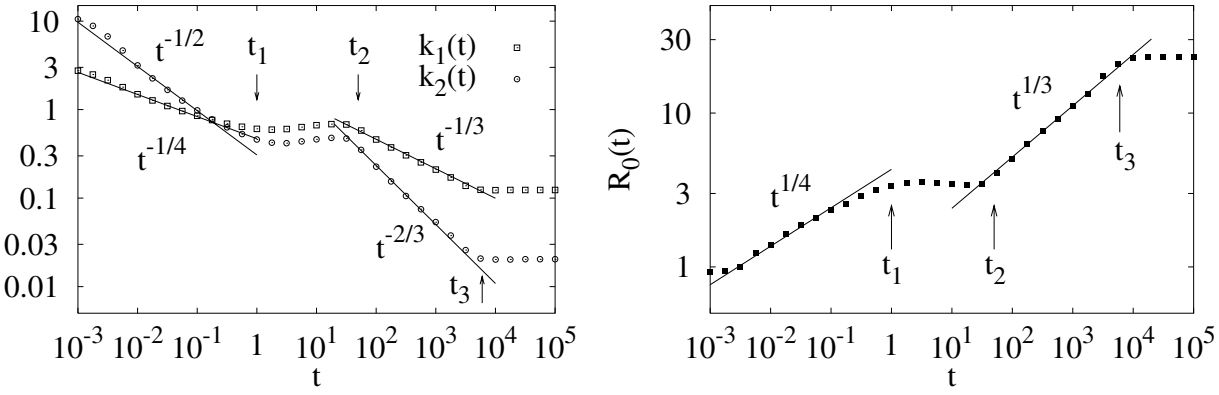

Figure 2.4: (a) First and second moments $k_1(t)$ and $k_2(t)$ of the circular averaged structure function $I(k,t)$ (see fig. 2.2) as a function of time. (b) First zero $R_0(t)$ of the circular averaged correlation function $g(r,t)$ (see fig. 2.3). It is possible to distinguish three different time regimes $t < t_1 \approx 1$, $t_1 < t < t_2 \approx 50$ and $t_2 < t < t_3 \approx 6000$. For $t > t_3$ the system reaches equilibrium.

comparable to $L/2$, i.e. for $t \gtrsim t_3 \simeq 6000$, the system has almost reached its equilibrium state and $k_1(t)$ saturates. As expected, the behavior of $k_2(t)$ resembles that of $k_1(t)$, that means $k_2(t) \sim k_1(t)^2$.

The first time regime for $t \lesssim t_1$ is strongly dependent on the initial conditions and is therefore not significant with respect to experiments. For the special initial conditions considered here, it can be explained as follows. For $t \lesssim t_1$ the exponential function in eq. (1.52) is approximately equal to 1 when $k \lesssim k_c$, while for $k \gg k_c$, $I(k,t)$ strongly decreases and this decrease is dominated by the quartic term in the dispersion relation $\omega_b(k)$. Since, for $k \lesssim k_c = 1$, $\exp(-2k^4 t) \approx 1$ (see also fig. 2.2a for small times), we can replace $\exp[2\omega_b(k)t]$ by $\exp(-2k^4 t)$ for all k and thus obtain

$$k_n(t) \approx \frac{\int_0^\infty dk\, k^n\, \exp(-2k^4 t)}{\int_0^\infty dk\, \exp(-2k^4 t)} = \frac{\Gamma(\frac{n+1}{4})}{\Gamma(\frac{1}{4})}(2t)^{-\frac{n}{4}}\ , \quad (n > -1) \tag{2.34}$$

This behavior ceases to be valid when $k_1(t)$ becomes comparable to the wavenumber k_m of the most unstable mode of the linearized theory, i.e. at $t_1 \propto k_m^4$.

For $t_1 \lesssim t \lesssim t_2$ all short wavelength modes have decayed and the remaining ones grow exponentially with time, with the maximal growth rate having wavenumber k_m. Hence $k_1(t) \simeq k_m$. At the end of this linear time regime, the nonlinear terms in the Cahn–Hilliard equation become important. To estimate t_2 we therefore require that the fluctuations $\langle[\phi(t) - \bar{\phi}]^2\rangle$ become comparable to $\phi_1^2 = \phi_2^2 = 1$. From a saddle–point approximation of the sharply peaked $I(k,t)$ at $k = k_m$ we obtain $t_2 \simeq 30$.

The various time regimes can also be identified in the first zero $R_0(t)$ of $g(r,t)$, as shown in fig. 2.4. The well–known overall behavior of spinodal decomposition in the bulk as described by the Cahn–Hilliard equation is thus reproduced by our numerical treatment.

2.2.2 Solutions for a Two Dimensional Slab

We now treat the situation of a binary mixture confined between two walls undergoing spinodal decomposition. Therefore we compare numerical solutions for the two dimensional CHE with analytical results derived for the demixing kinetics at early times [Fis97b, Fis98b]. At late times the decomposition within the slab is effectively one dimensional and coarsening happens via a period doubling mechanism [Lag71, Fra96] much slower than the Lifshitz–Slyozov growth.

The slab is confined by two walls at $y = 0$ and $y = L_y$ with equal properties, and periodic boundary conditions are used in the x–direction. The boundary conditions defining the walls are the no–flux condition eq. (2.25), and the parameters of the surface free energy f_s, eq. (2.27), specifying the second boundary condition are given by $h = 0$ and $g = 1$. The interfacial tension at the surface is $\sigma_s = 0$. For the sake of a convenient comparison with the linear theory, we study here the case of static boundary conditions, eq. (2.28). The parameters specifying the bulk free energy f_b, eq. (2.24), are $a = 0.5$ and $b = 1$.

Figure 2.5 shows snapshots of slab systems with various widths $L_y = 3, 4, 5$ and 10 at times $t = 1, 10, 100$. The system size in x–direction is $L_x = 80$ and the corresponding discretization length $\Delta x = 0.3125$. In the y–direction we choose $\Delta y = 0.1, 0.1, 0.125$, and 0.2 for $L_y = 3, 4, 5$ and 10, respectively. The maximum value of ϕ in each picture corresponds to color red, the minimum value to color blue, while values for ϕ in between correspond to colors ranging from orange over green to light blue. For all widths L_y droplet–like domains form, and, since $h = 0$, none of the two components is preferentially attracted by the walls. However, the domain pattern is less pronounced near the surfaces, since for $g > 0$ larger values of $|\phi|^2$ at the walls increase $f_s(\phi)$ and are therefore less likely. The droplets have a characteristic length that increases with time as in the bulk and, more interestingly, increases with decreasing L_y (at least for larger t). This result is in qualitative agreement with the predictions of the linear theory for the Cahn–Hilliard equation in slab geometry [Fis98b]. Moreover, that theory predicts the existence of a critical $L_y^{(\mathrm{crit})} \approx 2.5$ below which no spinodal decomposition should occur. Runs with $L_y = 1$ indeed yield an order parameter field ϕ being almost zero ($|\phi(x)| < 10^{-7}$) for times $t \gtrsim 1$, thus confirming the predicted absence of an instability.

For a quantitative comparison of the numerics with the predictions of the linear theory we consider the lateral correlation function

$$G_{\parallel}(x, y, t) = \langle \phi(x + x', y, t)\, \phi(x', y, t) \rangle_y - \langle \phi \rangle_y^2 \,, \tag{2.35}$$

where $\langle \ldots \rangle_y$ denotes an average over x' at fixed y and many initial configurations. The Fourier transform of the lateral correlation function $G_{\parallel}(x, y, t)$ with respect to the coordinate gives the lateral intermediate scattering function

$$I_{\parallel}(k_x, y, t) = (2\pi)^{-1} \int dx\, G_{\parallel}(x, y, t) \exp(i k_x x) \,. \tag{2.36}$$

Figure 2.6 shows $I_{\parallel}(k_x, y, t)$ for a slab of width $L_y = 5$ for 3 different times on the lefthand side as obtained by the numerics, and on the righthand side as resulting from the linear theory [Fis97b]. Averages are performed over 300 different initial conditions and over the two equivalent y–values in the symmetric slab. The agreement between the numerical results and the linear theory is good. The remaining deviations are due to the non–hermiticity of the linearized Cahn–Hilliard equation in combination with the boundary conditions (2.28). Therefore the eigenfunctions of

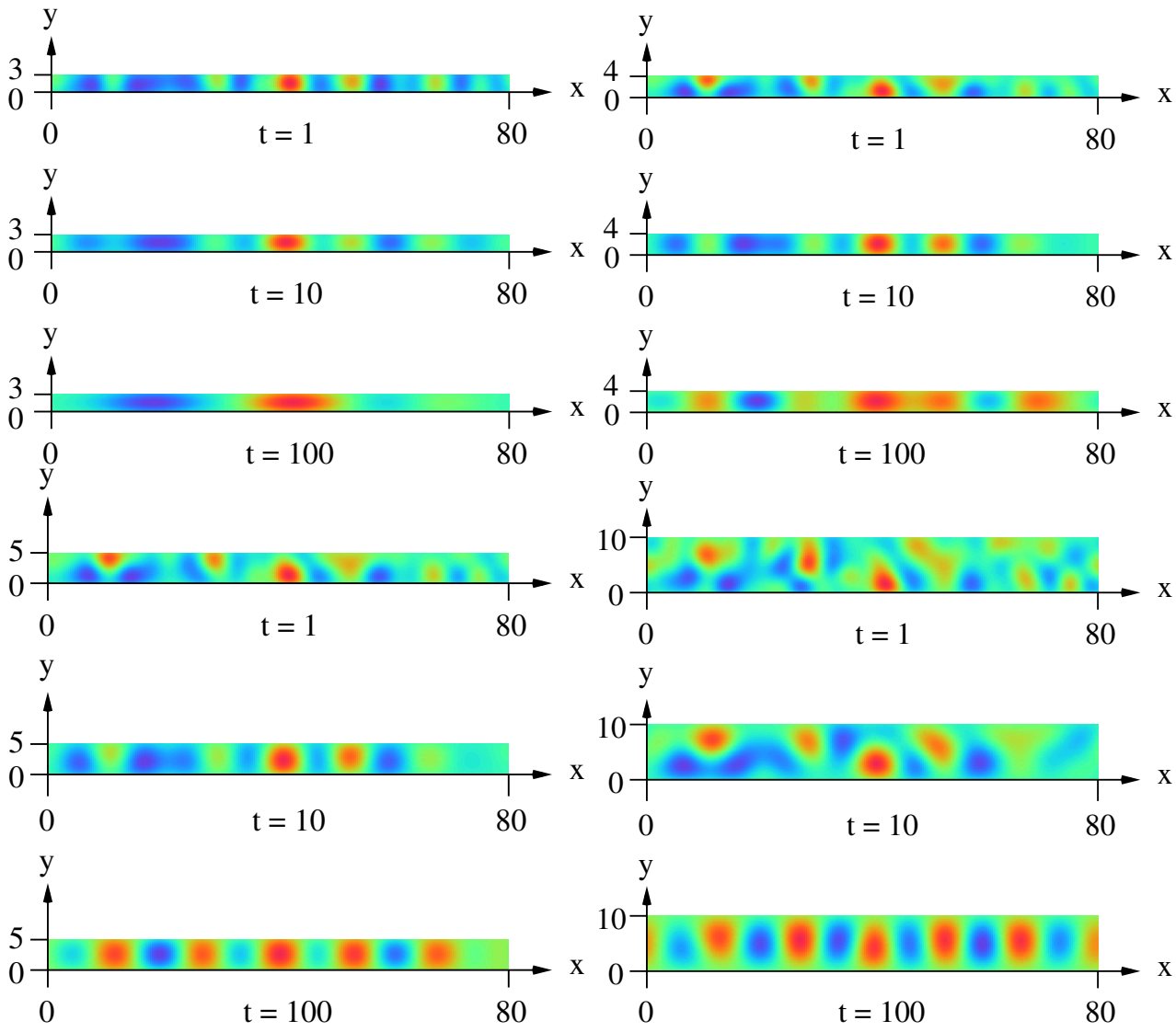

Figure 2.5: Snapshots of the emerging domain patterns in slab geometry for various fixed times after the quench. The thicknesses of the slabs are $L_y = 3$, 4, 5 and 10.

the linear system are strictly speaking non–orthogonal, by contrast to what was assumed in the calculation of $I_{\|}(k_x, y, t)$ in the framework of the linear theory.[1]

At late times fig. 2.5 suggests that the demixing should become essentially one dimensional. In such a one dimensional situation the coarsening is expected to proceed via a kind of *period–doubling* process [Lag71, Fra96], which actually refers to a process, where two neighboring domains of the same phase, that are originally separated by one domain of the other phase, coalesce by interdiffusion. In fact we always find such a period–doubling to take place for our parameter choice. An example is shown in fig. 2.7 for the slab with $L_y = 4$.

[1] In principle the set of eigenfunctions can be orthonormalized by Gram–Schmidt orthonormalization, but as the agreement between linear theory and numerical data already is good, this expensive step has been avoided.

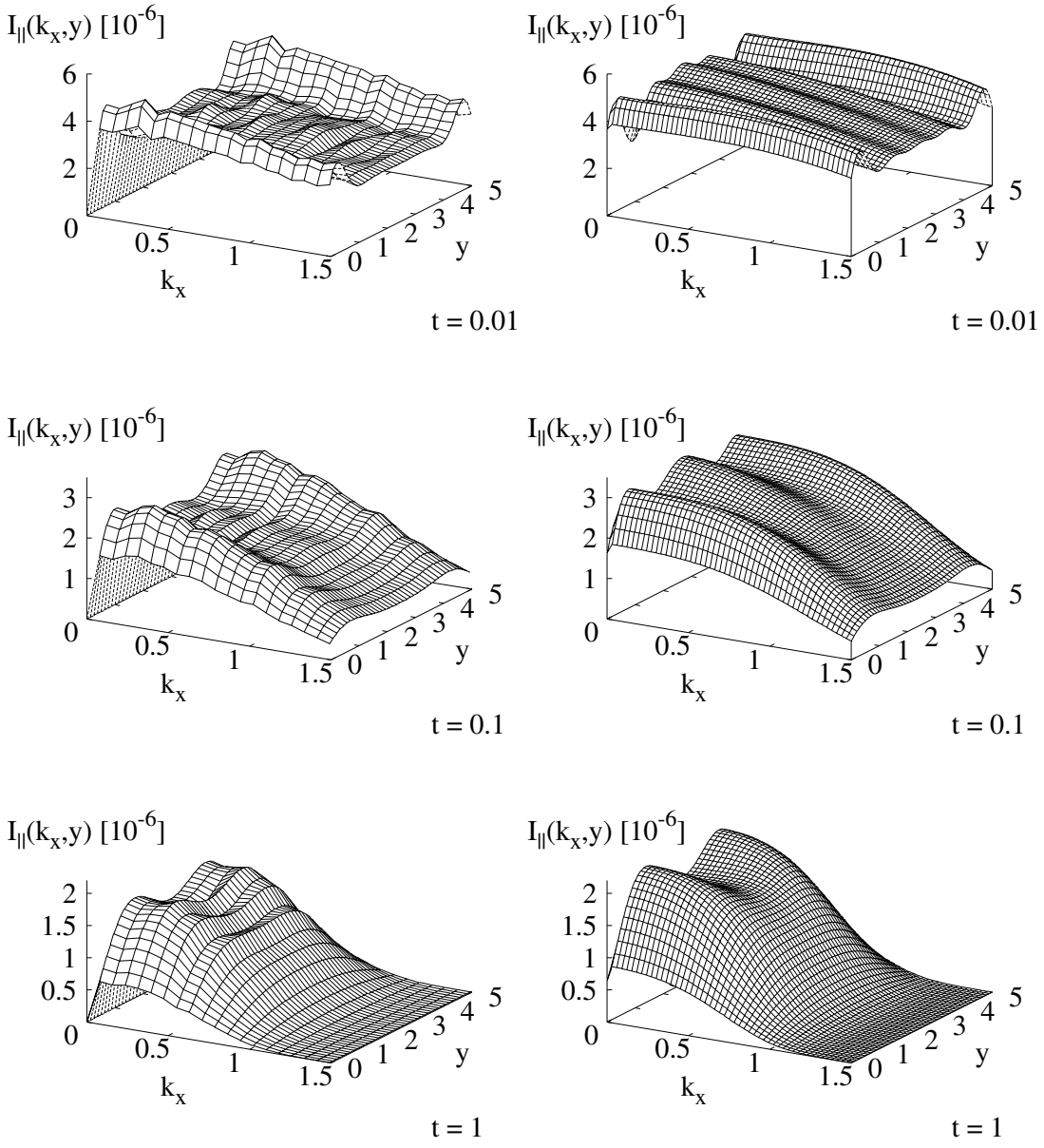

Figure 2.6: Comparison of the numerical results for the lateral intermediate scattering function $I_{\|}(k_x, y, t)$ at various fixed times (plots on the left hand side) with the predictions of the linear theory (plots on the right hand side).

To quantify this kind of lateral domain coarsening, we regard the first zero $R_{0,\|}(t)$ of $G_{\|}(x, y, t)$ with respect to x as a function of time. Since the domain size does not vary strongly with y, we determine $R_{0,\|}(t)$ at $y = 0$ without loss of generality. The results for various slab thicknesses L_y are given in fig. 2.8. For very short times we again find a power law behavior, as in the case of the bulk system. However, this regime is dominated by the initial conditions and of little experimental relevance. In a second time regime we find a plateau, where $R_{0,\|}(t)$ is almost

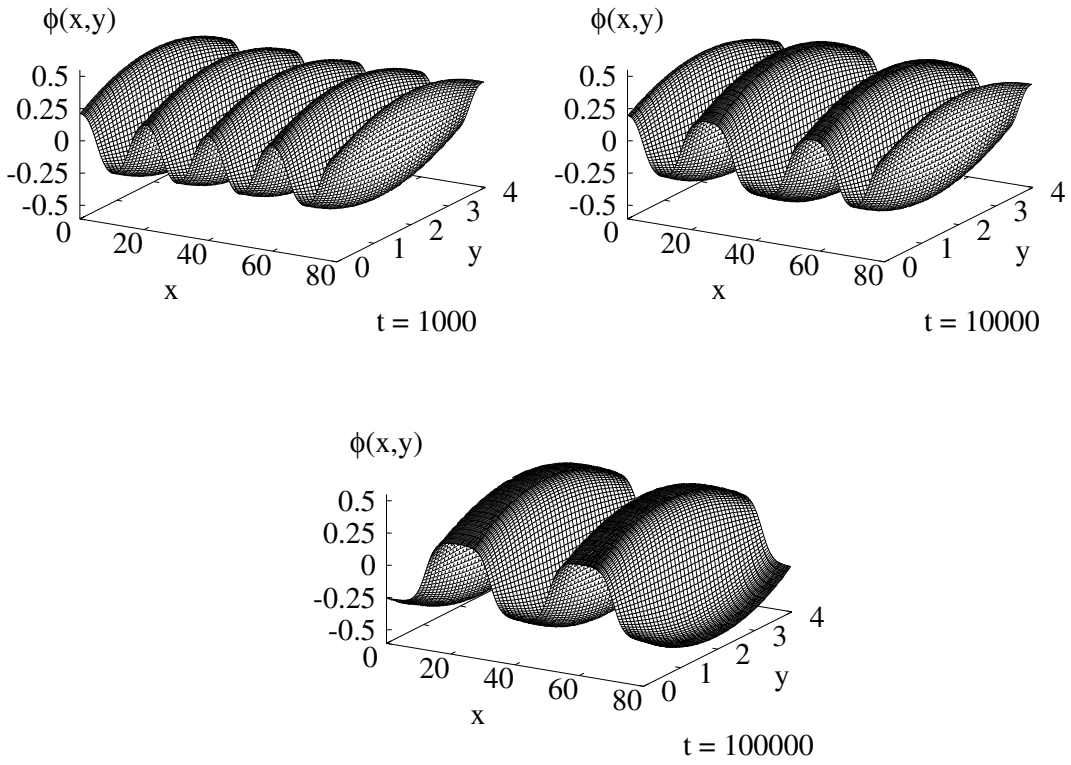

Figure 2.7: Example of the period–doubling process in the late stages demixing in a slab of thickness $L_y = 4$.

constant. This corresponds to the second regime in the bulk system where fluctuations grow exponentially. The lateral demixing length, given by the plateau value, grows with decreasing L_y as predicted by the linear theory. Moreover, the linear time regime is reached later for thinner slabs. We note, that the slight reduction of $R_{0,\|}(t)$ observed especially for $L_z = 10$, is due to a reorientation of the interfaces in direction perpendicular to the boundaries, cf. fig. 2.5 for $L_y = 10$ and $t = 10, 100$. Finally, domain coarsening sets in via a period doubling process, leading to pronounced steps in $R_{0,\|}(t)$, especially for thin films, and not to a uniform domain growth, as it is found in the bulk system. We note in passing that this very slow kinetics makes the use of an efficient and stable time integrator even more important.

2.3 Limitations of the Cahn–Hilliard Theory

With our numerical treatment, the problem of treating the CHE and similar equations numerically, covering the whole kinetic process from the earliest stages up to equilibrium for large enough systems, is satisfactory solved in two dimensions for bulk systems and for slab systems with generic boundary conditions. The suggested method can be straightforwardly extended to the three dimensional case. However, there are practical problems in doing so, because phys-

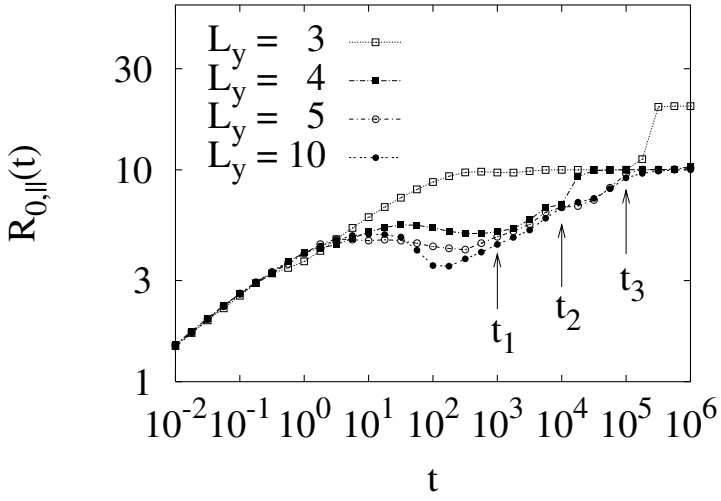

Figure 2.8: First zero $R_{0,\|}(t)$ of the lateral correlation function $G_\|(x, y, t)$ at the boundary $y = 0$ for various slab thicknesses L_y in double logarithmic representation. The marked times t_1, t_2 and t_3 correspond to different times in fig. 2.7.

ically interesting systems would require system sizes of $60 \times 60 \times 24$ bulk correlation lengths for a slab at least. This would correspond to approximately $5 \times 5 \times 2$ bulk demixing lengths. To obtain a reasonable space resolution one would have to solve of order 10^5 coupled nonlinear equations in each time step. Application of efficient Newton solvers to treat this problem would require computers with about 20 Gigabyte main memory, which are beyond present days standard computer capabilities, but might become available in a few years. First attempts, to improve the numerical algorithm and substitute Newton's method by alternative procedures requiring less memory capacities, lead to a reduction of the possible time steps Δt [Scr00]. But a combination of improved hardware and improved numerical methods is likely to overcome these problems.

As already mentioned in sec. 1.2.2, the CHE yields only qualitative results, if one is interested in the description of properties specific for polymeric systems. Of course the simplest way to improve the situation would be to substitute the Ginzburg–Landau functional $F_{\mathrm{GL}}[\phi]$, eq. (1.35), by the Flory–Huggins–de Gennes functional $F_{\mathrm{FHG}}[\phi]$, eq. (1.36), but in this case the numerical problems for three dimensional systems would still be the same, while the scale of the radius of gyration is not resolved in such a macroscopic description. Yet this scale becomes important in experiments, where spinodal decomposition of binary polymer blends on structured substrates with a periodicity comparable to $\bar{R}_G$ is studied [Roc99]. Other experiments consider blends of ultra thin films with film thicknesses of order $\bar{R}_G$ [Tan95, Erm98]. To describe such systems properly the scale of $\bar{R}_G$ has to be resolved by the theoretical model. In the following we will therefore consider a new approach, where polymers are treated as soft particles. While these kinds of models do not resolve the microscopic structure of the polymer, they do resolve the structure of polymers on the scale of $\bar{R}_G$, leading to a semi–macroscopic description.

3 Soft Particle Models

One way how a polymer chain can be described in terms of a soft particle model, was suggested by Murat and Kremer [Mur98]. In their original work they made a mapping of a bead–spring polymer model to a soft ellipsoid model. While we will closely follow their ideas regarding the setup of the model, the approach presented here is slightly more general.

There are two major conceptual points, how to treat slow kinetic processes and equilibrium properties of polymer systems. First, we wish to get rid of entanglement effects, that slow down the real kinetics of polymeric systems dramatically and make an equilibration of chain models difficult. Therefore we have to model the polymers in such a way, that the chains can cross each other, while taking into account the correct kinetics on larger times. Secondly, we reduce the number of degrees of freedom of a single polymer from $\mathcal{O}(\mathcal{N})$ to $\mathcal{O}(1)$. These two constraints lead to a representation of polymers as soft particles, which is not unreasonable, because real polymers are dilute objects on the scale of the radius of gyration and their radii overlap strongly in the melt. To reduce the number of degrees of freedom, each polymer is described by a finite set of variables $\{\mathbf{X}\}$, independent of the chain length N. That is to say, one polymer is mapped onto one soft particle, the state of which is fully determined by $\{\mathbf{X}\}$. This mapping is a two–step process in the sense, that in a first step a realistic molecular polymer model is mapped onto a coarse–grained chain model, see e.g. sec. 1.1.1. In a second step this chain model is mapped onto a soft particle. This has the advantage, that one has an improved control over the approximations involved and that the second coarse–graining step has to be done only once for each chain model.

However, the question remains, which kind of variables $\{\mathbf{X}\}$, that describe the properties of the soft particle, give a suitable representation of the chain molecule. The answer is that this depends on the problem we wish to treat with the soft particle model. A representation that is suitable in some regards, may not be suitable or inconvenient in others. Typically, the reason for an inappropriate description is the importance of physical processes on a scale that is not good enough resolved by the set $\{\mathbf{X}\}$.

In this chapter we describe the second coarse–graining step and give the definitions of some possible models. The numerical results of this work are restricted to the soft ellipsoid model, in order to have the possibility to compare the results with previous findings [Mur98]. Nevertheless, it is instructive to look at the soft ellipsoid model from a more general perspective.

3.1 Second Coarse–Graining Step

All single chain configurations, that lead to the same set $\{\mathbf{X}\}$ of variables, are treated as equivalent one particle states on the level of the soft particle model, cf. fig. 3.1. This means

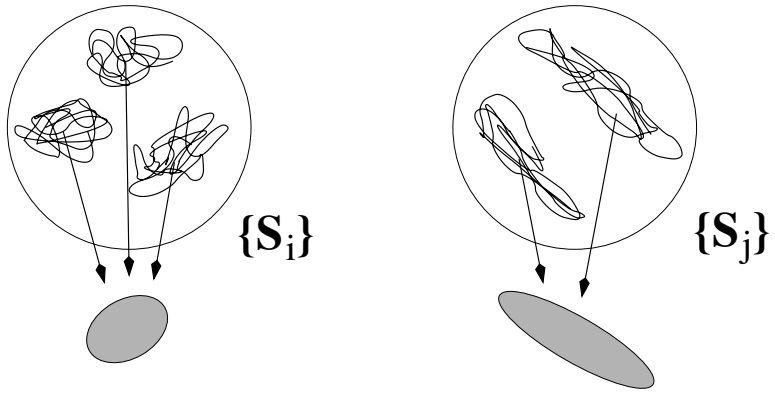

Figure 3.1: Illustration of the second coarse–graining step in the case of the soft ellipsoid model, $\{\mathbf{X}\} = \{\mathbf{S}\}$: All chain molecules i_n, that have the same eigenvalues $\mathbf{S}_i$ are mapped onto equivalent ellipsoids with identical properties. Here the index n simply numbers all equivalent chains. The properties of the ellipsoids are uniquely determined by the $\mathbf{S}_i$.

that in order to determine the properties of the soft particle as a function of $\{\mathbf{X}\}$ we have to average over all chain configurations with the set of variables $\{\mathbf{X}\}$ fixed. We choose the conditional monomer density $\varrho(\mathbf{y};\mathbf{X})$, that is the average monomer density of one chain where the particles state $\{\mathbf{X}\}$ is fixed, as the only input quantity for the interaction of the soft particles. But in principle multiple conditional densities, such as $\varrho^{(2)}(\mathbf{y}_1,\mathbf{y}_2;\mathbf{X}_1,\mathbf{X}_2)$ etc., could also enter the soft particle model. The variables $\mathbf{y}_k$ denote the position of monomers in the laboratory system, the $\mathbf{X}_i$ denote different states of soft particles. Furthermore we have to calculate the probability $P(\mathbf{X})$ of a certain set $\{\mathbf{X}\}$ as this will lead to an entropic contribution to the free energy of the model system.

The free energy of an ensemble of M soft particles then is a function of the set of variables $\{\mathbf{X}_i\}$, i.e. a function of all soft particles' remaining degrees of freedom. At this point we follow Murat and Kremer [Mur98] and make the phenomenological ansatz that the free energy splits into an intramolecular part, accounting for internal degrees of freedom, and an intermolecular part, which describes the interaction between the particles,

$$F = F_{\text{intra}} + F_{\text{inter}}\,. \tag{3.1}$$

The intramolecular part is given by the probability $P(\mathbf{X})$

$$F_{\text{intra}} = \sum_{i=1}^{M} F_{\text{intra}}^{(i)} = -k_B T \sum_{i=1}^{M} \ln P(\mathbf{X}_i)\,. \tag{3.2}$$

The interaction of the soft particles is chosen to be pairwise additive. The intermolecular part is therefore given by

$$F_{\text{inter}} = \frac{1}{2}\sum_{i=1}^{M}\sum_{j\neq i} F_{\text{inter}}^{(ij)} + \left(\frac{1}{2}\sum_{i=1}^{M} F_{\text{inter}}^{(ii)}\right)\,. \tag{3.3}$$

We put the second term in eq. (3.3) in parenthesis, since one may or may not include self–interaction terms, depending on the choice of the underlying single chain model. In the case

of self–avoiding chains excluded volume effects already give a contribution to F_{intra} due to the restriction of the configuration space by the interaction of different monomers of the polymer. Ideal chain models neglect the excluded volume effect, therefore the interaction of monomers of the same chain should be accounted for in F_{inter}.

The interaction between two soft particles is given by

$$F_{\text{inter}}^{(ij)} = \int d^3y \int d^3z \; v_{\text{eff}}(\mathbf{y},\mathbf{z}) \; \varrho_i'(\mathbf{y}) \; \varrho_j'(\mathbf{z}) \,, \tag{3.4}$$

where $\varrho_i'(\mathbf{y})$ is the monomer density of particle i in the laboratory fixed coordinate system. The effective pair potential $v_{\text{eff}}(\mathbf{y},\mathbf{z})$ between two monomers can also include indirect contributions mediated by solvent molecules. The simplest choice accounting for excluded volume effects is $v_{\text{eff}}(\mathbf{y},\mathbf{z}) = \hat{\epsilon}\, b^3 \delta(\mathbf{y}-\mathbf{z})$, cf. sec. 1.1.2, with $\hat{\epsilon}$ and b^3 being a "contact energy" and a "contact volume", respectively. In this case the interaction is given by the overlap integral of the monomer densities,

$$F_{\text{inter}}^{(ij)} = \hat{\epsilon}\, b^3 \int d^3y \; \varrho_i'(\mathbf{y}) \; \varrho_j'(\mathbf{y}) \,. \tag{3.5}$$

We note, that in the case of input chains with excluded volume, the interaction potential depends on the chain length N, too, i.e. $\hat{\epsilon} = \hat{\epsilon}(N)$. Otherwise the correct scaling of the particle size with chain length cannot be achieved in dense systems [Mur98]. Equations (3.1–3.3, 3.5) fix the thermodynamics of the model.

Generalizations to polymer mixtures are straightforward [Mur98]. In a binary polymer blend we have two types of polymers A and B. For simplicity we will assume that both types have the same polymerization degree, $N_A = N_B = N$, and that a polymer of each type interacts with a polymer of the same type with an interaction $\hat{\epsilon}_{AA} = \hat{\epsilon}_{BB} = \hat{\epsilon}$, while polymers of different types interact with $\hat{\epsilon}_{AB} = \hat{\epsilon}\,(1+\delta)$. We note in passing that $\hat{\epsilon}\delta/k_BT$ corresponds to the Flory–Huggins parameter χ of the lattice model, cf. eq. (1.29).

In principle the same variables as for a binary mixture (chain lengths N_A, N_B and interaction parameters $\hat{\epsilon}_{AA}$, $\hat{\epsilon}_{BB}$ and $\hat{\epsilon}_{AB}$, or δ respectively) can be used to describe diblock copolymers, if one considers both blocks separately. Only the intramolecular part has to be adjusted to account for the bond between the two blocks.

To summarize, the external parameters defining the thermodynamic state of a homogeneous system are the polymerization degree N, the overall monomer concentration $c = (N+1)M/V$, and the reduced interaction strength $\epsilon \equiv \hat{\epsilon}/k_BT$. In a binary blend (or diblock copolymer system) we in addition have the mismatch interaction δ and the concentration c_A (or fraction f_A) of A polymers (or blocks).

For describing kinetic properties we employ a discrete time Monte Carlo algorithm. The details of the configuration changes, i.e the Monte Carlo moves, depend on the specific soft particle model. A common feature of the discrete time Monte Carlo algorithm, however, is that the dynamics are purely diffusive and neglect advective processes due to hydrodynamic flows. Moreover, the dynamics do not capture any processes specific for polymers on time scales smaller than τ_d. As a consequence, when adjusting the Monte Carlo time step to real experimental time scales, one should take care that the dependence of τ_d on N will generally be different in the simulations and the real system.

3.2 Choice of the Chain Model

The input quantities $P(\mathbf{X})$ and $\varrho(\mathbf{y};\mathbf{X})$ have to be determined from a chain model for macromolecules. The question is, which chain model should be chosen.

Murat and Kremer chose the bead–spring model with purely repulsive Lennard–Jones interaction [Kre90] as the underlying single chain model and mapped the bead–spring chains onto soft ellipsoids. They argued, that the configuration space of a polymer in a melt equals the configuration space of a self–avoiding chain, only the statistical weight of these configurations is changed [Mur98]. Therefore the input–chain should be self–avoiding. Aiming at a quantitative description of polymer melts and blends, the size of the particles was adjusted to their size in simulations of the original bead–spring model. This was done by tuning the interaction parameter $\hat{\epsilon}$ as a function of N. Because the input quantities were determined only numerically, it was not possible to use their soft ellipsoid model directly. It would have been necessary to determine the input quantities again. Moreover, explicit chain simulations of dense systems would have been needed, to adjust $\hat{\epsilon}$.

Since we are interested mainly in the thermodynamic properties of polymer melts and mixtures, we choose the Gaussian chain as the underlying microscopic model to determine the input quantities $P(\mathbf{X})$ and $\varrho(\mathbf{y};\mathbf{X})$. Because we feel that it is worthy to investigate the general behavior of this kind of soft particle models, we study the simplest case first.

Moreover, the Gaussian chain model indeed provides an appropriate input model. When using Gaussian chains as an input, we take Flory's original argument, why chains are ideal in dense systems, literally, cf. sec. 1.1.3. The soft particles are described by a mean monomer density. The self–interaction leads to a swelling of the soft particles, while the surrounding particles compress them, cf. eqs. (3.3, 3.5). The interaction of one soft particle with itself and with other soft particles is treated on the same footing. This is reasonable, because the interaction of a monomer with an other monomer of the same polymer and a monomer of another polymer is equivalent – except, of course, for neighboring monomers along the same chain. Therefore the interaction term is in some sense self–consistent. As we will show in section 5.1 a tuning of $\hat{\epsilon}$ with N is thus no longer necessary and therefore no explicit chain simulations are needed.

Furthermore, the Gaussian chain model is generic, in a sense that all other ideal chain models reduce to it on length scales greater than Kuhn's segment length, cf. sec. 1.1.1. The first coarse–graining step, the mapping of realistic chains onto Gaussian coils, has already been performed for many different polymer models, using RIS–theory [Reh97]. Therefore it would be possible to build on a well established basis, if one wishes to make a direct connection to microscopic models or experiments and to obtain quantitative results. This kind of basis exists also concerning the previous knowledge of the input quantities, but despite this fact little is known about the precise quantities $P(\mathbf{X})$ and especially $\varrho(\mathbf{y};\mathbf{X})$ needed for our purposes. As those quantities are difficult to determine exactly, they will be provided by Monte Carlo simulations of single Gaussian chains. These results together with analytical considerations will lead to approximate, but closed forms for the input quantities making the model portable.

From a technical point of view, we also have the advantage that Gaussian chains are easily generated. Thus we are able to avoid costly simulations of a more realistic microscopic single chain model and to reduce statistical errors occurring necessarily in the determination of the multi dimensional functions $P(\mathbf{X})$ and $\varrho(\mathbf{y};\mathbf{X})$.

The results for the input quantities of the respective soft particle models are given directly in the following sections. Their form and derivation will be discussed in detail in chapter 4.

3.3 Soft Sphere Model

In a first step we adopt the common view, that a polymer has on average a sphere like shape with a radius given by its radius of gyration R_G defined in eq. 1.10. This leads to the simple soft particle model defined by the choice $\{\mathbf{X}\} = \{\mathbf{r}, R_G^2\}$. (An even simpler model could be achieved by replacing R_G by its average, however the information gained from such a model would probably be very small.)

The input quantities in this case are the probability distribution $P_R(R_G^2, N)$ and the spherically symmetric conditional monomer density $\varrho_r(\mathbf{x}; R_G^2, N)$, where $\mathbf{x} = \mathbf{y} - \mathbf{r}$ denotes the coordinates with respect to the center of mass $\mathbf{r}$.

A very accurate, though not exact form for $P_R(R_G^2, N)$ in the limit of large N is given by

$$P_R(R_G^2, N) \sim \frac{1}{2\,K_0(2\,d_R)\,R_G^2} \exp\left(-\frac{R_G^2}{a_R\,N} - d_R^2 \frac{a_R\,N}{R_G^2}\right) , \tag{3.6}$$

where a_R and d_R are constants given in tab. 3.1 and $K_0(.)$ denotes the modified Bessel function of zeroth order, cf. sec. 4.1.1. The conditional monomer density can be described by

$$\varrho_r\left(\mathbf{x}; R_G^2, N\right) = \frac{N+1}{R_G^3} \left(\frac{3}{2\pi}\right)^{3/2} \exp\left(-\frac{3}{2}\frac{\mathbf{x}^2}{R_G^2}\right) , \tag{3.7}$$

see sec. 4.2.1. The one particle monomer density in the laboratory system then is given by $\varrho'_{r,i}(\mathbf{y}) = \varrho_r(\mathbf{y} - \mathbf{r}_i; R_G^{(i)}, N)$. The integral in eq. (3.5) can be evaluated directly and amounts to a generalized Flory–Krigbaum potential [Flo50],

$$F_{\text{inter}}^{(ij)} = \frac{\hat{\epsilon} b^3 (N+1)^2}{\left[2\,\pi\sigma_r^2 \left(R_G^{(i)\,2} + R_G^{(j)\,2}\right)\right]^{3/2}} \exp\left[-\frac{1}{2\,\sigma_r^2} \frac{(\mathbf{r}_i - \mathbf{r}_j)^2}{R_G^{(i)\,2} + R_G^{(j)\,2}}\right] . \tag{3.8}$$

The two different Monte Carlo moves supplying the kinetics of the model are given by:

1. A translation of the center of mass $\mathbf{r}$ of one particle about a random vector $\Delta\mathbf{r}$, whose components are drawn from a uniform distribution in the interval $[-\Delta r_{\max}/2, \Delta r_{\max}/2]$.

2. A change of the size R_G^2, to which a random number ΔR_G^2 uniformly distributed in the interval $[\max(-\Delta R_{G\max}^2/2, -R_G^2), R_{G\max}^2/2]$ is added.

The changes ΔR_G^2 are restricted such that R_G^2 is always positive. Both, $(\Delta r_{\max})^2$ and $\Delta R_{G\max}^2$ are of the order of $\bar{R}_G^2$. The two possible moves are chosen with equal probability and one Monte Carlo step is defined as $2\,M$ trials to change the state of a soft sphere.

This model covers all basic aspects of the soft particle models presented here. It has the additional advantage that it is possible to do some analytical calculations for this model, because the interaction term eq. (3.8) is rather simple in comparison to the soft ellipsoid model.

3.4 Soft Ellipsoid Model

The mapping of a polymer onto a spherical particle involves an implicit average over all orientations. Therefore only the effective size of the particle given by R_G enters as an internal degree of freedom. However, as a random walk is a highly irregular object, the instantaneous shape of a random walk is far from being spherical. This has been predicted already by Kuhn [Kuh34] and has been confirmed by computer simulations, see e.g. [Sol71a, Sol71b], and by experiments [Hab00]. More precisely, spherical configurations constitute a set of probability measure zero [Eic77]. A representation that accounts better for this fact, is the description of the polymer as an ellipsoid.

A straightforward way to find an ellipsoidal form is to transform the particles' coordinates $\mathbf{y}_k$ into the principal axis system with coordinates $\mathbf{x}_k$. Instead of the inertial tensor, in polymer physics the radius of gyration tensor is used,

$$S_{\alpha\beta} = \frac{1}{N+1} \sum_{k=0}^{N} \left(y_\alpha^{(k)} - r_\alpha \right) \left(y_\beta^{(k)} - r_\beta \right) , \tag{3.9}$$

where $y_\alpha^{(k)}$ is the αth component of $\mathbf{y}_k$, and the constant monomer mass is omitted (or set to unity, defining the mass unit). The spatial extension of the ellipsoidal particle is given by the eigenvalues $\mathbf{S} = (S_1, S_2, S_3)$ of $S_{\alpha\beta}$. Without loss of generality we choose

$$S_1 \geq S_2 \geq S_3 , \tag{3.10}$$

i.e. we order the eigenvalues so that the first coordinate in the ellipsoid's coordinate system always refers to the largest axis, while the third coordinate refers to the smallest axis. Note, that

$$R_G^2 = S_1 + S_2 + S_3 , \tag{3.11}$$

which follows from the definitions eqs. (1.10, 3.9).

The orientation of the ellipsoidal particle in space is given by the orientation of the principal axes of $S_{\alpha\beta}$. Denoting the corresponding rotation matrix by $\mathcal{R}$, the principal axes transformation is given by

$$\mathbf{x} = \mathcal{R} \left(\mathbf{y} - \mathbf{r} \right) . \tag{3.12}$$

Table 3.1: Parameter defining $P_R(R_G^2)$ in eqs. (3.6, 4.10) and $P_\alpha(S_\alpha)$ in eqs. (3.15, 4.13)

R_G^2		S_α	S_1	S_2	S_3
n_R	1.0	n_α	1/2	5/2	4
a_R	0.08020	a_α	0.08065	0.01813	0.006031
d_R	1.842	d_α	1.096	1.998	2.684
$K_0(2d_R)$	0.015923	$K_{n_\alpha-1}(2d_\alpha)$	0.094551	0.0144146	0.0052767

The set of variables defining the state of the soft ellipsoidal particle is $\{\mathbf{X}\} = \{\mathbf{r}, S_{\alpha\beta}\}$. The dependence of the monomer density on the center of mass and on the spatial orientation of the principal axis follows from eq. (3.12). Therefore the set of different states that have to be distinguished in determining $\varrho(\mathbf{y};\mathbf{X})$ is reduced to the set of the three different eigenvalues, i.e. $\{\mathbf{X}\} = \{\mathbf{S}\}$. Thus a function $\varrho(\mathbf{x};\mathbf{S})$ is assigned to each ellipsoid in its coordinate system, which specifies the mean monomer density of the polymer for given eigenvalues $\mathbf{S}$. This means, that two ellipsoids i, j with $\mathbf{S}_i = \mathbf{S}_j$ have monomer densities $\varrho(\mathbf{x};\mathbf{S}_i)$, $\varrho(\mathbf{x};\mathbf{S}_j)$ that can be transformed into each other by a spatial rotation. In the laboratory fixed coordinate system the monomer density $\varrho_i'(\mathbf{y})$ of polymer i is given by

$$\varrho_i'(\mathbf{y}) = \varrho(\mathcal{R}_i(\mathbf{y} - \mathbf{r}_i);\mathbf{S}_i)\,. \tag{3.13}$$

The probability $P(\mathbf{S})$ for a polymer to have eigenvalues $\mathbf{S}$ and the conditional monomer density $\varrho(\mathbf{x};\mathbf{S})$ are the input quantities for the soft ellipsoid model. The distribution $P(\mathbf{S})$ can be approximated by a separation ansatz

$$P(\mathbf{S},N) = \prod_\alpha P_\alpha(S_\alpha,N) \sim \prod_\alpha \frac{1}{N}\tilde{P}_\alpha\left(\frac{S_\alpha}{N}\right) \tag{3.14}$$

of probability distributions $P_\alpha(S_\alpha)$ for the single eigenvalues S_α. Very good approximations for the $P_\alpha(S_\alpha)$ in the case of large N are given by scaling functions similar to eq. (3.6)

$$\frac{1}{N}\tilde{P}_\alpha\left(\frac{S_\alpha}{N}\right) = \frac{S_\alpha^{-n_\alpha}\,(a_\alpha d_\alpha N)^{n_\alpha-1}}{2\,K_{n_\alpha-1}(2\,d_\alpha)} \exp\left(-\frac{S_\alpha}{a_\alpha N} - d_\alpha^2\frac{a_\alpha N}{S_\alpha}\right)\,, \tag{3.15}$$

cf. sec. 4.1.2. The parameters n_α, a_α, and d_α are given in tab. 3.1 and $K_{n_\alpha-1}(.)$ denotes the modified Bessel function of $(n_\alpha-1)$th order. For the density $\varrho(\mathbf{x};\mathbf{S},N)$ we make a separation ansatz,

$$\varrho(\mathbf{x};\mathbf{S},N) = (N+1)\prod_\alpha \frac{1}{R_\alpha}\tilde{\varrho}_\alpha\left(\frac{x_\alpha}{R_\alpha}\right)\,, \tag{3.16}$$

where $\tilde{\varrho}_\alpha(u_\alpha)$ with $u_\alpha = x_\alpha/R_\alpha$, can be approximated by a superposition of Gaussians

Table 3.2: Numerical results for the constants defining $\tilde{\varrho}_\alpha(u_\alpha)$ in eqs. (3.17a-c).

$\sigma_1 = 0.48920$	$c_1 = 0.64528$	$\bar{u}_1 = 0.994$
$\sigma_2 = 1.06892$		
$\sigma_3 = 1.03009$		

$$\tilde{\varrho}_1(u_1) = \frac{1}{\sqrt{2\pi}\sigma_1(2+c_1)}\left[\exp\left(-\frac{(u_1-\bar{u}_1)^2}{2\sigma_1^2}\right)+ \exp\left(-\frac{(u_1+\bar{u}_1)^2}{2\sigma_1^2}\right)+c_1\exp\left(-\frac{u_1^2}{2\sigma_1^2}\right)\right] \tag{3.17a}$$

$$\tilde{\varrho}_2(u_2) = \frac{1}{\sqrt{2\pi}\sigma_2}\exp\left(-\frac{u_2^2}{2\sigma_2^2}\right) \tag{3.17b}$$

$$\tilde{\varrho}_3(u_3) = \frac{1}{\sqrt{2\pi}\sigma_3}\exp\left(-\frac{u_3^2}{2\sigma_3^2}\right)\,. \tag{3.17c}$$

The parameters σ_α, c_1, and $\bar{u}_1$ are given in tab. 3.2. This form is justified in sec. 4.2.2. An analytic calculation of F_{inter} is possible, the respective expressions are given in appendix C.1.

For describing kinetic properties we implement a discrete time Monte Carlo algorithm involving three different types of moves of a randomly chosen ellipsoid [Mur98]:

1. A translation, where the center of mass is displaced by a random vector $\Delta\mathbf{r}$, whose components are drawn from a uniform distribution in the interval $[-\Delta r_{\max}/2, \Delta r_{\max}/2]$.
2. A rotation of the ellipsoid with equal probability in the steradian 4π, cf. [Mil65].
3. A change of the ellipsoid's size, where random numbers ΔS_α uniformly distributed in the interval $[\max(-\Delta S_{\max,\alpha}/2, -S_\alpha), S_{\max,\alpha}/2]$ are added to the eigenvalues S_α.

We restricted the changes ΔS_α to values that result only in positive S_α. Moreover, for a move according to rule 3 it is possible that the order of the principal axes changes because of condition (3.10), which requires a simultaneous update of the orientation of the ellipsoid.

We still have to specify $\Delta r_{\max}$ and $\Delta S_{\max,\alpha}$. As we are mainly interested in the simulation of dense systems, we choose the changes to be of the order of the average ideal characteristic sizes

$$\Delta r_{\max} = K_r \bar{R}_G \quad \text{and} \quad \Delta S_{\max,\alpha} = K_s \langle S_\alpha \rangle\,, \tag{3.18}$$

with $\langle S_\alpha \rangle$ given in tab. B.1. Since processes on the scale of $\bar{R}_G$ are treated as elementary processes for the soft particle model, this is reasonable. The choice $K_r = 0.25$ and $K_s = 0.5$ leads to acceptance rates of about 0.5.

All possible moves are attempted with the same probability and we define one Monte Carlo step (MCS) as $3\,M$ trials to change the state of an ellipsoid. Further details of the algorithm are described in appendix D.

3.5 Disphere Model

In this and the following section we will propose soft particle models, where the concept of mapping one polymer onto one soft particle is modified, i.e. one polymer is mapped onto a small amount of soft particles with internal degrees of freedom. This is necessary when one thinks of generalizing the actual concept and modeling diblock copolymers or even more complicated

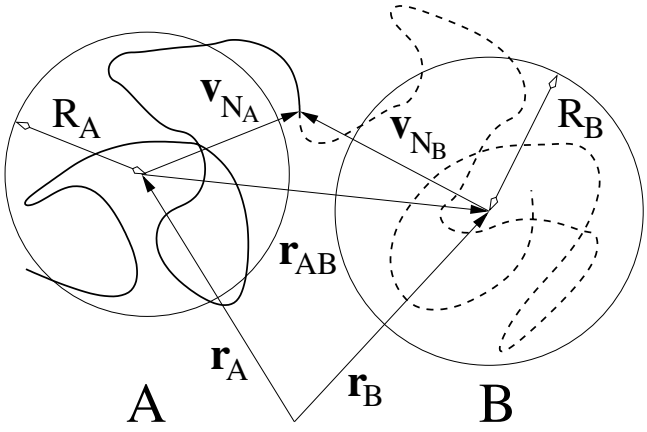

Figure 3.2: Schematic illustration of a diblock copolymer.

particles. Moreover, such an approach may lead to a more systematic coarse–graining procedure and a better control of the approximations involved [Kre01].

When thinking of modeling diblock copolymers in terms of a soft particle model, two monomer densities corresponding to the different blocks A and B have to be considered. While in principle it might be possible to map a whole diblock copolymer onto a soft ellipsoid, characterized by the eigenvalues S_α, the scaling ansatz eq. (3.16) would lead to wrong results. Chain simulations, for example, yield a different behavior of the one block radius of gyration R_A as a function of the interaction strength ϵ_{AB}, than the distance r_{AB} between the two centers of mass of both blocks [Hof97]. Moreover, a "rigid" ellipsoid would not have the necessary flexibility to describe multiblock copolymers. Therefore the model has to be adjusted.
Consider a diblock copolymer consisting of N_A monomers of type A and N_B monomers of type B. Let the index X denote both species ($X \in \{A, B\}$). The centers of mass $\mathbf{r}_X$ and the radii of gyration R_X of the two blocks are given by the usual definitions eq. (1.11) and eq. (1.10), only the sums are restricted to the respective blocks of the polymer. The distance between the centers of mass is given by $\mathbf{r}_{AB} = \mathbf{r}_B - \mathbf{r}_A$, see fig. 3.2. A reasonable choice for a model would be to describe both blocks in terms of a Gaussian sphere model, leading to a soft "disphere".[1] Therefore a set of variables $\{\mathbf{X}\} = \{\mathbf{r}_A, \mathbf{r}_B, R_A^2, R_B^2\}$ is appropriate. However, the state of such a disphere depends only on the distance r_{AB}. Dispheres with different $\mathbf{r}_A, \mathbf{r}_B$ but identical r_{AB} (and R_A^2, R_B^2) can be transformed into each other by a translation and rotation as in the case of the soft ellipsoids.

The input quantities in this case are the probability distribution $P_{AB}(r_{AB}^2, R_A^2, R_B^2, N_A, N_B)$ and two conditional monomer densities $\varrho_X(\mathbf{x}; \mathbf{r}_A, \mathbf{r}_B, R_A^2, R_B^2, N_A, N_B)$. The arguments N_A and N_B in these functions will be suppressed in the following. The combined probability distribution

$$P_{AB}(r_{AB}^2, R_A^2, R_B^2) = P_R(R_A^2, N_A)\, P_R(R_B^2, N_B)\, P_C(r_{AB}^2; R_A^2, R_B^2)\,, \tag{3.19}$$

can be written in terms of a conditional probability P_C that can be approximated by a function independent of N_A and N_B, cf. sec. 4.1.3,

[1] The term dipole is restricted to "charged" systems, no dipole moment exists for mass distributions in the sense of the limiting field of two point masses.

$$P_C(r_{AB}^2; R_A^2, R_B^2) \approx \sqrt{\frac{r_{AB}^2}{2\pi}} \left(\frac{3}{2\left(R_A^2 + R_B^2\right)} \right)^{3/2} \exp\left[-\frac{3}{2} \frac{r_{AB}^2}{2\left(R_A^2 + R_B^2\right)} \right] . \tag{3.20}$$

The probability distributions for the radii of gyration P_R are already given by eq. (3.6). In passing we note, that the part of F_{intra} corresponding to $P_C(r_{AB}^2; R_A^2, R_B^2)$ can be interpreted as an effective bond potential between the two different blocks, accounting for the fact, that the two blocks are actually linked together. The total conditional monomer density decomposes into the two densities of the different blocks

$$\varrho_{AB}\left(\mathbf{x}; \mathbf{r}_A, \mathbf{r}_B, R_A^2, R_B^2\right) = \varrho_A\left(\mathbf{x}; \mathbf{r}_A, \mathbf{r}_B, R_A^2, R_B^2\right) + \varrho_B\left(\mathbf{x}; \mathbf{r}_A, \mathbf{r}_B, R_A^2, R_B^2\right) . \tag{3.21}$$

As the two blocks have to be treated differently with respect to interaction it is convenient to work directly with the ϱ_X. Although the disphere and the ϱ_X have cylindric symmetry, it is convenient to approximate the block densities by the spherical symmetric forms of the Gaussian sphere model, see sec. 4.2.3, and write

$$\varrho_X\left(\mathbf{x}; \mathbf{r}_A, \mathbf{r}_B, R_A^2, R_B^2\right) \approx \varrho_r\left(\mathbf{x}; R_X, N_X\right) , \tag{3.22}$$

where ϱ_r is given by eq. (3.7). The monomer density of one block X of a copolymer i in the laboratory system is given by $\varrho'_{rX,i}(\mathbf{y}) = \varrho_r(\mathbf{y} - \mathbf{r}_X^{(i)}; R_X^{(i)}, N_X)$.

The interaction parameters $\hat{\epsilon}_{XY}$ between monomers of the same and of different kind can be chosen in analogy to the case of binary blends, cf. sec. 3.1. The summation in the expression for the interaction energy, eq. (3.3), has to be adjusted

$$F_{\text{inter}} = \frac{1}{2} \sum_{i=1}^{M} \sum_{j=1}^{M} \sum_{X=A}^{B} \sum_{Y=A}^{B} F_{\text{inter}}^{(iXjY)} \tag{3.23}$$

$$F_{\text{inter}}^{(iXjY)} = \hat{\epsilon}_{XY}\, b^3 \int d^3y\, \varrho'_{rXi}(\mathbf{y}) \varrho'_{rYj}(\mathbf{y}) . \tag{3.24}$$

Here we gave only the expression for a δ–Potential and Gaussian chains. Note, that this expression includes all kinds of self–interaction.

3.6 Multisphere Models

The model in the previous section might be generalized to multisphere models, to describe for example copolymers with more structure than two simple blocks. Instead of splitting a chain once, now the chain is divided into K parts. The set of internal variables is then given by $\{\mathbf{X}\} = \{\mathbf{r}_{X_i}, R_{X_i}\}, i = 1, \ldots, K$. While the monomer density $\varrho_{X_j}\left(\mathbf{x}; \{\mathbf{r}_{X_i}, R_{X_i}^2\}\right)$ for one part X_j of the copolymer can be again approximated by a spherical form in analogy to eqs. (3.7, 3.22), the probability distribution may be approximated by

$$P_{\{X_i\}}\left(\{\mathbf{r}_{X_i}, R_{X_i}^2\}\right) \approx \prod_{i=1}^{K} P_R(R_{X_i}^2) \prod_{i=1}^{K-1} P_C(r_{X_i X_{i+1}}^2; R_{X_i}^2, R_{X_{i+1}}^2) , \tag{3.25}$$

with $r_{X_i X_{i+1}}^2 = (\mathbf{r}_{X_{i+1}} - \mathbf{r}_{X_i})^2$. As before we omitted the obvious dependences on N_{X_i}. Therefore one polymer would be described by K soft particles with internal degrees of freedom R_{X_i}, that

are bound together by effective bond potentials essentially given by $\ln P_C$. The interaction terms have to be constructed in analogy to eq. (3.23). The approximations presented in this section would have to be tested. This is an important task for future developments.

An other aspect of such kind of models is that by setting all possible interaction energies equal ($\hat{\epsilon}_{XY} = \hat{\epsilon}$), we directly get a more detailed model for a homopolymer. The model corresponding to $K = 1$ is the Gaussian sphere model. As we will see in chapter 4, a multisphere model with four spheres of equal size should be very similar to the soft ellipsoid model. By dividing one chain into K parts, described by soft spheres, it would be possible to do a more systematic coarse–graining procedure [Kre01]. This would on one hand improve the control of the approximations involved in the second coarse–graining step, and on the other hand make a remapping of soft particles back to explicit chain models more transparent.

4 Geometry of the Gaussian Chain

While a careful consideration of the geometric properties of the Gaussian chain is indispensable, if one wishes to determine the input quantities for soft particle models of the type defined in the previous chapter, these properties are interesting in themselves, as they exhibit surprising features. Therefore in this chapter the respective probability distributions and the conditional monomer densities are investigated more profoundly. We determine explicit approximate formulae for the overall behavior of the input quantities based on Monte Carlo simulations and some new analytical calculations. The investigations are guided by well–known analytical results and asymptotic expansions, most of which can be found in ref. [Yam71].

In a first step we consider the respective distribution functions ordered according to the three different models, the Gaussian sphere model, the Gaussian ellipsoid model and the disphere model. Therefore we investigate the distributions for the squared radius of gyration R_G^2, the eigenvalues of the gyration tensor S_α, and the squared radii of gyration R_A^2, R_B^2 and the center of mass distance $\mathbf{r}_{AB}$. Then, in a second step, we determine the corresponding conditional monomer densities that are more involved.

The Gaussian chain model has been described in sec. 1.1.1. Essential for its definition is the probability distribution $p(\mathbf{u}_k)$ for the bond vectors $\mathbf{u}_k = \mathbf{y}_k - \mathbf{y}_{k-1}$ that is given by eq. (1.5), where again $\mathbf{y}_k$ denote the positions of the single beads. As already discussed in sec. 1.1.1, the root mean square bond length b can be identified with Kuhn's segment length l. Furthermore we may identify it with the length corresponding to the *contact volume* b^3 in eq. (3.5) and define b as our length unit, i.e. $b \equiv 1$.

The simulations of the Gaussian chain model are of standard Monte Carlo type. Averages have been taken over typically 10^7–10^9 different chain conformations, depending on the number of bonds N. In this chapter $\langle \dots \rangle$ denotes an average over an ensemble of Gaussian chains. All input quantities depend on the chain length N, but we take the freedom to suppress the argument N, whereever it seems to be appropriate.

4.1 Probability Distributions

The quantities considered in this section describe the distributions of the overall shape of a Gaussian chain. As highly elongated and strongly compressed conformations are improbable, because the respective configuration space is small, there will be typical (average) shapes, which are highly probable. In the following we will quantify this statement, by regarding well–known analytical calculations and new numerical results for the distribution functions of characteristic quantities, such as the radius of gyration R_G and the gyration tensor $S_{\alpha\beta}$.

4.1.1 Radius of Gyration

We first consider the distribution function $P_R(R_G^2, N)$ of the squared radius of gyration R_G^2. As we need some results from its derivation later on, we show, how an analytical expression can be obtained. First we consider the joint distribution function $P_j(\mathbf{v}_j, R_G^2)$, where $\mathbf{v}_j = \mathbf{y}_j - \mathbf{r}$ denotes the vector to a monomer j from the center of mass $\mathbf{r}$ defined in eq. (1.11). Given this distribution, $P_R(R_G^2)$ can be determined by integrating $P_j(\mathbf{v}_j, R_G^2)$ over $\mathbf{v}_j$. As only the distribution of the bond vectors $\mathbf{u}_k$ is given, both $\mathbf{v}_j$ and R_G^2 have to be expressed in terms of the $\mathbf{u}_k$, yielding

$$\mathbf{v}_j = \sum_{i=1}^{N} \psi_{ji}\, \mathbf{u}_i \quad \text{and} \quad R_G^2 = \sum_{k=1}^{N}\sum_{l=1}^{N} g_{kl}\, \mathbf{u}_k \mathbf{u}_l \,. \tag{4.1}$$

Here we defined

$$\psi_{ji} = H(j-i) + \frac{i}{N+1} - 1 \quad \text{and} \quad g_{kl} = \frac{1}{N}\sum_{j=1}^{N} \psi_{jk}\psi_{jl} \,, \tag{4.2}$$

where $H(i)$ is the discrete step function, i.e. $H(i) = 1$ for $i \geq 0$ and $H(i) = 0$ for $i < 0$. The bivariate distribution function is then given by

$$P_j(\mathbf{v}_j, R_G^2) = \int \prod_{i=1}^{N} d\mathbf{u}_i\, p(\mathbf{u}_i)\, \delta\left(\mathbf{v}_j - \sum_{i=1}^{N} \psi_{ji}\, \mathbf{u}_i\right)\, \delta\left(R_G^2 - \sum_{k=1}^{N}\sum_{l=1}^{N} g_{kl}\, \mathbf{u}_k \mathbf{u}_l\right) \,. \tag{4.3}$$

Introducing the Fourier representation of the Dirac δ–function, it is possible to do the integration of the $\mathbf{u}_i$ and the Fourier integrals corresponding to $\mathbf{v}_j$, yielding

$$P_j(\mathbf{v}_j, R_G^2) = \frac{1}{16\pi^{5/2}} \int_{-\infty}^{\infty} d\rho\, K(\rho) W_j^{-3/2}(\rho) \exp\left(-i\,\rho R_G^2 - \frac{\mathbf{v}_j^2}{4W_j(\rho)}\right) \,, \tag{4.4}$$

where ρ denotes the conjugate variable to R_G^2 in Fourier space. The functions $K(\rho)$ and $W_j(\rho)$ are in the limit of large N given by

$$K(\rho) = \left(\frac{\sin X(\rho)}{X(\rho)}\right)^{-3/2} \,, \quad \text{with} \quad X^2(\rho) = \frac{2}{3} i\,\rho N b^2 \,, \quad i = \sqrt{-1} \tag{4.5}$$

and

$$W_j(\rho) = \frac{1}{4}\sum_{k=1}^{N} \lambda_k^{-1}(\rho) \left(\sum_{l=1}^{N} \psi_{jl}\, Q_{lk}\right)^2 \,, \quad \text{with} \tag{4.6}$$

$$\lambda_k(\rho) = \frac{3}{2b^2}\left(1 - \frac{X^2(\rho)}{k^2\pi^2}\right) \,, \quad Q_{lk} = \left(\frac{2}{N}\right)^{1/2} \sin\left(\frac{\pi l k}{N}\right) \,. \tag{4.7}$$

We note at this point that both $K(\rho)$ and $W_j(\rho)$ depend on N. The distribution $P_R(R_G^2)$ can be determined from eq. (4.4) by integration over $\mathbf{v}_j$, yielding

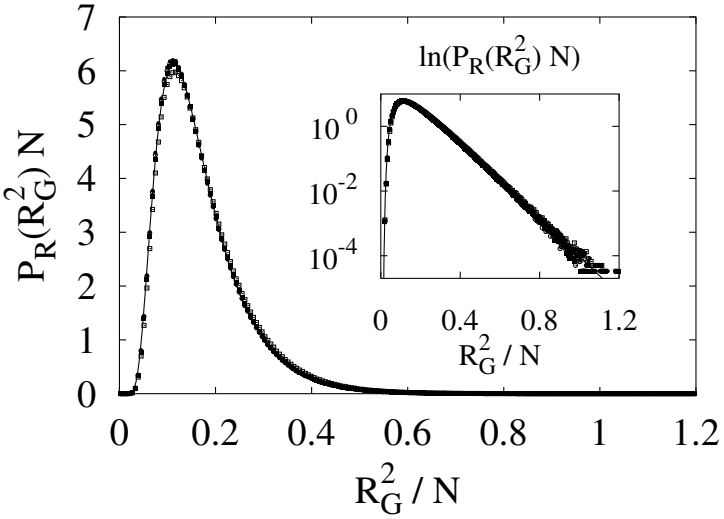

Figure 4.1: Numerical results of the scaled probability function $P_R(R_G^2)$ for $N = 30(\square)$, $100(\blacksquare)$, $300(\circ)$ and $1000(\bullet)$. The approximate function $P_R(R_G^2)$ defined in the text, cf. eq. (4.10) and tab. 3.1, is drawn as a solid line. The inset shows the same data in semi–logarithmic form to demonstrate the validity in the range of very small and very large R_G^2.

$$P_R(R_G^2) = \frac{1}{2\,\pi} \int_{-\infty}^{+\infty} d\rho\, K(\rho) \exp(-i\,\rho R_G^2)\,, \tag{4.8}$$

thus $K(\rho)$ is the *characteristic function* of $P_R(R_G^2)$. This expression is the starting point for series expansions and further approximations. The asymptotic behavior of P_R for large and small R_G, for example, is known from saddle–point approximations [Fix62, For63]. Also, P_R can be expressed in terms of a series expansion, see ref. [Yam71] and references therein. A closed approximate form for the overall behavior was proposed by Flory and Fisk [Flo66]. However, while reproducing the first moments of $P_R(R_G^2)$ fairly good, the form does not give the correct asymptotics for small values of R_G^2.

With regard to the determination of $P(\mathbf{S})$ we examine $P_R(R_G^2)$, using Monte Carlo simulations of the Gaussian chain, although an exact series expansion for $P_R(R_G^2)$ is known and could in principle be used for the Gaussian sphere model. It is our aim to derive a closed approximate form of P_R valid for large values of N.

For large $N \to \infty$, $P_R(R_G^2, N)$ obeys the random walk scaling

$$P_R(R_G^2, N) \sim \frac{1}{N} \tilde{P}_R\left(\frac{R_G^2}{N}\right), \quad \int_0^\infty du\, \tilde{P}_R(u) = 1\,. \tag{4.9}$$

The scaling function $\tilde{P}_R(u)$ behaves as $\tilde{P}_R(u) \sim u^{\nu_0} \exp(-C_0/u)$ for $u \to 0$ and $\tilde{P}_R(u) \sim u^{\nu_\infty} \exp(-C_\infty\, u)$ for $u \to \infty$ with C_0, C_∞, ν_0, and ν_∞ being constants [Fix62, For63]. From eq. (1.12) follows that the first moment of $\tilde{P}_R(u)$ must equal 1/6 in the limit of large N. Since the exponential terms dominate the behavior of $\tilde{P}_R(u)$ for small and large u we make the ansatz

$$\tilde{P}_R(u) \cong \frac{u^{-n_R}\,(a_R d_R)^{n_R - 1}}{2\,K_{n_R-1}(2\,d_R)} \exp\left(-\frac{u}{a_R} - d_R^2 \frac{a_R}{u}\right), \tag{4.10}$$

where $K_{n_R-1}(.)$ denotes the modified Bessel function of (n_R-1)th order and accounts for proper normalization. For simplicity we restrict n_R to half–integers, but it is not expected to equal $-\nu_0$ or $-\nu_\infty$. Since the form of the maximum turns out to depend sensitively on n_R, we determined n_R by a least squares fit of (4.10) to the Monte Carlo data in the region given by the full width at half maximum. After determining $n_R = 1$ by this procedure, we calculated the constants a_R and d_R from the first two moments of $\tilde{P}_R(u)$ (see app. B.2 and tab. 3.1).

Figure 4.1 shows that the scaling (4.9) is well obeyed for $N \gtrsim 30$ and that eq. (4.10) provides an excellent approximation to the simulated data. Moreover, higher moments $\langle R_G^{2m} \rangle$, $m = 2, 3, \ldots$ calculated by using eq. (4.10) deviate by less than one per cent from the exact result (see app. B.2). Therefore eq. (3.6) is a very good approximation. When examining chains of length $N = 2 \ldots 10$ (not shown), we found larger deviations from a scaling behavior.

4.1.2 Eigenvalues of the Gyration Tensor

The exact analytical form of the distribution function $P(\mathbf{S}, N)$ for Gaussian chains is rather complicated. It can be presented in terms of multiple integrals [Wei90], but an exact calculation from the respective formulae is very cumbersome from the numerical point of view. Useful explicit expressions are available only in the limit of large eigenvalues S_α [Wei90, Eic85]. While a closed approximate form for $P(\mathbf{S})$ was proposed by Stockmayer et al. [Gob74] in analogy to the result of Flory and Fisk for $P_R(R_G^2)$, it is also of limited use.

To find a useful approximate formula for $P(\mathbf{S}, N)$, we first consider the distributions

$$P_\alpha(S_\alpha, N) = \int d^2 S_\beta \, P(\mathbf{S}, N) \, , \quad \beta \neq \alpha \, , \tag{4.11}$$

of the single eigenvalues S_α, $\alpha = 1, 2, 3$. In view of eq. (3.11) these can be expected to behave similar to $P_R(R_G^2, N)$. Using the random walk scaling for large N, we write

$$P_\alpha(S_\alpha, N) \sim \frac{1}{N} \tilde{P}_\alpha \left(\frac{S_\alpha}{N} \right) , \quad \int_0^\infty du \, \tilde{P}_\alpha(u) = 1 \, , \tag{4.12}$$

with $\tilde{P}_\alpha(.)$ as in eq. (4.10), except for the fact that the parameters n_R, a_R, and d_R are replaced by n_α, a_α, and d_α. These parameters have been determined analogously to the procedure described in sec. 4.1.1 (for details see app. B.2) and they are listed in tab. 3.1. Again, we find that these functions give an excellent description of the simulated data, see fig. 4.2. The agreement is as good as for $P_R(R_G^2, N)$. In fact, these functions can hardly be distinguished from $P_R(R_G^2, N)$ looking at their form alone.

Next, in order to obtain the joint probability density $P(\mathbf{S}, N)$, we neglect correlations among the S_α, and write

$$\begin{aligned} P(\mathbf{S}, N) &= \prod_\alpha P_\alpha(S_\alpha, N) = \prod_\alpha \frac{1}{N} \, \tilde{P}_\alpha \left(\frac{S_\alpha}{N} \right) \\ &= \prod_\alpha \frac{S_\alpha^{-n_\alpha} \, (a_\alpha d_\alpha N)^{n_\alpha - 1}}{2 \, K_{n_\alpha - 1}(2 \, d_\alpha)} \, \exp \left(- \frac{S_\alpha}{a_\alpha N} - d_\alpha^2 \frac{a_\alpha N}{S_\alpha} \right) . \end{aligned} \tag{4.13}$$

A useful test of the accuracy of eq. (4.13) is to check whether the correlation coefficients

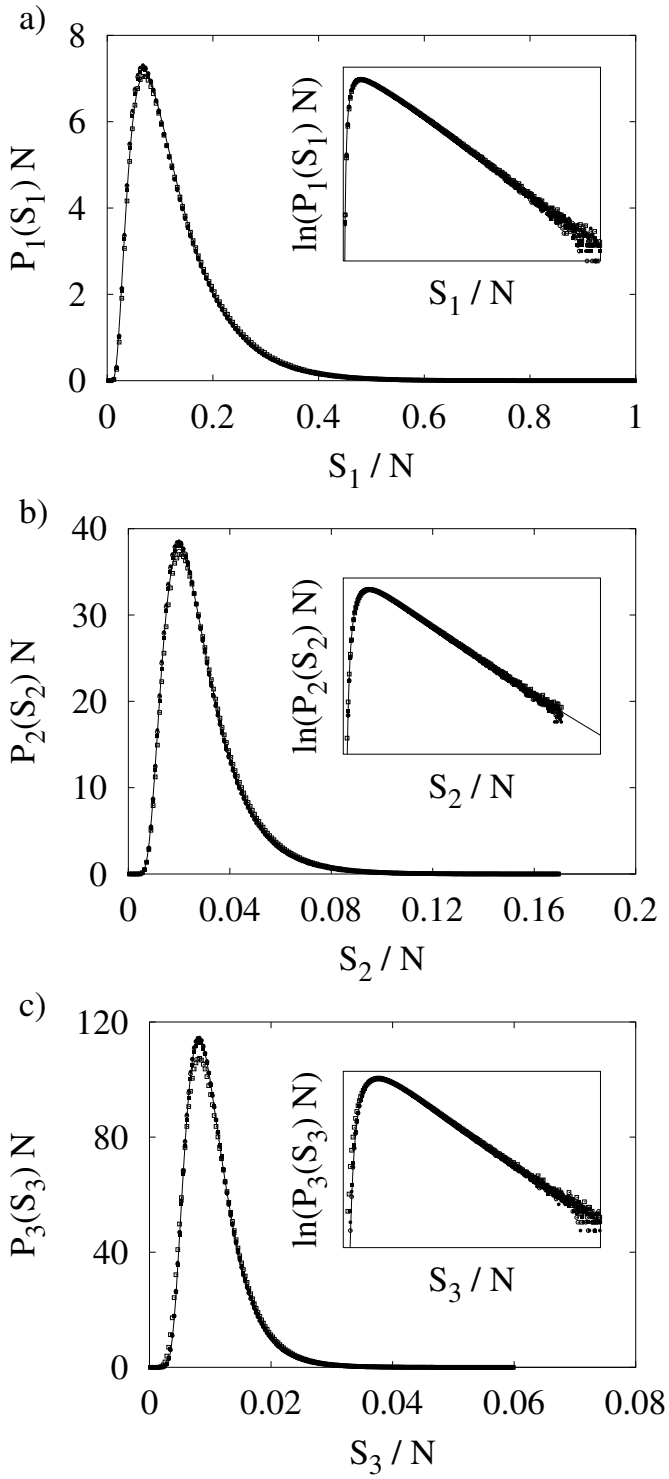

Figure 4.2: Comparison of Monte Carlo results for the scaled probability functions $P_\alpha(S_\alpha)$ for $N = 30(\square)$, $100(\blacksquare)$, $300(\circ)$ and $1000(\bullet)$ with the approximate formulae defined in eq. (4.13) and tab. 3.1. The insets show the respective data in semi–logarithmic form again.

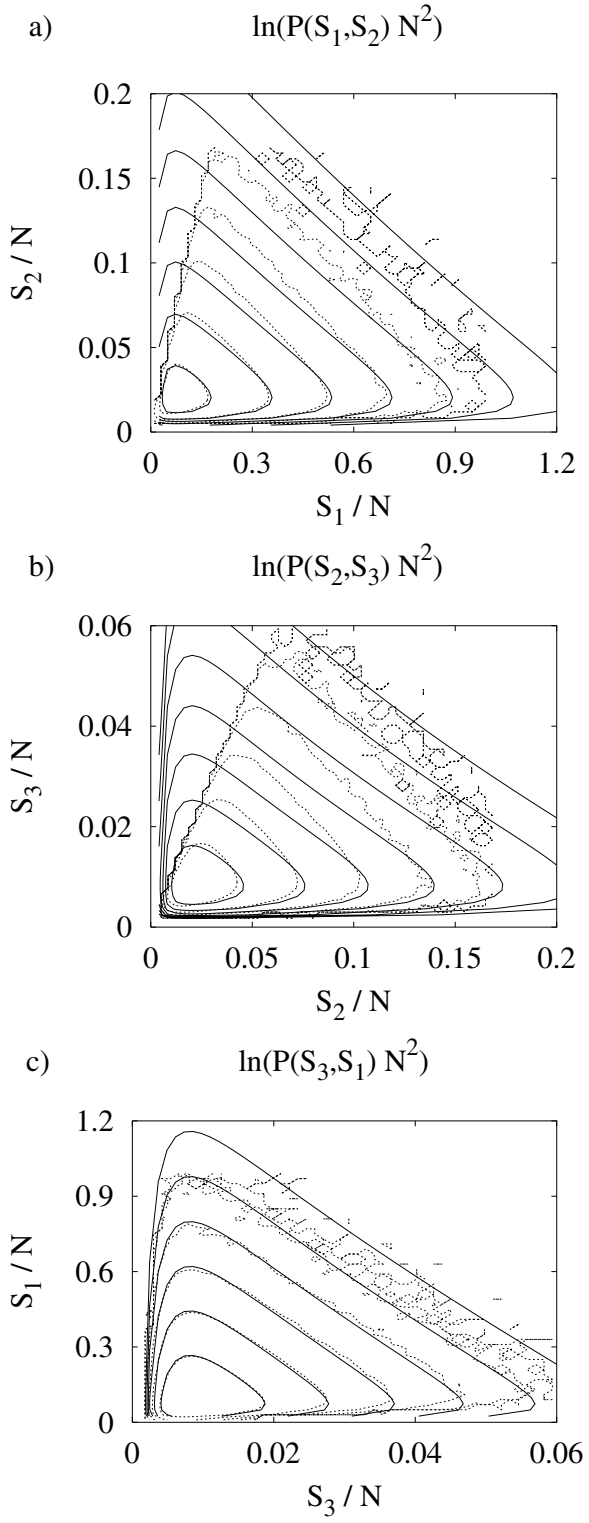

Figure 4.3: Scaled contour plots showing the comparison of $\ln(P_\alpha(S_\alpha)P_\beta(S_\beta)N^2)$ (straight lines) with numerical data of $\ln P(S_\alpha, S_\beta)$ (dashed lines). The isolines are drawn at function values of 10^n, where n is an arbitrary integer number.

$$\gamma_{\alpha\beta}^{(S)} \equiv \frac{\langle S_\alpha S_\beta\rangle - \langle S_\alpha\rangle\langle S_\beta\rangle}{\langle S_\alpha S_\beta\rangle}\,, \quad \alpha \neq \beta\,. \tag{4.14}$$

are much smaller than one. The results summarized in tab. 4.1 show that all $\gamma_{\alpha\beta}^{(S)}$ are less than 6%. We also checked whether the asphericity [Rud86]

$$\langle A\rangle = \frac{\langle R_G^4\rangle - 3\langle S_1S_2 + S_1S_3 + S_2S_3\rangle}{\langle R_G^4\rangle} \tag{4.15}$$

of the ellipsoids is significantly changed compared to the true value. From the simulations we find $\langle A\rangle \cong 0.527$, while from eq. (4.13) it follows $\langle A\rangle = 0.542$, which amounts to a relative error of about 3%.

A more sensitive test is the direct comparison of the joint probability densities

$$P(S_\alpha, S_\beta) = \int_0^\infty dS_\gamma\, P(\mathbf{S})\,, \quad \gamma \neq \alpha, \beta \tag{4.16}$$

with $P_\alpha(S_\alpha)P_\beta(S_\beta)$. As shown in fig. 4.3, the agreement between the ansatz (4.13) for $P(S_\alpha, S_\beta)$ (straight lines) and the true behavior obtained from the simulations (dashed lines) is good, except for the regions where $P(S_\alpha, S_\beta)$ becomes extremely small. For large values of S_α the Monte Carlo data are noisy due to statistical errors. We plotted the logarithm of $P(S_1, S_2)$ in fig. 4.3, since we are interested in determining $F_{\text{intra}} \propto \ln P(\mathbf{S})$.

The main restriction of (4.13) is that it does not obey the condition (3.10), i.e. $P(\mathbf{S}) = 0$ for $S_2, S_3 < S_1$ and $S_3 < S_2$. However, this poses no severe problem, because the difference in the three scales $\langle S_1\rangle : \langle S_2\rangle : \langle S_3\rangle = 12.07 : 2.717 : 1$, cf. tab. B.1, ensures that the location of the maximum of $P(\mathbf{S})$ is well separated from the region, where eq. (4.13) breaks down. Due to the exponential decrease $P_\alpha \propto \exp(-C_\alpha/S_\alpha)$ for small S_α, P is very small in the region, where it should be exactly zero.

4.1.3 Center of Mass Distance and Radii of Gyration

The description of a diblock copolymer in terms of a disphere model is based on the radii of gyration R_A, R_B of both blocks of the chain and the vector $\mathbf{r}_{AB}$ between the two centers of mass of the blocks. The radius of gyration of the total chain is given by the theorem of Steiner yielding, for $N, N_A, N_B \gg 1$,

$$N^2\, R_G^2 = NN_A\, R_A^2 + NN_B\, R_B^2 + N_AN_B\, r_{AB}^2\,. \tag{4.17}$$

The joint probability distribution $P_{AB}(r_{AB}^2, R_A^2, R_B^2)$ to find the squared center of mass separation r_{AB}^2 and the squared radii of gyration R_A^2 and R_B^2 of both parts of the chain has to our

Table 4.1: Results for the correlation coefficients to test ansatz eq. (4.13).

$(\langle S_1S_2\rangle - \langle S_1\rangle\langle S_2\rangle)/\langle S_1S_2\rangle = 0.054$
$(\langle S_2S_3\rangle - \langle S_2\rangle\langle S_3\rangle)/\langle S_2S_3\rangle = 0.059$
$(\langle S_3S_1\rangle - \langle S_3\rangle\langle S_1\rangle)/\langle S_3S_1\rangle = 0.017$

best knowledge not been investigated so far. We start the calculation of an explicit expression for $P_{AB}(r_{AB}^2, R_A^2, R_B^2)$ from the knowledge of the probability distribution $P_j(\mathbf{v}_j, R_G^2)$. Applying eq. (4.4) to both parts of the block copolymer, and noting that $\mathbf{r}_{AB} = \mathbf{v}_{N_A} - \mathbf{v}_{N_B}$, where both bond vectors point to the same connecting bead but from the two different centers of mass (cf. fig. 3.2), we find

$$P_{AB}(\mathbf{r}_{AB}, R_A^2, R_B^2) = \int_{-\infty}^{\infty} d\mathbf{v}_{N_A}\, d\mathbf{v}_{N_B}\, P_{N_A}(\mathbf{v}_{N_A}, R_A^2)\, P_{N_B}(\mathbf{v}_{N_B}, R_B^2)\, \delta[\mathbf{r}_{AB} - (\mathbf{v}_{N_A} - \mathbf{v}_{N_B})]\,, \quad (4.18)$$

where we used, that both parts of the chain are uncorrelated. The two integrations can be carried out leading to

$$\begin{aligned} P_{AB}(\mathbf{r}_{AB}, R_A^2, R_B^2) = \frac{1}{4\pi^2} \int_{-\infty}^{\infty} d\rho_A\, K_A(\rho_A)\, e^{-I\rho_A R_A^2} \int_{-\infty}^{\infty} d\rho_B\, K_B(\rho_B)\, e^{-I\rho_B R_B^2} \\ \times \frac{1}{(4\,\pi)^{3/2}} \frac{1}{[W_A(\rho_A) + W_B(\rho_B)]^{3/2}} \exp\left(-\frac{1}{4} \frac{r_{AB}^2}{[W_A(\rho_A) + W_B(\rho_B)]}\right)\,. \end{aligned} \quad (4.19)$$

Integrating eq. (4.19) over $\mathbf{r}_{AB}$ yields immediately $P(R_A^2, R_B^2) = P_R(R_A^2) P_R(R_B^2)$ as expected, because $K_A(\rho_A)$ and $K_B(\rho_B)$ are the characteristic functions of $P_R(R_A^2)$ and $P_R(R_B^2)$. Integration of eq. (4.19) over R_A^2 and R_B^2 leads to two δ–functions in the ρ_A and ρ_B spaces and yields, after determination of $W_A(0)$ and $W_B(0)$ (see below),

$$P_r(\mathbf{r}_{AB}, N) = \frac{1}{(2\pi)^{3/2}} \left(\frac{9}{Nb^2}\right)^{3/2} \exp\left(-\frac{9}{2} \frac{r_{AB}^2}{Nb^2}\right)\,, \quad (4.20)$$

a result in agreement with a direct calculation of the second moment of $\mathbf{r}_{AB}$. As $\mathbf{r}_{AB}$ consists of a sum of Gaussian variables, it follows that $P_r(\mathbf{r}_{AB}, N)$ is Gaussian, and therefore is determined by its second moment.

In the case considered here, the determination of $W_j(\rho)$ is simplified due to the fact, that $j = N_A, N_B >= i$ and thus $\psi_{N_A i} = i/(N_A+1)$ and $\psi_{N_B i} = i/(N_B+1)$, respectively. As the algebraic form is the same for both parts A and B of the chain, we consider only the case of A in the following. Transforming the summation over l in eq. (4.6) in the limit of large N into an integral, a straightforward calculation yields

$$W_A(\rho_A) = N_A b^2 \sum_{k=1}^{N_A} \frac{1}{3\pi^2 k^2 - 2i\rho_A N_A b^2}\,. \quad (4.21)$$

For $\rho_A = \rho_B = 0$ it follows immediately, that $W_A(0) + W_B(0) = Nb^2/18$, giving the right variance in eq. (4.20). For large N_A we find

$$W_A(\rho_A) = \frac{N_A b^2}{6} \left(\frac{1}{X_A^2} - \frac{\cos(X_A)}{X_A \sin(X_A)}\right)\,, \quad (4.22)$$

where the definition of X_A is analogous to eq. (4.5). We note in passing that this equation is not valid for X_A/π integer, especially not for $X_A = 0$. Inserting eqs. (4.5, 4.22) in eq. (4.19) yields an expression for P_{AB} in terms of a two dimensional Fourier integral. As an explicit expression for P_R could not be derived from eq. (4.8), it is unlikely that eq. (4.19) can be

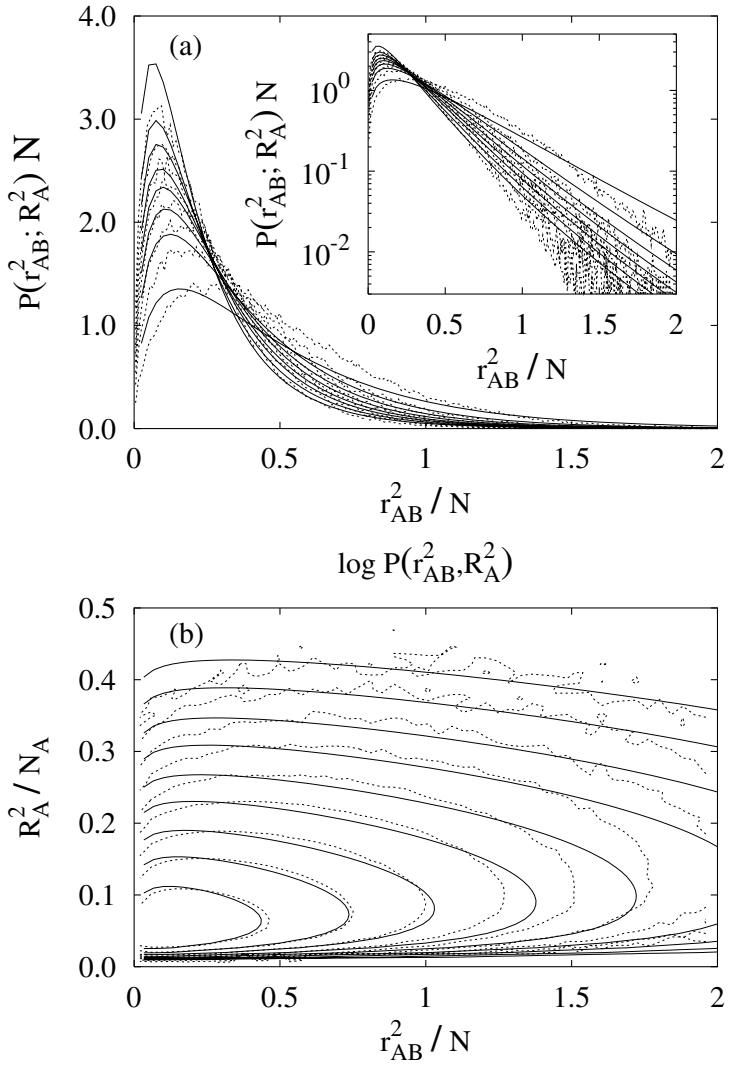

Figure 4.4: Comparison of Gaussian approximation, eq. (3.20), (straight lines) with Monte Carlo data (dotted lines) for Gaussian chains of length $N_A = N_B = 50$. (a) Conditional probability $P(r^2_{AB}; R^2_A)$ averaged over different regions in R^2_A–space. The inset shows the same data in semi–logarithmic representation. For larger R^2_A the peak in $P(r^2_{AB}; R^2_A)$ decreases and shifts to larger values of r^2_{AB}. (b) Joint probability $P(r^2_{AB}, R^2_A)$. The isolines are drawn at values of 10^n, where n is an arbitrary integer number.

transformed further to give an explicit form for $P_{AB}(\mathbf{r}_{AB}, R^2_A, R^2_B)$. Anyway, the integral is two dimensional and not three dimensional, as one would get from a straightforward calculation, starting from an equation analogous to eq. (4.3). Moreover, eq. (4.19) is a convenient starting point to calculate moments of P_{AB}. In this way correlations can be determined also, for example $\langle r^2_{AB} R^2_A \rangle = 2(\langle R^4_A \rangle + \langle R^2_A \rangle \langle R^2_B \rangle)$.

To proceed, approximations are necessary. As r^2_{AB}, R^2_A, and R^2_B are correlated, cf. eq. (4.17), and the correlation coefficients

$$\frac{\langle r_{AB}^2 R_A^2\rangle - \langle r_{AB}^2\rangle\langle R_A^2\rangle}{\langle r_{AB}^2 R_A^2\rangle} = \frac{4N_A}{19N_A + 15N_B} \overset{(N_A=N_B)}{=} \frac{2}{17} \tag{4.23}$$

are not small, a simple separation ansatz

$$P_{AB}(\mathbf{r}_{AB}, R_A^2, R_B^2) \approx P_R(R_A^2, N_A) P_R(R_B^2, N_B) P_r(\mathbf{r}_{AB}, N)\,, \tag{4.24}$$

as we used for $P(\mathbf{S})$, is not appropriate. Because we want to determine the overall behavior of P_{AB}, we will use a Gaussian approximation for the conditional probability

$$P_C(r_{AB}^2; R_A^2, R_B^2) = \frac{P_{AB}(r_{AB}^2, R_A^2, R_B^2)}{P_R(R_A^2, N_A) P_R(R_B^2, N_B)}\,. \tag{4.25}$$

From eq. (4.19) we calculate conditional moments

$$\langle r_{AB}^{2n}\rangle|_{R_A^2, R_B^2} = \int_{-\infty}^{+\infty} d\mathbf{r}_{AB}\, r_{AB}^{2n}\, P_C(r_{AB}^2; R_A^2, R_B^2)\,, \tag{4.26}$$

that still are functions of R_A^2 and R_B^2. It is possible, to determine the second moment exactly

$$\langle r_{AB}^2\rangle|_{R_A^2, R_B^2} = 2\,(R_A^2 + R_B^2) \equiv \sigma_{AB}^2(R_A^2, R_B^2)\,. \tag{4.27}$$

Using eq. (4.27), P_C is approximated by the Gaussian function, given in eq. (3.20). This form gives the correct values for the correlations $\langle r_{AB}^2 R_X^2\rangle$. As a test of the approximation, we show the distribution functions $P(r_{AB}^2; R_A^2)$ and $P(r_{AB}^2, R_A^2)$ and compare the Gaussian approximation with results of Monte Carlo simulations in fig. 4.4. To obtain the lines displayed in fig. 4.4a for $P(r_{AB}^2; R_A^2)$ we subdivided the R_A^2 axis in eight different intervals with the same statistical weight and averaged $P(r_{AB}^2; R_A^2)$ in these regions. The agreement of the Gaussian approximation, eq. (3.20) and the Monte Carlo data is satisfying. However, the exponential decrease for large r_{AB}^2 is somewhat underestimated in the approximation. The same is valid for the description of $P(r_{AB}^2, R_A^2)$, fig. 4.4b. An improved approximation of P_C similar to a cumulant expansion is given in app. B.4. However, this improvement is essentially made, in order to obtain a reference for the Gaussian approximation of P_C in simulations of the Gaussian disphere model.

4.2 Conditional Monomer Densities

The conditional monomer densities $\varrho(\mathbf{y}; \mathbf{X})$ are more complicated, than the distribution functions considered so far. The reason for this is that they are determined not by a total average of the whole ensemble of Gaussian chains, but by the average of a subensemble, determined by the condition that the set $\mathbf{X}$ is fixed. As little is known of these functions, we thus rely mainly on numerical results in their determination.

4.2.1 Spherical Density

We start the discussion not with a conditional monomer density, but with the average monomer density $\bar{\varrho}_r(\mathbf{x})$ of a Gaussian chain around its center of mass, $\mathbf{x} = \mathbf{y} - \mathbf{r}$. It can be calculated directly for large N [Yam71], although only in terms of a finite sum

$$\bar{\varrho}_r(\mathbf{x}) = \sum_{j=0}^{N} \left(\frac{3}{2\,\pi \langle \mathbf{x}_j^2 \rangle} \right)^{3/2} \exp\left(-\frac{3\,x^2}{2\langle \mathbf{x}_j^2 \rangle} \right) , \quad \text{with} \quad \langle \mathbf{x}_j^2 \rangle = b^2 \sum_{i=1}^{N} \psi_{ji}^2 , \tag{4.28}$$

and ψ_{ji} is given in eq. (4.2). As shown in [Yam71], an approximation of $\bar{\varrho}_r(\mathbf{x})$ by a Gaussian form

$$\bar{\varrho}_r(\mathbf{x}) \approx (N+1) \left(\frac{3}{2\,\pi \langle x^2 \rangle} \right)^{3/2} \exp\left(-\frac{3\,x^2}{2\langle x^2 \rangle} \right) , \tag{4.29}$$

is satisfying. We note that $\langle x^2 \rangle = \langle R_G^2 \rangle = Nb^2/6$. The essential point of this result is that on average the monomer density around the center of mass has a well defined extension and decays rapidly at distances larger $\bar{R}_G$. Moreover, the Gaussian form is useful for calculating the overlap of two densities.

The starting point for a direct calculation of the conditional spherical monomer density $\varrho_r(\mathbf{x}; R_G^2)$ is the bivariate distribution $P_j(\mathbf{v}_j, R_G^2)$ function given in eq. (4.3),

$$\varrho_r(\mathbf{x}; R_G^2) = \frac{1}{P_R(R_G^2)} \sum_{j=0}^{N} P_j(\mathbf{v}_j, R_G^2) . \tag{4.30}$$

A closed expression for $\varrho_r(\mathbf{x}; R_G^2)$ has not been obtained, but the asymptotic limit is known,

$$\varrho_r(\mathbf{x}; R_G^2) \to \frac{(N+1)}{2\,\pi^2 x^2} \frac{H(2R_G^2 - x^2)}{\sqrt{2R_G^2 - x^2}} , \text{ for } \quad R_G^2 \to \infty , \tag{4.31}$$

where $H(.)$ is the step function [Yam71].

We investigated $\varrho_r(\mathbf{x}; R_G^2)$ by means of Monte Carlo simulations. By the sampling procedure, chains are generated with a radius of gyration distributed according to $P_R(R_G^2)$, cf. eq. (4.10). To obtain the dependence of $\varrho_r(\mathbf{x}; R_G^2)$ on R_G, we averaged $\varrho_r(\mathbf{x}; R_G^2)$ over seven non–overlapping intervals in R_G^2 space and thus obtained seven different functions. The limiting positions $R_G^{(i)}$ of the intervals where chosen, such that

$$\int_0^{R_G^{(i)}} P_R(R_G^2)\, dR_G^2 = 1 - 10^{-i} , \qquad i = 1 \ldots 6 . \tag{4.32}$$

These functions have very different statistical weights. To account for the normalization

$$\int d^3x\, \varrho_r(\mathbf{x}; R_G^2) = N+1 \tag{4.33}$$

and the different extensions of the chains, we use the scaled variable $u = x/R_G$ and consider $\hat{\varrho}_r(u; R_G^2) = R_G^3 \varrho_r(R_G\, u; R_G^2)/(N+1)$. The results are given in fig. 4.5a. Also shown for comparison are the asymptotic limit of eq. (4.31) (dashed line), and a Gaussian approximation (straight line). The Monte Carlo data approaches the asymptotic limit for very large values of R_G only, which are highly improbable. Most configurations, however, are well described by the Gaussian approximation. We checked that, by choosing 20 intervals with equal statistical weight, instead of the seven intervals defined by eq. (4.32). As expected, the extension of the

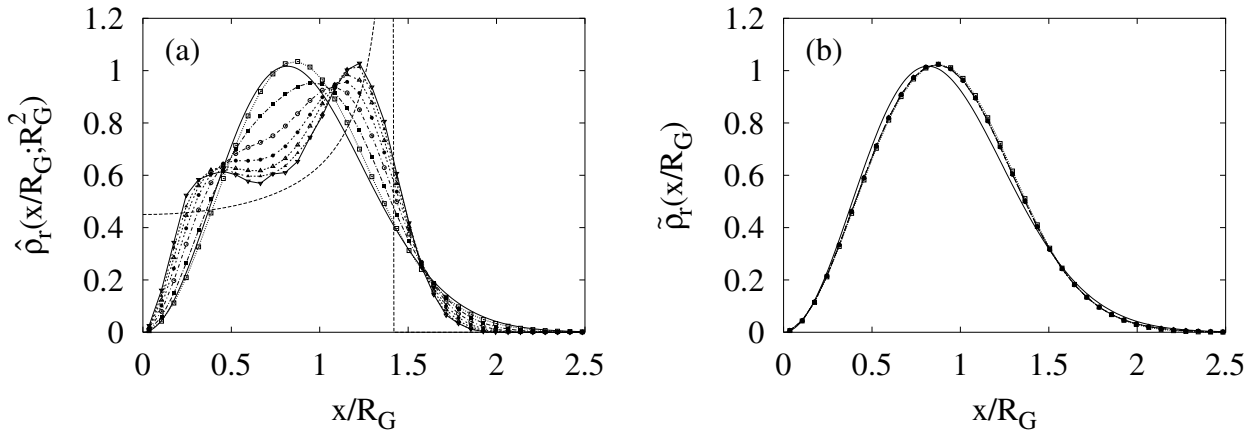

Figure 4.5: (a) Scaled and normalized conditional spherical monomer density $\hat{\varrho}_r(u;R_G)$. The asymptotic limit ($R_G^2 \to \infty$) (dashed line) and a Gaussian function (straight line) are shown for comparison. (b) Effective scaling function $\tilde{\varrho}_r(x/R_G)$ for $N = 10(\square), 30(\blacksquare), 100(\circ), 300(\bullet)$ and $1000(\triangle)$.

density is finite, and scales with R_G. However, since $\hat{\varrho}_r(u;R_G^2)$ is not a function of u only, there is no scaling of $\varrho_r(\mathbf{x};R_G^2)$ with R_G in a strict sense. To obtain a useful approximation, we write

$$\varrho(\mathbf{x};R_G^2,N) \approx \frac{N+1}{R_G^3}\,\tilde{\varrho}_r\left(\frac{x}{R_G}\right)\,, \tag{4.34}$$

where $\tilde{\varrho}_r(x/R_G) = \langle \hat{\varrho}_r(u;R_G^2)\rangle$ is an effective scaling function given in fig. 4.5b for various N. The function $\tilde{\varrho}_r(x/R_G)$ is independent on N and can be described by a Gaussian form. This yields the final result for $\varrho(\mathbf{x};R_G^2,N)$ given in eq. (3.7).

4.2.2 Ellipsoidal Density

The average monomer density in the principal axis system

$$\bar{\varrho}(\mathbf{x},N) \equiv \int d^3S\, P(\mathbf{S})\,\varrho(\mathbf{x};\mathbf{S},N) \tag{4.35}$$

has been investigated by means of Monte Carlo simulations for Gaussian chains by Janszen et al. [Jan96], and earlier for a model representing polypropylene by Theodorou and Suter [The85]. The most striking feature of these investigations is that $\bar{\varrho}(\mathbf{x},N)$ exhibits a bimodal shape with respect to the largest principal axis. However, for $\varrho(\mathbf{x};\mathbf{S},N)$ neither numerical studies nor exact analytical expression are available, not even for the asymptotic limit $\mathbf{S} \to \infty$.
Since $\varrho(\mathbf{x};\mathbf{S},N)$ is a function of many variables, various simplifications are necessary to allow for an efficient computation of the interaction terms in eq. (3.5). Murat and Kremer [Mur98] proposed a self–similar monomer distribution,

$$\varrho(\mathbf{x};\mathbf{S},N) = \frac{N+1}{\prod_\alpha R_\alpha}\,\tilde{\varrho}(\mathbf{x}/\mathbf{R})\,, \quad \text{where} \quad R_\alpha = S_\alpha^{1/2} \tag{4.36}$$

and we introduced the short–hand notation $\tilde{\varrho}(\mathbf{x}/\mathbf{R}) \equiv \tilde{\varrho}(x_1/R_1, x_2/R_2, x_3/R_3)$. In contrast to ref. [Mur98], we included the factor $[(N+1)/\prod_\alpha R_\alpha]$ in eq. (4.36) due to the normalization

$$\int d^3x\, \varrho(\mathbf{x}; \mathbf{S}, N) = N+1\,. \tag{4.37}$$

In view of the results obtained for $\varrho_r(\mathbf{x}; R_G^2, N)$ it is clear, that such an ansatz is not strictly valid. Nevertheless, it is a useful starting point for investigating the behavior of $\varrho(\mathbf{x}; \mathbf{S}, N)$.

Therefore, we consider the function $[\prod_\alpha R_\alpha]\, \varrho(\mathbf{x}; \mathbf{S}, N)/(N+1)$ in terms of the scaled variable $\mathbf{u} \equiv \mathbf{x}/\mathbf{R}$, i.e. we consider

$$\hat{\varrho}(\mathbf{u}; \mathbf{S}, N) \equiv \frac{\prod_\alpha R_\alpha}{N+1}\, \varrho(R_1 u_1, R_2 u_2, R_3 u_3; \mathbf{S}, N)\,. \tag{4.38}$$

If the scaling (4.36) would hold true, this function would equal $\tilde{\rho}(\mathbf{u})$, and hence any averaging over regions in $\mathbf{S}$–space would leave it invariant. In particular we define the scaled monomer density with respect to one principal axis α under the condition that one arbitrary eigenvalue corresponding to the axis β is given,

$$\hat{\varrho}_{\alpha\beta}(u_\alpha; S_\beta, N) \equiv \int_{-\infty}^{\infty} \prod_{\mu\neq\alpha} du_\mu \int_0^\infty \prod_{\nu\neq\beta} dS_\nu\, P(\mathbf{S}, N)\, \hat{\varrho}(\mathbf{u}; \mathbf{S}, N)\,. \tag{4.39}$$

These are nine different functions, and the Monte Carlo results for some of them are shown in fig. 4.6 for $N = 1000$. For other chain lengths ($N \gtrsim 30$) we find almost exactly the same functions, confirming the scaling with N. In order to obtain the functions displayed in the figure, we divided the S_α–axis into eight different intervals, delimited at positions $S_\beta^{(1)} \ldots S_\beta^{(9)}$, $S_\beta^{(1)} = 0$, $S_\beta^{(9)} = \infty$, each of them having the same statistical weight 1/8, i.e.

$$\int_{S_\beta^{(i)}}^{S_\beta^{(i+1)}} dS_\beta\; P_\beta(S_\beta) = \frac{1}{8}\,, \quad i = 1 \ldots 8\,, \tag{4.40}$$

and averaged $\hat{\varrho}_{\alpha\beta}(u_\alpha; S_\beta)$ in each of these intervals.

Figure 4.6a shows the eight resulting functions for $\hat{\varrho}_{11}(u_1; S_1, N)$. By contrast to the self–similarity assumption, the curves differ significantly from each other. They exhibit an unimodal shape for the smallest S_1 only, while for the most likely S_1, $\hat{\varrho}_{11}(u_1; S_1, N)$ has a bimodal shape, as one would expect from the results for $\bar{\varrho}(\mathbf{x}, N)$. This bimodal shape becomes more pronounced for larger S_1. For $\hat{\varrho}_{22}(u_2; S_2)$, shown in fig. 4.6b, the deviations from scaling are smaller and are appreciable only for the largest S_2, while for $\hat{\varrho}_{33}(u_3; S_3)$ in fig. 4.6c the deviations are insignificant. We also examined the six other functions and found that the deviations from scaling are small in all these cases.

In fact, knowing that the shape of $\bar{\varrho}(\mathbf{x}, N)$ in the x_1–direction is of bimodal type, while in the x_2–direction it is of unimodal type [Jan96], the breakdown of the self–similarity concept is not that unexpected. If scaling would hold true, the monomer densities with respect to some fixed $\mathbf{S}$ should correspond to the average monomer density $\bar{\varrho}(\mathbf{x}, N)$. However, if one considers the case of almost equal values of S_1 and S_2, i.e. $S_1 \gtrapprox S_2$, the monomer densities along the x_1– and x_2–direction should be the same due to symmetry in contrast to the scaling prediction.

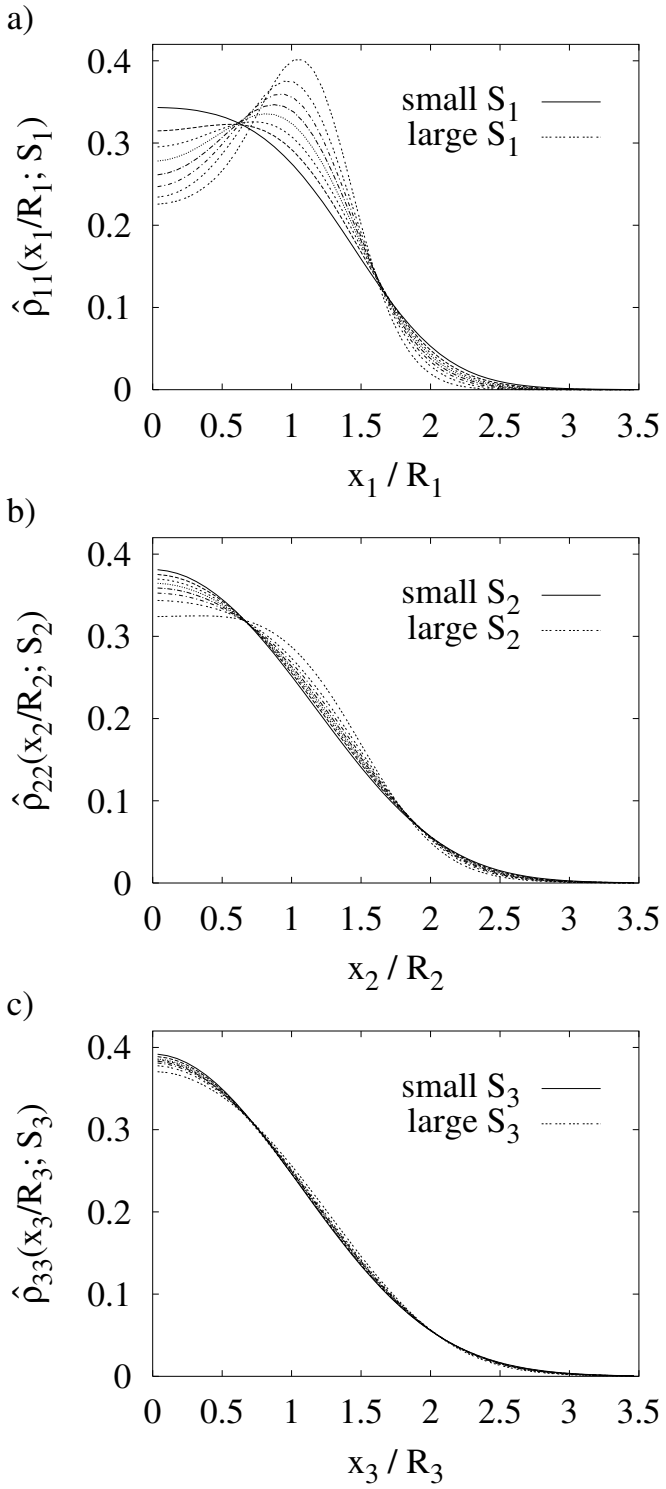

Figure 4.6: One dimensional conditional monomer densities $\hat{\varrho}_{\alpha\beta}(x_\alpha/R_\alpha; S_\beta)$ as functions of the scaled variables $u_\alpha = x_\alpha/R_\alpha$, to demonstrate the breakdown of condition (4.36) in a strict sense. The curves were sampled for chain lengths $N = 1000$.

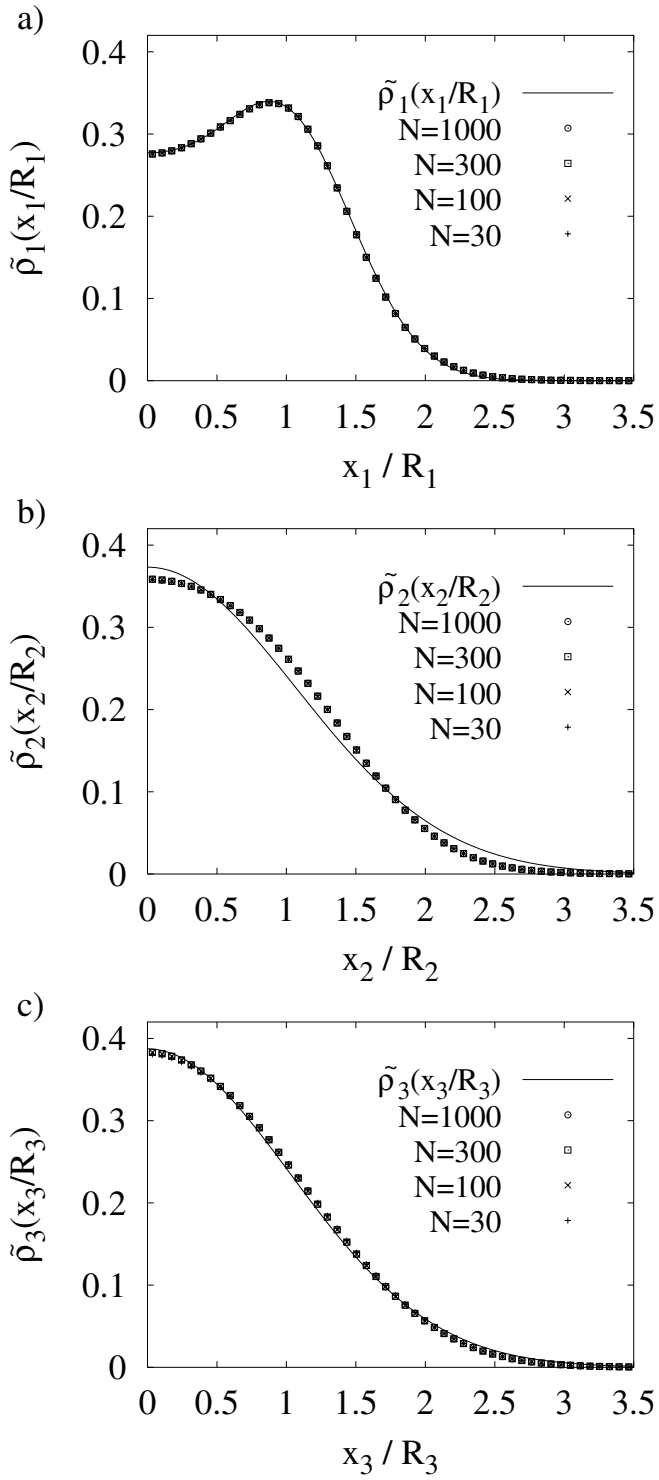

Figure 4.7: Effective scaling functions $\tilde{\varrho}_\alpha$ as defined in eq. (4.41) for different values of N. The solid lines denote the approximate forms given in eq. (3.17a-c).

Although the self–similarity assumption is not truely valid, it can be used as a good working tool for the following reasons. The monomer densities enter the calculation of F_{inter} via integrals, cf. eq. (3.5). For these integrals to be correctly calculated, it is important that the size of the region, where $\varrho(\mathbf{x}, \mathbf{S}, N)$ is non–neglible, scales properly. From fig. 4.6 one can see that this is indeed the case. Therefore, for our purposes it is sufficient to approximate the various functions shown in fig. 4.6a-c for different S_β by their average

$$\tilde{\varrho}_\alpha(u_\alpha) = \int_0^\infty dS_\beta \, P_\beta(S_\beta) \, \hat{\varrho}_{\alpha\beta}(u_\alpha; S_\beta, N) \, . \tag{4.41}$$

We marked these averaged monomer densities by a tilde, since one can view them as "effective scaling functions" representing $\tilde{\varrho}(\mathbf{u})$ from eq. (4.36) (after integrating out the two u_μ–coordinates orthogonal to u_α). Note that we suppressed the N–argument in the definition (4.41), since, as already mentioned, the dependence on N predicted by eq. (4.36) is valid. This validity can also be inferred directly from fig. 4.7, where the data for $N = 30, 100, 300,$ and 1000 can not be distinguished.

The scaled monomer densities $\tilde{\varrho}_\alpha(u_\alpha)$ with $u_\alpha = x_\alpha / R_\alpha$ shown in fig. 4.7 can be conveniently approximated by a superposition of Gaussians, given in eqs. (3.17a-c). The parameters σ_α, c_1, and $\bar{u}_1$ were determined by least squares fits and are given in tab. 3.2. While $\tilde{\varrho}_1(u_1)$ and $\tilde{\varrho}_3(u_3)$ are quite well approximated by eqs. (3.17a) and (3.17c), respectively, eq. (3.17b) does not provide such a good description. A better expression for $\tilde{\varrho}_2(u_2)$ can be achieved by adding shifted Gaussian functions as in eq. (3.17a), and is given explicitly in appendix B.3. However, we decided to deal with eq. (3.17b), because the better description increases the computation time of F_{inter} by a factor of four, but does not much improve the overall accuracy of $\varrho(\mathbf{x}; \mathbf{S})$. We note that the functions $\tilde{\varrho}_\alpha(u_\alpha)$ in eqs. (3.17a-c) should not be confused with the function $\bar{\rho}(\mathbf{x}, N)$ (or its "components" after integrating out two coordinates) that has been considered earlier by Janszen et al. [Jan96].

In order to specify the multivariate scaled density we employ, as for $P(\mathbf{S})$ before, a separation ansatz. This yields for $\varrho(\mathbf{x}; \mathbf{S}, N)$ from eq. (4.36) the final result

$$\varrho(\mathbf{x}; \mathbf{S}, N) = (N+1) \prod_\alpha \frac{\tilde{\varrho}_\alpha(x_\alpha / R_\alpha)}{R_\alpha} \, , \tag{4.42}$$

where $\tilde{\varrho}_\alpha(x_\alpha / R_\alpha)$ are taken from eqs. (3.17a-c). The separation ansatz may be used also without invoking the self–similarity assumption (4.36) in order to reduce the complexity of the multivariate density $\varrho(\mathbf{x}; \mathbf{S}, N)$.

To test the validity of the separation ansatz we define for each Gaussian chain by

$$v_\alpha = \frac{1}{N+1} \sum_{k=0}^{N} \frac{|x_\alpha^{(k)}|}{R_\alpha} \tag{4.43}$$

the (scaled) mean moduli of the monomer coordinates in the principal axis system, and check whether the correlation coefficients

$$\gamma_{\alpha\beta}^{(v)} \equiv \frac{\langle v_\alpha v_\beta \rangle - \langle v_\alpha \rangle \langle v_\beta \rangle}{\langle v_\alpha v_\beta \rangle} \, , \quad \alpha \neq \beta \, , \tag{4.44}$$

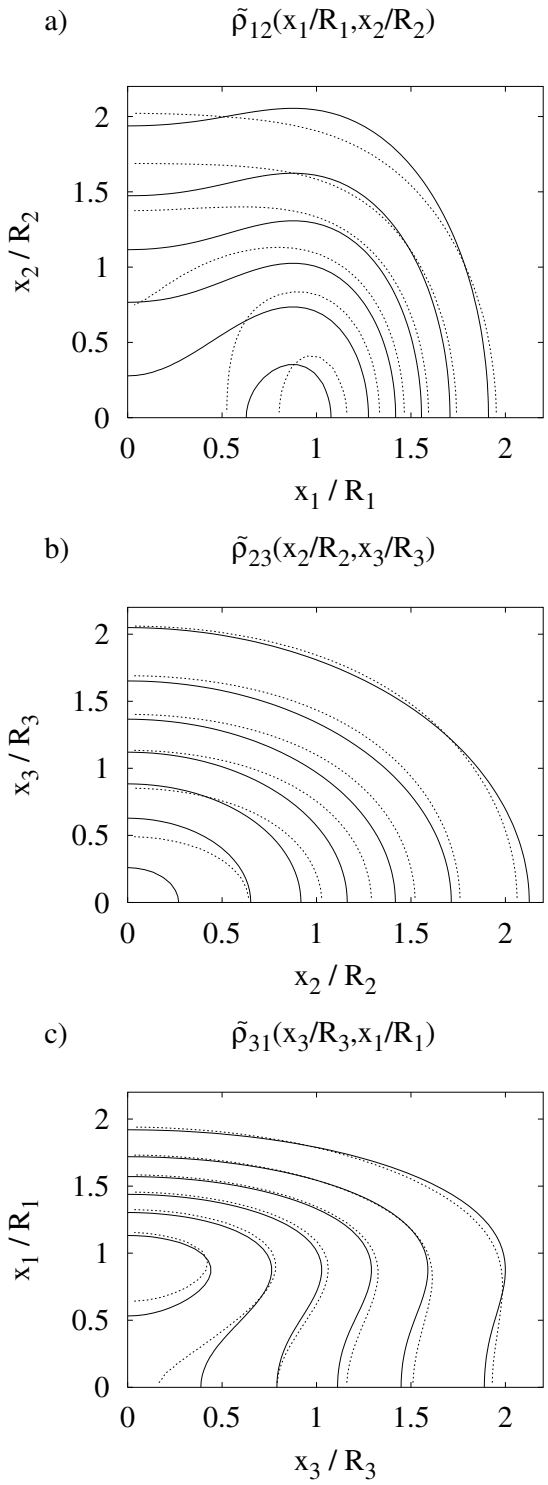

Figure 4.8: Contour plots showing the comparison of $\tilde{\varrho}_\alpha(x_\alpha/R_\alpha)\tilde{\varrho}_\beta(x_\beta/R_\beta)$ (straight lines) with numerical data of $\tilde{\varrho}_{\alpha\beta}(x_\alpha/R_\alpha, x_\beta/R_\beta)$ (dashed lines). The isolines are drawn at function values, which are integer multiples of 0.02.

are much smaller than one. Note that, because of the symmetry $\tilde{\varrho}_\alpha(u_\alpha) = \tilde{\varrho}_\alpha(-u_\alpha)$, we considered the moments of the moduli in eq. (4.44). As shown in tab. 4.2, we find $|\gamma^{(v)}_{\alpha\beta}|$ to be less than 5% in the simulations. Also, when comparing the two–variate densities

$$\tilde{\varrho}_{\alpha\beta}(u_\alpha, u_\beta) = \int_{-\infty}^{\infty} du_\gamma \, \tilde{\varrho}(\mathbf{u}) \, , \quad \gamma \neq \alpha, \beta \tag{4.45}$$

with the two–fold products $\tilde{\varrho}_\alpha(u_\alpha)\tilde{\varrho}_\beta(u_\beta)$ in fig. 4.8 a satisfactory agreement is obtained.

As an ultimate test of the separation ansatz we sampled the full three–variate scaled monomer density $\tilde{\varrho}(\mathbf{u})$ in the simulations. To this end, we subdivided the $\mathbf{u} = \mathbf{x}/\mathbf{R}$ space into small boxes of length $\Delta u_\alpha = 0.07$ and determined the mean number of monomers in each box by averaging over Gaussian chains irrespective of their $\mathbf{S}$. Then we calculated the relative error between the separation ansatz $\prod_\alpha \tilde{\varrho}_\alpha(u_\alpha)$ with $\tilde{\varrho}_\alpha(u_\alpha)$ from eqs. (3.17a-c) and the simulated $\tilde{\varrho}(\mathbf{u})$ as a function of $\tilde{\varrho}(\mathbf{u})$ (for all $\mathbf{u}$). We found that the relative error is confined to a narrow band of maximal 25% discrepancy except for very small $\tilde{\varrho}(\mathbf{u})$. These small $\tilde{\varrho}(\mathbf{u})$, however, are not important in the calculation of the overlap integrals in eq. (3.5).

The monomer density $\varrho(\mathbf{x}; \mathbf{S}, N)$ specified in eq. (3.16) allows us to calculate the overlap integrals and thus to determine F_{inter} from eq. (3.5) analytically, as explained in appendix C.1.

4.2.3 Cylindrical Densities

Determining the monomer density with respect to the center of mass only, yields a spherical shape. In the principal axis system a bimodal, dumbbell like shape was found. Now, defining one axis $\mathbf{r}_{AB}$ between the two centers of mass corresponding to the two blocks of the chain and regarding the monomer density with respect to this axis, we have cylindrical symmetry.

Since we are interested in determining $\varrho_X(\mathbf{x}; \mathbf{r}_{AB}, R_A^2, R_B^2)$, describing one block of the chain, we will investigate the form of the monomer density of one block parallel and perpendicular to $\mathbf{r}_{AB}$. We will restrict the discussion to the case of equally sized blocks ($N_A = N_B$).

At first glance one might think that the monomer distribution of one part of the chain is independent of the state of the other part, because all links are uncorrelated. Therefore it should be spherically symmetric with respect to its own center of mass. However, as the chain parts are connected at the ends, there is a correlation between the position of the last bead of part A and the center of mass of the other part $\mathbf{r}_B$. Thus strictly speaking

$$\varrho_X(\mathbf{x}; \mathbf{r}_{AB}, R_A^2, R_B^2) \neq \varrho_r(\mathbf{x}; R_X^2) \, , \tag{4.46}$$

where $\varrho_r(\mathbf{x}; R_X^2)$ is defined in eq. (4.30). This can be seen in fig. 4.9, where projections of the scaled conditional monomer density $\varrho_A(\mathbf{x}; \mathbf{r}_{AB}, R_A^2, R_B^2)$ are shown. The origin is defined

Table 4.2: Test of the ansatz eq. (3.16) with correlation coefficients defined in eq. (4.44).

$(\langle v_1 v_2 \rangle - \langle v_1 \rangle \langle v_2 \rangle) / \langle v_1 v_2 \rangle$	-0.048
$(\langle v_2 v_3 \rangle - \langle v_2 \rangle \langle v_3 \rangle) / \langle v_2 v_3 \rangle$	-0.027
$(\langle v_3 v_1 \rangle - \langle v_3 \rangle \langle v_1 \rangle) / \langle v_3 v_1 \rangle$	-0.018

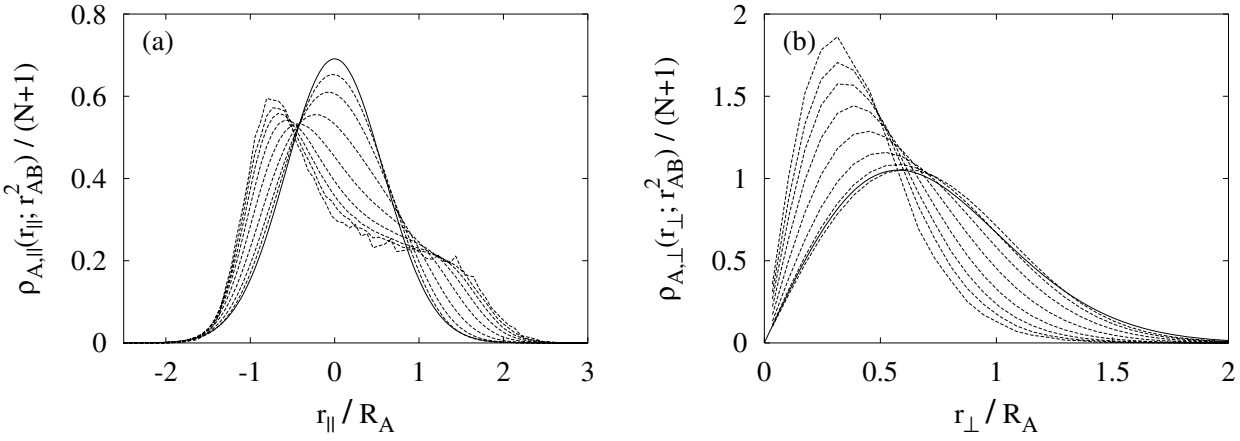

Figure 4.9: Projections of the conditional monomer density $\varrho_A(\mathbf{x}; \mathbf{r}_{AB})$ of one block (a) parallel and (b) perpendicular to $\mathbf{r}_{AB}$. The respective Gaussian functions, eq. (3.7), are draw for comparison (straight lines). The chain lengths are $N_A = N_B = 50$.

by the center of mass of block A, the parallel direction by $\mathbf{r}_{AB}$ and the center of block B is located in positive $r_\parallel$ direction. The data has been scaled with respect to R_A, cf. sec. 4.2.1, and averaged with respect to R_B. To obtain the dependency on r_{AB}^2, shown by different lines, a procedure analogous to the determination of the data for $\rho_r(\mathbf{x}; R_G^2)$ in sec. 4.2.1 has been carried out. However, here $P_r(r_{AB}^2)$ has to be replaced with $P_R(R_G^2)$ in eq. (4.32). Again the different graphs have very different statistical weights.

While most configurations are described well by the Gaussian approximation, eq. (3.7), there are deviations for very large values of r_{AB}^2. On one hand with increasing r_{AB}^2 the maximum of $\varrho_{A,\parallel}(\mathbf{x}; \mathbf{r}_{AB})$ shifts to smaller values of $r_\parallel$ and a shoulder of the density emerges in opposite direction, fig. 4.9a. On the other hand, the extension of the density in direction perpendicular to $\mathbf{r}_{AB}$ shrinks, fig. 4.9b. Therefore the block density is elongated with respect to $\mathbf{r}_{AB}$ and shortened in perpendicular direction. However, the overall scale is not drastically altered. The extension is still of order R_A, only the positions, where the densities go to zero, are changed by a factor of at most two for the values observed. Therefore the Gaussian approximation, eq. (3.7), is a reasonable starting point for the disphere model.

4.3 Origin of the Bimodal Form

In this section we briefly address the origin of the bimodal shape of the monomer density with respect to the largest principal axis. As the bimodal shape occurs also in the average density $\bar{\varrho}$, we will discuss this simpler case.

Janszen et al. have analyzed the shape of a random walk in the principal axis system [Jan96]. Further on, they separated the chain into two equal blocks, defining the first block A and the second block B by the positions of their centers of mass $\mathbf{r}_A$ and $\mathbf{r}_B$, and recorded the average monomer density of block A in the principal axis system of the whole chain, finding an egg–like shape. They pointed out, that this shape is observed only in the principal axis system of the total chain, while in the principal axis system of block A the bimodal form would emerge

again. They claimed, that the natural segregation of the chain into two parts (in which case a definition of a first and second block is unambiguously possible) is responsible for the bimodal shape. We will refine this statement in the following.

Therefore we consider a Gaussian chain not with respect to its principal axis system, but with respect to the axis $\mathbf{r}_{AB} = \mathbf{r}_B - \mathbf{r}_A$. There is a strong correlation between $\mathbf{r}_{AB}$ and the first principal axis. This can be seen directly by determining the distribution of the projection between the two normalized vectors either numerically or from the following simple argument: When considering the chain as a disphere, consisting of two equal parts with average radii of gyration $\langle R_A^2\rangle = \langle R_G\rangle/2$, we can calculate an average squared radius of gyration $\langle S_\parallel\rangle$ parallel to $\mathbf{r}_{AB}$ from the theorem of Steiner $\langle S_\parallel\rangle = \langle R_A^2\rangle/3 + \langle r_{AB}^2\rangle/4 = 2\langle R_G^2\rangle/3$. An analogous result for a perpendicular direction yields $\langle S_\perp\rangle = \langle R_A^2\rangle/3 = \langle R_G^2\rangle/6$. As $\langle S_\perp\rangle = \langle S_\parallel\rangle/4$, the average extension of the random walk in direction perpendicular to $\mathbf{r}_{AB}$ is only half its extension in parallel direction, a very direct argument why typically the random walk is not spherical. The inertia moment Θ of a rigid body with respect to an arbitrary axis in space, characterized by its normalized projections on the principal axis system (r_1, r_2, r_3), is given by an equation describing an ellipsoid,

$$\Theta = \Theta_1 r_1^2 + \Theta_2 r_2^2 + \Theta_3 r_3^3 \,. \tag{4.47}$$

The eigenvalues of the inertia tensor are denoted by Θ_α. Dividing eq. (4.47) by the mass $N\,m$, taking the average and neglecting correlations, we find

$$\langle S_\parallel\rangle \approx \langle S_1\rangle\langle r_{1,\parallel}^2\rangle + \langle S_2\rangle\langle r_{2,\parallel}^2\rangle + \langle S_3\rangle\langle r_{3,\parallel}^3\rangle \,. \tag{4.48}$$

Knowing $\langle S_\parallel\rangle$ and $\langle S_\alpha\rangle$ in terms of $\langle R_G^2\rangle$, cf. tab. B.1, we can estimate the typical squared projection of $\mathbf{r}_{AB}$ on the first principal axis. Noting $\langle r_{3,\parallel}^2\rangle = 1 - \langle r_{1,\parallel}^2\rangle - \langle r_{2,\parallel}^2\rangle$ and $\langle r_{2,\parallel}^2\rangle \in [0, 1-\langle r_{1,\parallel}^2\rangle]$, we find $\langle r_{1,\parallel}^2\rangle \in [0.83, 0.86] \gg 1/3$, where the last value is the reference for random orientation. The numeric value $\langle r_{1,\parallel}^2\rangle = 0.85$ confirms the estimate. Therefore $\mathbf{r}_{AB}$ is almost parallel to the first principal axis and we can discuss the bimodal shape with respect to $\mathbf{r}_{AB}$.[1] Because the typical extension of a block is given by $\langle R_A^2\rangle = N/12$ and the typical distance between the two centers of mass is $\langle r_{AB}^2\rangle = N/3$ the criterion for the occurrence of a bimodal form $\sqrt{\langle r_{AB}^2\rangle/2\langle R_A^2\rangle} = \sqrt{2} \gtrsim 1$ is fulfilled.

By dividing the chain not into two but into four equal parts and assigning the whole mass of the four blocks to the respective centers of mass, not only one axis $\mathbf{r}_{AB}$, but a coordinate system is defined. This is the principal axis system of the foursphere model. Numerically we find, that the principal axis system of the foursphere model almost coincides with the exact principal axis system of the chain. Therefore a description of a Gaussian chain in terms of an ellipsoidal model and in terms of a foursphere model should be very similar.

Finally, it is interesting, to compare figs. 4.9a and 4.6a, having the strong correlation between the two axes $\mathbf{r}_{AB}$ and the first principal axis in mind. The more pronounced bimodality, found in the principal axis system for large values S_1, is reflected in the monomer density parallel to $\mathbf{r}_{AB}$ for large r_{AB}^2. The respective configurations on average consist of two balls at each end with higher monomer density that are connected by a rod like region with smaller monomer density, where principally the bonds are oriented in one direction. The whole shape

[1] Numerical investigations confirm that the bimodal shape is observed with respect to $\mathbf{r}_{AB}$.

is therefore dumbbell like and with increasing S_1, or r_{AB}^2 respectively, the dumbbell stretches, i.e. the rod elongates and the balls shrink.

This behavior is also reflected in the results for $\varrho_r(\mathbf{x}; R_G^2)$ for large R_G, cf. fig. 4.5. In this limit the value of R_G^2 is dominated by S_1 even more than on average, cf. fig. 4.3, i.e. $R_G^2 \simeq S_1$. The maximum of the monomer density shifts to higher values of r/R_G for large R_G. From the spherically symmetric point of view, this behavior is difficult to explain, because this shape resembles some kind of hollow sphere. But from the considerations above, this shift can be interpreted by the elongation of the dumbbell, because the two balls of the dumbell are responsible for the maximum in $\varrho_r(\mathbf{x}; R_G^2)$ in the limit of high R_G.

4.4 Summary

To summarize this section, we determined the input quantities for the different models, defined in chapter 3, and expressed them in approximate, but closed form. All approximations have been tested extensively against numerical results. Despite approximate, the input quantities capture the essential features found for Gaussian chains: The normal random walk scaling with N, the strong asphericity of the chains in the respective coordinate systems, the bimodal form of the monomer density and its rapid decay beyond cutoff lengths that scale linearly with R_α. Finally, the origin of the bimodal form could be explained by simple considerations of the disphere model.

5 GEM: Bulk Systems

To give a reasonable description of polymer systems, the models defined in chapter 3 should exhibit several essential features. First of all, they should show the right scaling behavior of various properties with chain length N in dense systems [Mur98]. Secondly, characteristic features of polymer physics on the scale of R_G, such as the correlation hole [Gen79] should be found. Finally, the kinematic description for times larger τ_d (but small against the hydrodynamic regime) ought to be correct.

In this chapter we will investigate properties of the Gaussian Ellipsoid Model (GEM) in homogeneous and inhomogeneous bulk systems, and show that the GEM provides a suitable description of polymer systems on the time and length scales intended.

5.1 Homogeneous Melt

To show that the GEM reproduces the most important semi–macroscopic properties of dilute and dense polymeric systems, we investigate the following quantities: The scaling properties of the radius of gyration $\bar{R}_G$ upon N and c, the scaling behavior of the distribution $P_R(R_G^2, N)$ in a dense homogenous system of interacting ellipsoids, and the existence and scaling of the correlation hole. Concerning the kinetic properties, we show that the ellipsoids show normal diffusion for times $t > \tau_d$ and that other occurring correlation times are of order or smaller than τ_d.

All simulation results in this section are for systems with at least $M = 1000$ ellipsoids. The considered chain lengths are in the range $N = 30, \ldots, 400$, therefore the systems correspond to polymer systems consisting of order 10^5 monomers. Equilibrium averages were taken over several thousand Monte Carlo Steps (MCS).

5.1.1 Static Properties

As discussed in sec. 3.2, the free energy as given in eqs. (3.1–3.3, 3.5) is a Flory–like description of polymers. Accordingly, the gyration radius of a free ellipsoid, that only interacts with itself but not with other ellipsoids, scales as $R_G^2 \sim N^{6/5}$ [Gen79], see fig. 5.1a.

In order to obtain the dependence on ϵ also, we redo some Flory type calculation, where for simplicity we consider soft spheres instead of soft ellipsoids. Therefore, the intra–molecular free energy is based on $P_R(R_G^2)$ in eq. (3.6) instead of $P(\mathbf{S})$, and the monomer density is given by eq. (3.7) and the corresponding self–interaction term by eq. (3.8) instead of the expressions for the GEM, but this will only change prefactors and not the scaling behavior itself. Putting everything together, we obtain for the free energy of a single self–interacting soft sphere

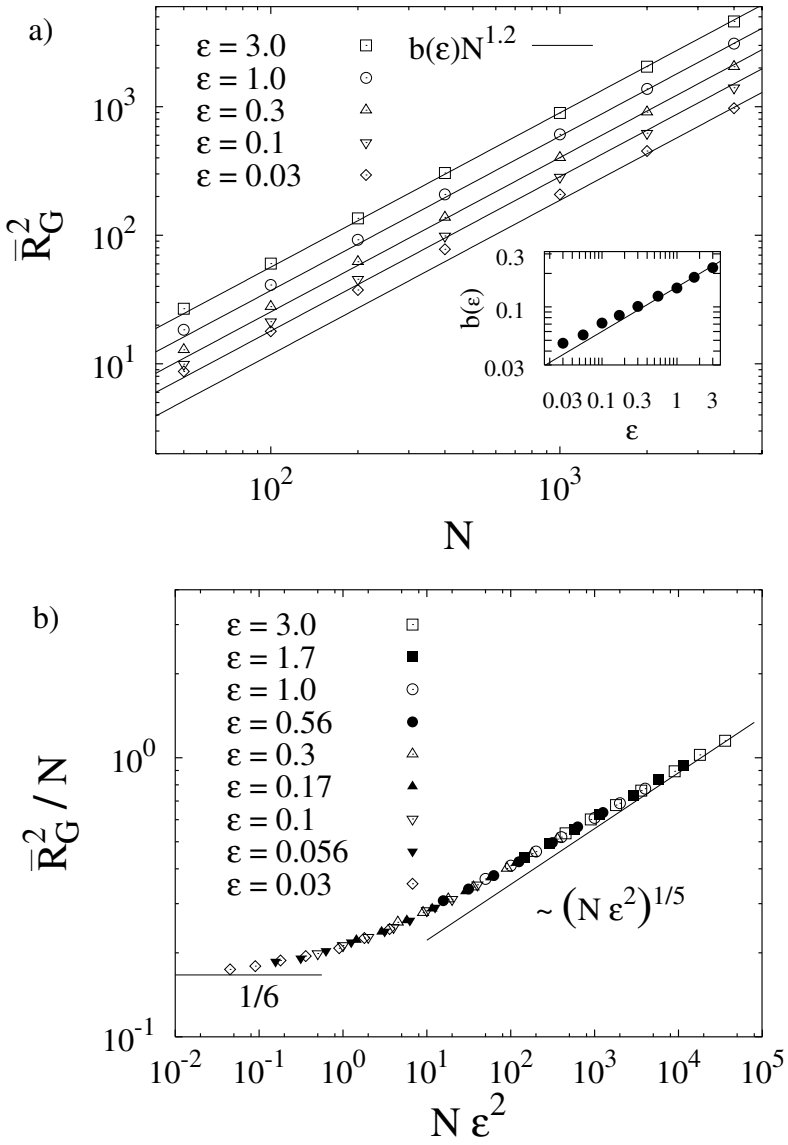

Figure 5.1: a) Mean squared gyration radius of free ($c \to 0$), but self–interacting ellipsoids as a function of N, displayed for various values of the interaction strength ϵ. The Flory result $\bar{R}_G^2 \propto N^{6/5}$ is shown for comparison. The inset shows the dependence on ϵ. The line indicates a power law $b(\epsilon) \propto \epsilon^{2/5}$. b) Scaling plot showing the crossover from Gauss to Flory type behavior.

$$\frac{F_{\text{sphere}}^{(ii)}(R_G^2)}{k_B T} = \text{const.} - \ln\left(\frac{N}{R_G^2}\right) + \frac{R_G^2}{a_R N} + d_R^2 \frac{a_R N}{R_G^2} + \epsilon \frac{(N+1)^2}{32}\left(\frac{3}{\pi R_G^2}\right)^{3/2} . \tag{5.1}$$

The most probable value $R_{G,0}^2$ results from minimizing with respect to R_G^2,

$$\frac{1}{R_{G,0}^2} + \frac{1}{a_R N} - d_R^2 \frac{a_R N}{R_{G,0}^4} - \epsilon \frac{3(N+1)^2}{64\, R_{G,0}^5}\left(\frac{3}{\pi}\right)^{3/2} = 0 . \tag{5.2}$$

This equation has the asymptotic solution

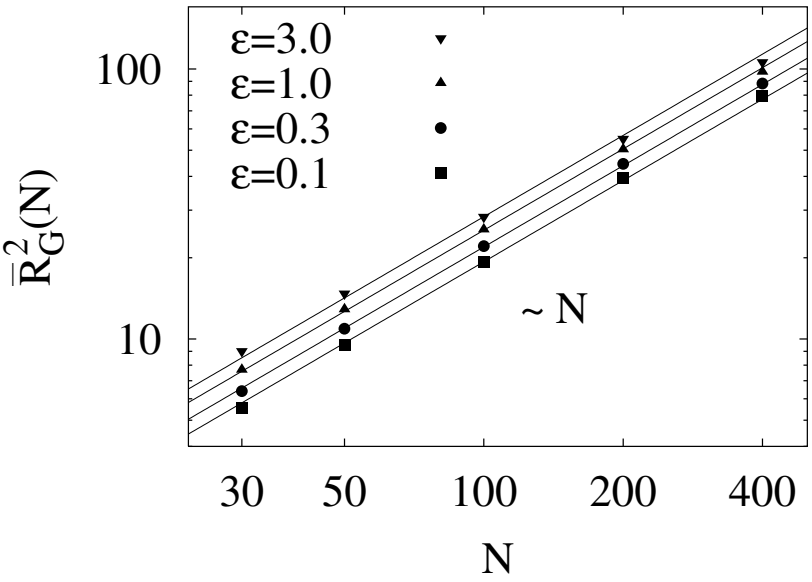

Figure 5.2: Squared gyration radius $\bar{R}_G^2$ as a function of N in a dense ($c = 0.85$) system of $M = 1000 \to 4000$ ellipsoids for various values of ϵ (double–logarithmic representation). In all cases a linear behavior is observed.

$$R_{G,0}^2 \sim \left(\frac{3}{\pi}\right)^{3/5} \left(\frac{3}{64}\,\epsilon\right)^{2/5} N^{6/5}\,. \tag{5.3}$$

Since $\bar{R}_G^2 \sim R_{G,0}^2$, we expect $\bar{R}_G^2 \sim \epsilon^{2/5}$ in reasonable agreement with the numerical results for free, self–interacting ellipsoids, see fig. 5.1a.

For small ϵ, one should recover the Gaussian behavior, i.e. we expect $\bar{R}_G^2 \sim N$ for $\epsilon \ll \epsilon_\star(N)$. On the other hand, the scaling (5.3) must hold true for $\epsilon \gg \epsilon_\star(N)$. Thus, from continuity, we find $\epsilon_\star(N) \sim N^{-1/2}$. The corresponding scaling form $\bar{R}_G^2(N,\epsilon) = N f(\epsilon^2 N)$ with $f(u) \sim \text{const.}$ for $u \to 0$ and $f(u) \sim u^{1/5}$ for $u \to \infty$ is verified in fig. 5.1b.

We now consider systems composed of many interacting ellipsoids. As discussed in sec. 1.1.3, the Flory type scaling (5.3) changes to a normal random walk scaling if the monomer concentration c exceeds the overlap concentration $c_\star$. That this is indeed the case is shown in fig. 5.2. Approaching $c_\star$ from below we can write $(c_\star/N)^{-1/3} \sim \bar{R}_G(N,\epsilon) \sim \epsilon^{1/5} N^{3/5}$ (for $\epsilon \gg N^{-1/2}$), i.e. $c_\star \sim \epsilon^{-3/5} N^{-4/5}$. Therefore we expect more generally the scaling form [Gen79]

$$\bar{R}_G^2(N,\epsilon,c) = \epsilon^{2/5} N^{6/5} f(c\,\epsilon^{3/5} N^{4/5}) \tag{5.4}$$

with $f(u) \to \text{const.}$ for $u \ll 1$ and $f(u) \to u^{-1/4}$ for $u \gg 1$, to describe the crossover from dilute to dense systems. Accordingly, we have $\bar{R}_G^2 \sim \epsilon^{1/4} c^{-1/4} N$ for $c\,\epsilon^{3/5} N^{4/5} \gg 1$. To demonstrate the validity of the overall scaling predicted by eq. (5.4), we show in fig. 5.3 as an example $\bar{R}_G^2/N^{6/5}$ as a function of $cN^{4/5}$ for a fixed value $\epsilon = 1.0$. As can be seen from the figure, the data for different c and N all collapse onto a common master curve. We note that the scaling (5.4) is followed only for $\epsilon \gg N^{-1/2}$. For $\epsilon \ll N^{-1/2}$ by contrast, the ellipsoids would always exhibit Gauss type behavior.

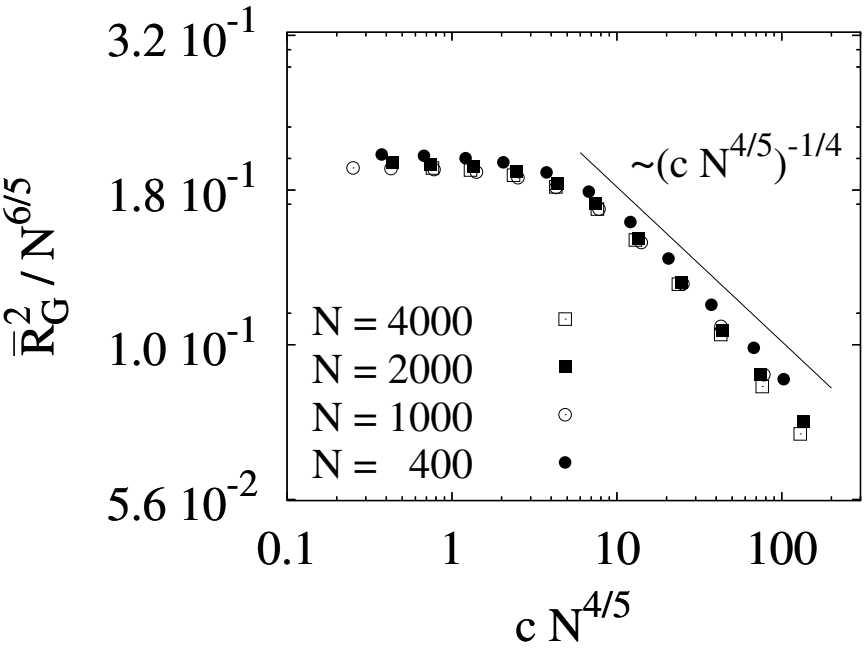

Figure 5.3: Test of the scaling relation (5.4) for fixed $\epsilon = 1.0$ (double–logarithmic representation). For small concentrations, the chains are almost free and $\bar{R}_G^2$ saturates, corresponding to Flory–type behavior. In the region of high concentration the expected scaling relation is almost fulfilled.

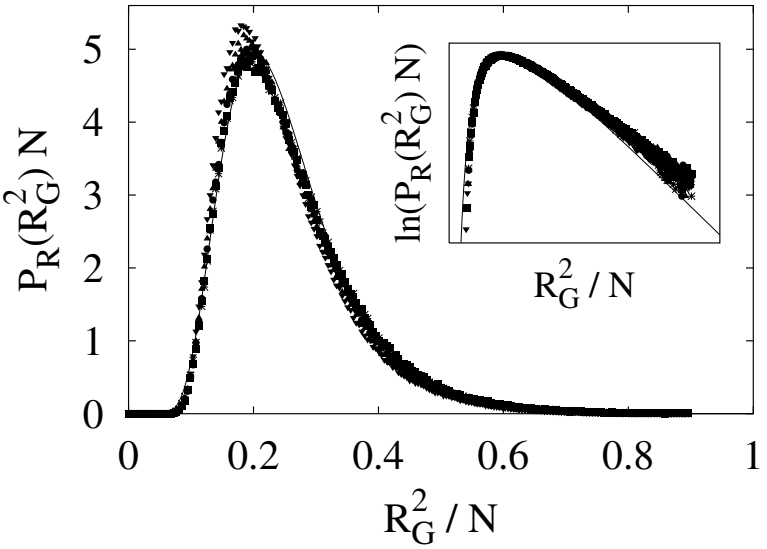

Figure 5.4: Scaling behavior of the distribution function $P_R(R_G^2)$ in a melt system for fixed $c = 0.85$, $\epsilon = 1.0$, and various $N = 30$ ($*$), 50 (■), 100 (•), 200 (▲), and 400 (▼). The solid line refers to the function defined in eq. (4.10) with parameters $a_R = 0.0665$ and $d_R = 3.52$. The inset shows the same data in semi–logarithmic representation.

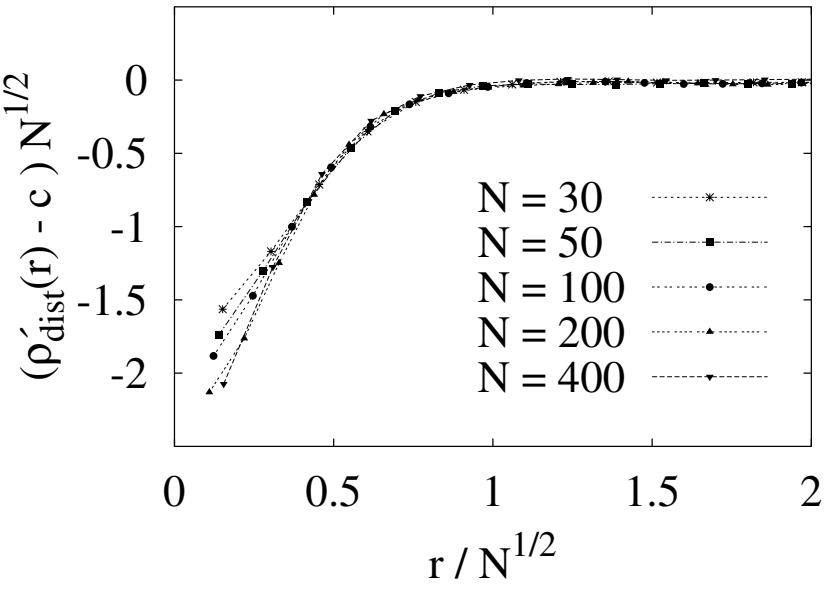

Figure 5.5: Scaling plot of the correlation hole for fixed $c = 0.85$ and $\epsilon = 1.0$ and various N.

We further show in fig. 5.4 that the distribution function $P_R(R_G^2, N)$ for dense systems ($c \gg c_\star$) obeys the same type of scaling as for non–interacting Gaussian chains, eq. (4.9), $P_R(R_G^2, N) \sim N^{-1}\tilde{P}_R(R_G^2/N)$. In particular, the ansatz (4.10) can be used equally well for $\tilde{P}_R(u)$ up to a change of the parameters a_R, and d_R (see tab. 3.1 and the values given in the caption of fig. 5.4).

It is worth noting that the correct scaling (5.4) in this case does not arise from the blob picture, as described in sec. 1.1.3, because the blob size ξ_m is smaller than S_3 and does not occur in the ellipsoid model. Rather the behavior arises from continuity between both regimes.

To complete our study of the static properties of dense homogeneous systems, we discuss the properties of the so–called correlation hole [Gen79]. Therefore we determine the mean monomer density of all ellipsoids except the ith one as a function of the distance from the center of mass of ellipsoid i,

$$\varrho'_{\text{dist}}(r, N) = \left\langle \sum_{j \neq i} \varrho'_j(\mathbf{y} - \mathbf{r}_i, N) \right\rangle . \tag{5.5}$$

After performing the average in eq. (5.5), this mean monomer density of "distinct ellipsoids" is equal for all i and depends on $r = |\mathbf{y}|$ only. For large $r \gtrsim \bar{R}_G$, $\varrho'_{\text{dist}}(r) \to c$, while for small $r \ll \bar{R}_G$, $\varrho'_{\text{dist}}(r)$ must be smaller than c due to the fact that ellipsoid i has been excluded from the sum in eq. (5.5). Since $4\pi \int_0^\infty dr\, r^2 \left[\varrho'_{\text{dist}}(r, N) - c\right] = -(N+1)$, we expect a scaling $\left[\varrho'_{\text{dist}}(r, N) - c\right] \sim N^{-1/2} f(rN^{-1/2})$ for the correlation hole, in reasonable agreement with the simulated results shown in fig. 5.5.

5.1.2 Kinetic Properties

Now we discuss the dynamical behavior of the system. As can be seen from fig. 5.6, the time–dependent mean square displacement $\langle[\mathbf{r}_i(t) - \mathbf{r}_i(0)]^2\rangle$ of an ellipsoid exhibits normal diffusive behavior for times $t > \tau_d$. The disentanglement time τ_d can be identified with the average time an ellipsoid needs to diffuse over a distance $\bar{R}_G$. The short time regime $t < \tau_d$ is not of interest here, since we do not intend to capture the complicated dynamics of polymer systems on these time scales, cf. sec. 1.1.4. In particular, the diffusion coefficient

$$D = \lim_{t\to\infty} \frac{\langle[\mathbf{r}_i(t) - \mathbf{r}_i(0)]^2\rangle}{6\,t} \tag{5.6}$$

will usually not exhibit the desired scaling with N, e.g. $D \sim N^{-1}$ for Rouse chains or $D \sim N^{-2}$ for entangled chains.

In fact, because D depends on $\Delta r_{\max}$, and $\Delta r_{\max}$ is chosen to be some fraction K_r of $\bar{R}_G \sim N^{1/2}$, see sec. 3.4, the variation of D with N is influenced by the simulation procedure itself, i.e. by the value of K_r. For the choice $K_r = 0.25$ used in our simulations, D increases with N, see fig. 5.6, but other choices lead to a different behavior. Conceptually, this is not a crucial problem. Since the elementary time scale τ_0 in the Monte Carlo procedure is arbitrary, cf. app. D, we can always adjust $\tau_0 = \tau_0(N)$ in order to reproduce the desired N dependence.

Apart from the characteristic time scale τ_d for translational motion, there are two other characteristic time scales τ_S and τ_O in the model, which refer to the change of shape and orientation of the ellipsoids. These can be identified by the decay of the respective correlation

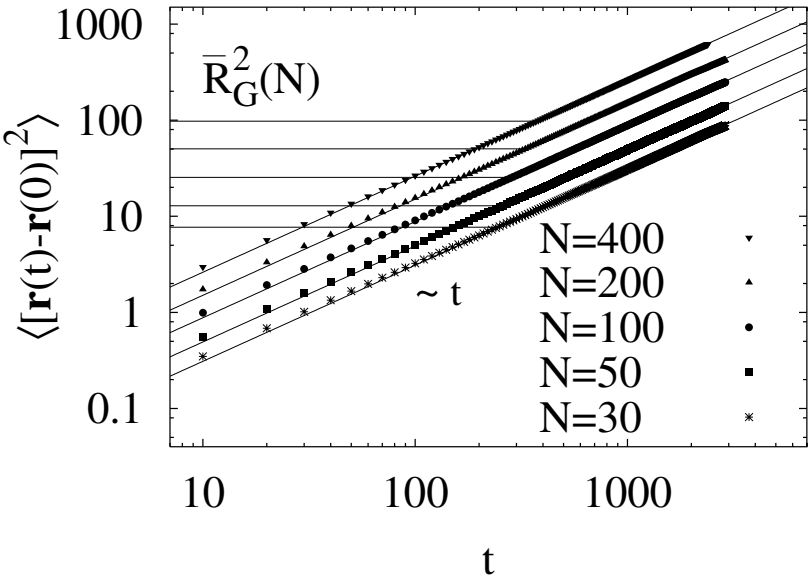

Figure 5.6: Mean square displacement $\langle[\mathbf{r}(t) - \mathbf{r}(0)]^2\rangle$ as a function of time for various values of N in a dense system ($c = 0.85$, $\epsilon = 1.0$). The lines indicate a linear growth. For comparison the mean squared radius of gyration $\bar{R}_G^2$ in the melt is indicated for the respective N.

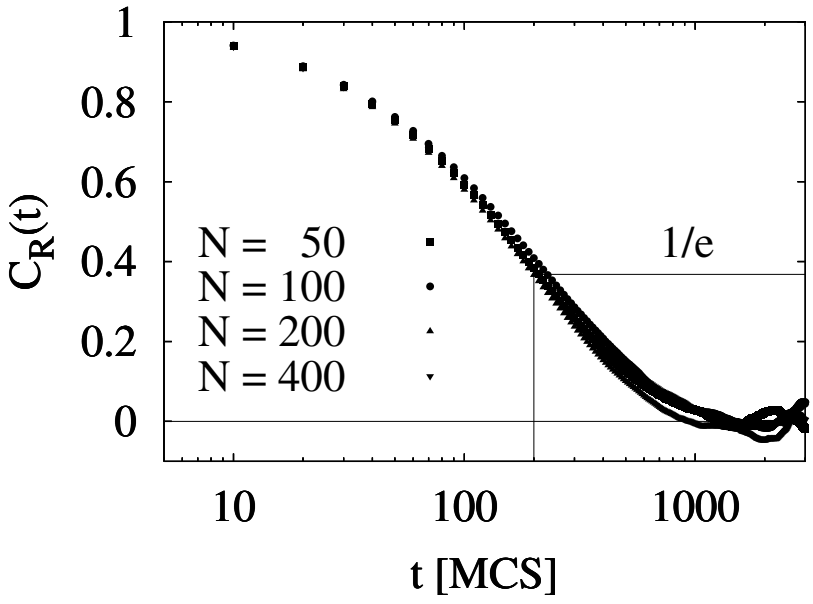

Figure 5.7: Autocorrelation function $C_R(t)$ of the squared radius of gyration for $K_S = 0.5$. The correlation time τ_S is almost independent on N and of order τ_d.

functions. For example, τ_S may be identified by the time, where the normalized autocorrelation function of the squared radius of gyration

$$C_R(t) = \frac{\langle R_G^2(t) R_G^2(0)\rangle - \langle R_G^2\rangle^2}{\langle R_G^4\rangle - \langle R_G^2\rangle^2} \tag{5.7}$$

has decayed to $1/e$. Respectively, the decay of the autocorrelation function

$$C_O(t) = \langle \mathbf{e}_1(t) \cdot \mathbf{e}_1(0)\rangle \,, \tag{5.8}$$

where $\mathbf{e}_1$ is a unit vector pointing in the direction of the first principal axis, i.e. the normalized first eigenvector of $S_{\alpha\beta}$, defines the reorientation time τ_O. A more convenient and stable way, leading to the same result, is to determine the characteristic times by taking the time integral over the respective autocorrelation functions.

As an example of these correlation functions, we show $C_R(t)$ in fig. 5.7 for $K_s = 0.5$ and various N. The results are almost independent on N in this case. The correlation time τ_S is approximately 180–220 MCS for all N and therefore of order τ_d.

An adjustment of τ_S and τ_O to real situations is again possible by tuning K_S properly, or by restricting the rotational movements of the ellipsoids. It is worth noting that, when altering K_r or K_s we observed a change of τ_d and τ_S respectively, but found almost no effect on the other time scales. Therefore the parameters K_r and K_s can be adjusted independently. For our choice, $K_r = 0.25$, $K_S = 0.5$ and free rotation, τ_d is the largest characteristic time scale. Accordingly, for the time scales $t \gtrsim \tau_d$ of interest here, we have not to bother about shape–sensitive or orientational correlations.

5.2 Binary Mixture

In this section we present the results for a binary mixture of M_A polymers of type A and M_B polymers of type B. We denote the fraction of chains of type A with $f_A = M_A/M$, and the fraction of chains of the other type B with $f_B = M_B/M$, where $M = M_A + M_B$. The interaction parameter is always $\epsilon = 1.0$ and the total monomer concentration is $c = 0.85$ corresponding to dense systems. We consider chains of equal length ($N_A = N_B = N$), in which case the fractions equal the (spatially averaged) monomer concentrations $f_A = \phi_A$ and $f_B = \phi_B$, cf. sec. 1.2.1.

5.2.1 Coexistence Curve

First we determine the coexistence curve. The simulations are conducted for a semi–grand–canonical ensemble [Bin95b, Lan00], i.e. we keep the total particle number M fixed and allow the fractions f_A and f_B to fluctuate. To this end we allow particles to change their identity in the Monte Carlo simulation in addition to the other possible moves. The order parameter ϕ is defined by $\phi \equiv |\phi_A - \phi_B|$, where we use the symmetry and take the absolute value for convenience. For $T < T_c$ the distribution $D(\phi)$ of the order parameter has a maximum at a finite value $\phi_{\max} = |\phi_1| = |\phi_2| > 0$, while for $T > T_c$, $\phi_{\max} = 0$.

A convenient way to identify the phase transition in the simulation is to determine the average $\langle\phi\rangle$. For $T \ll T_c$, $D(\phi)$ becomes sharply peaked and $\langle\phi\rangle \simeq \phi_{\max}$. For $T > T_c$, $\langle\phi\rangle$ is a measure of the width of $D(\phi)$ rather than an estimate of $\phi_{\max} = 0$. However, for $T \gg T_c$ the width becomes very small and $\langle\phi\rangle$ also. Accordingly, the critical temperature can be estimated from the region, where $\langle\phi\rangle$ goes from large finite values to zero, see fig. 5.8. For a precise

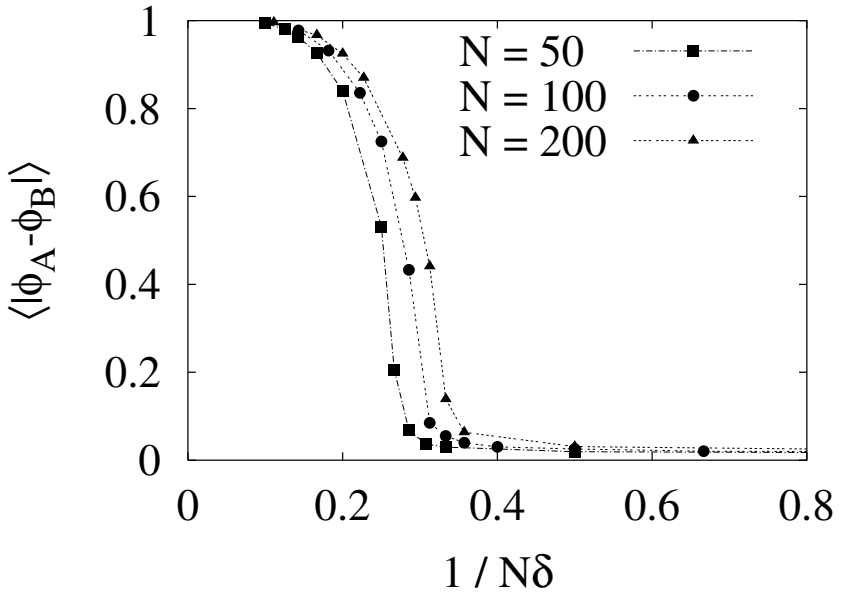

Figure 5.8: The order parameter $\langle|\phi_A - \phi_B|\rangle$ plotted versus $1/N\delta = k_B T/N(\hat{\epsilon}_{AB} - \hat{\epsilon})$ for chains of length $N = 50, 100$ and 200. The transition temperature scales roughly with $1/N$.

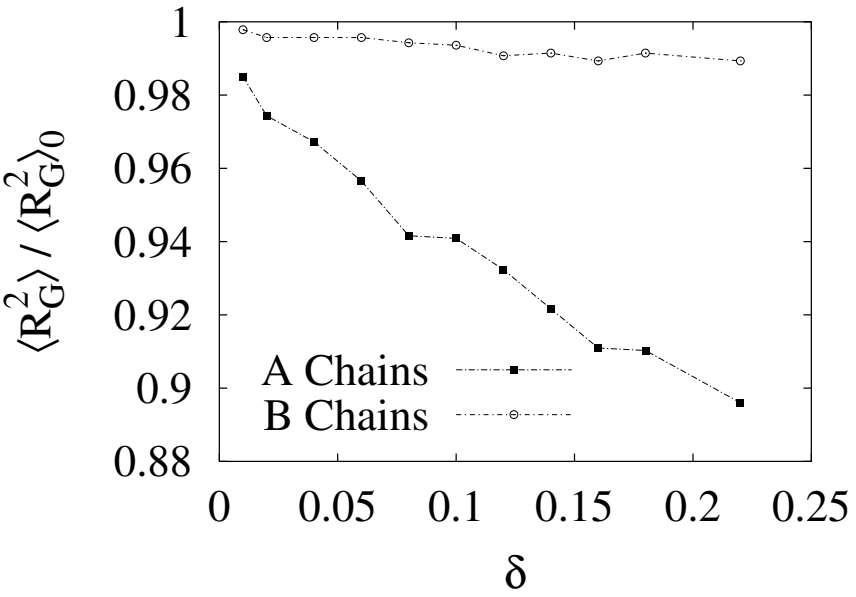

Figure 5.9: Squared radius of gyration chains in minority ($\phi_A = 0.1$) and majority ($\phi_B = 0.9$) as a function of the mismatch parameter δ. The simulation was performed for $M = 4000$ ellipsoids with $N = 50$.

determination of T_c, which is not our goal at this point, a finite size scaling analysis would be necessary [Bin81, Bin95b].

We investigated systems of $M = 4000, 3000$ and 2000 ellipsoids corresponding to chain lengths $N = 50, 100$ and 200 respectively, carrying out runs over 4000 MCS. In fig. 5.8 we show $\langle\phi\rangle = \langle|\phi_A - \phi_B|\rangle$ as a function of $1/N\delta = k_{\mathrm{B}}T/N(\hat{\epsilon}_{AB} - \hat{\epsilon})$. The scaling of the coexistence curve with N is not perfect, as one would expect from Flory–Huggings theory, cf. sec. 1.2.1, since more precisely $k_{\mathrm{B}}T_c/\delta = A\,N + B$. The occurrence of an additional constant B can be attributed to a correction due to the free ends of the chain [Bin95b, Deu93]. A similar behavior of the phase diagram in dependence on N has been found in simulations with explicit chains and in experiments [Geh92].

5.2.2 Chain Dimensions in a Blend

An interesting physical effect in polymer blends is that the chains of the minority phase reduce their size to minimize the repulsive interaction with those of the majority phase [Bin95b, Sar88]. In fig. 5.9 we present the results for the average squared gyration radius of the two different components A and B, divided by the pure melt value $\langle R_G^2\rangle_0$ for $\delta = 0$. The fraction of B–particles was kept fixed at $\phi_B = 0.9$. As can be seen from the figure, the particles in the minority shrink much more strongly than those in the majority. A detailed discussion of the interplay between thermodynamics and chain conformations can be found in ref. [Mül98].

5.2.3 Spinodal Decomposition

To study the spontaneous phase separation in the GEM we consider an equilibrated symmetric blend ($\phi_A = 0.5$) for $\delta = 0$ and increase the mismatch parameter instantaneously to $\delta = 0.2$ at time $t = 0$. The power spectrum of the concentration fluctuations is given by the intermediate scattering function

$$I(k,t) = \langle \rho_A(\mathbf{k},t)\rho_A(-\mathbf{k},t)\rangle - c_A^2\,\delta(\mathbf{k})\,, \tag{5.9}$$

where $\rho_A(\mathbf{k},t)$ is the Fourier transform of the total monomer density $\varrho'_A(\mathbf{y},t) = \sum_{i=1}^{M_A} \varrho'_{A,i}(\mathbf{y},t)$ of A–ellipsoids. The power spectrum depends on $k = |\mathbf{k}|$ only and an explicit expression of

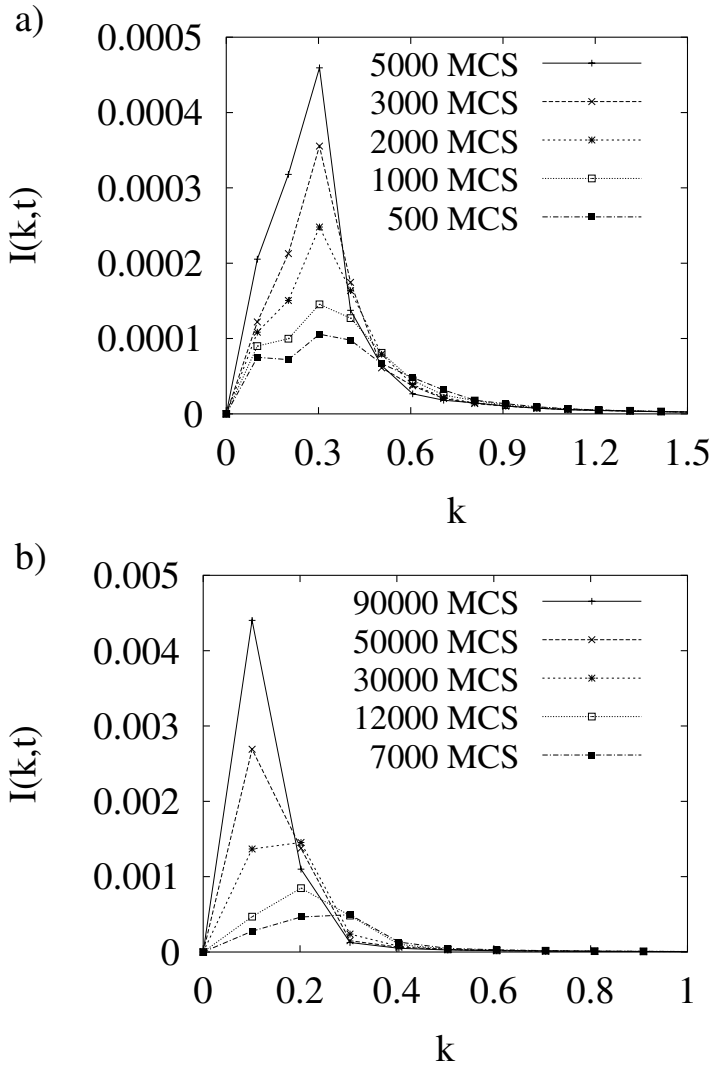

Figure 5.10: Intermediate scattering function $I(k,t)$ as a function of k for various times t. a) In the early time–regime the structure develops around some fixed characteristic wavelength. b) For later times, the peak position of $I(k,t)$ shifts to smaller values of k due to the coarsening of the domain patterns. The data are determined for a system of $M = 4000$ ellipsoids with $N = 50$.

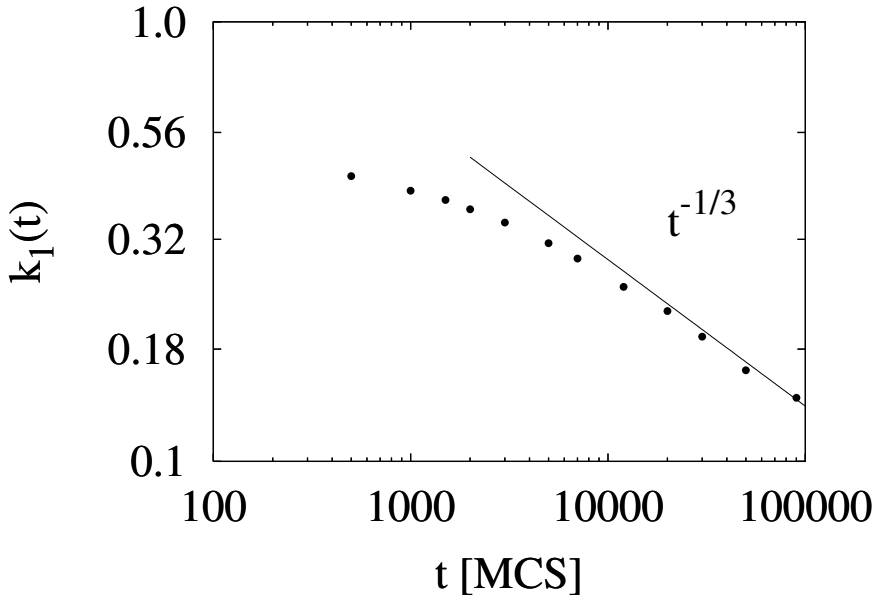

Figure 5.11: Time dependence of the normalized first moment of the intermediate scattering function measuring the inverse domain size in double–logarithmic representation, see eq. (2.33). At late stages the asymptotic Lifshitz–Slyozov behavior $k_1(t) \sim t^{-1/3}$ is approached.

$I(k,t)$ in terms of particle positions, orientations and sizes is derived in app. C.3.

The results for $I(k,t)$ are presented in fig. 5.10. At early times a peak develops in $I(k,t)$, which is associated with a characteristic demixing length. For $t \leq 5000$ MCS the peak position is almost constant in time. At later times the domain pattern begins to coarsen and the peak of $I(k,t)$ shifts to smaller values of k. These two observed time regimes are in accordance with expectations of the Cahn–Hilliard theory, discussed in sec. 1.3.1.

To quantify the coarsening process we consider the normalized first moment of the intermediate scattering function, see eq. (2.33) for $n = 1$, which is a measure of the inverse domain size in fig. 5.11. For short times ($t_0 = 500$ MCS), the bulk demixing length can be estimated by $\lambda_m \approx 2\pi/k_1(t_0) \approx 14$. For later times the results point to an asymptotic approach towards the Lifshitz–Slyozov growth law $k_1(t) \sim t^{-1/3}$, cf. eq. (1.54). We note that in more detailed microscopic models it is hard to reach the asymptotic coarsening regime due to the slow diffusion of the chain molecules. Nevertheless, in some simulations of such models the Lifshitz–Slyozov growth law could be seen [Sar91, Bro93].

6 GEM: Slab Geometry

In the last chapter we have verified that the Gaussian ellipsoid model (GEM) can reproduce the basic scaling relations and kinetic properties of polymeric systems on large time and length scales. Now, we extend this study to systems in confined geometries. Our aim is twofold: One one hand we wish to demonstrate that the GEM can also give a reasonable description of polymer systems in the presence of confinements. On the other hand we try to simulate experimental relevant situations, discussed in sec. 1.4.

The interactions of the ellipsoids with the confining walls are modeled by a linear coupling of the monomer densities with an external wall potential. First, we give some representative results for homopolymer systems. In particular, we show density profiles as well as wall induced shape and orientation effects and compare them to results of explicit chain simulations.

Afterwards we study phase separation phenomena in binary mixtures of two polymers A and B. The dependence of the lateral demixing length on the film thickness in the case of neutral walls is investigated, and agreement with results derived on the basis of Ginzburg–Landau type treatments [Fis98b] is found. Finally, we examine structured systems, where one wall is considered to be chemically patterned. This situation corresponds to the experiments with prepatterned substrates described in sec. 1.4. The structuring of the surface induces a periodicity in the polymer blend and leads to different equilibrium patterns as a function of the ratio of pattern periodicity and film thickness. In particular, the kinetic pathways of the demixing processes towards different equilibrium structures are studied.

6.1 Wall Interactions

In the presence of boundaries the interaction between the particles and the surfaces has to be accounted for in the free energy functional (3.1). Therefore we make an ansatz and add a term F_{wall} to the free energy functional,

$$F = F_{\text{intra}} + F_{\text{inter}} + F_{\text{wall}} \,. \tag{6.1}$$

The intramolecular and intermolecular parts F_{intra} and F_{inter} are given in eqs. (3.2, 3.3, 3.5). The additional interaction term between the polymers and the walls is chosen to be of the form

$$F_{\text{wall}} \;=\; \sum_{i=1}^{M} F_{\text{wall}}^{(i)} = \sum_{i=1}^{M} \int d^3y \;\varrho_i'(\mathbf{y})\; V_w(z)\,, \tag{6.2}$$

$$V_w(z) \;=\; \hat{\epsilon}_w \left[\exp\left(-\frac{z}{2\,l_w}\right) + \exp\left(-\frac{L_z - z}{2\,l_w}\right)\right] \,, \tag{6.3}$$

where $\hat{\epsilon}_w$ is the strength of the monomer–wall interaction and the wall interaction range l_w characterizes the hardness of the wall. The slab thickness is given by L_z. Note, however, that for the special form of the external potential defined in eq. (6.3) two parameters $\hat{\epsilon}_w/k_BT = 1$ and L_z are equivalent to two other parameters $\hat{\epsilon}_w/k_BT = \epsilon_w$ and $L_z - 2l_w \ln \epsilon_w$, respectively, assuming all other parameters to be constant. This means that a change of the amplitude $\hat{\epsilon}_w$ is equivalent to a spatial shift of the wall potential. Without loss of generality we therefore set $\hat{\epsilon}_w/k_BT = 1$ in the following and define L_z as our film thickness. This is reasonable, since for $l_w \to 0$ the system becomes confined by hard walls at positions $z = 0$ and $z = L_z$.

An exponential wall potential is frequently used to model a laterally structureless and purely repulsive wall [Isr00]. Here, it has the advantage, that the overlap between the potential and the monomer densities, that are of Gaussian form, are analytically integrable. The formulas are given in appendix C.2. By choosing small values for l_w one can model hard substrates, while for large l_w one models soft substrates, that e.g. correspond to polymer films on polymer brushes [Gre95]. We note that the unperturbed monomer densities are used in eq. (6.2). Hence, we do not a priori build in layering effects which are typically observed in simulations of polymer melts close to walls [Yoo95]. This is in the spirit of the GEM, where the unperturbed chain is used as input and all other properties are determined by interaction terms. In summary, eqs. (6.1–6.3) define the thermodynamics of the model for a homogeneous system of ellipsoids in a film geometry.

The necessary modifications of the interactions between ellipsoids for the description of binary blends are given in sec. 3.1. Introduction of a mismatch parameter δ that accounts for the incompatibility of both components leads to phase separation. To describe different interactions between the substrates and the two components, we introduce an additional wall mismatch parameter δ_w, with $-1 < \delta_w < 1$. The interaction parameters $\hat{\epsilon}_w(1 + \delta_w)$ and $\hat{\epsilon}_w(1 - \delta_w)$ refer to the A– and B–components, respectively. Note that the mismatch parameters δ and δ_w only change the strength of the repulsive monomer–monomer or monomer–wall interactions. Phase separation is thus driven by the disparity of excluded volume interactions, and not by attraction.

Throughout this chapter the simulations were carried out for ellipsoids corresponding to a chain length of $N = 50$. Further on, we always choose $\epsilon_w = \epsilon = 1$. For given film thickness L_z we determine the lateral dimension L by requiring a constant "bulk monomer concentration" $c = M(N+1)/L_z L^2 = 0.85$.

6.2 Effects of Hard Walls on Homogeneous Systems

In this section we present the results for homogeneous ellipsoid systems bound by two walls in thermal equilibrium. We consider various film thicknesses in the range $L_z = 1.5, \ldots, 25$ and a fixed number of particles $M = 2000$. The resulting geometries are listed in tab. 6.1. The systems are thermalized several thousand Monte Carlo steps (MCS) and averages are taken over at least 10000 MCS.
As a reference length to compare with, we use the unperturbed average radius of gyration in a bulk system with monomer concentration $\bar{c} = 0.85$, which is given by, cf. fig. 5.2,

$$\bar{R}_G = 3.6\,. \tag{6.4}$$

Table 6.1: System sizes for homogeneous films.

L_z	25	17	12.5	10	8
L_x, L_y	69.28	84.02	97.98	109.54	122.47
L_z	6	4	3	2	1.5
L_x, L_y	141.42	173.21	200.00	244.95	282.84

6.2.1 Concentration of Monomers and of Centers of Mass

The results for the concentration of the monomers

$$c(z) = \sum_{i=1}^{M} \int dx\, dy\, \varrho_i'(\mathbf{y}) \tag{6.5}$$

and the concentration of the centers of mass $c_{\rm cm}$ are shown in fig. 6.1 for a thick film ($L_z = 25$), where bulk–like features are found inside the slab. Two wall interaction ranges are considered. In the first case, $l_w = 0.5$, meaning that $2\,l_w$ is equal to the average bond length of the Gaussian chain molecules. In the second case the interaction range is much smaller, $l_w = 0.15$, modeling a harder wall. In both cases, the concentration profiles rapidly decay to zero as $z \to 0$. However, whereas the profile of the center of mass, $c_{\rm cm}$, is zero at $z = 0$, justifying our definition of the film thickness, the monomer concentration vanishes only for $z < 0$. This behavior reflects the softness of the wall potential, which is also responsible for less pronounced layering effects,

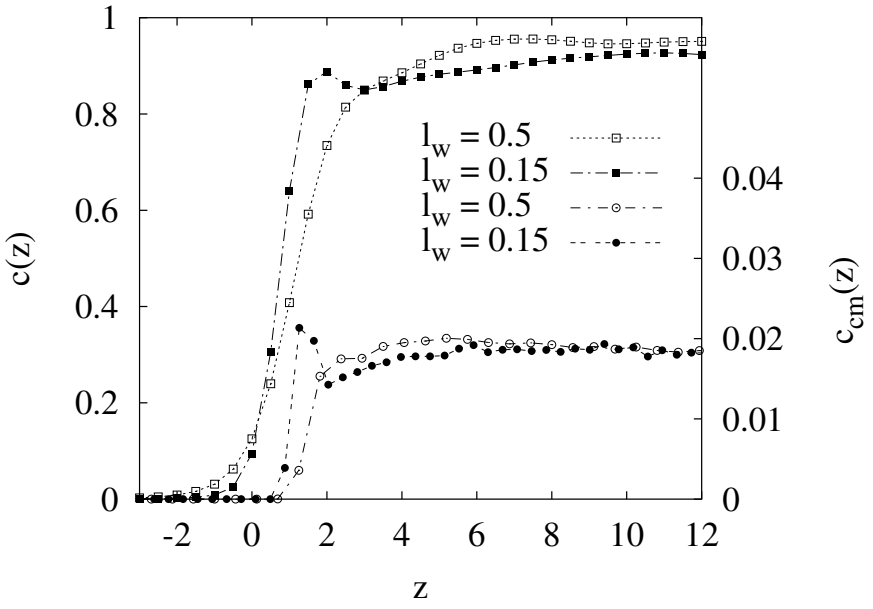

Figure 6.1: Monomer density $c(z)$ (upper curves) and center of mass density $c_{\rm cm}(z)$ (lower curves) for wall potentials with $l_w = 0.5$ (open symbols) and $l_w = 0.15$ (full symbols). The film width is $L_z = 25$.

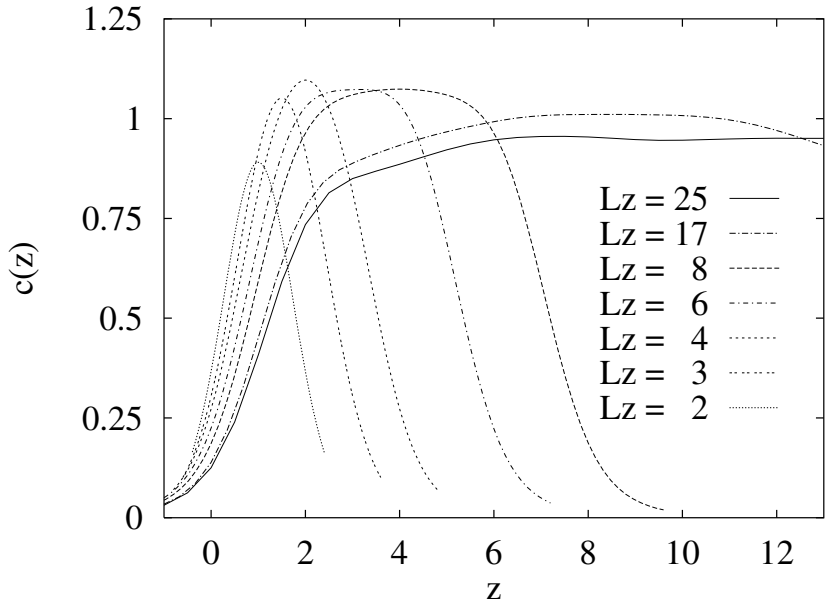

Figure 6.2: Monomer density as a function of distance z from the wall for $l_w = 0.5$ for various film thicknesses L_z.

typically observed in polymer melts confined between strongly repulsive walls [Yoo95, Mis01]. Here, we find the signature of these density oscillations only for $l_w = 0.15$, whereas the softer wall gives rise to a monomer profile comparable to that obtained for small bulk concentrations in the hard wall case [Yet94, Yet90].

The monomer concentration profiles for different film thicknesses L_z are shown in fig. 6.2 for the case $l_w = 0.5$. For the thicker slabs ($L_z = 17, 25$) a plateau in the profiles is reached at a distance of about $2\,\bar{R}_G$ from the wall. However, the plateau value still varies slightly with the system size and is larger than the bulk value $\bar{c} = 0.85$, that will be obtained for $L_z \to \infty$. For $L_z < 4\,\bar{R}_G$ the films do not show bulk–like behavior any more. The profile rather runs through a pronounced maximum $c_{\max}$ at $z = L_z/2$.

If L_z decreases, starting from $L_z = 25$, $c_{\max}$ first increases. The reason is that the smaller the thickness is, the more relevant is the reduction of the monomer density close to the walls for the overall film behavior. To keep the density constant, this has to be compensated by a higher density in the film center. For $L_z < 4$, however, we observe the opposite trend, i.e. a decrease of $c_{\max}$. This is due to the fact that the overlap of the wall potentials becomes important. This overlap effectively decreases the gradient of the wall potential and thus allows the monomers to penetrate the wall more deeply. The increased monomer density in the wall region entails a reduction of the density in the middle of the film in comparison to the thicker films. The relative changes of $c_{\max}$ are about 20 percent. In the case of harder walls ($l_w = 0.15$) we found a stronger variation and the largest value $c_{\max} = 1.36$ is obtained for $L = 3$. With respect to the binary mixtures studied in sec. 6.3 we wanted to keep the influence of these concentration variations small. We thus chose $l_w = 0.5$ in the following discussion. However, very similar results have been obtained for $l_w = 0.15$.

6.2.2 Orientation

We now study the orientation of the ellipsoids as a function of the distance of the center of mass, z, from the wall.

Let us denote by $\mathcal{R}_{\alpha\beta}$ the matrix, that defines the orientation of the principal axes with respect to the laboratory coordinate system, cf. eq. (3.12). As $\mathcal{R}_{\alpha\beta}$ consists of the normalized eigenvectors of the principal axis system, $\sum_\beta \mathcal{R}^2_{\alpha\beta} = 1$ holds. In an ensemble of randomly oriented ellipsoids the average value of all squared matrix elements is $\langle \mathcal{R}^2_{\alpha\beta} \rangle = 1/3$. Thus we expect this value for large distances z from the walls. A parallel orientation of one of the principal axis α to the laboratory axis β corresponds to $\langle \mathcal{R}^2_{\alpha\beta} \rangle = 1$, while a perpendicular orientation corresponds to $\langle \mathcal{R}^2_{\alpha\beta} \rangle = 0$. Hence $\mathcal{R}^2_{\alpha\beta}$ is a convenient measure to characterize the orientation. In the following, we denote an average of some quantity Q over all particles, whose center of mass is at distance z from the left wall by $\langle Q(z) \rangle$.

Figure 6.3 shows the results for the orientation of the principal axis with respect to the z–axis, i.e. perpendicular to the walls for different film thicknesses. We remind the reader that the system of principal axes is chosen such that $S_x \geq S_y \geq S_z$. For thick films ($L_z = 17$), we find $\langle \mathcal{R}^2_{\alpha z}(z) \rangle = 1/3$ far from the walls, as expected. When approaching the wall the smallest principal axis, z, becomes aligned perpendicular to the wall, $\langle \mathcal{R}^2_{zz}(z) \rangle \approx 1$, while the other two principal axes become aligned parallel. This behavior is observed for all film thicknesses and is also found in other simulations [Bas00b]. We used the symmetry with respect to $L_z/2$ in the representation of the data. The non–continuous drop to zero at $z \approx 0$ is an artefact of the analysis, because the center of mass density goes to zero in this region, cf. fig. 6.1.

The anisotropy in the orientation occurs on a length scale $2\bar{R}_G$ at most. The range is smaller along the y–principal axis than along the x–principal axis, since due to $S_x > S_y$ the energy cost for a rotation of the y–axis in the direction of the z–laboratory axis is smaller than that of the x–principal axis. It is remarkable that the anisotropy effect shows only very little dependence on the film thickness, even when L_z becomes comparable to or smaller than $\bar{R}_G$.

6.2.3 Deformation

Figure 6.4 shows how the shape of the ellipsoids is altered by the presence of the walls. For large distances, we find that the averaged eigenvalues $\langle S_\alpha(z) \rangle$ are independent of z and coincide with the bulk values, $\bar{S}_x = 10.1, \bar{S}_y = 2.0$ and $\bar{S}_z = 0.71$.

However, the ellipsoids near the walls are distorted. The size of the two major axes x and y is enhanced, whereas $\langle S_z(z) \rangle$ is reduced. When z increases, $\langle S_z(z) \rangle$ approaches the bulk value almost monotonously, while $\langle S_x(z) \rangle$ and $\langle S_y(z) \rangle$ run through a minimum before crossing over to the bulk behavior. This indicates that the ellipsoids near the surface are strongly oblate. Such an influence of a repulsive wall on the structure of the chains is also confirmed by other simulations, see refs. [Mis01, Bas00b]. As the film thickness L_z decreases, we find that the maximal values of $\langle S_z(z) \rangle$ become smaller for $L_z < 2\bar{R}_G$.

6.2.4 Discussion

Combining the results of the orientational properties and the deformation we find that ellipsoids at a distance $z > 2\bar{R}_G$ are virtually unperturbed by the boundaries and exhibit bulk behavior.

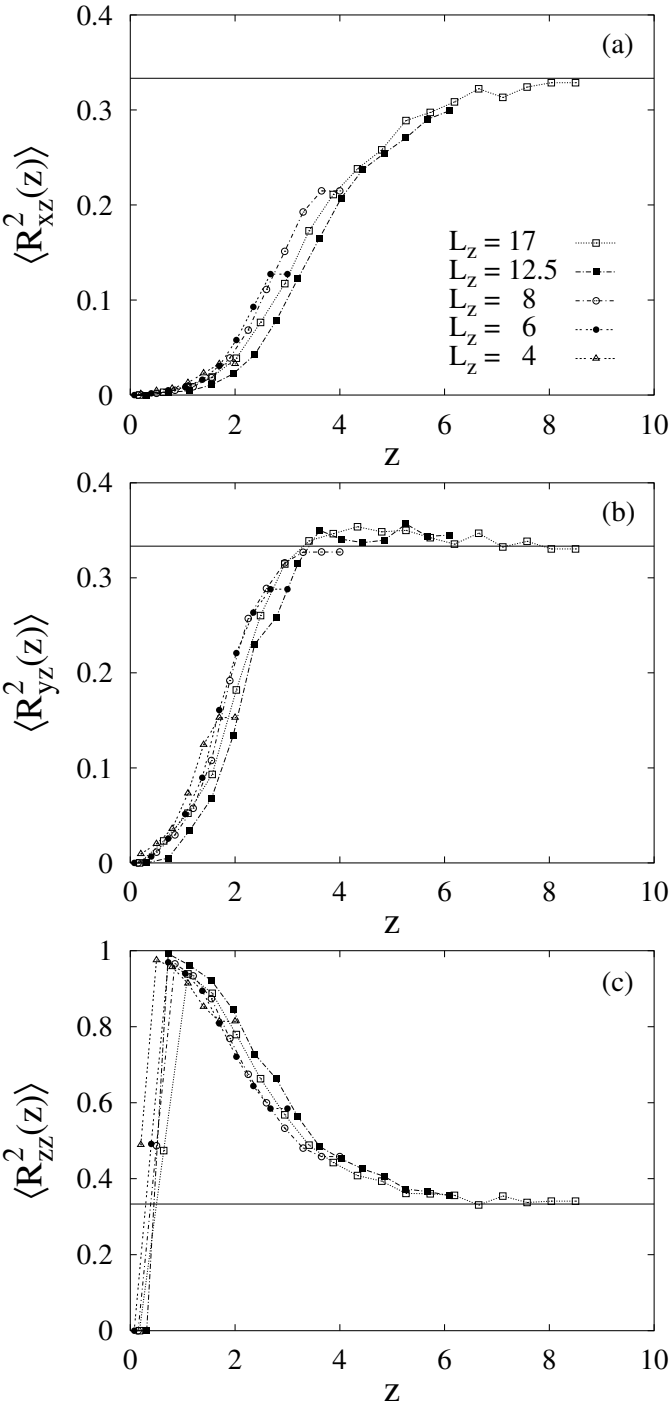

Figure 6.3: Lateral averaged squared matrix elements $\langle \mathcal{R}^2_{\alpha\beta}(z)\rangle$ are shown, characterizing the orientation of the ellipsoids with respect to the z–axis of the system. The alignment of the principal axis corresponding to the largest eigenvalue is given in (a), to the second eigenvalue in (b), and to the smallest one in (c). The expected value 1/3 for totally random oriented ellipsoids is marked in as a straight line. The results are shown for different film widths L_z and $l_w = 0.5$.

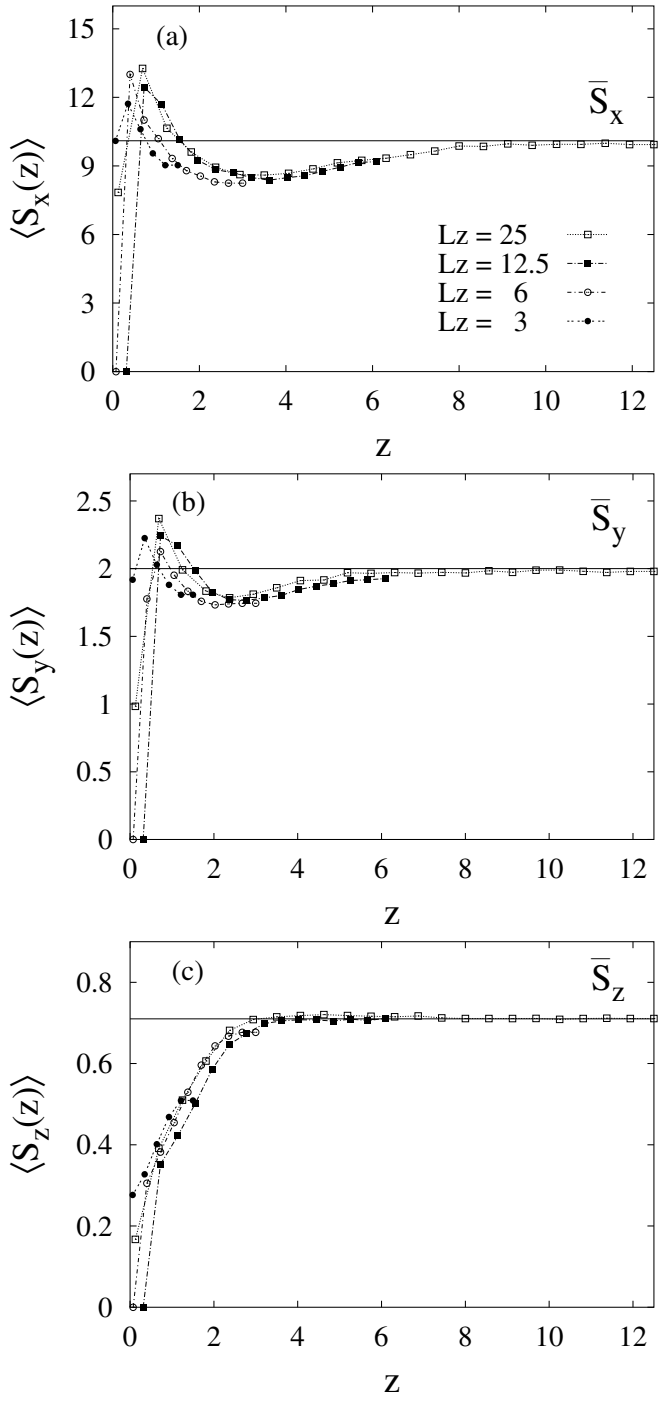

Figure 6.4: Lateral averaged eigenvalues $\langle S_\alpha(z) \rangle$ as a function of the separation z from the wall. The expected bulk values from simulations with periodic boundary conditions are shown additionally. The results are given for different film widths L_z and $l_w = 0.5$.

On approaching the walls there is a slight deformation of the two major principal axes, accompanied by an alignment of the principal axes. This alignment continues monotonously, up to the point, where the smallest principal axis of the ellipsoids is oriented perpendicular to the walls. Near the walls, the ellipsoids are compressed in z–direction and elongated with respect to the two major axes, thus exhibiting an almost two dimensional behavior.

It is interesting to compare these findings with results obtained by other authors. Let us mention that the analysis of the shape of polymers near walls is usually based on "components" of the radius of gyration with respect to the laboratory system. These components are the square roots of the diagonal elements of the radius of gyration tensor,

$$R_{G\alpha} = \sqrt{S_{\alpha\alpha}} \quad \text{or} \quad R^2_{G\parallel} \equiv S_{xx} + S_{yy}\,, R^2_{G\perp} \equiv S_{zz}\,. \tag{6.6}$$

It is clear that

$$S_{\alpha\beta} = \sum_\gamma \mathcal{R}_{\gamma\alpha} S_\gamma \mathcal{R}_{\gamma\beta}\,, \quad \text{in particular} \quad S_{\alpha\alpha} = \sum_\gamma \mathcal{R}^2_{\gamma\alpha} S_\gamma\,. \tag{6.7}$$

This kind of analysis makes it difficult to distinguish between an orientation and a deformation of the polymer coils.

When calculating the quantities $\langle R^2_{G\parallel}(z)\rangle$ and $\langle R^2_{G\perp}(z)\rangle$ for our model, we find reasonable agreement with the results of other simulations, see refs. [Mis01, Bas00b], namely an increase of $\langle R^2_{G\parallel}(z)\rangle$ near the wall and a strong decrease of $\langle R^2_{G\perp}(z)\rangle$. The results for $\langle R^2_{G\parallel}(z)\rangle$ are similar to that for $\langle S_x(z)\rangle$ and $\langle S_y(z)\rangle$ in fig. 6.4, and the results for $\langle R^2_{G\perp}(z)\rangle$ are similar to $\langle S_z(z)\rangle$, except that the extrema near the walls are more pronounced.

Pai–Panandiker et al. [Pan97] examined orientational effects of the end–to–end vector in a Monte Carlo simulation of dense polymer films. They found an increasing alignment of the end–to–end vector with reducing L_z, but averaged their quantities over the whole film. As there is a strong correlation between the end–to–end vector and the major principal axis x, their results support the picture presented above.

The work of Vliet and Brinke [Vli90] is dealing with a principal axis transformation to analyze orientational degrees of freedom, for a single self–avoiding walk confined between two hard walls. The main conclusion of this work is that with decreasing film thickness the principal axis of the polymers are aligned due to the confinement, long before their shape changes. While their situation is not directly comparable to the case of a polymer melt between two plates considered here, our results support the view that the orientational effect is dominant. This is not unexpected, as a reorientation of the polymer only constraints on one or two degrees of freedom, while a deformation affects the whole chain statistics, therefore affecting of the order of N degrees of freedom.

Table 6.2: System sizes for films of binary mixtures.

L_z	50	25	12.5	6	4	3	2
L_x, L_y	69.28	97.98	138.56	200.00	244.95	282.84	346.41

6.3 Binary Blends in Thin Films

For homogeneous systems we have considered equilibrium properties solely. Now, in the case of binary blends we focus on the kinetic properties of the systems, i.e. on spinodal decomposition in slab geometry. We investigate the case of binary blends between homogeneous and neutral walls, as well as the case of surface directed spinodal decomposition. However, to obtain the critical temperatures $T_c(L_z)$, we first determine the phase diagrams' dependence on the slab thickness L_z. Additionally, we analyze orientation and deformation of the ellipsoids at phase boundaries, in a similar way as for ellipsoids near a wall.

We always consider a symmetric composition, where the fraction of the A–component is $f_A = 0.5$. Except for the studies of surface directed spinodal decomposition, we consider the effect of two neutral ($\delta_w = 0$) and planar walls on a binary mixture of ellipsoids. Results will be discussed for fixed $l_w = 1/2$. The number of particles in the systems are $M = 4000$ and the resulting geometries of the simulated systems are listed in tab. 6.2.

6.3.1 Dependence of the Phase Diagram on the Film Thickness

For temperatures below a critical temperature T_c, separation into two phases, rich in type A and type B polymers, occurs. The coexistence curve for bulk systems has been determined in sec. 5.2.1. In thin films, however, the critical temperature T_c depends on film thickness L_z. Ginzburg–Landau theory [Tag93] predicts and simulations [Rou95] have shown that

$$\frac{T_c(\infty) - T_c(L_z)}{T_c(\infty)} \propto \frac{1}{L_z}, \quad \text{for} \quad L_z \ll Nb, \quad \text{and} \tag{6.8}$$

$$\frac{T_c(\infty) - T_c(L_z)}{T_c(\infty)} \propto \frac{1}{L_z^2}, \quad \text{for} \quad L_z \gg Nb. \tag{6.9}$$

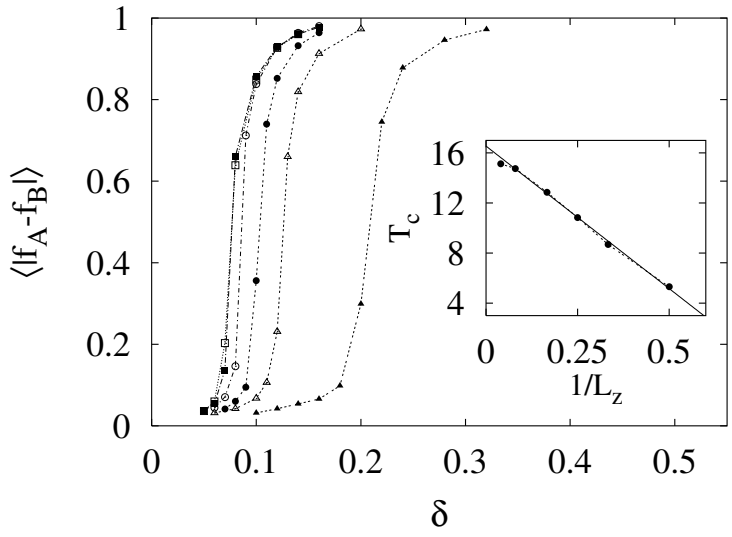

Figure 6.5: Coexistence curves for different film thicknesses $L_z = 25(\square)$, $12.5(\blacksquare)$, $6(\circ)$, $4(\bullet)$, $3(\triangle)$, and $2(\blacktriangle)$. The extrapolated critical temperatures as a function of $1/L_z$ are given in the inset.

Equations (6.8, 6.9) hold as long as the chain conformations are virtually unperturbed, i.e. $L_z > \bar{R}_G$, and mean field theory applies. This requires that the bulk correlation length ξ, characterizing the interfacial width close to T_c, is smaller than the crossover length $\xi_\times \propto Nb$, which determines the change from Ising–type to mean field behavior [Rou95]. While for $L_z \ll Nb$, eq. (6.8), the surface interaction is dominant, it is the finite size of the film, which determines the shift of T_c for $L_z \gg Nb$, eq. (6.9). Since $N = 50$ and $2 \leq L_z \leq 25$ in our case, we expect eq. (6.8) to apply, at least for $L_z > \bar{R}_G = 3.6$, cf. eq. (6.4).

For the sake of efficiency the simulations are carried out in a semi–grand–canonical ensemble [Bin95b, Lan00], i.e. the total number of particles is fixed, while the fractions f_A and f_B of A and B polymers can fluctuate. Averages are performed over several thousand MCS. Figure 6.5 shows the order parameter $\langle |f_A - f_B| \rangle$ as a function of the mismatch parameter δ for various L_z.

In order to test, if our model obeys eq. (6.8), we simply estimated $\delta_c \propto 1/T_c$ from an extrapolation of the steepest descent of the coexistence curve to zero. No detailed finite size analysis of the lateral dimension L was attempted. Such an analysis does not seem to be really necessary, since $T_c(L, L_z)$ monotonously approaches the asymptotic limit $T_c(L_z)$ for large enough L [Rou95]. For the L–values used in this study, see tab. 6.2, an inspection of fig. 5 of [Rou95] suggests that qualitatively reliable results should be obtained from our estimates of T_c. In fact, we see that T_c decreases with L_z. The inset of fig. 6.5 shows that $T_c(L_z) - T_c(\infty) \propto -1/L_z$, in agreement with eq. (6.8).

6.3.2 Orientation at Phase Boundaries

To study the influence of phase boundaries on the internal degrees of freedom of the ellipsoids, we prepared a fully phase separated system with periodic boundary conditions in all directions $L = L_z = 62.14$. The A–ellipsoids are randomly distributed in the half–space $z = (0, L_z/2)$ and the B–ellipsoids in the half–space $z = (L_z/2, L_z)$. We chose $\delta = 0.2$, which corresponds to the strong segregation regime, cf. fig. 6.5 for thick films. The system was thermalized for 2000 MCS, a time much larger than the autocorrelation times τ_S and τ_O of the internal degrees of freedom, cf. sec. 5.1.2. Moreover, this time is sufficient for an ellipsoid to diffuse typically over the distance from one interface to the center of one of the two phases. All averages were recorded over additional 18000 MCS.

In fig. 6.6a the different center of mass densities for both components $c_{\mathrm{cm},A}$, $c_{\mathrm{cm},B}$, and $c_{\mathrm{cm}} = c_{\mathrm{cm},A} + c_{\mathrm{cm},B}$, normalized by the chain length ($N = 50$) are displayed. We see that the total density c_{cm} of the ellipsoids becomes smaller at the interfaces in order to reduce the interaction between the mixture components. An additional effect occurs in fig. 6.6b, where the squared matrix elements $\langle \mathcal{R}^2_{\alpha z} \rangle$ are shown. Comparable to the behavior near a wall, cf. sec. 6.2.2, the ellipsoids align their x–axis (largest principal axis) parallel to the interface, while the z–axis (smallest principal axis) tends to be oriented perpendicular to the interface. However, this effect is much less pronounced than for walls. In particular, there is almost no effect on the orientation of the y–axis.
Finally, fig. 6.6c characterizes the deformation of the ellipsoids via the eigenvalues S_α that are normalized by their bulk values. Near the interfaces the ellipsoids are compressed with respect to all axes. The relative compression increases with the length of the principal axis, meaning that the asphericity becomes reduced. This effect was also observed in extensive Monte Carlo

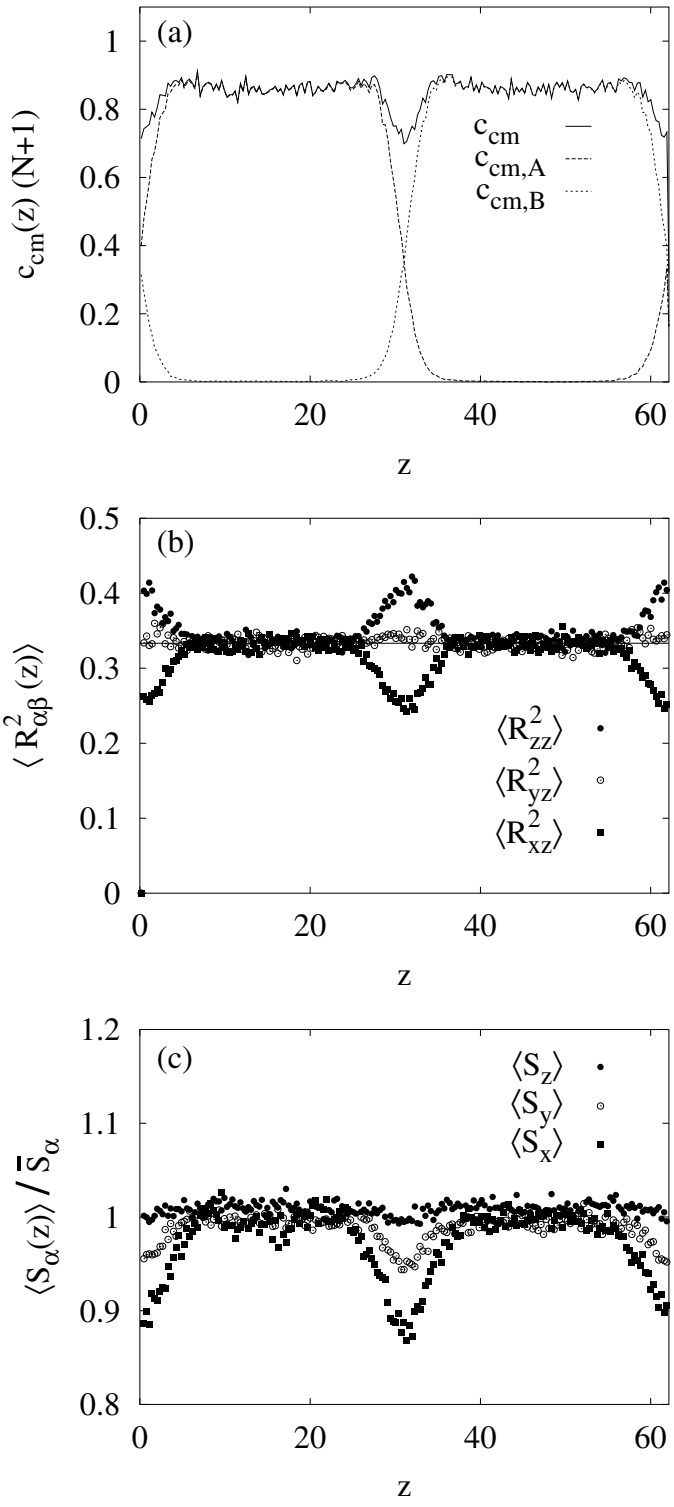

Figure 6.6: Normalized center of mass density (a), squared rotational matrix elements (b) and eigenvalues (c) as a function of distance z from the interfaces for a separated A–B mixture.

simulations of the bond–fluctuation lattice model [Mül95] and is analogous to the reduction of the radius of gyration in a strongly segregated mixture, where the polymers of the minority component shrink to reduce energetically unfavorable contacts with the surrounding majority phase [Eur01, Mül98].

6.3.3 Spinodal Decomposition between Neutral Walls

As already discussed in sec. 2.2.2, studies based on time dependent Ginzburg–Landau theory [Fis98b] have shown that for spinodal decomposition in thin neutral films lateral decomposition waves of a characteristic wavelength $k_{\parallel,m}$ characterize the domain pattern at short times. These studies predict that $k_{\parallel,m}$ becomes smaller with decreasing L_z, when $L_z \lesssim \lambda_m$, where λ_m denotes the bulk demixing length. Furthermore, if $L_z \lesssim \lambda_m$, the growth rates of the decomposition modes become smaller so that the overall demixing process slows down. These predicitions are confirmed by the numerical studies of the Cahn–Hilliard equation presented in sec. 2.2.2, cf. fig. 2.8. However, the question remains, whether these effects can be found in more realistic models as the GEM, too.

Therefore we consider a system confined between two planar and neutral walls ($\delta_w = 0$) that is prepared at infinite temperature at a time $t < 0$. All orientations and particle positions are random and the distribution of the eigenvalues is given by those of free Gaussian chains. At $t = 0$ we quench the system into the spinodal region of the phase diagram by setting $\epsilon \equiv \hat{\epsilon}/k_B T = 1$ and $\delta = 0.2$ (for $L_z = 2$ we used $\delta = 0.25$).

To quantify the demixing process of the films, we determine the lateral intermediate scattering function

$$I_\parallel(k_\parallel, z, t) = \langle \rho_{A\parallel}(\mathbf{k}_\parallel, z, t)\rho_{A\parallel}(-\mathbf{k}_\parallel, z, t)\rangle - c_A^2 \delta(\mathbf{k}_\parallel)\,, \tag{6.10}$$

where $\rho_{A\parallel}(\mathbf{k}_\parallel, z, t)$ is the Fourier transform of the total monomer density

$$\varrho'_A(\mathbf{y}, t) = \sum_{i=1}^{M_A} \varrho'_{i,A}(\mathbf{y}, t) \tag{6.11}$$

of the A–chains with respect to the lateral coordinates x, y. The power–spectrum depends on $k_\parallel \equiv \left(k_x^2 + k_y^2\right)^{1/2}$ only, therefore it is possible to perform an additional circular average in the k_x, k_y–space, cf. eq. (2.32). An explicit expression for $\rho_{A\parallel}(\mathbf{k}_\parallel, z, t)$ is given in appendix C.4.

Figures 6.7a-c show $I_\parallel(k_\parallel, z, t)$ for a slab of thickness $L_z = 6$ and various fixed times. As one can see from these figures, $I_\parallel(k_\parallel, z, t)$ exhibits a maximum that corresponds to a characteristic size $2\pi/k_{\parallel,m}$ of the A and B rich domains in the lateral direction. With increasing time the maximum grows and shifts to smaller values of $k_\parallel$, reflecting lateral domain coarsening.
To quantify the speed of this domain coarsening and to examine its dependence on film thickness L_z, we consider the first moment of $I_\parallel(k_\parallel, z, t)$ averaged over z,

$$k_{1,\parallel}(t) \equiv \frac{1}{L_z}\int_0^{L_z} dz\, \frac{\int_0^\infty dk_\parallel\, k_\parallel\, I_\parallel(k_\parallel, z, t)}{\int_0^\infty dk_\parallel\, I_\parallel(k_\parallel, z, t)}\,. \tag{6.12}$$

This quantity is a measure of the average lateral domain size as a function of time. The results are given in fig. 6.8 for different values of L_z.

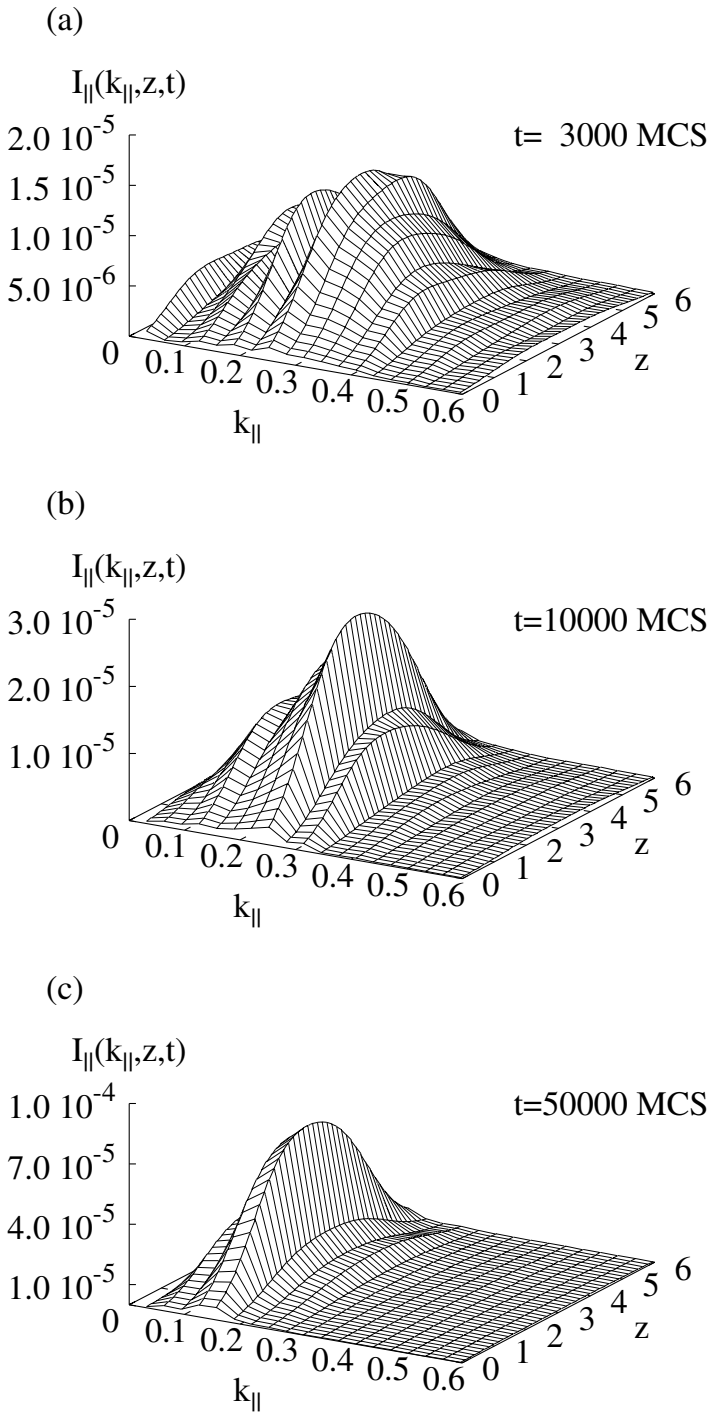

Figure 6.7: Lateral intermediate scattering function $I_{||}(k_{||}, z, t)$ for a film of thickness $L_z = 6$ shown at various times (a) $t = 3000$ MCS, (b) $t = 10000$ MCS and (c) $t = 50000$ MCS.

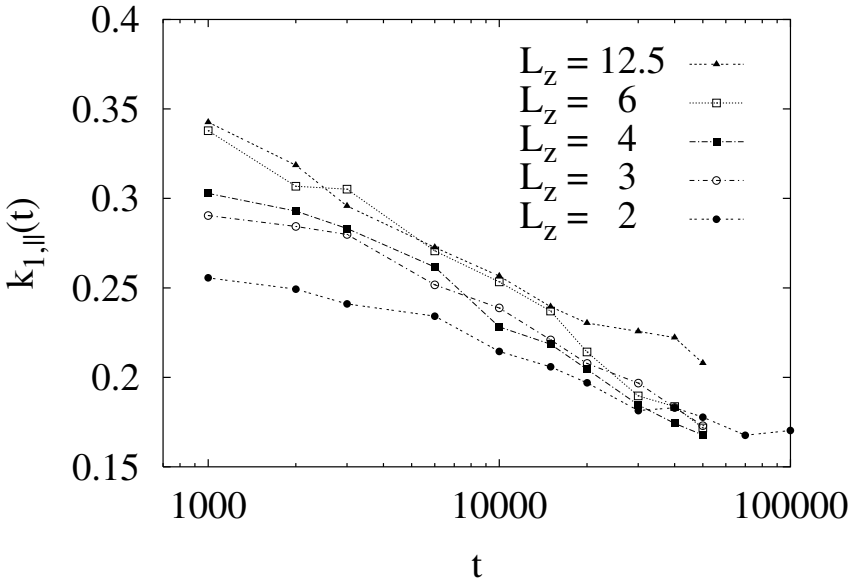

Figure 6.8: Film averaged first moment of the lateral intermediate scattering function $k_{1,\|}(t)$, eq. (6.12), as a function of time for different film thicknesses L_z.

In our system the bulk demixing length λ_m can be estimated by $\lambda_m \approx 2\pi/k_1(t_0) \approx 14$, cf. fig. 5.11 for ($t_0 = 500$ MCS). From this we expect that the effects predicted by time dependent Ginzburg–Landau theory should occur for $L_z \lesssim 14$.

Indeed, we find that $k_{1,\|}(t_0)$ determined at $t_0 = 1000$ MCS shrinks with decreasing L_z, cf. fig. 6.8. Moreover, in the thinner films the coarsening sets in later, which can be seen by the fact that curves at equal times have a steeper slope for thick films than for thin ones. This supports the result that the growth rates of the decomposition modes decrease. We note that these effects are not due to a shift of the critical temperature T_c with L_z. We carried out additional simulations with a mismatch $\delta = 0.3$ for $L_z = 2, 3, 4$ and found that the lateral demixing length depends only weakly on the mismatch parameter at fixed film width.

In summary, this results support the predictions of time dependent Ginzburg–Landau theory, i.e. the increase of the lateral demixing length and the slowing down of the demixing kinetics for $L_z < \lambda_m$. This qualitative agreement is obtained without any special wall potential or tuning of the parameters, supporting the view that the effects occur quite generally. However, a suppression of spinodal decomposition below a critical film thickness L_c, is not found. This is due to the fact that noise terms in the kinetic equations of the Cahn–Hilliard theory have been neglected.

6.3.4 Surface Directed Spinodal Decomposition

Now, we investigate the situation, where the walls are not neutral, but prefer one of both components A or B. In the present case both walls attract ellipsoids of component B with equal strength. The wall mismatch parameter is $\delta_w = 0.5$.

Figure 6.9 shows the emerging monomer concentrations $c_B(z)$, averaged over the lateral

dimensions. For rather large slabs ($L_z = 50$) symmetric SDW's form, cf. fig. 6.9a. Their wavelength at short times is given by the bulk demixing length $\lambda_m \approx 14$, and increases at large times due to domain coarsening. Finally, at $t = 100000$ MCS a B–A–B stripped pattern has formed in the z–direction. In the case of thin films ($L_z = 12.5$, cf. fig. 6.9b), this kind of pattern emerges already for short times ($t = 1000$ MCS). For $L_z \lesssim \lambda_m$ the propagation of the SDW is suppressed, and only a fast segregation of the B–components at the walls occur, cf. sec. 2.1. For even thinner films ($L_z = 6$) the two maxima seen in fig. 6.9b, are less pronounced and merge into one in the case of $L_z = 3$.

These results demonstrate, that the introduction of the wall mismatch parameter δ_w leads to the expected behavior concerning the formation of SDW's. They should be regarded as a first step towards the studies of patterned surfaces presented in the next section.

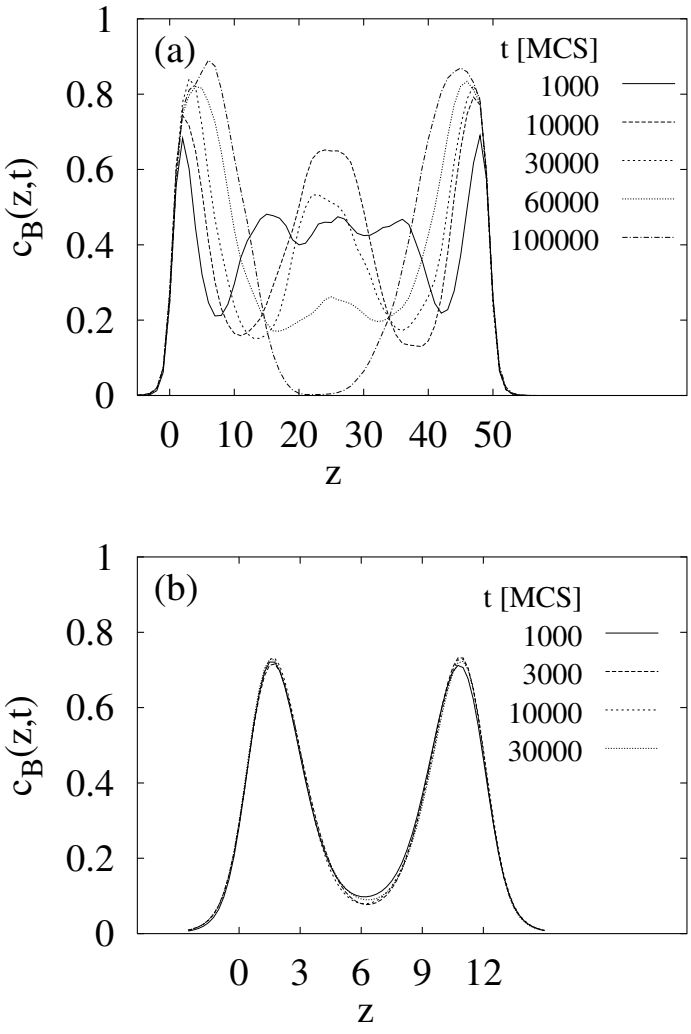

Figure 6.9: Laterally averaged monomer concentration $c_B(z,t)$ of the B–ellipsoids, for different times, in a film of thickness (a) $L_z = 50$ and (b) $L_z = 12.5$. The mismatch wall interaction is $\delta_w = 0.5$ for both walls.

6.4 Structured Surfaces

In this section we study polymer mixtures between two walls where one of the two surfaces is chemically patterned. One part of the patterned wall attracts component A, while the other part attracts component B. The second homogeneous wall is neutral with respect to the two components. The surface pattern is a periodic arrangement of equally spaced stripes, cf. fig. 6.10, modeled by a surface potential

$$V_w(y,z) = \hat{\epsilon}_w \exp\left(-\frac{z}{2\,l_w}\right)\left[1 \pm \delta_w \cos\left(\frac{2\pi\, y}{L_\parallel}\right)\right] . \tag{6.13}$$

The positive sign refers to component A, the negative to component B. As for homogeneous walls, the overlap integral (6.2) can be calculated analytically, see app. C.2.

Our focus is on the influence of the film thickness L_z and of the pattern periodicity $L_\parallel$ on the demixing process. This has been addressed in some of the experiments described in sec. 1.4. We first study the emerging equilibrium structures and afterwards the kinetics of demixing in such systems.

In the following we consider the case $l_w = 0.5$ and $\delta_w = 0.5$, where both components are strongly favored by the respective parts of the wall. All other parameters are the same as in the

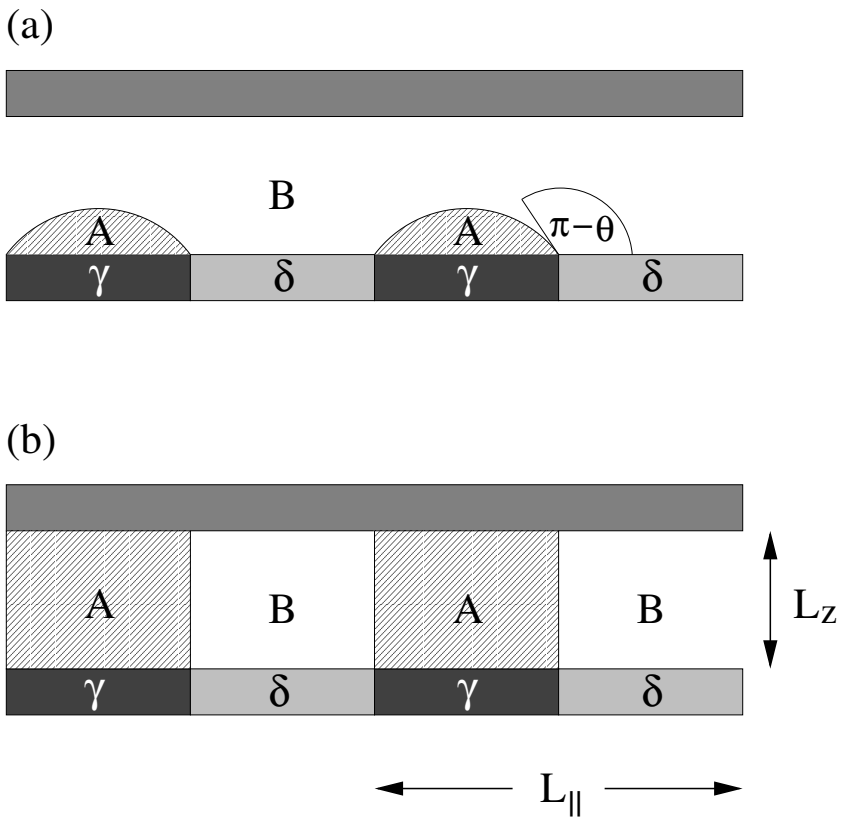

Figure 6.10: Two possible structures on a patterned substrate. Upper figure (a): The polymer film is only patterned near the surface ("partial structure"). Lower figure (b): The polymer structure induced by the surface penetrates the film ("full structure").

Table 6.3: System sizes for films of binary mixtures on structured surfaces.

$L_\parallel = 50$:					
L_z	50	25	12.5	6	4
L_y	–	100	150	200	250
L_x	–	96.26	128.34	200.53	240.64
$L_\parallel = 25$:					
L_z	50	25	12.5	6	4
L_y	75	100	150	200	250
L_x	64.17	96.26	128.34	200.53	240.64
$L_\parallel = 12.5$:					
L_z	50	25	12.5	6	4
L_y	75	100	137.5	200	250
L_x	64.17	96.26	140.01	200.53	240.64
$L_\parallel = 6$:					
L_z	50	25	12.5	6	4
L_y	72	102	138	204	246
L_x	66.84	94.37	139.50	196.60	244.55

previous section. The different geometries, i.e. the combinations of L_z and $L_\parallel$, are summarized in tab. 6.3. As we require L_y to be an integer multiple of $L_\parallel$ and we work with a fixed number of particles $M = 4000$, we adjusted L_x so that the monomer density is constant.

6.4.1 Structural Phase Diagram

To determine the resulting equilibrium structures in dependence on film thickness L_z and pattern periodicity $L_\parallel$, we carried out simulations in a semi–grand–canonical ensemble. The quantities of interest are determined after an equilibrated stationary domain pattern has evolved.

To characterize the equilibrium patterns we recorded the center of mass density c_{cm}. Two representative results for a slab of thickness $L_z = 6$ are given in fig. 6.11. It shows the normalized center of mass density $(N+1)\,c_{\mathrm{cm}}$ as a function of one laboratory axis (y or z), while the density profile was integrated over the respective remaining axes. For $L_\parallel = 25$ in fig. 6.11a, the A and B ellipsoids are separated in a periodic manner due to the structure of the wall. As one can see from the inset, this structure propagates through the whole film. We call this pattern a "full structure". By contrast, for $L_\parallel = 6$ in fig. 6.11b, the periodic behavior is confined to a small region near the structured surface, cf. the inset. In this case, small cylindrical caps of one phase are present at the favored parts of the surface. Thus a "partial structure" is stable in this case. These situations, full and partial structures, are schematically depicted in fig. 6.10.

A systematic study of the emerging structures as a function of L_z and $L_\parallel$ is shown in fig. 6.12. The ($L_\parallel$,L_z)–plane is divided into two regions, where systems with small $L_\parallel$ and large L_z are only partially structured, while systems with large $L_\parallel$ and small L_z are fully structured. To explain this behavior, we associate with the half periods of the cosine term in eq. (6.13) two

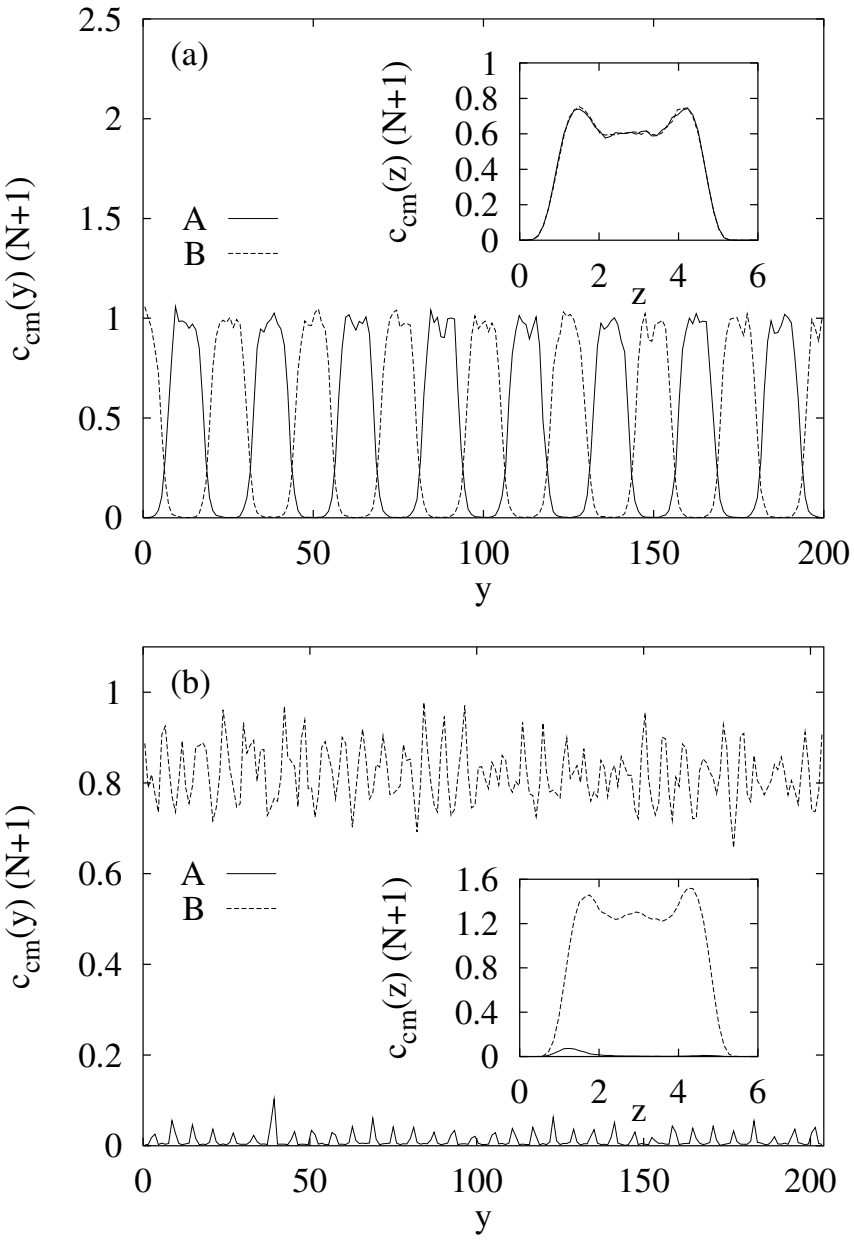

Figure 6.11: Results for the normalized center of mass density c_{cm} as a function of y and z (shown in the respective inset) in the case of (a) full, and (b) partial structure. The film thickness is $L_z = 6$ in both cases and the periodicity of the structure is (a) $L_{\|} = 25$ and (b) $L_{\|} = 6$.

homogeneous surface regions γ and δ, cf. fig. 6.10. The contact angles in these regions are

$$\cos\theta_\gamma = \frac{\sigma_{A\gamma} - \sigma_{B\gamma}}{\sigma_{AB}} \quad \text{and} \quad \cos\theta_\delta = \frac{\sigma_{A\delta} - \sigma_{B\delta}}{\sigma_{AB}}\,. \tag{6.14}$$

Near the γ–δ interface the contact angle θ can assume any value between the two limiting cases θ_γ and θ_δ [Len98]. Requiring without loss of generality that $c_A \leq c_B$, the contact angle

is restricted to $0 \leq \theta \leq \pi/2$. A simple consideration of the area of the interfaces in both cases (a) and (b) given in fig. 6.10 yields a difference of the free energy

$$\Delta F = \sigma_{AB} L_x L_y \left(2L_z - \frac{\theta}{2 \sin \theta} L_{\|} \right) . \tag{6.15}$$

The transition between both structures occurs, if $\Delta F = 0$, resulting in

$$\frac{L_z}{L_{\|}} = \frac{\theta}{4 \sin \theta} . \tag{6.16}$$

The crossover regime between the two structures in the L_z–$L_{\|}$ diagram is between the two lines with slope 1/4 (for $\theta \to 0$) and slope $\pi/8$ (for $\theta \to \pi/2$). Both lines are marked in fig. 6.12 for comparison, showing agreement with the simulations.

This result is also confirmed by experiments of an AC demixing process in thin films on an ABC–triblock copolymer brush, cf. the experiments of Fukunaga et al. [Fuk00] described in sec. 1.4. The different geometry in the experiment yields only a different constant in the righthand side of eq. (6.16). Moreover, in the experiment the substrate itself consists of polymer block of type A and type B, therefore effectively only one interfacial tension σ_{AB} has to be considered and the ratio $L_z/L_{\|}$ can be determined directly.

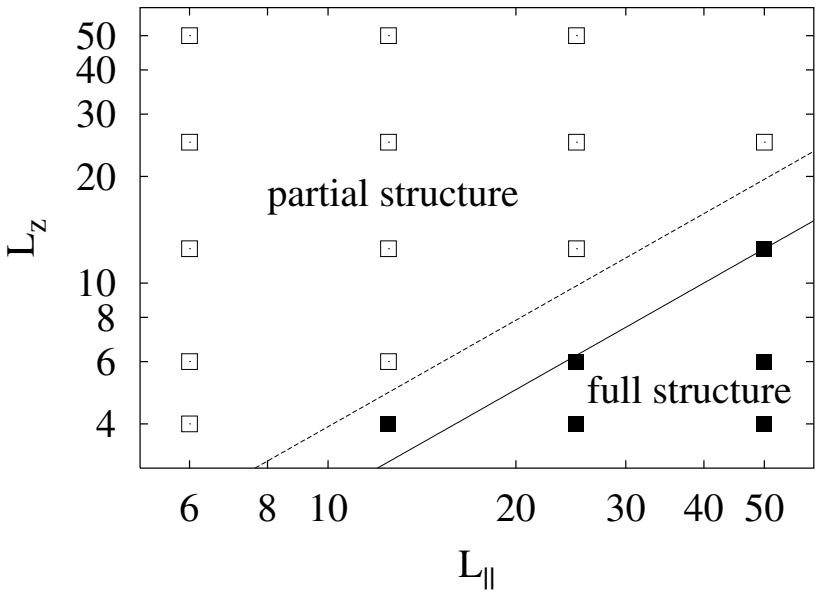

Figure 6.12: Regions in the L_z–$L_{\|}$ plane, where the domain pattern in the slab is fully structured (■) and only partially structured (□), in double logarithmic representation. The dividing lines are given by the two limiting cases of eq. (6.16), $L_z = 1/4\, L_{\|}$ (straight line) and $L_z = \pi/8\, L_{\|}$ (dashed line).

6.4.2 Pattern Directed Spinodal Decomposition

In this section we consider the kinetics of a system similar to the one described in the previous section, but for fixed fraction $f_A = 0.5$. The initial conditions are as in sec. 6.3.3.

The intermediate scattering function

$$I_y(k_y, z, t) = \int_0^\infty dk_x \, I_{\|}(\mathbf{k}_{\|}, z, t) \,, \tag{6.17}$$

with $I_{\|}(\mathbf{k}_{\|}, z, t)$ given in eq. (6.10) characterizes the domain formation with respect to the pattern–direction.

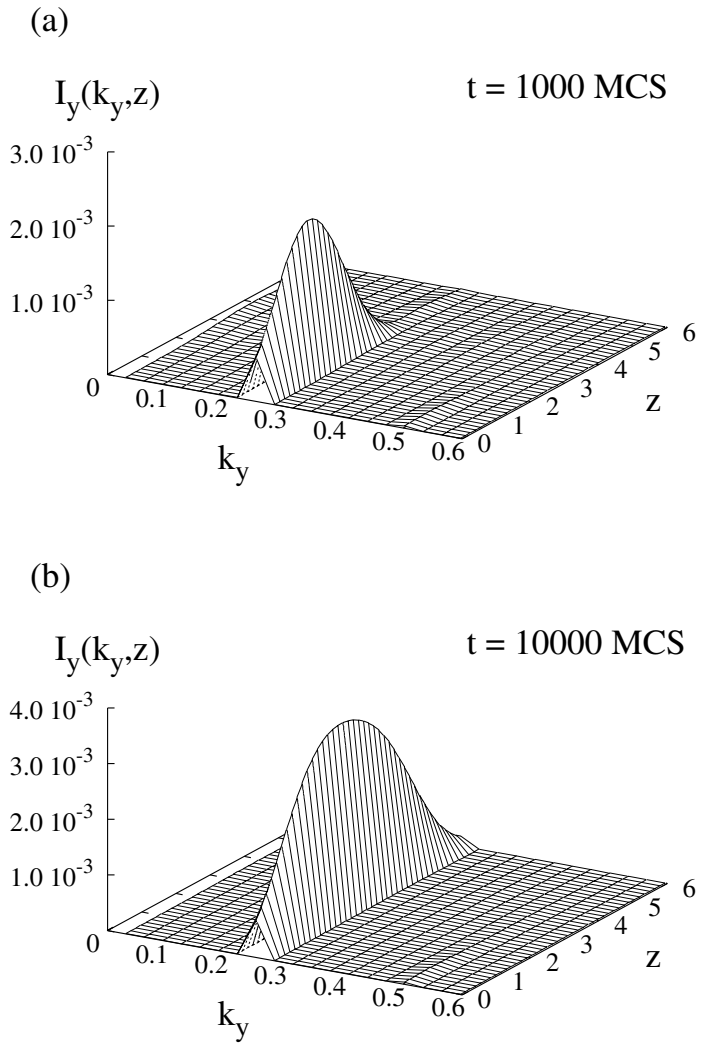

Figure 6.13: Intermediate scattering function $I_y(k_y, z, t)$ for a system of $L_{\|} = 25$ and $L_z = 6$ at times (a) $t = 1000$ MCS and (b) $t = 10000$ MCS. The patterned structure is stable throughout the whole film.

The situation corresponding to a full structure in equilibrium is given in fig. 6.13, where $I_y(k_y, z, t)$ is shown for a thin slab of thickness $L_z = 6$ and pattern periodicity $L_{\|} = 25$, at two times. At early times ($t = 1000$ MCS, see fig. 6.13a), a dominant structure arises near the patterned substrate on the length scale $k_y^{-1} = L_{\|}/2\pi$. This structure propagates in z–direction until it reaches the opposite wall ($t = 10000$ MCS, see fig. 6.13b). At later times, this structure is stable, as one would expect from fig. 6.12. We determined no further change in $I_y(k_y, z, t)$ until $t = 30000$ MCS.

Figure 6.14 shows $I_y(k_y, z, t)$ for a film of thickness $L_z = 25$ and pattern periodicity $L_{\|} = 12.5$. This case corresponds to a partial structure in equilibrium. The pattern–induced demixing is much faster than the lateral spinodal decomposition. The pattern–induced struc-

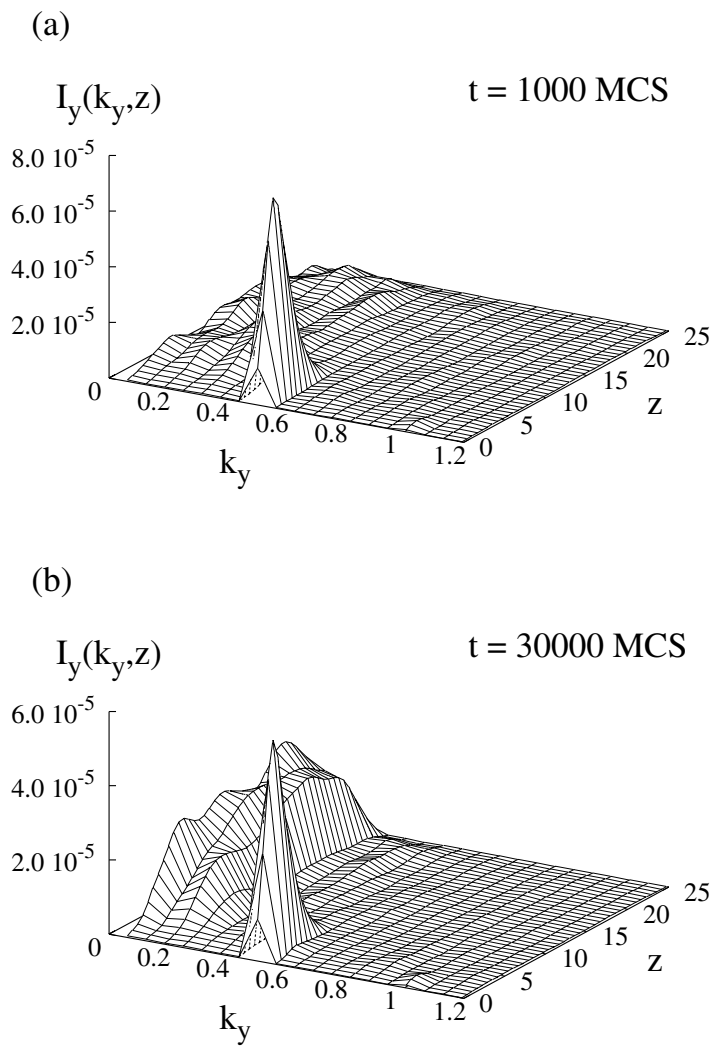

Figure 6.14: Intermediate scattering function $I_y(k_y, z, t)$ for a system of $L_{\|} = 12.5$ and $L_z = 25$ at times (a) $t = 1000$ MCS and (b) $t = 30000$ MCS. Lateral domain coarsening occurs away from the vicinity of the patterned wall. Near the wall the structure changes only weakly.

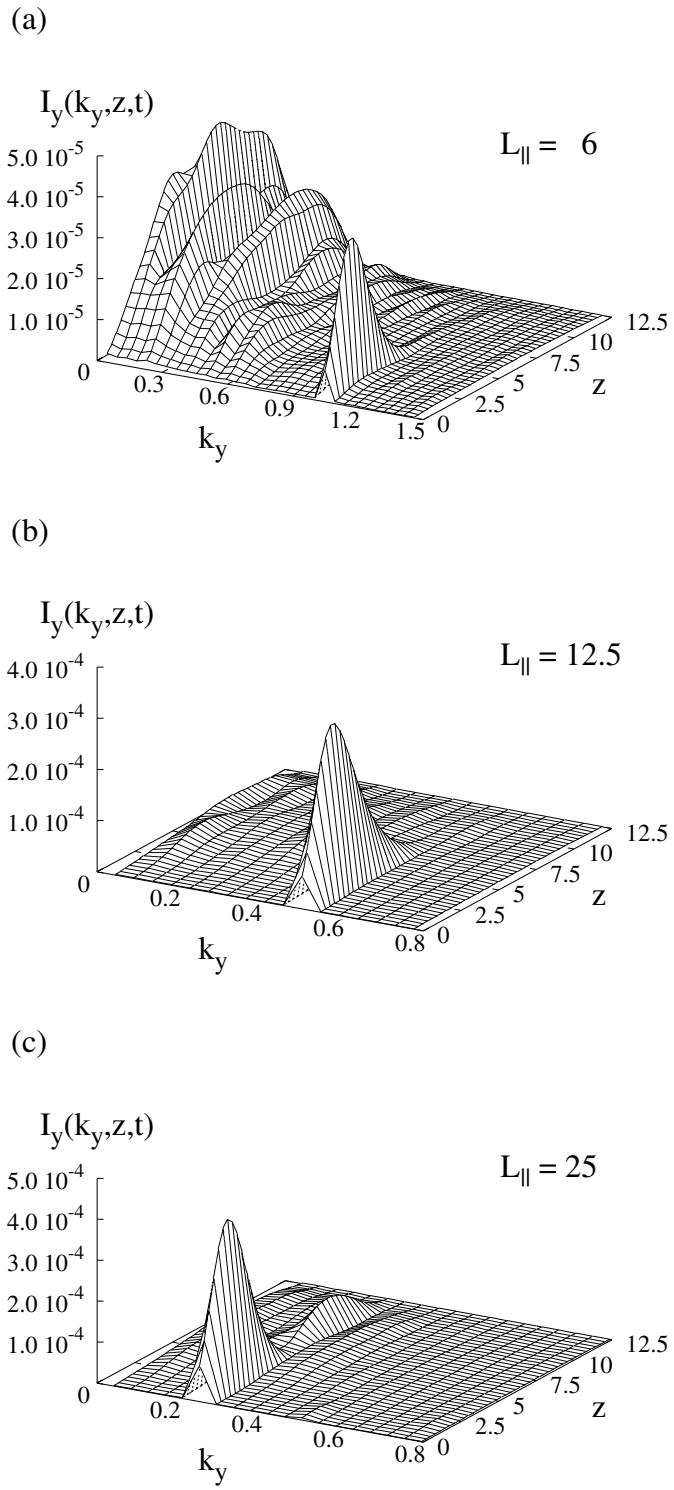

Figure 6.15: Intermediate scattering function $I_y(k_y, z, t)$ for early demixing times $t = 1000$ MCS and film thickness $L_z = 12.5$. The pattern periodicity is (a) $L_{||} = 6$, (b) $L_{||} = 12.5$ and (c) $L_{||} = 25$.

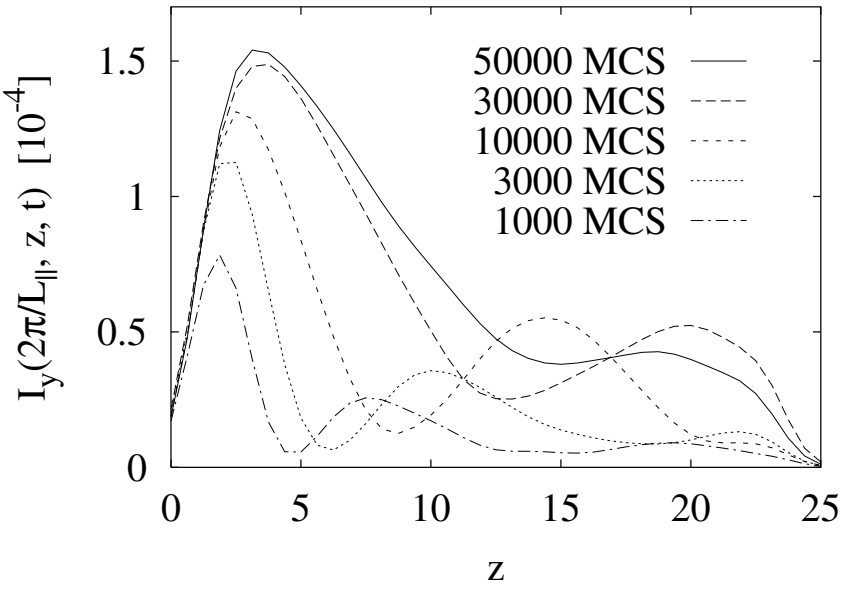

Figure 6.16: Intermediate scattering function $I_y(2\pi/L_\parallel, z, t)$ as a function of time. The film thickness is $L_z = 25$ and the pattern periodicity $L_\parallel = 50$.

ture for small values of z leads to a much larger corresponding peak in $I_y(k_y, z, t)$, fig. 6.14a, than the disordered lateral domain pattern emerging for larger z. The ordered periodic structure propagates into the film over a finite distance only ($z \approx 6$, see fig. 6.14b). For later times ($t = 30000$ MCS), the amplitude of the lateral decomposition waves is comparable to the amplitude of the pattern–induced waves. However, the peak in $I_y(k_y, z, t)$ occurs at smaller values of k_y. Thus, the periodic domain structure is stable near the patterned wall, but further away the domain pattern coarsens.

Such a behavior, i.e. a rapid formation of a patterned equilibrium structure in thin films, but a lateral domain coarsening afterwards in thick films, has also been observed in numerical treatments of the Cahn–Hilliard equation with appropriate boundary conditions [Kar98, Kie99] and in experiments [Kar98]. Moreover the equilibrium structures that have been found in ref. [Roc99], i.e. large scale phase separation far away from a nanoscopically patterned wall, but a remaining structure near the wall, cf. sec. 1.4, agree with the present results.

In both cases considered so far the periodicity $L_\parallel$ was comparable to or larger than the bulk demixing length λ_m. The question arises of what happens for $L_\parallel \ll \lambda_m$. In this case, we expect that the patterned surface induces structures, which are too small to drive spinodal decomposition because the interfacial energy of such structures is higher than the free energy gained by decomposition.

To investigate the interplay between the two length scales $L_\parallel$ and λ_m we consider a slab of thickness $L_z = 12.5$ and vary $L_\parallel$. We note that strictly speaking, $\lambda_{\parallel,m}$ is the relevant length scale for lateral decomposition in a slab. However, for $L_z = 12.5$ the demixing length $\lambda_{\parallel,m}$ is close to the bulk value λ_m, cf. sec. 6.3.3.

Figure 6.15 shows corresponding lateral structure factors $I_y(k_y, z, t)$ for $t = 1000$ MCS and

for $L_{\|} = 6, 12.5$, and 25. In the case of $L_{\|} = 6 \ll \lambda_m$, fig. 6.15a, the peaks corresponding to the surface induced structure and the lateral modes are comparable. The demixing process is not dominated by the surface–induced pattern. Also, the induced structure develops much more slowly compared to the case of $L_{\|} = 12.5 \simeq \lambda_m$, shown in fig. 6.15b. In this case, the peak corresponding to the ordered structure is a factor of about 10 higher, and the lateral demixing modes are thus almost invisible. For $L_{\|} = 25 \gg \lambda_m$ a double peak structure emerges. This can be interpreted in terms of a pattern directed spinodal decomposition wave, i.e. if one looked at the concentration fluctuations $\delta c_A(\mathbf{y}) = \varrho'_A(\mathbf{y}) - c_A$ in the yz–plane and labeled positive and negative regions of $\delta c_A(\mathbf{y})$ black and white respectively, one would see a checkerboard–like pattern [Kie99].

To see more directly how in the last case such a pattern propagates into the film, we plotted in fig. 6.16 the intermediate scattering function $I_y(2\pi/L_{\|}, z, t)$ as a function of z for various times t for a system with $L_z = 25$ and $L_{\|} = 50$. This picture describes how the surface–induced periodic domain patterns grow in perpendicular direction. Since our film thickness is limited, we did not try to quantify the propagation of this kind of kinetics further. For very large film thicknesses we would expect the usual Lifshitz–Slyozov domain growth to occur at large times.

7 Summary and Outlook

In this work we described long–time kinetic properties of polymeric systems. Particularly we considered the case of a binary polymer blend confined between two walls that could be homogeneous or heterogeneous.

Since the long–time kinetics can hardly be reached within models that resolve the chain structure of the polymers, coarse–grained models have to be used. We employed two kinds of treatments: First, we used a description based on time dependent Ginzburg–Landau theory, i.e. on the Cahn–Hilliard equation (CHE) that describes the kinetics of the systems via a nonlinear partial differential equation for the order parameter field. Secondly, we treated the systems in the framework of soft particle models. In this case one polymer is mapped onto one soft particle with internal degrees of freedom. The chain structure is not resolved, but the polymer is modeled by a monomer density for a given state – or shape – of the chain. The kinetics of the system is supplied by a discrete time Monte Carlo algorithm.

A good phenomenological description of phase separation processes is given by the CHE that in the case of confinements is supplied by appropriate boundary conditions. From the analytic solution of the linearized problem that is valid for short times, a criterion for the suppression of surface directed spinodal decomposition in thin films could be derived. According to this no SDW occurs if the film thickness is smaller than half the critical wavelength, $L < L_{\mathrm{crit}} = \pi/k_c$.

A numerical solution of the CHE is complicated by the fact, that the corresponding line system is stiff. This strongly restricts the size of the possible time–steps for explicit methods in order to avoid numerical instabilities. This problem was solved by applying an implicit time–stepping scheme that allows to explore the whole kinetics of phase separation until equilibrium. The efficiency of the method is particularly of importance considering the new time scales arising in confined systems. Especially the period doubling process occurring in the late stages of quasi one dimensional phase separation could be explored. However, the implicit method involves the inversion of huge matrices in the solution of coupled nonlinear equations by Newton's method and therefore is at the moment practicably in two dimensions only.

Therefore soft particle models have been developed, based on ideas by Murat and Kremer [Mur98]. Hereby the free energy functional of the system is decomposed into an intramolecular and an intermolecular part, the first being determined by the probability for the internal states of the particle, the second by the intermolecular interaction energy of the monomer densities. However, instead of using self–avoiding chains as an input, as in ref. [Mur98], in the present work Gaussian chains provide the underlying chain model. The self–interaction of the chains, i.e. interaction of different monomers of one polymer, is treated consistently on the same footing as the interaction of monomers belonging to different polymers.

The main advantage of this approach is that the model now fulfills the basic scaling relations of polymer systems without the necessity to adjust the interaction parameter as a function of chain length. Particularly, no simulations of explicit chains are therefore needed in the setup of the model. Further on, for Gaussian chains the monomer densities can be approximately described by simple functions, allowing for an efficient analytical calculation of the overlap and making the model highly portable.

While the input quantities are given for some possible soft particle models, i.e. for a description as spheres, ellipsoids and dispheres, the simulations were done for the Gaussian ellipsoid model (GEM). Within the GEM it has been shown that not only many features characteristic for polymeric systems can be found, for example, the correlation hole in a homogeneous melt or the orientation and deformation of the particles' conformations at phase boundaries, but moreover the model is very efficient, such that the late stages of phase separation processes can be reached.

Finally, confined systems were studied with the GEM. For a binary blend confined between two homogeneous neutral walls an increase of the lateral demixing length $\lambda_{\parallel,m}$ and the corresponding demixing times with decreasing slab thickness was found for $L_z < \lambda_m$. This supports the results based on the CHE, but now in a more realistic model, and suggests that experimental studies of this effect should be promising.

The case, where one of the two walls is structured, corresponds to experiments that try to transfer the pattern of the substrate on the domain pattern. Two different equilibrium patterns are found. Either the structure propagates through the whole film, leading to a striped demixing pattern ("full structure"), or the surface induced structure occurs only in the vicinity of the wall ("partial structure"). Which pattern emerges, depends on the ratio $L_z/L_\parallel$ only. This is explained by a consideration of the involved surface energies.

Different equilibrium patterns lead to different kinetic pathways for spinodal decomposition in such a film. In the case of an equilibrium pattern with full structure, pattern directed spinodal decomposition is the dominant process. The periodic ordered pattern freezes after reaching the opposite wall. On the other hand, the penetration depth of the pattern directed spinodal wave remains finite and lateral domain coarsening takes place in the late stages of decomposition. In the case of small pattern periodicity ($L_\parallel < \lambda_m$), pattern directed spinodal decomposition is less pronounced, as the pattern induces unfavorable structures with too large interfaces.

In summary, we showed that the kind of soft particle models developed in this work supply a useful and very efficient tool, to study polymer systems on large time and length scales. While a direct connection between soft particles and Gaussian chains exists, no simulations of systems of chain models are needed in the implementation. The models are especially well suited, to study phase separation processes.

There are many applications that can be thought of. First of all, it should be interesting to study diblock copolymers with the disphere model. In such systems it is difficult to simulate even the phase diagram with chain models, because a possible incommensurability between the periodicity of the microphase separated structure and the system size can lead to strong finite size effects [Bin94, Bin99]. Therefore large systems are needed in the simulations that can be provided by soft particle models. The influence of the morphology on the long–time

diffusive behavior of diblock copolymers has been investigated experimentally [Pap00], but is still poorly understood from a theoretical point of view. In this respect simulations based on the disphere model may help to identify the underlying processes.

From a more conceptual point of view, it is important to examine the hierarchy of possible multisphere models that have been proposed in sec. 3.6. This would not only lead to a deeper understanding of the second coarsening step, but provide a more direct connection to chain models and make a remapping, i.e. a substitution of soft particles by chain molecules, easier. Moreover, it could be thought of basing a thermalization procedure for explicit chain models on this hierarchy. Large scale structures could hereby be thermalized on a very coarse scale, while small scale structures could be treated on a finer scale.

A Line System for the CHE

Here we give the discretization of the Cahn–Hilliard equation (2.23) and the boundary conditions eqs. (2.26a,b) and their static version eqs. (2.28a,b). Since the CHE (2.23a) is valid also at the boundary, eqs. (2.26a,b) are rewritten by

$$\frac{\partial^2\mu}{\partial x^2}(x,0) + \frac{\partial^2\mu}{\partial y^2}(x,0) = -\Gamma_s\left[-\frac{\partial\phi}{\partial y}(x,0) - \sigma_s\frac{\partial^2\phi}{\partial x^2}(x,0) + f_s'\big(\phi(x,0)\big)\right] \tag{A.1a}$$

$$\frac{\partial^2\mu}{\partial x^2}(x,L_y) + \frac{\partial^2\mu}{\partial y^2}(x,L_y) = -\Gamma_s\left[\frac{\partial\phi}{\partial y}(x,L_y) - \sigma_s\frac{\partial^2\phi}{\partial x^2}(x,L_y) + f_s'\big(\phi(x,L_y)\big)\right], \tag{A.1b}$$

for all times t. In this section we suppress the time argument wherever it is convenient. Denoting the number of grid points by N_x and N_y in x and y direction, we define $\Delta x := L_x/N_x$ and $\Delta y := L_y/N_y$ in the bulk case, but $\Delta y := L_y/(N_y-1)$ in slab geometry. The space grid is defined by

$$\Omega_{\Delta x,\Delta y} := \big\{(i\Delta x, j\Delta y)\,\big|\, i = 0,\ldots,N_x-1,\, j = 0,\ldots,N_y-1\big\}, \tag{A.2}$$

the set of interior grid points is defined by

$$\Omega^{(\mathrm{int})}_{\Delta x,\Delta y} := \big\{(i\Delta x, j\Delta y)\,\big|\, i = 1,\ldots,N_x-2,\, j = 1,\ldots,N_y-2\big\}, \tag{A.3}$$

and the set of boundary grid points is given by

$$\delta\Omega_{\Delta x,\Delta y} := \Omega_{\Delta x,\Delta y}\backslash\Omega^{(\mathrm{int})}_{\Delta x,\Delta y}. \tag{A.4}$$

For the grid functions we use the notation

$$\phi_{i,j}(t) := \phi(i\Delta x, j\Delta y, t), \qquad \mu_{i,j}(t) := \mu(i\Delta x, j\Delta y, t). \tag{A.5}$$

To deduce an appropriate semi–discrete model for the underlying continuous problem, the spatial derivatives of some function $f = f(x,y)$ are replaced by standard symmetric difference formulae of order 2. In terms of the discrete $f_{i,j}$

$$\frac{\partial f}{\partial x} = \frac{f_{i+1,j} - f_{i-1,j}}{2\Delta x} + \mathcal{O}(\Delta x^3), \qquad \frac{\partial^2 f}{\partial x^2} = \frac{f_{i+1,j} + f_{i-1,j} - 2f_{i,j}}{\Delta x^2} + \mathcal{O}(\Delta x^3), \tag{A.6}$$

$$\frac{\partial f}{\partial y} = \alpha\,\frac{f_{i,j+1} - f_{i,j-1}}{2\Delta x} + \mathcal{O}(\Delta y^3), \qquad \frac{\partial^2 f}{\partial y^2} = \alpha^2\,\frac{f_{i,j+1} + f_{i,j-1} - 2f_{i,j}}{\Delta x^2} + \mathcal{O}(\Delta y^3). \tag{A.7}$$

Here we defined $\alpha := \Delta x/\Delta y$. The discrete versions of the continuous eqs. (2.23) yield a $N_x \times N_y$ dimensional system of coupled ordinary differential equations

$$\frac{\partial}{\partial t}\phi_{i,j}(t) = \frac{1}{\Delta x^2}\left[\mu_{i+1,j} + \mu_{i-1,j} + \alpha^2(\mu_{i,j+1} + \mu_{i,j-1}) - 2\gamma\,\mu_{i,j}\right] \tag{A.8a}$$

$$\mu_{i,j}(t) = -\frac{1}{\Delta x^2}\left[\phi_{i+1,j} + \phi_{i-1,j} + \alpha^2(\phi_{i,j+1} + \phi_{i,j-1}) - 2\gamma\,\phi_{i,j}\right] + f_b'\big(\phi_{i,j}\big)\,, \tag{A.8b}$$

with $\gamma \equiv (1+\alpha^2)$. In the determination of $\partial_t\phi_{i,j}(t)$ and $\mu_{i,j}(t)$ with grid points $(i\Delta x, j\Delta y) \in \delta\Omega_{\Delta x,\Delta y}$, virtual variables occur, corresponding to grid points that are not in $\Omega_{\Delta x,\Delta y}$. These virtual variables have to be replaced by the boundary conditions. In the bulk case the virtual variables in eq. (A.8a) can be replaced by the discrete periodic boundary conditions

$$\mu_{-1,j}(t) = \mu_{N_x-1}(t)\,, \qquad \mu_{N_x,j}(t) = \mu_{0,j}(t)\,, \qquad j = 0,\ldots,N_y-1\,, \tag{A.9}$$

$$\mu_{i,-1}(t) = \mu_{i,N_y-1}(t)\,, \qquad \mu_{i,N_y}(t) = \mu_{i,0}(t)\,, \qquad i = 0,\ldots,N_x-1\,. \tag{A.10}$$

In the case of a slab eq. (A.10) is replaced by the discretization of the no–flux condition (2.25)

$$\mu_{i,-1}(t) = \mu_{i,1}(t)\,, \qquad \mu_{i,N_y}(t) = \mu_{i,N_y-2}(t)\,, \qquad i = 0,\ldots,N_x-1\,. \tag{A.11}$$

Note, that the splitting of the original CHE into two equations with an explicit representation of μ leads to a convenient use of the no–flux condition to eliminate the virtual variables. To determine the virtual variables in eq. (A.8b), we discretize the second boundary condition. In the bulk case this leads to

$$\phi_{-1,j}(t) = \phi_{N_x-1,j}(t)\,, \qquad \phi_{N_x,j}(t) = \phi_{0,j}(t)\,, \qquad j = 0,\ldots,N_y-1\,, \tag{A.12}$$

$$\phi_{i,-1}(t) = \phi_{i,N_y-1}(t)\,, \qquad \phi_{i,N_y}(t) = \phi_{i,0}(t)\,, \qquad i = 0,\ldots,N_x-1\,. \tag{A.13}$$

In the case of a slab, we have to discretize eqs. (A.1a,b). We start with the lower boundary $(y = 0)$ and obtain

$$\frac{1}{\Delta x^2}\left[\mu_{i+1,0} + \mu_{i-1,0} + \alpha^2(\mu_{i,1} + \mu_{i,-1}) - 2\gamma\,\mu_{i,0}\right] = \Gamma_s\left[\alpha\,\frac{\phi_{i,1} - \phi_{i,-1}}{2\Delta x} + \sigma_s\,\frac{\phi_{i+1,0} + \phi_{i-1,0} - 2\phi_{i,0}}{\Delta x^2} - f_s'\big(\phi_{i,0}\big)\right]. \tag{A.14}$$

Solving this equation for $\phi_{i,-1}$ and using eq. (A.11) yields

$$\phi_{i,-1} = \phi_{i,1} + \frac{2\sigma_s}{\alpha\Delta x}\left[\phi_{i+1,0} + \phi_{i-1,0} - 2\phi_{i,0}\right] - \frac{2\Delta x}{\alpha}f_s'\big(\phi_{i,0}\big) - \frac{2}{\alpha\Gamma_s\Delta x}\left[\mu_{i+1,0} + \mu_{i-1,0} + 2\alpha^2\mu_{i,1} - 2\gamma\,\mu_{i,0}\right]. \tag{A.15}$$

Note, that by periodicity $\phi_{-1,0} = \phi_{N_x-1,0}$ and $\phi_{N_x,0} = \phi_{0,0}$. Inserting eq. (A.15) in eq. (A.8b) for $j = 0$ yields

$$\mu_{i,0} = -\frac{1}{\Delta x^2}\left[\phi_{i+1,0} + \phi_{i-1,0} + 2\alpha^2\phi_{i,1} - 2\gamma\,\phi_{i,0}\right] - \frac{2\sigma_s\alpha}{\Delta x^3}\left[\phi_{i+1,0} + \phi_{i-1,0} - 2\phi_{i,0}\right] + \frac{2\alpha}{\Delta x}f_s'\big(\phi_{i,0}\big) + \frac{2\alpha}{\Gamma_s\Delta x^3}\left[\mu_{i+1,0} + \mu_{i-1,0} + 2\alpha^2\mu_{i,1} - 2\gamma\,\mu_{i,0}\right] + f_b'\big(\phi_{i,0}\big)\,. \tag{A.16}$$

This is a system of linear equations for the $\mu_{i,0}$,

$$\mathcal{A}_{ij}\,\mu_{j,0} = \beta_i^{(\mathrm{low})} \tag{A.17}$$

with the matrix

$$\mathcal{A} \;\equiv\; \mathcal{I} + \frac{2\alpha}{\Gamma_s \Delta x^3} \begin{pmatrix} 2\gamma & -1 & 0 & 0 & \dots & 0 & -1 \\ -1 & 2\gamma & -1 & 0 & \dots & 0 & 0 \\ & \ddots & \ddots & \ddots & & & \\ & & & & & & \\ & & & \ddots & \ddots & \ddots & \\ 0 & 0 & \dots & 0 & -1 & 2\gamma & -1 \\ -1 & 0 & \dots & 0 & 0 & -1 & 2\gamma \end{pmatrix}, \tag{A.18}$$

where $\mathcal{I}$ denotes the identity matrix. The inhomogeneity is given by

$$\begin{aligned} \beta_i^{(\mathrm{low})} \equiv \frac{4\alpha^3}{\Gamma_s \Delta x^3}\mu_{i,1} - \frac{1}{\Delta x^2}\big[\phi_{i+1,0} + \phi_{i-1,0} + 2\alpha^2\phi_{i,1} - 2\gamma\,\phi_{i,0}\big] \\ - \frac{2\sigma_s\alpha}{\Delta x^3}\big[\phi_{i+1,0} + \phi_{i-1,0} - 2\phi_{i,0}\big] + \frac{2\alpha}{\Delta x} f_s'\big(\phi_{i,0}\big) + f_b'\big(\phi_{i,0}\big)\,. \end{aligned} \tag{A.19}$$

An analogous calculation for the upper boundary ($y = N_y - 1$) yields

$$\mathcal{A}_{ij}\,\mu_{j,N_y-1} = \beta_i^{(\mathrm{up})}\,, \tag{A.20}$$

with

$$\begin{aligned} \beta_i^{(\mathrm{up})} \equiv \frac{4\alpha^3}{\Gamma_s \Delta x^3}\mu_{i,N_y-2} - \frac{1}{\Delta x^2}\big[\phi_{i+1,N_y-1} + \phi_{i-1,N_y-1} + 2\alpha^2\phi_{i,N_y-2} - 2\gamma\,\phi_{i,N_y-1}\big] \\ - \frac{2\sigma_s\alpha}{\Delta x^3}\big[\phi_{i+1,N_y-1} + \phi_{i-1,N_y-1} - 2\phi_{i,N_y-1}\big] + \frac{2\alpha}{\Delta x} f_s'\big(\phi_{i,N_y-1}\big) + f_b'\big(\phi_{i,N_y-1}\big)\,. \end{aligned} \tag{A.21}$$

Since $\mathcal{A}$ is positive definite, eqs. (A.17, A.20) have a unique solution for every $\alpha, \Delta x$ and $\Gamma_s > 0$. The inverse matrix $\mathcal{A}^{-1}$ can be determined before time integration by *Choleski*–decomposition $\mathcal{L}\mathcal{L}^{-1} = \mathcal{A}$, yielding $\mathcal{A}^{-1} = (\mathcal{L}^{-1})^T\mathcal{L}^{-1}$, where $\mathcal{L}^{-1} \equiv \mathcal{N}$, with

$$\mathcal{N}_{ij} = \begin{cases} 0 & \text{for} \quad j > i \\ \mathcal{L}_{ii}^{-1} & \text{for} \quad j = i \\ -\mathcal{L}_{ii}^{-1}\sum_{k=j}^{i-1}\mathcal{L}_{ik}\mathcal{N}_{kj} & \text{for} \quad j < i \end{cases}. \tag{A.22}$$

In the case of quasi–static boundary conditions (eqs. (2.28a,b) corresponding to $\Gamma_s \to \infty$), no system of equations has to be solved ($\mathcal{A} = \mathcal{I}$). Thus $\mu_{j,0} = \beta_i^{(\mathrm{low})}$ and $\mu_{j,N_y-1} = \beta_i^{(\mathrm{up})}$, where the terms $\propto \mu_{i,1}$ and $\propto \mu_{i,N_y-2}$ vanish in eqs. (A.19, A.21).

To summarize, the problem to be solved numerically consists of the ordinary differential equation (A.8a), together with the replacements (A.9, A.10) for the chemical potential in the bulk case and (A.9, A.11) in the slab case. The variables for the chemical potential $\mu_{i,j}$ themselves are given in eq. (A.8b) with the replacements (A.12, A.13) in the bulk case and the special representations of $\mu_{i,0}$ and μ_{i,N_y-1} given by eqs. (A.17, A.20) in the slab situation. The system of differential equations is completed by the initial value condition

$$\phi_{i,j}(0) = \phi(i\Delta x, j\Delta y, 0)\,. \tag{A.23}$$

B Properties of Gaussian Chains

B.1 Averages of Gaussian Chains

Here we present moments of the eigenvalues **S** as obtained by Monte Carlo simulation. Table B.1 displays results for chains of length $N = 1000$ averaged over 10^7 different realizations. The data for the radius of gyration R_G are given for the sake of comparison. The deviations from the exact values for $N \to \infty$ are due to statistical errors and finite chain lengths.

Table B.1: Moments of the eigenvalues **S** as determined by Monte Carlo simulation.

$\langle R_G^2\rangle/N$	0.16685	$\langle R_G^4\rangle/N^2$	0.035302
$\langle S_1\rangle/N$	0.12758	$\langle S_1^2\rangle/N^2$	0.023009
$\langle S_2\rangle/N$	0.028708	$\langle S_2^2\rangle/N^2$	0.0010300
$\langle S_3\rangle/N$	0.010568	$\langle S_3^2\rangle/N^2$	0.00013143
$\langle S_1S_2\rangle/N^2$	0.0038714	$\langle S_1^3\rangle/N^3$	0.0055805
$\langle S_2S_3\rangle/N^2$	0.00032239	$\langle S_2^3\rangle/N^3$	$4.6206\,10^{-5}$
$\langle S_3S_1\rangle/N^2$	0.0013717	$\langle S_3^3\rangle/N^3$	$1.9338\,10^{-6}$

B.2 Parameters of the Distribution Functions

The determination of the parameters of $P_R(R_G^2)$ and $P_\alpha(S_\alpha)$ is based on the fact that the moments of the heuristic functions are calculable analytically. Therefore we define the constants a_R and d_R for $P_R(R_G^2)$ in such a way, that the first two moments $\langle R_G^2\rangle$ and $\langle R_G^4\rangle$ are exact in the limit $N \to \infty$. With this definition and the well known results $\langle R_G^2\rangle \sim N/6$ and $\langle R_G^4\rangle \sim 19\,N^2/540$, cf. [Yam71], we are led to the two equations

$$a_R = \frac{1}{6}\frac{K_0(2d_R)}{d_R K_1(2d_R)} \quad \text{and} \quad \frac{K_0(2d_R)K_2(2d_R)}{36\,K_1^2(2d_R)} = \frac{19}{540}\,. \tag{B.1}$$

At this point we also give a more quantitative test of $P_R(R_G^2)$ by comparison of the higher moments of R_G^2. The asymptotic exact result for the third moment is $\langle R_G^6\rangle/N^3 = 631/68040 \approx 0.009274$, while we find $\langle R_G^6\rangle/N^3 = 0.009280$. For the fourth moment the exact result $\langle R_G^8\rangle/N^4 = 1219/408240 \approx 0.002986$ has to be compared with $\langle R_G^8\rangle/N^4 = 0.003000$.

For $P_\alpha(S_\alpha)$ the same procedure leads to

$$\frac{\langle S_\alpha\rangle}{d_\alpha}\frac{K_{n_\alpha-1}(2d_\alpha)}{K_{n_\alpha-2}(2d_\alpha)} = a_\alpha \quad \text{and} \quad \frac{K_{n_\alpha-3}(2d_\alpha)K_{n_\alpha-1}(2d_\alpha)}{K^2_{n_\alpha-2}(2d_\alpha)} = \frac{\langle S_\alpha^2\rangle}{\langle S_\alpha\rangle^2} \; . \tag{B.2}$$

Since no exact analytical result for the moments $\langle S_\alpha^m\rangle$ exists to our knowledge, these quantities are determined by Monte Carlo simulations of Gaussian chains of length $N = 1000$. The results are given in tab. B.1.

B.3 Improved Formula for the Monomer Density

For the sake of completeness, we present an improved heuristic formula for the density of the x_2–axis:

$$\tilde{\varrho}_2(u_2) = \frac{1}{\sqrt{2\pi}2\,\sigma_2'}\left[\exp\left(-\frac{(u_2-\bar{u}_2)^2}{2\,{\sigma_2'}^2}\right)+\exp\left(-\frac{(u_2+\bar{u}_2)^2}{2\,{\sigma_2'}^2}\right)\right] \tag{B.3}$$

A least squares fit of the constants yields $\bar{u}_2 = 0.674$ and $\sigma_2' = 0.748$.

B.4 Improved Calculation of $P_C(r_{AB}^2; R_A^2, R_B^2)$

Here, we present an improved approximation for $P_C(r_{AB}^2; R_A^2, R_B^2)$. On this behalf, we make the ansatz

$$P_C(r_{AB}^2; R_A^2, R_B^2) \propto \sqrt{\frac{r_{AB}^2}{2\pi}}\left(\frac{3}{\sigma_0^2}\right)^{3/2}\exp\left(-\frac{3}{2}\frac{r_{AB}^2}{\sigma_0^2}\right)\left(1+a_1\frac{r_{AB}^2}{\sigma_0^2}+a_2\frac{r_{AB}^4}{\sigma_0^4}\right) \; , \tag{B.4}$$

which is inspired by the cumulant expansion. The coefficients σ_0^2, a_1 and a_2 are to be determined by the conditional moments defined in eq. 4.26.

It is possible, to determine approximatively higher moments than the second one from eq. (4.19),

$$\langle r_{AB}^4\rangle|_{R_A^2,R_B^2} \approx \frac{5}{3}\left[\sigma_{AB}^4 - \left(R_A^4+R_B^4\right)\right] \tag{B.5}$$

$$\langle r_{AB}^6\rangle|_{R_A^2,R_B^2} \approx \frac{35}{9}\left[\sigma_{AB}^6 - 2\left(2\,R_A^6+3\,R_A^4R_B^2+3\,R_A^2R_B^4+2\,R_B^6\right)\right] \; . \tag{B.6}$$

In the determination of the fourth and sixth moment some integrals are neglected, that could not be solved exactly. We checked the accuracy of the expressions (B.5, B.6) by Monte Carlo simulations and found a satisfying agreement, the relative error being smaller than about 0.1 in the regions of high probability $P(R_A^2, R_B^2)$, justifying the result a posteriori.

Then the coefficients σ_0^2, a_1 and a_2 are given in terms of the conditional moments (4.27, B.5, B.6). As to be expected for this kind of treatment (a cutoff cumulant expansion), the polynomial term is negative for large $u_{AB} = r_{AB}^2/\sigma_0^2$ and thus also P_C. This failure can be compensated by increasing the degree of the polynomial by one and requiring, that this polynomial has a minimum, where the original polynomial goes to zero, thus determining the coefficient a_3. The

spurious error for large u_{AB} can be minimized by dividing the polynomial by a suitable term, leading to

$$P_C(r_{AB}^2; R_A^2, R_B^2) = C\sqrt{\frac{r_{AB}^2}{2\pi}}\left(\frac{3}{\sigma_0^2}\right)^{\frac{3}{2}} \exp\left(-\frac{3}{2}u_{AB}\right)\left(\frac{1 + a_1 u_{AB} + a_2 u_{AB}^2 + a_3 u_{AB}^3}{1 + a_3 u_{AB}^3}\right) . \quad \text{(B.7)}$$

As we are mainly interested in determining F_{intra}, the determination of the normalization factor C is of minor importance, because it leads to an additive constant only. (If necessary, it can be determined either numerically or in terms of a modified hypergeometric function.)

In principle, a systematic polynomial expansion of this kind is possible, the coefficients a_i being determined by higher conditional moments.

C Calculation of Integrals

C.1 Ellipsoid–Ellipsoid Interaction

In this section we derive an explicit expression for the interaction between two ellipsoids, defined in eq. (3.5) in the case that the monomer densities are given by eq. (3.17).

When inserting eqs. (3.17, 3.16) into eqs. (3.13, 3.5) the calculation of F_{inter} reduces to a sum of nine terms of the form

$$\int_{-\infty}^{+\infty} d^3y \; \chi^{(1)}(\mathbf{y})\, \chi^{(2)}(\mathbf{y})\,, \tag{C.1}$$

where the functions $\chi^{(j)}(\mathbf{y})\;,\; j=1,2$ are given by

$$\begin{aligned} \chi^{(j)}(\mathbf{y}) &= \frac{1}{(2\pi)^{3/2}\prod_{\alpha=1}^{3}\sigma_\alpha^{(j)}} \exp\left(-\frac{1}{2}\sum_\alpha\left(\frac{x_\alpha^{(j)}(\mathbf{y})}{\sigma_\alpha^{(j)}}\right)^2\right)\;, \quad \text{with} \\ x_\alpha^{(j)}(\mathbf{y}) &= \sum_\beta \mathcal{R}_{\alpha\beta}^{(j)}(y_\beta - w_\beta^{(j)}) \quad \text{and} \quad \sigma_\alpha^{(j)} = R_\alpha^{(j)}\sigma_\alpha\,. \end{aligned} \tag{C.2}$$

The σ_α were defined in eq. (3.17) and specified in tab. 3.2. Moreover, $w_\alpha^{(j)} = \pm\mathcal{R}_{1,\alpha}R_1^{(j)}\bar{u}_1 + r_\alpha^{(j)}$ or $w_\alpha^{(j)} = r_\alpha^{(j)}$ depending on which of the three terms in eq. (3.17a) contributes to $\chi^{(j)}(\mathbf{y})$. With the definitions

$$\sigma \equiv \prod_{\alpha=1}^{3}\sigma_\alpha^{(1)}\sigma_\alpha^{(2)} \quad \text{and} \quad T(\mathbf{y}) \equiv \sum_{\alpha=1}^{3}\left\{\left(\frac{x_\alpha^{(1)}(\mathbf{y})}{\sigma_\alpha^{(1)}}\right)^2 + \left(\frac{x_\alpha^{(2)}(\mathbf{y})}{\sigma_\alpha^{(2)}}\right)^2\right\} \tag{C.3}$$

expression (C.1) reads

$$\frac{1}{(2\pi)^3\sigma}\int_{-\infty}^{+\infty} d^3y \, \exp\left[-\frac{1}{2}\,T(\mathbf{y})\right]\;. \tag{C.4}$$

Since

$$\sum_\gamma\left(\frac{x_\gamma^{(j)}(\mathbf{y})}{\sigma_\gamma^{(j)}}\right)^2 = \sum_{\alpha,\beta}\mathcal{L}_{\alpha\beta}^{(j)}\left(y_\alpha y_\beta - 2w_\alpha^{(j)}y_\beta + w_\alpha^{(j)}w_\beta^{(j)}\right)\;, \quad \text{with} \quad \mathcal{L}_{\alpha\beta}^{(j)} = \sum_\gamma \frac{\mathcal{R}_{\gamma\alpha}^{(j)}\mathcal{R}_{\gamma\beta}^{(j)}}{\left(\sigma_\gamma^{(j)}\right)^2}\,, \tag{C.5}$$

it follows that

$$T(\mathbf{y}) = \sum_{\alpha,\beta} \mathcal{A}_{\alpha\beta} y_\alpha y_\beta + \sum_\alpha B_\alpha y_\alpha + C\,, \quad \text{where} \quad \mathcal{A}_{\alpha\beta} = \mathcal{L}^{(1)}_{\alpha\beta} + \mathcal{L}^{(2)}_{\alpha\beta}\,,$$
$$B_\alpha = -2 \sum_\beta \left(\mathcal{L}^{(1)}_{\beta\alpha} w^{(1)}_\beta + \mathcal{L}^{(2)}_{\beta\alpha} w^{(2)}_\beta \right), \quad \text{and} \quad C = \sum_{\alpha,\beta} \left(\mathcal{L}^{(1)}_{\alpha\beta} w^{(1)}_\alpha w^{(1)}_\beta + \mathcal{L}^{(2)}_{\alpha\beta} w^{(2)}_\alpha w^{(2)}_\beta \right). \quad \text{(C.6)}$$

The quadratic form (C.6) can be rewritten as

$$T(\mathbf{y}) = \sum_{\alpha,\beta} (y_\alpha - w_\alpha)\, \mathcal{D}_{\alpha\beta}\, (y_\beta - w_\beta) + E\,, \quad \text{(C.7)}$$

which yields

$$\int_{-\infty}^{+\infty} d^3y\, \chi^{(1)}(\mathbf{y})\, \chi^{(2)}(\mathbf{y}) = \frac{\exp(-E/2)}{(2\pi)^{3/2} \sigma \sqrt{\det \mathcal{D}}}\,, \quad \text{(C.8)}$$

$$4 \det \mathcal{D} = 4\, \mathcal{A}_{11}\mathcal{A}_{22}\mathcal{A}_{33} + \mathcal{A}_{12}\mathcal{A}_{13}\mathcal{A}_{23} - \mathcal{A}^2_{13}\mathcal{A}_{22} - \mathcal{A}^2_{23}\mathcal{A}_{11} - \mathcal{A}^2_{12}\mathcal{A}_{33}\,, \quad \text{(C.9)}$$

$$\begin{aligned} E = C \;+\; & \Big[B_1^2(\mathcal{A}_{23}^2 - 4\,\mathcal{A}_{22}\mathcal{A}_{33}) + B_2^2(\mathcal{A}_{13}^2 - 4\,\mathcal{A}_{11}\mathcal{A}_{33}) + B_3^2(\mathcal{A}_{12}^2 - 4\,\mathcal{A}_{11}\mathcal{A}_{33}) \\ + \;& 2\,B_1B_2(2\,\mathcal{A}_{12}\mathcal{A}_{33} - \mathcal{A}_{13}\mathcal{A}_{23}) + 2\,B_1B_3(2\,\mathcal{A}_{13}\mathcal{A}_{22} - \mathcal{A}_{12}\mathcal{A}_{23}) \\ + \;& 2\,B_2B_3(2\,\mathcal{A}_{23}\mathcal{A}_{11} - \mathcal{A}_{12}\mathcal{A}_{13}) \Big] \frac{1}{16 \det \mathcal{D}}\,. \end{aligned} \quad \text{(C.10)}$$

C.2 Ellipsoid–Wall Interaction

The integrals in eq. (6.2) with a potential of the form eq. (6.3) and monomer densities, that are essentially sums and products of Gaussian functions, see eq. (3.17), can be cast into the more general form already treated in the previous section C.1. The six resulting integrals of eq. (6.2) are of the form

$$\int_{-\infty}^{+\infty} d^3y\; \chi(\mathbf{y})\, \psi(y_3)\,, \quad \text{(C.11)}$$

where

$$\psi(y_3) = \exp\left(\pm \frac{y_3}{2\, l_w} \right) \quad \text{(C.12)}$$

and

$$\chi(\mathbf{y}) = \frac{1}{(2\pi)^{3/2} \prod_{\alpha=1}^3 \tilde{\sigma}_\alpha} \exp\left(-\frac{1}{2} \sum_\alpha \left(\frac{x_\alpha(\mathbf{y})}{\tilde{\sigma}_\alpha} \right)^2 \right), \quad \text{with}$$
$$x_\alpha(\mathbf{y}) = \sum_\beta \mathcal{R}_{\alpha\beta}(y_\beta - w_\beta) \quad \text{and} \quad \tilde{\sigma}_\alpha = R_\alpha \sigma_\alpha\,. \quad \text{(C.13)}$$

The notation and the definitions are the same as in sec. C.1. An analogous calculation yields the same result for the integral as in eqs. (C.8–C.10), except for the values of $\mathcal{A}_{\alpha\beta}, B_\alpha$ and C, that in the present case read

$$\mathcal{A}_{\alpha\beta} = \mathcal{L}_{\alpha\beta}\,, \quad B_\alpha = \mp\frac{\delta_{\alpha 3}}{l_w} - 2\sum_\beta \mathcal{L}_{\beta\alpha} w_\beta\,, \quad \text{and} \quad C = \sum_{\alpha,\beta} \mathcal{L}_{\alpha\beta} w_\alpha w_\beta\,. \tag{C.14}$$

The negative sign in front of the Kronecker–delta in eq. (C.14) corresponds to the positive sign in eq. (C.12) and vice versa.

In the case of a patterned substrate, we define $l_\parallel = L_\parallel/4\pi$ and write for the first part of the wall potential

$$V_w(y_2, y_3) = \hat{\epsilon}_w \exp\left(-\frac{y_3}{2l_w}\right)\left[1 \pm \delta_w \cosh\left(\frac{iy_2}{2l_\parallel}\right)\right]\,. \tag{C.15}$$

Thus the integration of the respective exponential functions can be performed as above. Only the form of B_α changes, which now reads

$$B_\alpha = \frac{\delta_{\alpha 3}}{l_w} \mp \frac{\delta_{\alpha 2} i}{l_\parallel} - 2\sum_\beta \mathcal{L}_{\beta\alpha} w_\beta\,, \tag{C.16}$$

where the negative sign refers to the first imaginary exponential function in eq. (C.15), while the positive sign refers to the second one, respectively.

C.3 Fourier Transform of the Monomer Density

For a total monomer density defined by

$$\varrho'(\mathbf{y}) \equiv \frac{1}{M(N+1)} \sum_{i=1}^{M} \varrho_i'(\mathbf{y})\,, \tag{C.17}$$

the Fourier transform is given by

$$\rho(\mathbf{k}) = \int_{-\infty}^{\infty} d^3y\, \varrho'(\mathbf{y})\, \exp(-i\,\mathbf{k}\cdot\mathbf{y})\,. \tag{C.18}$$

Inserting the $\varrho_i'(\mathbf{y})$ from eq. (3.13) with (3.17, 3.16) yields

$$\rho(\mathbf{k}) = \frac{1}{2+c_1}\frac{1}{M}\sum_{i=1}^{M}\left\{\int_{-\infty}^{\infty} d^3y\, e^{-i\,\mathbf{k}\cdot\mathbf{y}}\left[\chi_{\mathrm{a}}^{(i)}(\mathbf{y}) + \chi_{\mathrm{b}}^{(i)}(\mathbf{y}) + c_1\,\chi_{\mathrm{c}}^{(i)}(\mathbf{y})\right]\right\}\,. \tag{C.19}$$

The three different functions $\chi_{\mathrm{a}}^{(i)}(\mathbf{y})$, $\chi_{\mathrm{b}}^{(i)}(\mathbf{y})$ and $\chi_{\mathrm{c}}^{(i)}(\mathbf{y})$ are defined in eq. (C.2), where all different kinds of $w_\alpha^{(j)}$ occur, i.e. $w_{\alpha,\mathrm{a}}^{(j)} = +\mathcal{R}_{1,\alpha} R_1^{(j)} \bar{u}_1 + r_\alpha^{(j)}$, $w_{\alpha,\mathrm{b}}^{(j)} = -\mathcal{R}_{1,\alpha} R_1^{(j)} \bar{u}_1 + r_\alpha^{(j)}$ and

$w_{\alpha,c}^{(j)} = r_\alpha^{(j)}$, respectively. The integration is straightforward yielding the final result

$$\rho(\mathbf{k}) = \frac{1}{(2+c_1)\sigma_1\sigma_2\sigma_3}\frac{1}{M}\sum_{i=1}^{M}\frac{1}{\sqrt{S_1^{(i)}S_2^{(i)}S_3^{(i)}}}\frac{1}{\sqrt{\det\mathcal{G}^{(i)}}}\exp\left(-\frac{1}{2}\sum_{\alpha,\beta}k_\alpha\mathcal{G}_{\alpha\beta}^{(i)^{-1}}k_\beta\right) \times\exp\left(-i\sum_\beta k_\beta r_\beta^{(i)}\right)\left[2\cos\left(\sum_\beta k_\beta\mathcal{R}_{1\beta}^{(i)}R_1^{(i)}\bar{u}_1\right)+c_1\right]. \quad \text{(C.20)}$$

Here we defined

$$\mathcal{G}_{\alpha\beta}^{(i)} \equiv \sum_\gamma g_\gamma^{(i)}\mathcal{R}_{\gamma\alpha}^{(i)}\mathcal{R}_{\gamma\beta}^{(i)} \quad \text{(C.21)}$$

$$g_\gamma^{(i)} \equiv \left(\left(\sigma_1^2S_1^{(i)}\right)^{-1},\left(\sigma_2^2S_2^{(i)}\right)^{-1},\left(\sigma_3^2S_3^{(i)}\right)^{-1}\right). \quad \text{(C.22)}$$

The center of mass of the ith particle is denoted by $r_\beta^{(i)}$. The intermediate scattering function is then obtained by using eq. (C.20) in eq. (5.9) for all times t (for the A ellipsoids).

C.4 Lateral Fourier Transform of the Density

The calculation of

$$\rho_\parallel(\mathbf{k}_\parallel,y_3) = \frac{1}{M(N+1)}\sum_{i=1}^{M}\int_{-\infty}^{+\infty}d^2y_\parallel\, e^{-i\mathbf{k}_\parallel\cdot\mathbf{y}_\parallel}\varrho_i'(\mathbf{y}_\parallel,y_3) \quad \text{(C.23)}$$

is analogous to the derivation of $\rho(\mathbf{k})$ given in app. C.3, except that no Fourier transform with respect to the y_3–direction is carried out. We only give the result,

$$\rho_\parallel(\mathbf{k}_\parallel,y_3) = \frac{1}{\sqrt{2\pi}}\frac{1}{(2+c_1)\sigma_1\sigma_2\sigma_3}\frac{1}{M}\sum_{i=1}^{M}\frac{1}{\sqrt{S_1^{(i)}S_2^{(i)}S_3^{(i)}}}\frac{1}{\sqrt{\det\mathcal{G}^{(i)}}}\frac{1}{\sqrt{2\,\mathcal{G}_{33}^{(i)^{-1}}}}\times$$
$$\exp\left(-\frac{1}{2}\sum_{\alpha=1}^{2}\sum_{\beta=1}^{2}k_\alpha\mathcal{G}_{\alpha\beta}^{(i)^{-1}}k_\beta\right)\exp\left[\frac{1}{2}\left(\frac{i\left(y_3-r_3^{(i)}\right)}{\sqrt{2\,\mathcal{G}_{33}^{(i)^{-1}}}}-\frac{1}{2\sqrt{2\,\mathcal{G}_{33}^{(i)^{-1}}}}\sum_{\beta=1}^{2}k_\beta G_{3\beta}^{(i)}\right)^2\right]\times$$
$$\exp\left(-i\sum_{\beta=1}^{2}k_\beta r_\beta^{(i)}\right)\times\left\{\exp\left(-\frac{1}{2}\frac{\left(\mathcal{R}_{13}^{(i)}\bar{u}_1\right)^2S_1^{(i)}}{2\,\mathcal{G}_{33}^{(i)^{-1}}}\right)\times\right.$$
$$\left.2\cos\left[\frac{\mathcal{R}_{13}\bar{u}_1\sqrt{S_1^{(i)}}}{2\,\mathcal{G}_{33}^{(i)^{-1}}}\left(i\left(y_3-r_3^{(i)}\right)-\frac{1}{2}\sum_{\beta=1}^{2}k_\beta G_{3\beta}^{(i)}\right)+\sum_{\alpha=1}^{2}k_\alpha\mathcal{R}_{1\alpha}\bar{u}_1\sqrt{S_1^{(i)}}\right]+c_1\right\}, \quad \text{(C.24)}$$

with the definitions (C.21, C.22) for $\mathcal{G}_{\alpha\beta}^{(i)}$ and $g_\gamma^{(i)}$ respectively, and

$$G_{3\beta}^{(i)} \equiv \mathcal{G}_{\beta 3}^{(i)^{-1}} + \mathcal{G}_{3\beta}^{(i)^{-1}} \,. \tag{C.25}$$

The quantities $\mathcal{R}_{\alpha\beta}^{(i)}$ and $r_{\alpha}^{(i)}$ denote the rotation matrix and the center of mass of the ith particle respectively. The constants $\sigma_1, \sigma_2, \sigma_3, c_1$ and $\bar{u}_1$ are given in tab. 3.2. Using eq. (C.24) it is straightforward to calculate the lateral intermediate scattering function, eq. (6.10).

D GEM: Algorithm

In this section we describe the algorithm used in the simulations of the GEM. The Monte Carlo method is well established, for an introduction see refs. [Lan00, New99, Bin95a]. Therefore we just discuss the data structures and procedures allowing for a fast computation of the interaction term F_{inter}, which poses the main challenge for the setup of an optimal algorithm.

The first optimization step has already been done, by approximating the densities by a product of a superposition of Gaussian functions, cf. eqs. (3.16, 3.17), and calculating the involved integrals analytically, see app. C.1. Therefore it is not necessary to determine numerically three dimensional integrals for every calculation. Nevertheless, the optimization of the algorithm is still a challenge, because in a dense system one polymer overlaps with many other ones.

D.1 Data Structure

It is crucial to calculate only those interaction terms, which contribute significantly to F_{inter}. Therefore, the monomer density has to be cutoff at a certain length and we choose this cutoff to be $u_{\text{cut}} \equiv x_{\alpha,\text{cut}}/R_\alpha = 2.2$, cf. fig. 4.7. The neighbors of a polymer are defined as those polymers, which interpenetrate each other within their cutoff shape. Because the ellipsoids are strongly aspherical, a simple test of the distance between the centers of mass is not efficient enough.

In order to determine whether two ellipsoids are neighbors, we introduced a grid of cells, with a spatial discretization length given by the smallest significant scale, $G_c \equiv 2\, u_{\text{cut}} \sqrt{\langle S_3 \rangle}$. The final equilibrium size of $\langle S_3 \rangle$ in a dense system is not known a priory, therefore $\langle S_3 \rangle = 0.010568N$ is taken from the free Gaussian chain, cf. tab. B.1. In a dense system $\langle S_3 \rangle$ will be larger, cf. fig. 5.2, but the dependence on ϵ is rather weak, and the loss in efficiency is not crucial. We note in passing, that in a dilute system $\langle S_3 \rangle$ of the Gaussian chain is much too small, because in this case $\langle S_3 \rangle \sim N^{6/5}$ instead of $\langle S_3 \rangle \sim N$. This poses no problem with respect to efficiency, since in a dilute system the number of neighbors is small, and the calculation is much faster than in a dense system.

To every cell in the grid then is assigned a list of polymers, that overlap with the cell, and conversely, to every polymer is assigned a list of cells, which it covers. Determining the neighbors j of one polymer i is simple: One goes through the list of cells assigned to polymer i, determines all polymers j that are associated with each member of this list and finally sorts out multiple occurrences of j. For each polymer we also keep a list entailing the neighbors with the respective interaction energies, and the total value of the interaction energy with the neighbors.

We note that in the case of confining walls the interaction between the walls and the ellipsoids is never cut off. In the case of thick slabs, most computational time is consumed by the calculation of the ellipsoid–ellipsoid interaction and a cutoff of the wall–ellipsoid would not increase efficiency significantly. For thin slabs, a proper calculation of the wall interaction is indispensable. Moreover, in thin slabs the calculation is faster, because the average number of neighbors is smaller.

D.2 Algorithm

For performing one elementary step of the Monte Carlo simulation, we try to change either the orientation $\mathcal{R}_{\alpha\beta}$, the center of mass position $\mathbf{r}$ or the eigenvalues $\mathbf{S}$ of one randomly chosen ellipsoid as explained in sec. 3.4. Therefore a test–ellipsoid is generated and its free energy compared to the original one. We note that this test–ellipsoid has its own neighbor– and grid–lists.

A trial for a change from an initial state i to a final state f is accepted with a probability p_{if} given by the Glauber rule, i.e.

$$p_{if} = \frac{1}{2}\left[1 - \tanh\left(\frac{F_f - F_i}{2\,k_\mathrm{B}T}\right)\right] , \tag{D.1}$$

where F_i and F_f are the free energies of the initial and final state, respectively.

If the move is accepted, all relevant data have to be updated. First, this is done with the grid. Then all neighbor lists are updated. The ellipsoid is removed from the lists of its neighbors in the old state and inserted in the neighbor lists of its new neighbors. Especially its new total interaction energy with all neighbors has to be updated. Finally, the state of the test–ellipsoid is assigned to the state of the chosen ellipsoid.

In this way, the algorithm minimizes the calculations necessary to determine F_inter. Nevertheless, the calculation of F_inter consumes the main part of the CPU time. Therefore we parallelized this part, thus speeding up the simulation by a factor of 1.5 on a two processor machine.

With the method described here, a fast calculation of F_inter is possible. The time for calculation depends essentially both on the overall monomer concentration c and on N (or on $\bar{R}_G$), because these quantities determine the average number of neighbors of one particle.

D.3 Standard Initial Conditions

Unless noted otherwise, the initial conditions are as follows: The center of mass positions of the ellipsoids are randomly distributed within the simulation box. The orientations of the ellipsoids are random, and the eigenvalues $\mathbf{S}_i$ are drawn from the distribution $P(\mathbf{S}, N)$ for the non–interacting Gaussian chains given in eq. (4.11). The S_α are sorted afterwards according to rule (3.10).

Bibliography

[Bas00a] J. Baschnagel, K. Binder, P. Doruker, A. A. Gusev, O. Hahn, K. Kremer, W. L. Mattice, F. Müller–Plathe, M. Murat, W. Paul, S. Santos, U. W. Suter, and V. Tries, "Bridging the Gap Between Atomistic and Coarse–Grained Models of Polymers: Status and Perspectives", Advances in Polymer Science **152**, 41 (2000).

[Bas00b] J. Baschnagel, K. Binder, and A. Milchev, "Mobility of Polymers Near Surfaces" in *Polymer Surfaces, Interfaces and Thin Films*, ed. A. Karim and S. Kumar, World Scientific, Singapore (2000), and references therein.

[Bin81] K. Binder, Z. Phys. B **43**, 119 (1981).

[Bin83] K. Binder, "Critical Behaviour at Surfaces" in *Phase Transitions and Critical Phenomena* **8**, ed. C. Domb and J. L. Lebowitz, London Academic Press (1983).

[Bin91a] K. Binder and H. L. Frisch, Z. Phys. B **84**, 403 (1991).

[Bin91b] K. Binder, "Spinodal Decomposition" in *Materials Science and Technology* **5**, 405, ed. Cahn, Haasen, and Kramer, VCH Weinheim (1991).

[Bin94] K. Binder, "Phase Transitions in Polymer Blends and Block Copolymer Melts: Some Recent Developments", Advances in Polymer Science **112**, 183 (1994).

[Bin95a] *Monte Carlo and Molecular Dynamics Simulations in Polymer Science*, ed. K. Binder, Oxford University Press, New York (1995).

[Bin95b] K. Binder, "Monte Carlo Studies of Polymer Blends and Block Copolymer Thermodynamics", in ref. [Bin95a], 356, and references therein.

[Bin98] K. Binder, J. Non-Equil. Thermodyn. **23**, 1 (1998).

[Bin99] K. Binder, "Phase Transitions of Polymer Blends and Block Copolymer Melts in Thin Films", Advances in Polymer Science **138**, 1 (1999).

[Böl98] M. Böltau, S. Walheim, J. Mlynek, G. Krausch, and U. Steiner, Nature **391**, 877 (1998).

[Bra94] A. J. Bray, Adv. Phys. **43**, 357 (1994).

[Bro93] G. Brown and A. Chakrabarti, Phys. Rev. E **48**, 3705 (1993).

[Bru92] F. Bruder and R. Brenn, Phys. Rev. Lett. **69**, 624 (1992).

[Cha95] P. M. Chaikin and T. C. Lubensky, *Principles of Condensed Matter Physics*, Cambridge University Press (1995).

[Deu93] H.–P. Deutsch and K. Binder, J. Phys. (France) II **3**, 1049 (1993).

[Doi88] M. Doi and S. F. Edwards, *The Theory of Polymer Dynamics*, Oxford Science Publications (1988).

[Eic77] B. E. Eichinger, Macromolecules **10**, 671 (1977).

[Eic85] B. E. Eichinger, Macromolecules **18**, 211 (1985).

[Erm98] B. D. Ermi, A. Karim, and J. F. Douglas, J. Poly. Sci. B: Poly. Phys. **36**, 191 (1998).

[Eur01] F. Eurich and P. Maass, J. Chem. Phys. **114**, 7655 (2001).

[Eur02] F. Eurich, P. Maass, and J. Baschnagel, J. Chem. Phys. **117**, 4564 (2002).

[Fis97a] H. P. Fischer, P. Maass, and W. Dieterich, Phys. Rev. Lett. **79**, 893 (1997).

[Fis97b] H. P. Fischer, *Zur Theorie der spinodalen Entmischung: Wandeffekte und Ordnungsbildung*, UFO–Dissertation **326**, UFO Atelier für Gestaltung & Verlag (1997), ISBN 3–930803–25–9.

[Fis98a] H. P. Fischer, J. Reinhard, W. Dieterich, J.–F. Gouyet, P. Maass, A. Majhofer, and D. Reinel, J. Chem. Phys. **108**, 3028 (1998).

[Fis98b] H. P. Fischer, P. Maass, and W. Dieterich, Europhys. Lett. **42**, 49 (1998).

[Fix62] M. Fixman, J. Chem. Phys. **36**, 306 (1962).

[Flo50] P. J. Flory and W. R. Krigbaum, J. Chem. Phys. **18**, 1086 (1950).

[Flo66] P. J. Flory and S. Fisk, J. Chem. Phys. **44**, 2243 (1966).

[Flo74] P. J. Flory, Macromolecules **7**, 381 (1974).

[For63] W. C. Forsman and R. E. Hughes, J. Chem. Phys. **38**, 2118 (1963).

[Fra96] A. A. Fraerman, A. S. Mel'nikov, I. M. Nefedov, I. A. Shereshevskii, and A. V. Shpiro, Phys. Rev. B **55**, 6316 (1996).

[Fri95] H. L. Frisch, P. Nielaba, and K. Binder, Phys. Rev. E **52**, 2848 (1995); Phys. Rev. E **57**, 1205 (1998).

[Fri99] H. L. Frisch, S. Puri, and P. Nielaba, J. Chem. Phys. **110**, 10514 (1999).

[Fuk00] K. Fukunaga, H. Elbs, and G. Krausch, Langmuir **16**, 3474 (2000).

[Geh92] M. D. Gehlsen, J. H. Rosedale, F. S. Bates, C. D. Wignall, and K. Almdal, Phys. Rev. Lett. **68**, 2452 (1992).

[Gen79] P.–G. de Gennes, *Scaling Concepts in Polymer Physics*, Cornell University Press, Ithaca, New York (1979).

[Gen80] P.–G. de Gennes, J. Chem. Phys. **72**, 4756 (1980).

[Gre95] G. S. Grest and M. Murat "Computer Simulations of Tethered Chains" in ref. [Bin95a], 476, and references therein.

[Gro94] A. Y. Grosberg and A. R. Khokhlov, *Statistical Physics of Macromolecules*, AIP Press (1994).

[Gob74] W. Gobush, K. Šolc, and W. H. Stockmayer, J. Chem. Phys. **60**, 12 (1974).

[Hab00] C. Haber, S. A. Rulz, and D. Wirtz, PNAS **97**, 10792 (2000).

[Hof97] A. Hoffmann, J. U. Sommer, and A. Blumen, J. Chem. Phys. **106**, 6709 (1997).

[Hon81] K. M. Hong and J. Noolandi, Macromolecules **14**, 727 (1981).

[Isr00] J. Israelachvili, *Intermolecular and Surface Forces*, Academic Press, San Diego (2000).

[Jan96] H. W. H. M. Janszen, T. A. Tervoort, and P. Cifra, Macromolecules **29**, 5678 (1996).

[Kar98] A. Karim, J. F. Douglas, B. P. Lee, S. C. Glotzer, J. A. Rogers, R. J. Jackman, E. J. Amis, and G. M. Whitesides, Phys. Rev. E **57**, R6273 (1998).

[Ken01] R. Kenzler, F. Eurich, P. Maass, B. Rinn, J. Schropp, E. Bohl, and W. Dieterich, Comp. Phys. Comm. **133**, 139 (2001).

[Kie99] L. Kielhorn and M. Muthukumar, J. Chem. Phys. **111**, 2259 (1999).

[Kra93] G. Krausch, C. Dai, E. J. Kramer, and J. F. Marko, Macromolecules **26**, 5566 (1993).

[Kra95] G. Krausch, "Surface Induced Self Assembly in Thin Polymer Films", in Materials Science and Engineering **R14**, 1 (1995).

[Kre90] K. Kremer and G. S. Grest, J. Chem. Phys. **92**, 5057 (1990).

[Kre95] K. Kremer ans G. S. Grest, "Entanglement Effects in Polymer Melts and Networks", in ref. [Bin95a], 194, and references therein.

[Kre00] T. Kreer, J. Baschnagel, M. Müller, and K. Binder, Macromolecules **34**, 1105 (2001).

[Kre01] K. Kremer, private communication.

[Kuh34] W. Kuhn, Kolloid–Zeitschrift **68**, 2 (1934).

[Lan00] D. P. Landau and K. Binder, *A Guide to Monte–Carlo Simulations in Statistical Physics*, Cambridge University Press (2000).

[Lag71] J. S. Langer, Annals of Physics **65**, 53 (1971).

[Lag92] J. S. Langer, "An Introduction to the Kinetics of First–Order Phase Transition", in *Solids far from equilibrium*, ed. C. Godrèche, Cambridge University Press (1992).

[Len98] P. Lenz and R. Lipowski, Phys. Rev. Lett. **80**, 1920 (1998).

[Lou00] A. A. Louis, P. G. Bolhuis, J. P. Hansen, and E. J. Meijer, Phys. Rev. Lett. **85**, 2522 (2000).

[Mat94] M. W. Matsen and M. Schick, Phys. Rev. Lett. **72**, 2660 (1994).

[Mil65] R. E. Miles, Biometrika **52**, 636 (1965).

[Min98] S. T. Milner and T. C. B. Mc Leish, Phys. Rev. Lett. **81**, 725 (1998).

[Mis01] C. Mischler, J. Baschnagel, and K. Binder, Adv. Coll. Interf. Sci. **94**, 197 (2001), and references therein.

[Mül95] M. Müller, K. Binder, and W. Oed, J. Chem. Soc. Faraday Trans. **91**, 2369 (1995).

[Mül98] M. Müller, Macromolecules **31**, 9044 (1998).

[Mur98] M. Murat and K. Kremer, J. Chem. Phys. **108**, 4340 (1998).

[New99] M. E. J. Newman and G. T. Barkema, *Monte Carlo Methods in Statistical Physics*, Clarenton Press, Oxford (1999).

[Oon87] Y. Oono and S. Puri, Phys. Rev. Lett. **58**, 836 (1987).

[Pan97] R. S. Pai–Panandiker, J. R. Dorgan, and T. Pakula, Macromolecules **30**, 6348 (1997).

[Pap00] C. M. Papadakis, K. Almdal, K. Mortensen, F. Rittig, and P. Štěpánek, Macomol. Symp. **162**, 275 (2000).

[Pau95] W. Paul and J. Baschnagel, "Monte Carlo Simulations of the Glass Transition of Polymers", in ref. [Bin95a], 307, and references therein.

[Pre95] W. H. Press, S. A. Teukolsky, W. T. Vetterling, and B. P. Flannery, *Numerical Recipies in C*, 2nd edition, Cambridge University Press (1995).

[Pur97] S. Puri and H. L. Frisch, J. Phys.: Condens. Matter **9**, 2109 (1997).

[Rac01] R. Racke and S. Zheng, Konstanzer Schriften in Mathematik und Informatik **150**, ISSN 1430–3558 (2001).

[Reh97] M. Rehan, W. L. Mattice, and U. W. Suter, "Rotational Isomeric State Models in Macromolecular Systems", Advances in Polymer Science **131/132**, Springer (1997).

[Rei01] E. Reister, M. Müller, and K. Binder, Phys. Rev. E **64**, 041804 (2001).

[Roc99] L. Rockford, Y. Liu, P. Mansky, and T. P. Russell, Phys. Rev. Lett. **82**, 2602 (1999).

[Rou95] Y. Rouault, J. Baschnagel, and K. Binder, J. Stat. Phys. **80**, 1009 (1995).

[Rud86] J. Rudnick and G. Gaspari, J. Phys. A **19**, L191 (1986).

[Sap96] D. Sappelt, *Spinodale Entmischung mit glassartiger Erstarrung einer Phase*, UFO–Dissertation **309**, UFO Atelier für Gestaltung & Verlag (1997), ISBN 3–930803–08–9.

[Sar88] A. Sariban and K. Binder, Macromolecules **21**, 711 (1988).

[Sar91] A. Sariban and K. Binder, Macromolecules **24**, 578 (1991).

[Sch98] F. Schmid, J. Phys.: Condens. Mat. **10**, 8105 (1998).

[Scr00] J. Schropp, private communication.

[Sol71a] K. Šolc and W. H. Stockmayer, J. Chem. Phys. **54**, 2756 (1971).

[Sol71b] K. Šolc, J. Chem. Phys. **55**, 335 (1971).

[Str95] W. A. Strauss, *Partielle Differentialgleichungen – Eine Einführung*, chapter 5, Vieweg (1995).

[Stu96] A. M. Stuart and A. R. Humphries, *Dynamical Systems and Numerical Analysis*, section 5.6, Cambridge Monographs on Applied and Computational Mathematics (1996).

[Sun96] L. Sung, A. Karim, J. F. Douglas, and C. C. Han, Phys. Rev. Lett. **76**, 4368 (1996).

[Tan95] K. Tanaka, J.–S. Yoon, A. Takahara, and T. Kajiyama, Macromolecules **28**, 934 (1995).

[Tag93] H. Tang, I. Szleifer, and S. K. Kumar, J. Chem. Phys. **100**, 5367 (1993).

[The85] D. N. Theodorou and U. W. Suter, Macromolecules **18**, 1206 (1985).

[Vli90] J. H. van Vliet and G. ten Brinke, J. Chem. Phys. **93**, 1436 (1990).

[Wal00] S. Walheim, *Micrometer and Sub–Micrometer Structure Formation of Phase Separating Polymer Films*, Konstanzer Online–Publikations–System, http://www.ub.uni-konstanz.de/kops/volltexte/2000/552.

[Wei90] G. Wei and B. E. Eichinger, Macromolecules **23**, 4845, (1990).

[Yam71] H. Yamakawa, *Modern Theory of Polymer Solutions*, Harper & Row, New York (1971).

[Yet90] A. Yethiraj and C. K. Hall, Macromolecules **23**, 1865 (1990).

[Yet94] A. Yethiraj, J. Chem. Phys. **101**, 2489 (1994).

[Yoo95] D. Y. Yoon, M. Vacatello, and G. D. Smith "Simulation Studies of Polymer Melts at Interfaces" in ref. [Bin95a], 433, and references therein.

Last Not Least...

Zum Schluss möchte ich mich ganz herzlich bei all denjenigen bedanken, die zum Gelingen dieser Arbeit beigetragen haben.

Meinem Doktorvater Prof. Dr. Philipp Maaß danke ich für die hervorragende Betreuung der Arbeit. Ich habe von ihm nicht nur viel über physikalische Denkweisen, sondern auch über Politik in der Wissenschaft gelernt. Dabei hatten wir zusammen viel zu lachen, auch dann, wenn ich nicht mehr gesehen habe, wie es gerade weiter gehen soll.

Prof. Dr. Wolfgang Dieterich danke ich für seine Anregungen und das stete Interesse, dass er meiner Arbeit entgegen gebracht hat, sowie die Möglichkeiten, die sich mir an seinem Lehrstuhl geboten haben.

Dr. Bernd Rinn danke ich für die interessanten Diskussionen, die sich quer über den Schreibtisch hinweg ergeben haben, und dafür, dass er viele meiner Computerprobleme gelöst hat. Insbesondere hat er ein Parallelisierungspaket geschrieben, das für meine Simulationen sehr hilfreich war.

Bei Dr. Hans–Peter Fischer bedanke ich mich dafür, dass er mir die Cahn–Hilliard Theorie erklärt hat, sowie für einige wirklich gute Filmtipps.

Für die gute und konstruktive Zusammenarbeit bei den numerischen Arbeiten zur Cahn–Hilliard Theorie, bedanke ich mich bei Prof. Dr. Erich Bohl, Dr. Johannes Schropp und Rainer Kenzler.

Prof. Dr. Andrzej Majhofer und Prof. Dr. Kurt Kremer danke ich für interessante Diskussionen und wertvolle Hinweise zu vollkommen unterschiedlichen Aspekten dieser Arbeit.

Bei Prof. Dr. Jörg Baschnagel bedanke ich mich für die wunderbare Gastfreundschaft während meines Aufenthaltes in Straßburg, sowie die fruchtbare Zusammenarbeit bei den Arbeiten zum Gauß'schen Ellipsoid Modell in begrenzten Geometrien. Dr. Albert Johner danke ich dafür, dass er mir mit seiner immensen analytischen Erfahrung an mancher Stelle weiter geholfen hat.

Für die finanzielle Unterstützung dieses Aufenthalts und meiner Arbeit im Rahmen des European Graduate College "Soft Condensed Matter" danke ich der Deutschen Forschungsgemeinschaft und dem Ministère de l'Education Nationale, de la Recherche et de la Technologie. Für die finanzielle Unterstützung im Rahmen des Sonderforschungsbereichs 513 "Nanostrukturen an Grenzflächen und Oberflächen" danke ich nochmals der Deutschen Forschungsgemeinschaft.

Für eine exzellente Systemadministration und Unterstützung bezüglich aller auftretender Computerprobleme sei Stefan Heinrichs, Dr. Jochen Hoffmann, Dr. Dirk Löding, und allen anderen, die damit zu tun hatten und zu tun haben, ganz herzlich gedankt.

Oliver Dürr und Falk Scheffler danke ich für das Korrekturlesen dieser Arbeit und ihre hilfreichen Verbesserungsvorschläge. Renate Beck hat mir das Leben nicht nur durch das Anfertigen von Abbildungen erleichtert, sondern vor allem auch sehr viel alltäglichen "Kleinkram" abgenommen. Dafür bin ich ihr sehr dankbar.

Ich danke meinen momentanen und ehemaligen Kollegen Ronny Bartsch, Ulrich Braunschweig, Roland Bunting, Joachim Buschle, Dr. Arno Heinen, Timm Höhr, Dr. Michael Kessler, Dr. Peter Pendzig, Dr. Johannes Reinhard, Jörg Rottler, sowie den bereits Genannten, für die angenehme Atmosphäre, die vielen fachlichen und nicht fachlichen Gespräche, die ungezählten Kuchen und dafür, dass ich mich in den letzten Jahren am Lehrstuhl Dieterich sehr wohl gefühlt habe.

Nicht zuletzt danke ich meinen Eltern für ihre stete, liebevolle Unterstützung.